Colloidal hard spheres: Triumphs, challenges, and mysteries

C. Patrick Royall[*]

*Gulliver UMR CNRS 7083, ESPCI Paris, Université PSL, 75005 Paris, France,
School of Physics, H. H. Wills Physics Laboratory, University of Bristol,
Tyndall Avenue, Bristol BS8 1TL, United Kingdom,
and School of Chemistry, University of Bristol,
Cantock's Close, Bristol BS8 1TS, United Kingdom*

Patrick Charbonneau

*Department of Chemistry, Duke University, Durham, North Carolina 27708, USA
and Department of Physics, Duke University, Durham, North Carolina 27708, USA*

Marjolein Dijkstra

*Soft Condensed Matter and Biophysics, Debye Institute for Nanomaterials Science,
Utrecht University, Princetonplein 1, 3584 CC Utrecht, The Netherlands*

John Russo

*Department of Physics, Sapienza University of Rome,
Piazzale Aldo Moro 5, 00185 Rome, Italy*

Frank Smallenburg

Université Paris-Saclay, CNRS, Laboratoire de Physique des Solides, 91405 Orsay, France

Thomas Speck

*Institut für Theoretische Physik IV, Universität Stuttgart,
Heisenbergstraße 3, 70569 Stuttgart, Germany*

Chantal Valeriani

*Departamento de Estructura de la Materia, Fisica Termica y Electronica,
Facultad de Ciencias Fisicas, Universidad Complutense de Madrid, 28040 Madrid, Spain*

(published 12 November 2024)

The simplicity of hard spheres as a model system is deceptive. Although the particles interact solely through volume exclusion, that nevertheless suffices for a wealth of static and dynamical phenomena to emerge, making the model an important target for achieving a comprehensive understanding of matter. In addition, while real colloidal suspensions are typically governed by complex interactions, Pusey and Van Megen [Nature **320**, 340 (1986)] demonstrated that suitably tuned suspensions result in hard-sphere-like behavior, thus bringing a valuable experimental complement to the renowned theoretical model. Colloidal hard spheres are thus both a material in their own right and a platform upon which phenomena exhibited by simple materials can be explored in great detail. The various purposes enable a particular synergy between experiment, theory, and computer simulation. The extensive body of work on colloidal hard spheres, which ranges from their equilibrium properties, such as phase behavior, interfaces, and confinement, to some of the nonequilibrium phenomena they exhibit, such as sedimentation, glass formation, and nucleation, is reviewed here.

CONTENTS

[*]Contact author: paddy.royall@espci.psl.eu

I. INTRODUCTION

Polymers, liquid crystals, surfactants, and colloidal dispersions are key material pillars of soft matter. While physicists have long focused on the study of the first three, colloids did not receive comparable attention until relatively recently. Only thanks to significant advancements in the synthesis of colloidal particles in the second half of the 20th century, motivated by both industrial interest (Vanderhoff *et al.*, 1956; Vincent, 2012; Tadros, 2018) and scientific curiosity (Fijnaut *et al.*, 1978), did the field come to light. The potential of hard-sphere-like colloidal dispersions as physical models of "simple liquids" exhibiting a fluid-crystal phase transition (Poon, Pusey, and Lekkerkerker, 1996; Frenkel, 2002; Evans, Frenkel, and Dijkstra, 2019) was subsequently developed by Hachisu and Kobayashi (1974), Kose and Hachisu (1974), and Vrij *et al.* (1978). Hard-sphere particles, which are impenetrable at distances less than their diameter σ and otherwise do not interact (see Fig. 1), had long been the object of theoretical enquiry but had until then largely remained but an experimental fantasy; see Sec. II.

During the 1960s, 1970s, and 1980s, advancements in colloid synthesis in industry (Walbridge and Waters, 1966; Barrett, 1973) and by pioneering colloid scientist Ron Ottewill (Cairns *et al.*, 1976; Antl *et al.*, 1986), combined with the
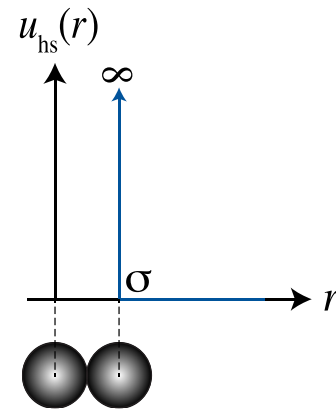

FIG. 1. Hard-sphere pair interaction potential $u_{hs}(r)$ as a function of the center-to-center distance r between particles of diameter σ.
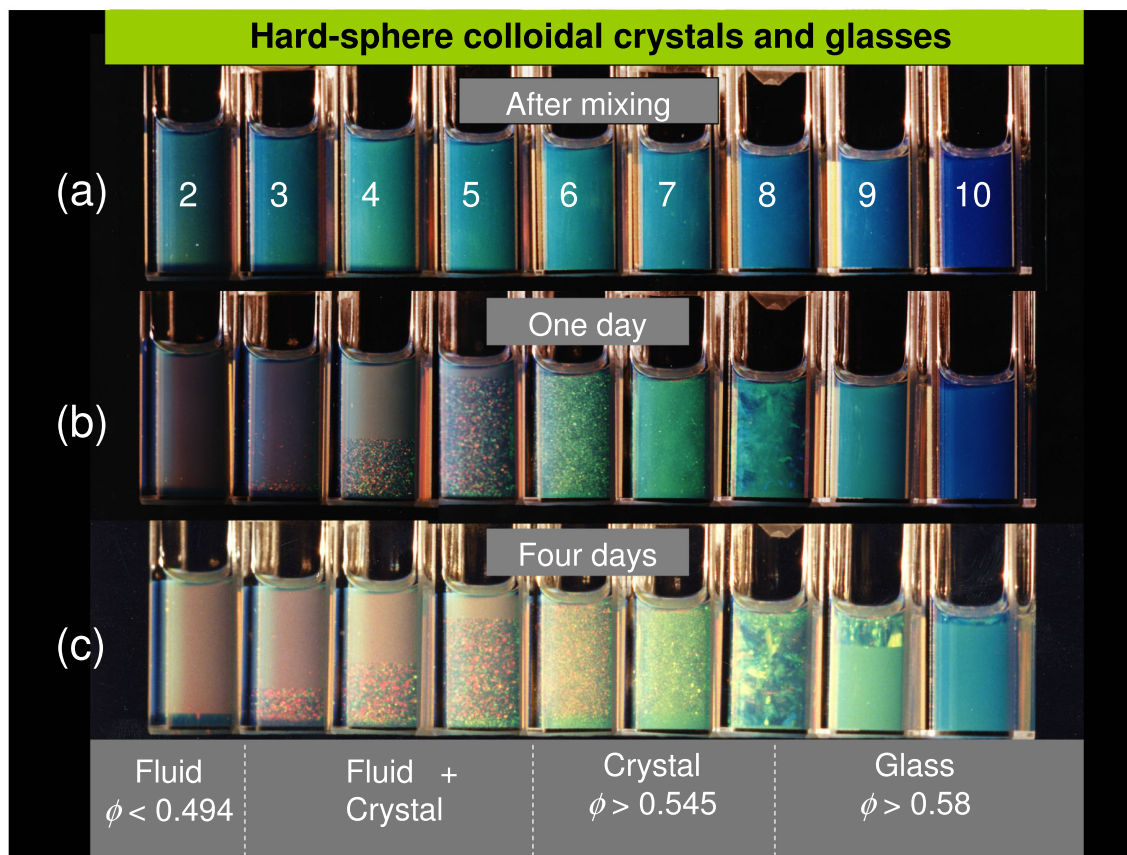
FIG. 2. The colloidal hard spheres observed by Pusey and van Megen are depicted (a) immediately, (b) one, and (c) four days after mixing. After four days, the system is presumed to have completed its phase separation. Volume fraction increases from left to right, with effective values (determined by reference to the phase behavior) $\phi = 0.491, 0.517, 0.525, 0.542, 0.568, 0.593, 0.611, 0.637$, and 0.654 for samples 2–10, respectively. The samples range from a fluid phase to a fluid coexisting with an iridescent crystal; at slightly larger volume fractions the entire sample is crystalline, while at yet higher volume fractions glassy amorphous states are encountered. These states initially "coexist" with the crystal until the entire sample may ultimately crystallize. From Pusey *et al.*, 2009.

application of light scattering by soft-matter physicists Peter Pusey and Bill van Megen, led to the development of a well-controlled colloidal model system (Fig. 2) (van Megen *et al.*, 1985, 1987; Pusey and van Megen, 1986). Pusey and van Megen then not only convincingly demonstrated hard-sphere freezing (Fig. 3), thus experimentally validating theoretical (Kirkwood and Monroe, 1940) and computer simulation (Alder and Wainwright, 1957; Wood and Jacobson, 1957) predictions from generations prior, but also (and perhaps more importantly) elegantly demonstrated the epistemic potential of colloidal suspensions.

Underlying the newfound physical interest is the fact that colloidal particles, like atoms and molecules, exhibit thermal motion that allows them to explore configurational space and self-assemble into different phases, such as colloidal crystals, liquids, and gases (Fig. 3). Of the plethora of possible colloidal systems, hard spheres have naturally emerged as the benchmark. Despite the challenge of synthesizing perfectly hard colloids, micron-sized hard spheres have four key strengths: (i) they have a single control parameter, the volume fraction ϕ; (ii) they are classical in nature, thus enabling accurate comparison with a broad array of theoretical predictions and large-scale computer simulation; (iii) they diffuse their own radius on the order of seconds, thus making their

dynamics readily accessible in experiments; and (iv) their size makes them amenable to optical techniques such as light scattering and confocal microscopy, thus enabling accurate measurements of spatial and dynamical correlations and even particle positions, without the need for large facilities such as synchotrons. Colloidal hard spheres are therefore prized model systems. Quantitative tests and validations with theory nevertheless remain challenging. In this review, we specifically take a critical look at what has been achieved and what challenges remain to be faced in using colloids to verify theory. We also emphasize the experimental observations that have yet to be given an accurate theoretical description.

To manage the scope of this review, we largely restrain our consideration to experiments with colloids. Only where exceptionally relevant do we mention work with nanoparticles [see Boles, Engel, and Talapin (2016) for a dedicated review] or with granular matter [for which reviews were given by Forterre and Pouliquen (2008), Liu and Nagel (2010), Torquato and Stillinger (2010), van Hecke (2010), Bi *et al.* (2015), Charbonneau *et al.* (2017), and Arceri, Corwin, and O'Hern (2023)]. Where possible, we have referenced relevant review papers from these other fields, but we request grace from the reader regarding important material that we may have missed. We nevertheless hope that our review conveys the
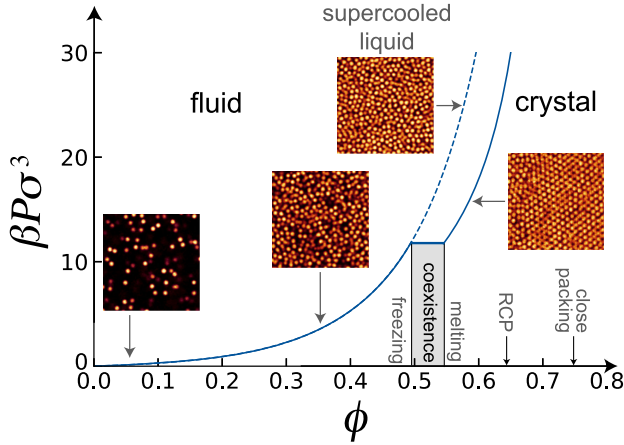
FIG. 3. Equation of state and phase diagram of hard spheres. The pressure $\beta P\sigma^3$ as a function of volume fraction ϕ [the solid blue (dark gray) line] is approximately given by the Carnahan-Starling expression (Carnahan and Starling, 1969) for the fluid and by that of Hall (1972) for the crystal. The metastable extension of the fluid branch [the dashed blue (dark gray) line] is where slow dynamics and the hard-sphere supercooled liquids and glass transition can be found; see Sec. XII. Indicated on the x axis are the fluid and crystal phases, along with freezing volume fraction $\phi_f = 0.492$, melting volume fraction $\phi_m = 0.543$, and phase coexistence at pressure $\beta P\sigma^3 = 11.6$; see Sec. VII.A. Also indicated are random close packing $\phi_{rcp} \approx 0.64$ and crystal close packing $\phi_{cp} = \pi/3\sqrt{2} = 0.740\ldots$. Approximate state points of the confocal microscopy images are denoted by gray arrows.

contention that similar behavior can be observed in very different systems, and that the transfer of ideas between these fields can be a fruitful source of future research objectives.

Even after taking these thematic restrictions into account, the Table of Contents hints at the wide reach of the remaining scope. Because at first glance going through this entire review may seem daunting, we note that Secs. II–VI deal with the historical perspective and methodology, with the results from hard-sphere colloids appearing in Sec. VII onward. We also single out a few highlights.

- Phase behavior: colloidal experiments confirm the entropy-driven fluid-crystal transition in hard-sphere systems; see Sec. VII.
- Fluid structure: experimental measures validate pair structure estimates and track the development of even higher-order structures; see Sec. VII.
- Interfaces: the interfacial free energy underlies the barrier to nucleation, and grain boundaries in hard-sphere systems form a fundamental model for a key failure mechanism in crystalline materials; see Sec. VIII.
- Binary mixtures: colloidal suspensions have fueled the exploration of the rich phase behavior of multicomponent systems; see Sec. IX.
- Confinement: the stabilization of a wealth of different structural arrangements of hard spheres has been achieved in both experiments and simulations; see Sec. X.
- Far-from-equilibrium behavior: hard spheres have been instrumental in disentangling hydrodynamic interactions from distortions of the local structure to, *inter alia*, shed light on the phenomenon of shear thickening; see Sec. XI.

- Glass transition: colloidal hard spheres have markedly advanced the understanding of glasses thanks to their simplicity and the possibility of imaging them in real space, thus providing access to a host of properties that are difficult to access in molecular systems; see Sec. XII.
- Nucleation: the ability to directly image hard spheres enabled the first direct observation of a critical nucleus, which has made it possible to test more stringently the approximations that underlie classical nucleation theory; see Sec. XIII.

We trust that this tantalizing selection will motivate at least a few of the more hesitant readers to continue through. In experiment, colloidal hard spheres are studied in three dimensions and quasi two dimensions. The majority of the work described in this review pertains to three dimensions, so where appropriate (quasi) two dimensions is explicitly mentioned.

Before embarking on the bulk of this review, a few essential quantities must be defined. We have already encountered the first one: the hard-sphere diameter σ; see Fig. 1. Although in theory it is a well-defined quantity, in practice it may refer to the effective diameter, the hydrodynamic diameter, or the mean diameter in a suspension of slightly size polydisperse colloidal particles; see Sec. III.D. The second quantity was also previously alluded to: the number density of N colloids within a volume V, i.e., $\rho = N/V$. More often, we will employ the dimensionless volume (or packing) fraction $\phi = Nv_1/V = \pi\sigma^3\rho/6$, with $v_1 = \pi\sigma^3/6$ the volume of a single three-dimensional (3D) sphere. The conjugate variable to density is the pressure P, our third quantity. It is often beneficial to consider the dimensionless reduced pressure $Z = \beta P/\rho$ (also known as the compressibility factor), which combines pressure with density and the inverse temperature $\beta = (k_B T)^{-1}$, where k_B is Boltzmann's constant and T is the temperature. Note that in the case of colloidal hard spheres, the relevant quantity is the *osmotic* pressure. The final quantity is the Brownian time taken by an isolated sphere to diffuse by its own radius

$$\tau_B = \frac{(\sigma/2)^2}{D_0} = \frac{3\pi\eta\sigma^3}{4k_B T}, \tag{1}$$

where D_0 is the bare diffusion coefficient and η is the solvent viscosity.

As Fig. 1 makes clear, the potential energy in a hard-sphere system is zero. This means that only entropy contributes to the phase behavior. Furthermore, provided that the temperature is nonzero, i.e., the system is thermal, temperature plays no role in the behavior of the system beyond scaling the timescale, as shown in Eq. (1). Note that it is this independence of temperature that leads to density (or volume fraction or pressure) being the sole control parameter for hard spheres.

II. HISTORICAL BACKGROUND

Given the extended and intricate history of hard spheres before they became an object of experimental study, a *longue durée* overview of the topic is in order. This section summarizes the distinct histories of hard spheres as a model of matter and as colloidal particles that mimic that model.

A. History of hard-sphere models

Describing atoms as hard elastic spheres (akin to billiard balls) finds its origin in the early days of the kinetic theory of gases (Brush, 2003). The laws of impact derived in the 17th century underlie the first such theory, which was formulated by Bernoulli in the early 18th century. That approach, however, was deemed disputable at the time and did not have much immediate scientific impact. Further formalization by Maxwell in the mid-1800s, which built explicitly on "systems of particles acting on each other only by impact," was more kindly received and substantially further developed (Brush, 2003). In the words of science historian Stephen Brush, this *exercise in mechanics* "not only helped establish the theory, but laid the foundations for modern statistical mechanics."

It is therefore unsurprising that van der Waals's attempt at a microscopic model of condensation, a couple of decades later, used a model effectively consisting of hard spheres with weak, fairly short-range attractive forces (Nairn and Kilpatrick, 1972; Brush, 1976).[1] Interestingly, van der Waals's description gave the correct second virial coefficient B_2 for the reference model (Brush, 1976). Virial coefficients, which characterize how the equation of state for the pressure P as a function of density ρ deviates from the ideal gas reference, i.e.,

$$Z = \frac{\beta P}{\rho} = 1 + \sum_i B_{i+1}\rho^i, \qquad (2)$$

quickly became an important tool to characterize models of intermolecular interactions. (An example is shown in Fig. 3. See Secs. VI.A and VII.C for further discussion.) For hard spheres, B_3 and B_4 were hence determined by Boltzmann before the end of the 19th century (Nairn and Kilpatrick, 1972). Beyond that point, however, the algebra is intractable. It therefore took more than 50 years and the advent of electronic computers for estimates of higher-order coefficients to be obtained. The numerical determination of B_5 by Rosenbluth and Rosenbluth (1954) renewed the quest for accurate estimates, which currently extend up to B_{12} (Clisby and McCoy, 2006; Wheatley, 2013).

Hard spheres also formed the basis for studying liquid structure. Early experiments with lead shot in the 1920s (Smith, Foote, and Busang, 1929) and with hard gelatin balls in the 1930s (Morrell and Hildebrand, 1936) were followed after the war by Bernal's extensive work with ball bearings (Bernal and Mason, 1960; Finney, 2013) and by more controlled theoretical descriptions, as further discussed in Sec. XII.H. Hard spheres also contributed to establishing the scaled particle theory of liquids (Reiss, Frisch, and Lebowitz, 1959) and were considered by Wertheim (1963) as a solution of the Percus-Yevick approximation to the Ornstein-Zernike equation that formally describes the liquid structure. Hard spheres were subsequently a natural object for other integral equation approaches (Rowlinson, 2005; Hansen and McDonald, 2013); see also Sec. VI.A.

A parallel research effort into hard spheres stemmed from Kirkwood's speculation (Kirkwood, 1939), which he quickly substantiated with his postdoctoral research associate Elizabeth Monroe (Kirkwood and Monroe, 1940, 1941; Kirkwood, 1951), that a hard-sphere fluid becomes unstable to crystallization at high density (Hoddeson *et al.*, 1992; Charbonneau, 2025); see Fig. 3. The somewhat surprising proposal that the ordered phase could be entropically more favorable than the dense (and disordered) liquid was independently formulated by Fisher (1955) a decade later and validated by early simulations using molecular dynamics by Alder and Wainwright (1957) and Monte Carlo sampling by Wood and Jacobson (1957).[2] The physicality of such a phenomenon, however, was not immediately obvious. The debate notably included a couple of even-split votes about the question at conferences (Uhlenbeck *et al.*, 1963). The result nevertheless seeded a plethora of computational advances, as recently reviewed by Battimelli, Ciccotti, and Greco (2020).

The study of the crystal state of hard spheres also has a long history. (That of disordered jammed packings of hard spheres is somewhat more recent; see Sec. XII.H.) The Kepler conjecture for their densest packing (their infinite-pressure state with a packing fraction $\phi_{cp} = \pi/3\sqrt{2}$) dates back to the 17th century and was rigorously proven by Hales only this century (Aste and Weaire, 2008; Hales *et al.*, 2017). Finite-pressure descriptions of hard-sphere crystals are less ancient but have reasonably rich antecedents as well. Their familiar description in terms of free volume, known as cell theory (Sec. VI.B), takes root in various attempts to characterize the *liquid state* in the 1930s (Rowlinson, 2005). The free-volume description became a useful reference for hard-sphere crystals only in the 1950s (Wood, 1952; Salsburg and Wood, 1962) and persists to this day in the pedagogical literature (Barrat and Hansen, 2003; Kamien, 2007). However, because the associated corrections are less well controlled and are computationally harder to evaluate than for the virial series [see Charbonneau, Morse *et al.* (2021) and references therein], cell theory has not been as quantitatively influential.

B. The foretelling: How PMMA colloids came to be

Despite the extended theoretical importance of hard spheres, the system long remained but a distant abstraction as far as experiments were concerned. It is only through a gradual increase in the control over colloidal experiments that the state of affairs has changed. In this section, we focus on the developments that have led to the sterically stabilized polymethyl methacrylate (PMMA) system. Although other systems have been used such as sterically stabilized silica, aqueous electrostatically stabilized systems such as polystyrene and silica, and what are now termed microgels (for example, synthesized from polystyrene) (Russel, Saville, and Schowalter, 1989; Hunter, 2001; Royall, Poon, and Weeks,

---

[1]We now know the van der Waals equation of state to be exact only for a one-dimensional system with infinitely long-range and weak attraction (Kac, Uhlenbeck, and Hemmer, 1963; Hansen and McDonald, 2013; Niss, 2018).

[2]It is important to note that the contributions of coders for many of these works were not acknowledged through authorship (Battimelli, Ciccotti, and Greco, 2020). The author lists of these works therefore do not fully reflect the array of intellectual contributions that went into their realization.

2013) (see Sec. III.B), PMMA-based colloids have predominated since their introduction. During the first 10–15 years of its use[3] and as the field burgeoned, any particle softness has been attributed to the steric stabilization layer, which is much shorter than the particle diameter. Because PMMA particles have a bulk modulus that is orders of magnitude larger, the tiny stabilization layer only slightly perturbs the system away from true hard-sphere behavior; see Sec. III.C.

The origins of modern colloid science may be traced back to the latter part of the 19th century with the emergence of physical chemistry as a distinct discipline (Vincent, 2012, 2018) and early discoveries such as the first synthetic suspension of optically active gold nanoparticles by Faraday (1859) and the use of colloidal sedimentation profiles to determine Boltzmann's constant by Perrin (1913). A major challenge to the use and application of colloidal suspensions is that they typically aggregate irreversibly when concentrated. Understanding of this phenomenon took a great leap forward with the independent development during World War II [by Derjaguin and Landau (1941) in the Soviet Union and by Verwey and Overbeek (1948) in the Netherlands] of the Derjaguin-Landau-Verwey-Overbeek (DLVO) theory for the interactions between charged colloids. The DLVO theory notably provided a first-principles explanation for the long-noted *salting out* phenomenon for aqueous suspensions of both colloids and proteins, in which salt addition leads to aggregation and precipitation.

Colloid synthesis further progressed in the postwar years (Vanderhoff *et al.*, 1956; Ihler, 1979), not least because certain industrial products, especially paint and coatings, called for novel stabilization schemes (Barrett, 1973). It had long been known that adding colloidal spheres to a solution increases viscosity (Batchelor, 1967), hence when in the 1960s control was sought over the rheology of paint and coatings, adding colloids seemed like a natural solution. However, these largely oil-based products [this being long before legislation promoted the use of water-based coatings, which release fewer volatile organic compounds as they dry (Derksen, Cuperus, and Kloster, 1995)] called for stabilizing colloids in nonaqueous solvents. In these systems, electrostatic charging was assumed to be negligible and therefore incapable of stabilizing colloidal dispersions. [It was not until the turn of the third millennium that electrostatic charging in nonaqueous solvents would be investigated thoroughly; see Sec. III.C (Yethiraj and van Blaaderen, 2003; Roberts *et al.*, 2007; Royall, Poon, and Weeks, 2013; Royall *et al.*, 2021).] Another method for stabilization was therefore sought out.

Inspiration came from prior advances in polymer physics, notably those of Flory (de Gennes, 1979). The loss of configurational entropy for polymers grafted to surfaces was proposed as a colloidal stabilization mechanism. Early work included the stabilization of carbon black through physisorption of aromatic hydrocarbons (van der Waarden, 1950; Overbeek, 1966). In the 1960s, steric stabilization was first combined with a relatively monodisperse nonaqueous colloidal system at Imperial Chemical Industries (ICI), a major paint and coating manufacturer of the time, by coating PMMA particles with polyhydroxysteric acid (PHSA) (Walbridge and Waters, 1966; Barrett, 1973). In the UK, leading academic research in colloids was then taking place at Cambridge University, University College London, and the University of Bristol (Vincent, 2012). In Bristol, in particular, Ottewill had strong links with ICI from where sterically stabilized PMMA was initially obtained. Once synthesized at Bristol (Cairns *et al.*, 1976), these particles played a central role in the hard-sphere story. They not only closely approximated the model of interest but also were amenable to solvents that match their refractive index and mass density. As we later see, the former is essential for light scattering (Sec. IV.A), and both are necessary for confocal microscopy (Sec. IV.B).

In 1974, Ottewill met Pusey, who was then based at Malvern, close to Bristol, and the two became interested in exploring light scattering as a means of studying strongly interacting colloidal systems (Pusey, Vaughan, and Williams, 1974; Brown *et al.*, 1975) and of studying the PMMA system (Brown *et al.*, 1975). With the arrival in Bristol of van Megen from the Royal Melbourne Institute of Technology and through a series of extended back-and-forth visits, Ottewill's ability to synthesize the hard-sphere-like PMMA and Pusey's interest in these systems naturally led to the series of seminal papers that gave rise to Fig. 2; see van Megen *et al.* (1985, 1987) and Pusey and van Megen (1986, 1987).

III. REALIZING HARD-SPHERE SYSTEMS

In this section, we discuss the main experimental methods that have been brought to bear on the study of colloidal hard spheres. For a more general treatment of colloidal synthesis, see the reviews by Ihler (1979), Russel, Saville, and Schowalter (1989), and Hunter (2001). We emphasize that in experiments truly hard spheres do not exist (Poon, Weeks, and Royall, 2012; Royall, Poon, and Weeks, 2013). To show how far real experimental systems deviate from hard spheres, we discuss different mappings to hard spheres in Sec. III.D.

A. Experimental methods to prepare hard-sphere-like systems

Experimental techniques for colloidal hard spheres fall into three main categories: synthesis, characterization, and observation. Spanning the chemical synthesis, design, and construction of suitable apparatuses (in particular, light-scattering setups and microscopes), as well as data analysis, experiments on hard-sphere-like systems are truly multidisciplinary. It is common for particular individuals to focus on one or two of these. Concerning synthesis, we note that there is no commercial supplier for the canonical sterically stabilized PMMA suspensions[4] discussed in Sec. II.B. [A short review of PMMA synthesis was given by Dullens (2006).] Here we focus mainly on the characterization and observation of colloidal hard-sphere suspensions.

---

[3]Specifically, before the density matching of larger PMMA particles for confocal microscopy around the millenium; see Sec. III.C.

[4]Even worse, the PHSA synthesis is challenging to reproduce, leading to polydisperse, or colloidally unstable, PMMA particles. At present the global stocks of PHSA are less than 10 kg.

In addition to identifying the "hardness" of individual particles (see Sec. III.C), determining the polydispersity of the overall suspension is also key. This property is typically expressed[5] as the standard deviation of the particle diameter normalized by the mean diameter expressed as a percentage s. For PMMA synthesis, a "good" level of polydispersity is considered to be $s \lesssim 5\%$, such that the system crystallizes as readily as in the monodisperse case. (See Sec. VII.B for a detailed discussion of the impact of polydispersity on the phase behavior.) Colloids produced from other materials, such as polystyrene, can exhibit significantly lower polydispersity down to $s \approx 1\%$ (Vanderhoff *et al.*, 1956; Russel, Saville, and Schowalter, 1989).

We emphasize that polydispersity distributions in experimental systems cannot be prescribed. While in numerical simulations one may easily change from Gaussian, to top hat or log-normal distributions, in experiments the distribution is at the mercy of the particular synthesis. Even bimodal distributions can arise following secondary nucleation reactions that give rise to a second wave of colloids (Kawaguchi and Ito, 2005).

B. Synthesizing hard-sphere-like colloidal particles

The method adopted for PMMA synthesis was *dispersion polymerization* (Barrett, 1973; Kawaguchi and Ito, 2005). In this approach, the methyl-methacrylate monomers and methacrylic acid are dispersed in a suitable solvent (typically an alkane). Under the action of an *initiator*, polymerization begins at a somewhat elevated temperature (around $80\,^\circ\mathrm{C}$) and in principle proceeds until the monomer is exhausted. Relatively early in the polymerization process, the initially transparent solution acquires a bluish tint due to the growing polymers falling out of solution and condensing into colloids that scatter predominately blue light. As the particles grow, the suspension turns white as the colloids begin to scatter light of all wavelengths. PHSA is added to the synthesis and is typically physisorbed to provide steric stabilization. In this way, the sterically stabilized PMMA system was born (Walbridge and Waters, 1966; Barrett, 1973; Cairns *et al.*, 1976; Antl *et al.*, 1986). The monomer concentration controls the particle size, thus enabling binary systems with a given size ratio to be synthesized or a system whose size optimized density matching (easier with small particles) against higher-quality imaging (better with large particles) (Bosma *et al.*, 2002; Poon, Weeks, and Royall, 2012).

Synthetic improvements include (i) partial control over the particle size by the monomer concentration (Bosma *et al.*, 2002; Poon, Weeks, and Royall, 2012), (ii) locking the stabilizer such that it is covalently bonded to the PMMA polymer backbone, and (iii) cross-linking the PMMA chain. The last characteristic prevents particles from swelling and dissolving in a good solvent. Using such cross-linked

particles as a core is important for confocal microscopy because it enables a PMMA shell to be grown around the particle[6] (Dullens *et al.*, 2003; Dullens, 2006): if the initial step (the core) is labeled with a fluorescent dye and the shell is unlabeled, then tracking particle locations with confocal microscopy is much easier, thanks to the clean separation between different fluorescent cores (van Blaaderen, Imhof *et al.*, 1992; Ivlev *et al.*, 2012); see Sec. IV.B.

While many key early hard-sphere experiments were carried out with sterically stabilized PMMA, and indeed most of the work that we consider used PMMA colloids, it is far from the only material of interest. Silica may also be stabilized in a nonaqueous solvent (van Helden and Vrij, 1980). Aqueous systems of polystyrene and silica colloids form reasonable approximations to hard spheres, as do microgel particles (Royall, Poon, and Weeks, 2013) and emulsion droplets (Dong *et al.*, 2022). Because the diameter of microgel particles can be tuned *in situ*, the effective volume fraction can be changed at will, and therefore a single sample can access multiple state points (Yunker *et al.*, 2014).

Two promising systems have been developed more recently. One involves the use of an aqueous copolymer of fluorinated methacrylate and methacrylate with a tunable density and refractive index, as demonstrated by Kodger, Guerra, and Sprakel (2015). The other involves the use of 3-(trimethoxysilyl)propyl methacrylate particles (Liu *et al.*, 2016, 2019; van der Wel *et al.*, 2017). Impressive results also have been obtained with nanoparticles, whose small size enables faster diffusion than for the larger colloids and their self-assembly into larger structures (Boles, Engel, and Talapin, 2016); see Sec. IV.C. Early work in the same size range used microemulsions, which are thermodynamically stable droplets of nanometer dimensions (despite their name).

C. Interactions in real hard-sphere-like systems

Central to identifying the state point of a hard-sphere-like system is determining the effective volume fraction ϕ_{eff}, as reviewed by Poon, Weeks, and Royall (2012) and Royall, Poon, and Weeks (2013). The notion of an effective hard-sphere diameter is more fully discussed in Sec. III.D, but we here introduce interactions commonly used in experiments to mimic hard spheres. We consider two particle diameters $\sigma = 200$ and 2000 nm, which roughly reflects the range of colloid sizes used in the work discussed here. We note the impact of the colloid size upon the system dynamics (Sec. IV.C) and their applicability for particular experimental techniques (Sec. IV).

While we have discussed the origins of some hard-sphere experimental systems, we should assess how close to hard spheres these truly are (Poon, Weeks, and Royall, 2012; Royall, Poon, and Weeks, 2013). Here we provide a summary for the purposes of this review. Practical hard-sphere-like systems fall into three broad categories, as illustrated in Fig. 4. Colloidal stabilization can be achieved either via (a) steric

---

[5]An unbiased way to characterize the distribution remains to be identified. Even the laborious method of sizing every particle by electron microscopy likely samples from a biased set of particles due to inhomogeneities during evaporation in preparing the sample.

[6]The particles used by Kose and Hachisu (1974) had little in common with modern PMMA particles other than their chemical nature. In particular, they were not sterically stabilized.
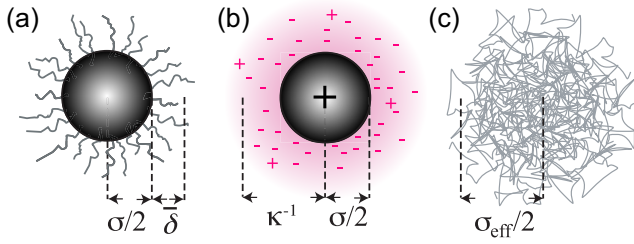
FIG. 4.   Schematic representation of various models for hard-sphere colloids. (a) A sterically stabilized particle has surface "hairs" (not to scale) of average thickness $\bar{\delta}$, resulting in a core-stabilizer diameter $\sigma_{cs} = \sigma_c + 2\bar{\delta}$. (b) A charged colloid has an electrical double layer (shaded area) that gives rise to an effective diameter σ_{eff}. (c) A microgel particle is a heavily cross-linked polymer. From Royall, Poon, and Weeks, 2013.

FIG. 5.   Estimate of effective colloid-colloid interactions for various hard-sphere-like scenarios for particle diameters (a) $\sigma = 200$ nm and (b) $\sigma = 2000$ nm. Shown is steric stabilization [the pink (pale gray) line], a strong electrostatic interaction [the solid blue (dark gray) line], and a weak electrostatic interaction [the dashed blue (dark gray) line]. See the text for additional details. From Royall, Poon, and Weeks, 2013.

stabilization or (b) charge stabilization. Because (c) microgel particles consist of densely cross-linked polymers in a swelling solvent, they do not explicitly need stabilization (Lyon and Fernandez-Nieves, 2012; Schneider *et al.*, 2017). The hardness of microgel colloids depends on the quality of the solvent and the degree of cross-linking and can be density dependent (Royall, Poon, and Weeks, 2013). Emulsion droplets are an intermediate case. They use a molecularly thin layer of surfactant for stabilization. Although these particles are liquid, even a microscopic ($\lesssim 1$ nm^2) change in surface area leads to an interfacial free-energy cost of the order of $k_{\text{B}}T$. The softness of mesoscopic-scale droplets is therefore limited (Morse and Witten, 1993; Lacasse, Grest, and Levin, 1996; Dong *et al.*, 2022). However, in practice excess surfactant in solution can act to significantly reduce the free-energy cost of increasing surface area, and therefore emulsion droplets can often be easy to deform.

Softness due to stabilization. A sterically stabilized particle is shown schematically in Fig. 4(a). Royall, Poon, and Weeks (2013) previously reviewed ways to obtain an effective hard-sphere diameter for these particles by mapping various hard-sphere properties; see Sec. III.D. A mapping is also possible via direct measurements of colloidal interactions. This procedure has been applied to polyhydroxystearic acid-stabilized PMMA particles, whose interactions were measured with the surface force apparatus and were found to be well described by an inverse power-law potential with energy scale[7] ϵ_{ipl} (Bryant *et al.*, 2002),

$$u_s(r) \approx \epsilon_{\text{ipl}} \left(\frac{\sigma}{r}\right)^n, \tag{3}$$

where σ denotes the particle diameter and r indicates the interparticle distance. The relative range of u_s depends on the particle size. For example, $n = 170$ was determined for particles with a diameter of $\sigma = 200$ nm. Likewise, the strength of the interactions also depends on the particle size, with $u_s(\sigma) = 146 \, k_{\text{B}}T$ reported for $\sigma = 200$ nm, as indicated

by the pink line in Fig. 5(a). For larger particles ($\sigma = 2000$ nm), $n = 1800$ and $u_s(\sigma) \approx 1800 k_{\text{B}}T$ were determined [Fig. 5(b), pink line] (Bryant *et al.*, 2002). The results of Bryant *et al.* (2002) quantified what is physically obvious, namely, that for a fixed length of stabilizing hairs larger particles are relatively harder. Similar conclusions were obtained in the rheological study of Mewis *et al.* (1989), who varied the thickness of the stabilizing layer.

Electrostatics. It is now generally accepted that immersion of a colloid in a liquid gives rise to some degree of charging (Yethiraj and van Blaaderen, 2003; Leunissen, 2006; Roberts *et al.*, 2007; Royall, Poon, and Weeks, 2013). This charge is a potential source of softness that should always be considered in experiments. In determining the degree of softness due to electrostatic interactions, the linearized Poisson-Boltzmann theory is incorporated into the DLVO theory (Verwey and Overbeek, 1948) to describe the interactions between charged colloids. The original DLVO potential consists of van der Waals (vdW) and electrostatic components. The vdW contribution often becomes small due to refractive index matching between colloids and solvent, as in the case of light scattering or 3D microscopy. In the case of quasi-2D systems or techniques that do not require index matching, such as rheology, electrostatic stabilization ensures that particles do not come sufficiently close together for vdW interactions to become important. Therefore, we henceforth neglect vdW interactions except where explicitly stated.

We are often interested in systems in which sterically stabilized particles become charged. In this case, we can consider an interparticle potential consisting of a steric repulsion $u_s(r)$ and an electrostatic interaction, which in linearized Poisson-Boltzmann theory has a Yukawa form $u_{\text{Yuk}}(r)$,

$$u(r) = u_s(r) + u_{\text{vdW}}(r) + u_{\text{Yuk}}(r), \tag{4}$$

$$u_{\text{Yuk}}(r) = \epsilon_{\text{Yuk}} \frac{\exp\left[-\kappa(r - \sigma)\right]}{r/\sigma}, \tag{5}$$

where $\kappa = \sqrt{4\pi\lambda_B \rho_{\text{ion}}}$ is the inverse Debye screening length, with ρ_{ion} the number density of monovalent counterions and

---

[7]While an inverse power law is, of course, long-range, unlike the steric stabilization, here we follow the work of Bryant *et al.* (2002).
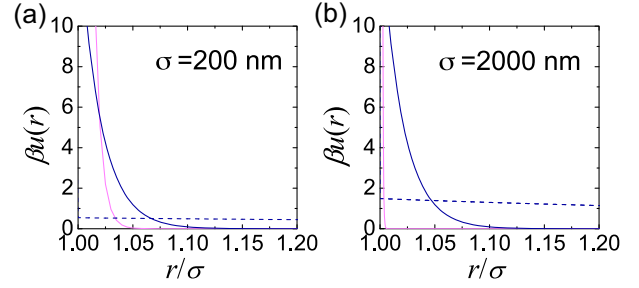
coions, and ϵ_{Yuk} denotes the contact value of the Yukawa interaction given by

$$\beta\epsilon_{\mathrm{Yuk}} = \frac{Z_e^2}{(1 + \kappa\sigma/2)^2}\frac{\lambda_B}{\sigma}, \tag{6}$$

with Z_e the number of electronic charges on the colloid. The Bjerrum length

$$\lambda_B = \frac{e^2}{4\pi\epsilon_0\epsilon_r k_{\mathrm{B}}T} \tag{7}$$

is the distance at which the interaction energy between two elementary charges equals $k_{\mathrm{B}}T$, e is the electronic elementary charge, ϵ_0 is the permittivity of the vacuum, and ϵ_r is the relative dielectric constant.

We first consider the case of aqueous systems in which the charging is strong. In three dimensions, most work with aqueous systems has used rather small colloids. We estimate the electrostatic interaction potential by plotting the solid blue line in Fig. 5(a), where we evaluate the Yukawa interaction (5) as follows. We assume that salt is added such that the Debye length is 4 nm. It has been suggested that an upper bound for the effective charge in many systems (Alexander *et al.*, 1984) can be described by the rule of thumb $Z_e\lambda_B/\sigma \approx 6$. For higher values of the colloid charge, the electric field at distances beyond the Stern layer reduces to the electric field corresponding to the effective charge due to ion condensation (Alexander *et al.*, 1984; Russel, Saville, and Schowalter, 1989). For colloids with $\sigma = 200$ nm in water, this leads to an effective colloid charge of $Z_e = 1500$. The resulting electrostatic interaction [represented by the solid blue line in Fig. 5(a)] demonstrates a noticeable degree of softness.

Sterically stabilized PMMA is used in nonaqueous solvents. For example, the work of Pusey and van Megen (1986) used a mixture of *cis*-decalin and carbon disulfide with a dielectric constant $\epsilon_r = 2.64$, which leads to a Bjerrum length $\lambda_B \approx 21$ nm. With ionic sizes in the range of $\lesssim 1$ nm, one expects strong coupling between oppositely charged ions and, consequently, little dissociation of surface groups. It was therefore a long-held assumption that electrostatics could be safely neglected. However, more recent work has demonstrated that some electrostatic charging is always present (Yethiraj and van Blaaderen, 2003; Leunissen, 2006; Roberts *et al.*, 2007; Klix *et al.*, 2013).

To evaluate electrostatic interactions in solvents with such low dielectric constants, we again use the $Z_e\lambda_B/\sigma \approx 6$ criterion with a Debye length of $\kappa^{-1} = 5$ μm, which is consistent with measurements of the small ionic strength found in such solvents (Klix *et al.*, 2013). We can then evaluate Eq. (5) for particles with diameters of $\sigma = 200$ and 2000 nm [the blue dashed lines in Figs. 5(a) and 5(b), respectively]. The electrostatic repulsion changes only slightly over the chosen range. Note that for smaller particles ($\sigma = 200$ nm) these parameters correspond to an electrostatic charge of just $Z_e = 2$. Although small, comparable values have been measured in experiments (Klix *et al.*, 2013). In this case, it is highly probable that the spherically symmetric DLVO approach would not be accurate. However, the effects seem

to be small enough that one can reasonably neglect electrostatic charging for this combination of solvent dielectric constant and particle size. Larger colloids, however, require density matching to suppress sedimentation. Since two of the denser solvents used in experiments, namely, tetrachloroethylene (TCE) and carbon tetrachloride, can be readily absorbed by PMMA, both the density and the refractive index of the particles change, resulting in a turbid system characterized by substantial vdW attractions. The hard-sphere-like behavior of the particles is then lost (Ohtsuka, Royall, and Tanaka, 2008; Royall, Poon, and Weeks, 2013). Recent work has nevertheless found excellent hard-sphere behavior using a solvent mixture with TCE (Kale *et al.*, 2023).

Finally, we consider stronger electrostatic charging in the PMMA system often applied in studies using confocal microscopy for larger colloids with $\sigma = 2000$ nm. The solvents used for light scattering with the smaller PMMA particles have a relative dielectric constant of $\epsilon_r \approx 2$. Relative to these, the density matching mixture of cyclohexyl bromide (CHB) and *cis*-decalin has a dielectric constant of $\epsilon_r = 5.4$, which is due to the CHB component with $\epsilon_r = 7.9$. While nonaqueous, the dielectric constant is nevertheless much higher than the aforementioned one and tetrabutyl ammonium bromide (or a similar salt) is typically used to screen the electrostatic interactions (Yethiraj and van Blaaderen, 2003). CHB advantageously appears to be less aggressive toward the PMMA particles than does TCE, for example, with less absorption and swelling. If we again use the same criterion $Z_e\lambda_B/\sigma \approx 6$, we arrive at $Z_e \approx 500$. The Debye length corresponding to a saturated solution of this salt is around $\kappa^{-1} \approx 100$ nm (Royall, Leunissen, and van Blaaderen, 2003; Leunissen, 2006; Royall *et al.*, 2006). Evaluating Eq. (5) then gives the solid blue line in Fig. 5(b), which exhibits a considerable degree of softness. Therefore, for the larger PMMA particles, which require density matching, one can either accept some softness and add salt or risk attractions due to solvent absorption (in the case of TCE, for example).

Imaging quasi-2D or strongly confined systems [obtained, for example, by sedimenting particles onto a substrate (Ivlev *et al.*, 2012)] is somewhat exempted from such drawbacks. For example, polystyrene colloids in an aqueous solvent with a suitable amount of salt added are hard, as the Debye length of a few nanometers is much less than the micron-scale particle diameter (Royall, Poon, and Weeks, 2013). Particles with a size of 3–5 μm are readily imaged and their gravitational length[8] can be $\approx 0.01\sigma$, so out-of-plane motion is small (Marcus and Rice, 1997; Brunner *et al.*, 2003; Williams *et al.*, 2013, 2015; Yunker *et al.*, 2014; Thorneywork, Abbott *et al.*, 2017).

D. Mapping soft spheres to hard spheres

As discussed, real colloids inevitably display some degree of softness. To compare experiments with theory and simulations, it is therefore important to be able to map the behavior

---

[8]The gravitational length is a measure of vertical movement due to thermal energy; see Sec. XI.A.

of colloids to that of perfect hard spheres. Mapping entails finding an effective hard-sphere diameter σ_{eff} such that one may translate the experimentally controllable particle number density ρ to an effective hard-sphere volume fraction ϕ_{eff} using $\phi_{\text{eff}} = \pi \sigma_{\text{eff}}^3 \rho / 6$. Two distinct approaches can be used to determine σ_{eff}: directly from the interaction potential and indirectly from the observed behavior of the system. The latter method rests on the assumption that the weight fraction (which may be accurately determined) at freezing may be taken to correspond to the freezing volume fraction. This provides a calibration of the volume fraction through an accurately known quantity. Developments of this method to address the effects of gravitational settling are discussed in Sec. VII.

For a known interaction potential, several analytical routes to estimate an effective hard-sphere diameter have been proposed. Arguably the simplest one is to set an effective hard-sphere diameter σ_{kT} such that the interparticle repulsive energy at this center-to-center separation between two particles is equal to the thermal energy $k_{\text{B}}T$. A more sophisticated approach that entails taking into account the functional behavior of the pair interaction was proposed by Barker and Henderson (BH) (Barker and Henderson, 1967),

$$\sigma_{\text{BH}} = \int_0^\infty dr \{1 - \exp[-\beta u(r)]\}. \tag{8}$$

An alternative mapping due to Andersen, Weeks, and Chandler (1971) takes into account the structure of a hard-sphere reference fluid at the same density, making the effective diameter density dependent. This approximation has been shown to be effective for mapping the structural relaxation time of soft spheres near the glass transition to the hard-sphere model (Schmiedeberg *et al.*, 2011). For the commonly used Weeks-Chandler-Andersen potential (Weeks, Chandler, and Andersen, 1971), both the Barker-Henderson and Andersen-Weeks-Chandler mappings have been shown to provide excellent phase behavior predictions at sufficiently low temperatures (Dasgupta, Coli, and Dijkstra, 2020; Attia, Dyre, and Pedersen, 2022). However, for higher temperatures (or, equivalently, particles that are less hard-sphere-like) significant deviations emerge. As a result, care is needed when interpreting the results of this type of mapping in colloidal systems (Royall, Poon, and Weeks, 2013). The situation is illustrated for a model system of charged colloids in Fig. 6, where the fluid-crystal phase boundaries from simulations (Hynninen and Dijkstra, 2003) are mapped to hard spheres using σ_{kT} and σ_{BH}. Both approaches present significant deviations from true hard spheres. The fluid-crystal coexistence gap is also narrower than that for the model system. Therefore, as corroborated by simulation work showing that nucleation barriers continue to be sensitive to the softness even at screening lengths on the order of a few percent of the particle diameter (de Jager and Filion, 2022), simply obtaining σ_{eff} may not suffice to confidently reproduce hard-sphere behavior.

The second option is to measure quantities that depend on volume fraction. Structural quantities such as the radial distribution function may be compared with simulation or theory (Royall, Louis, and Tanaka, 2007; Thorneywork *et al.*,
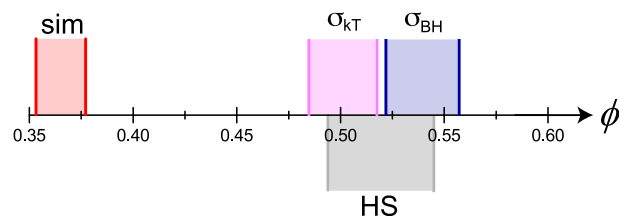

FIG. 6. Mapping the phase behavior of weakly charged hard-core colloids to pure hard spheres. The hypothetical particles have a diameter $\sigma = 2$ μm and an electrostatic charge $Z = 500$. The Debye screening length of the solvent is $\kappa^{-1} = 100$ nm, which is typical for nonaqueous solvents (Royall, van Roij, and van Blaaderen, 2005). The fluid-solid coexistence gap of the hypothetical charged-colloid system as a function of the packing fraction ϕ is taken from simulations (red, "sim") (Hynninen and Dijkstra, 2003) and is mapped to pure hard spheres while assuming that the effective hard-sphere diameter corresponds to the interaction potential $\beta u(\sigma_{\text{kT}}) = 1$ (lilac, σ_{kT}) and using the mapping of Eq. (8) (blue, σ_{BH}). The phase diagram of pure hard spheres (gray, HS) is shown for comparison.

2014; Royall, Williams, and Tanaka, 2018; Kale *et al.*, 2023); see Sec. VII.D. However, for dense hard spheres, these pair correlations vary slowly with ϕ. Alternatively, one can choose a quantity that strongly depends on ϕ, such as the relaxation time at high volume fraction (see Fig. 39 in Sec. XII) or higher-order structural observables (see Fig. 15 in Sec. VII.D) (Pinchaipat *et al.*, 2017; Royall, Williams, and Tanaka, 2018). However, it is important to note that there is absolutely no guarantee that different methods give the same mapping. For example, higher-order structure measurements are highly sensitive to missing (or "ghost") particles (see Sec. IV.B), while measuring dynamics in real space is more sensitive to errors in particle positions.

In short, nearly hard spheres, whether realized in experiments or in simulations, can closely approach the behavior of true hard spheres, but subtle differences persist. Choosing an effective diameter is an essential step in assigning an effective packing fraction to an experimental system, and hence in comparing its behavior to hard-sphere simulations or theory. However, no unambiguous definition of such an effective packing fraction exists, and different approaches result in different estimates.

E. Accuracy in hard-sphere experiments

The previous discussion makes clear that, with care, an effective hard-sphere volume fraction may be deduced for an experimental system, but a degree of uncertainty necessarily persists due to (i) softness arising from electrostatics, stabilization, or other sources; (ii) attraction originating from vdW interactions or other sources; and (iii) polydispersity[9] s. These features pertain to the particles alone. For nonaqueous systems, in particular, other parameters might affect the state point, including the solvent choice, its age and purity, and the

---

[9]There are even occasional reports of breakdowns in spherical symmetry in the effective interactions (Reinke *et al.*, 2007; Klix *et al.*, 2013).

ambient temperature and humidity (which are often not controlled in colloid laboratories).

Even if these uncertainties could somehow be mitigated, there remains a fundamental aspect of colloidal systems that sets them apart from most materials in that model colloids are a synthetic material. As noted, sterically stabilized PMMA colloids, for instance, cannot be purchased commercially; they need to be synthesized, typically in small batches of 10–1000 g. Therefore, even if the aforementioned quantities were somehow characterized for a given synthesis (which would entail a sizable amount of work), once that batch is exhausted, the operation would need to be carried out again for a subsequent synthesis.

In other words, colloidal systems are not as well characterized as atomic and molecular systems. One container of argon of sufficient purity has the same characteristics as another container of the same material. However, like homemade cakes, colloidal hard spheres from two different syntheses are nonidentical. That is, the concept of an accurate measurement of a physical property fundamentally differs. For example, the triple point temperature of argon is 83.8058 K, i.e., known to six significant figures, drawing on many successive and increasingly accurate measurements of the same material. Such an accuracy is essentially impossible to achieve in colloids. This realization brings us to the question of just how much accuracy can be expected in colloidal experiments. Poon, Weeks, and Royall (2012) concluded that a relative error in volume fraction around the freezing transition of 6% might be reasonable. Our opinion is that when careful comparisons are made, as described in Sec. III.D, an absolute error of 1% in the volume fraction seems to be achievable, albeit not always realized. In the remainder of this review, we revisit the impact of colloidal-level accuracy when appropriate.

A more far-reaching interpretation of accuracy in the context of this review is to consider what is meant by *hard* spheres. This matter is not as straightforward as it might first seem, as whether or not a system is sufficiently similar to hard spheres depends on the physical property considered. For example, it has long been known that even soft repulsive particles have a fluid structure similar to that of hard spheres (Weeks, Chandler, and Andersen, 1971). By contrast, phase boundaries are highly sensitive to the interaction details. For this review, we state that systems that are not hard-sphere-like (i) are so soft that they form a bcc crystal (i.e., their phase behavior differs qualitatively from that of hard spheres); (ii) attract each other significantly, by which we mean a well depth of $0.5k_BT$ or above; and (iii) use the temperature rather than the volume fraction as the control parameter. Beyond these three criteria, the degree of hardness required for our purposes is therefore context dependent. The interparticle interactions in the work that we discuss in this review should then be understood to be sufficiently hard for hard-sphere-like behavior to be observed in the given context. We nevertheless specifically discuss certain instances where the degree of hardness is particularly relevant.

IV. MEASURING HARD SPHERES *IN VITRO*

We now turn to techniques for analyzing colloidal hard spheres in experiments. The configurations adopted by the
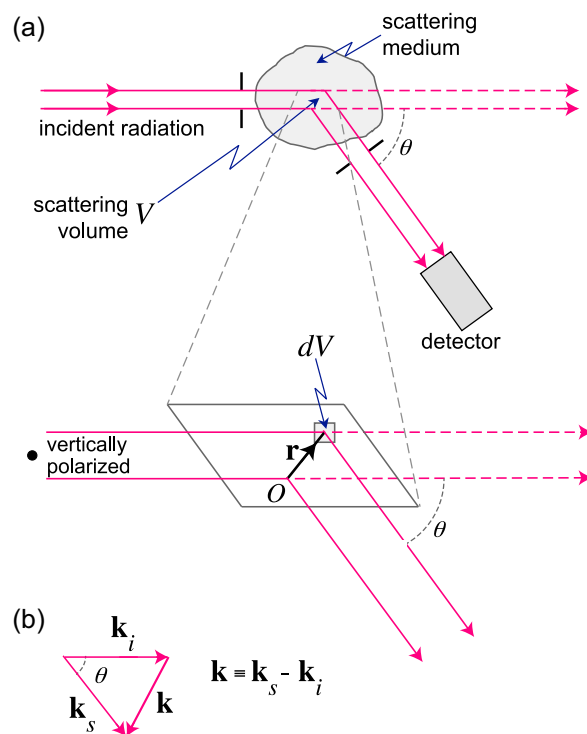
FIG. 7. Schematic of a light-scattering setup. (a) Global view of the setup. In the expanded view, scattering through an angle θ is indicated in a small volume dV. (b) Close-up of the scattering volume with the scattering wave vector $\mathbf{k}$ defined in terms of the wave vector of the incident $\mathbf{k}_i$ and scattered $\mathbf{k}_s$ light and also the scattering angle θ. Adapted from Pusey, 2002.

particles and their dynamics are the main quantities of interest. The experimental work that we review primarily used direct observation through microscopy or scattering methods. [Rheological approaches have been reviewed elsewhere (Larson, 1998; Jacob, Moghimi, and Petekidis, 2019; Wagner, 2022).] While some scattering studies of hard spheres have used neutron (Cebula *et al.*, 1981; de Kruif *et al.*, 1988) and small-angle x-ray scattering (Petukhov *et al.*, 2002), as well as more exotic x-ray scattering methods (Wochner *et al.*, 2009), most have used light scattering. The last method is therefore the focus of our discussion.

A. Light scattering

Characterization of materials via the scattering of electromagnetic radiation dates back almost to the discovery of x rays, whose wavelength is comparable to length scales relevant to atomic and molecular systems. The colloidal length scale corresponds to the longer wavelength of visible light, which is scattered by spatial and dynamical fluctuations in the refractive index of the sample studied. A typical light-scattering setup is illustrated in Fig. 7 via a global view and by a close-up of the scattering volume with the scattering wave vector $\mathbf{k}$ defined in terms of the wave vector of the incident $\mathbf{k}_i$ and scattered $\mathbf{k}_s$ light, together with the scattering angle θ.

The key observables in light scattering are the intensity of the scattered light $I(\mathbf{k}, t)$ and its time correlation. Here $\mathbf{k}$ is the wave vector through which the light is scattered, t is the time,

and **r** is the particle position (Fig. 7). The scattered intensity is then (Pusey, 2002)

$$I(\mathbf{k}, t) = \frac{E_0^2}{r^2} \sum_{j=1}^{N} \sum_{k=1}^{N} b_j(\mathbf{k}, t) b_k^*(\mathbf{k}, t)$$
$$\times \exp\{-i\mathbf{k} \cdot [\mathbf{r}_j(t) - \mathbf{r}_k(t)]\}, \qquad (9)$$

where E_0 is the amplitude of the incident light field and b_i is the scattering length of the ith particle and is closely related to the form factor.

Static light scattering. In the case of static light scattering (SLS) temporal quantities are averaged over time. From Eq. (9) for a given $b(\mathbf{k}, t)$ (which can be readily calculated for spheres made of a material with a fixed refractive index) we can then obtain the structure factor (Pusey, 2002)

$$S(\mathbf{k}) = \frac{1}{N} \sum_{j=1}^{N} \sum_{k=1}^{N} \langle \exp[-i\mathbf{k} \cdot (\mathbf{r}_j - \mathbf{r}_k)] \rangle, \qquad (10)$$

and therefore its Fourier transform, the radial distribution function $g(r)$. This quantity also provides a link to the thermodynamics of the system, as in the long-wavelength limit it is related to the isothermal (osmotic) compressibility χ_T,

$$\lim_{k \to 0} S(k) = \rho k_B T \chi_T = k_B T \left(\frac{\partial \rho}{\partial P} \right)_T. \qquad (11)$$

Light scattering has been applied to soft-matter systems since the 1930s (Doty and Edsall, 1951), for instance, by Doty and Steiner (1952). Famed crystallographer Rosalind Franklin and co-workers (Klug, Franklin, and Humphreys-Owen, 1959) were among the first to study colloidal-type crystals of charged viruses. The approach benefited massively from Spectra-Physics lasers becoming commercially available in 1962.

Pusey was an early champion of light scattering. Because synthetic colloids held the promise of being more robust than viruses, he arranged to receive polystyrene samples from the Bristol colloid group via Ottewill and Vincent; see Sec. II.B. This enabled Pusey's pioneering work on determining static structure factors from the mid-1970s onward (Pusey *et al.*, 1972; Brown *et al.*, 1975), which complemented other work on colloidal crystals (Hiltner and Krieger, 1969; Williams and Crandall, 1974). When one uses light scattering for denser suspensions (by which we mean denser than the dilute limit, $\phi \gtrsim 0.01$), precise refractive index matching between colloids and solvent is essential, as noted in Sec. II.B.

Dynamic light scattering. As Eq. (9) makes clear, determining time correlations in the fluctuations in refractive index (in the scattered form of the so-called speckle pattern) can reveal dynamical behavior, i.e., dynamic light scattering (DLS). In the 1960s, the pioneers in the field used a spectral technique to analyze the speckle pattern (Clark, Lunacek, and Benedek, 1970; Cummins and Swinney, 1970) that was experimentally tedious, while the now dominant technique uses the time correlation of detected photons (frequently called photon correlation spectroscopy) (Foord *et al.*, 1970).

The key quantity measured in DLS is the normalized time-correlation function

$$g^{(2)}(k, \tau) \equiv \frac{\langle I(\mathbf{k}, \tau) I(\mathbf{k}, 0) \rangle}{\langle I(\mathbf{k}) \rangle^2}. \qquad (12)$$

Note that $g^{(2)}(k, \tau)$ is intimately related to a key dynamical property, the intermediate scattering function $F(k, \tau)$, via the Siegert relation

$$F(k, \tau) = \sqrt{g^{(2)}(k, \tau) - 1}, \qquad (13)$$

which holds only if the scattered field is distributed over the scattering volume according to a Gaussian distribution. This means that the scattering volume can be divided into a large number of subregions and the scattered intensities of these subregions are statistically independent (Aschinger and Winter, 2012). Equation (13) constituted the mainstay of dynamical measurements of hard-sphere systems until dynamical analysis using confocal microscopy became available around the turn of the millennium.

A significant advantage of DLS over confocal microscopy is the possibility to access a broader range of timescales. Microscopy is limited to a relatively narrow time window relative to DLS. Both fast ($< 10^{-2}$ s) and long timescales ($> 10^4$ s) are inaccessible, the former due to the scan time and the latter due to limitations in sample stability. (See also the discussion concerning the consequences of particle size in Sec. IV.C.)

More exotic light scattering: Small angles, multiple length scales, and multiple colors. While the essential methods of light scattering were established by the mid-1970s, the technique has since developed considerably. As Fig. 7 makes clear, going to small angles (small-angle light scattering) probes smaller wave vectors and larger real-space length scales (Cipelletti and Weitz, 1999). Mounting multiple detectors, such as one corresponding to a "standard" wave vector around $2\pi/\sigma$ and one at a smaller angle $\ll 2\pi/\sigma$, then enables multiple length scales to be probed simultaneously. This approach has since been implemented to great effect (Tamborini and Cipelletti, 2012; Franke, Golde, and Schöpe, 2014). Other developments include two-color techniques that enable more turbid samples to be studied (Schätzel, 1991; Segrè, Behrend, and Pusey, 1995; Segrè, van Megen *et al.*, 1995; Moussaïd and Pusey, 1999). Another approach is to consider strongly scattered light, which then opens the door to studying highly turbid samples: *diffusing wave spectroscopy.* This technique was developed in the late 1980s and avoids the need for a precise matching of refractive index between particles and solvent (Maret and Wolf, 1987; Weitz *et al.*, 1989, 1993). More recent advances such as multispeckle correlation spectroscopy enable simultaneous measurements of dynamical and spatial heterogeneities (Golde, Franke, and Schöpe, 2013; Golde, Palberg, and Schöpe, 2016).

B. Optical microscopy and particle-resolved studies

Unlike atomistic systems, colloids are amenable to *in situ* observation via light microscopy techniques. Analysis of such real-space images of colloidal hard-sphere systems dates back
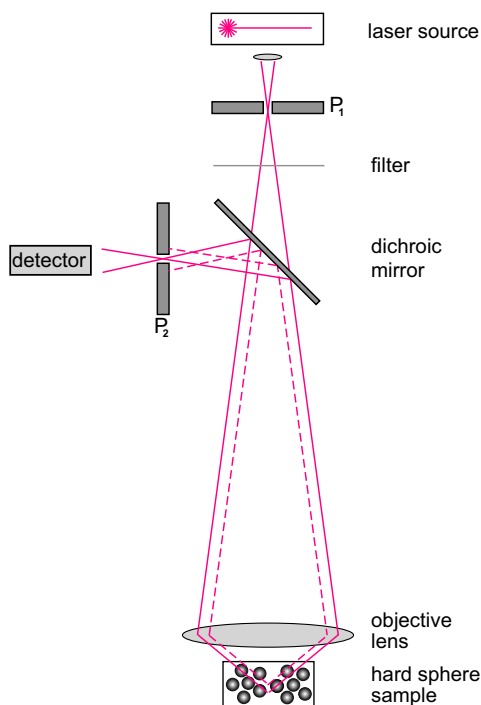
FIG. 8. The principle of confocal microscopy in the conventional epi-illumination mode. In epi-illumination, the objective and condenser lenses are the same, and the dichroic mirror allows the illuminating beam to pass through while reflecting the returning beam to the detector. Light is focused onto a point in the sample by the condenser lens. The confocal pinhole rejects all light except that from the focal point (dotted lines show reflection of light from out-of-focus regions). In this way, only one point in a 3D sample is in focus, and the incident beam is scanned relative to the sample to generate a 3D image. Epi-illumination records fluorescent light emitted by the sample, so the distribution of fluorescent dye is imaged.

to at least the early 1970s, with the work of Kose *et al.* (1973), Kose and Hachisu (1976), and Okamoto and Hachisu (1977), but antecedents can be found in the Bragg scattering study of "colloidal" crystals of viruses of Klug, Franklin, and Humphreys-Owen (1959). Microscopy work may be broadly classified into two categories: one in which individual particles are resolved [so–called particle-resolved studies (Ivlev *et al.*, 2012)] and the other in which particles are too small to be resolved. In the case of particle-resolved studies of 3D systems, some kind of 3D imaging is important. Here *confocal* microscopy is essential. A schematic of a confocal microscope is shown in Fig. 8. Like light scattering, confocal microscopy as a practical experimental technique was transformed by the advent of lasers.

Since the signal recorded in epi-illumination confocal microscopy is the distribution of fluorescent dye, some form of labeling of colloidal particles (or solvent) is necessary. Novel fluorescent particles suitable for confocal microscopy were developed by van Blaaderen, Imhof *et al.* (1992). The additional synthetic step of growing an undyed shell around the fluorescently labeled core contributed greatly to the ability to distinguish among particles; see Sec. III.B. To our knowledge, the first 3D imaging of hard-sphere-like systems with

confocal microscopy was that of van Blaaderen, Imhof *et al.* (1992), who observed colloidal crystals and glasses. The field, which has since grown markedly, has also been extensively reviewed (Hunter and Weeks, 2012; Ivlev *et al.*, 2012). Confocal microscopy has since been developed to incorporate a shear stage, as discussed in Secs. XI and XII.J (Besseling *et al.*, 2009; Lin *et al.*, 2014), and optical tweezers (see later discussion).

Particle tracking. In a seminal paper, Crocker and Grier (1996) developed an algorithm for tracking the coordinates of colloidal particles from microscopy data. This approach interpreted bright pixels as potential particle centers. In the Crocker and Grier method, the trial centers are subsequently refined through a series of criteria, such as being the center of an object weighted by pixel intensity and being far enough away from other objects that other particles do not overlap. Note that the majority of work on 2D hard-sphere systems has been carried out using microscopy, as such systems are less amenable to scattering techniques.

While the algorithms introduced by Crocker and Grier (1996) for quasi-2D systems have undoubtedly formed the backbone of most work since, note that more sophisticated approaches are available. van Blaaderen and Wiltzius (1995) sought to improve the tracking accuracy in the axial direction by fitting a Gaussian to the integrated intensities in each plane that constituted a given colloid. The early work examined hard-sphere glasses and crystals, i.e., colloidal solids in which diffusion could be neglected (van Blaaderen and Wiltzius, 1995). Even though this method made imaging easier, the slow scan rates needed to acquire images with low noise left dynamical information beyond reach. For a quasi-2D system, time-resolved tracking was carried out by the mid-1990s (Marcus, Lin, and Rice, 1996). In 3D systems, two breakthrough papers, published simultaneously in 2000, obtained dynamical information by tracking particle coordinates over time (Kegel and van Blaaderen, 2000; Weeks *et al.*, 2000). This local information led to a breakthrough experimental measurement of dynamical heterogeneity, a particularly important characteristic of glass physics; see Sec. XII.

More recently Jenkins and Egelhaaf (2008) pushed the limits of the technique as they sought to identify contacts between colloids in a dense sediment through ultrahigh precision coordinate determination. Such precision was achieved by first obtaining an empirical image of a colloid, which could then be compared to the original image. Further systematic improvements in this direction were made by Gao and Kilfoil (2009). Other, more specialized developments include the algorithmic advances in image processing of Lu *et al.* (2006), which have since allowed for real-time tracking of experiments, rather than their *post facto* analysis. This distinction is particularly significant because the spatial region of interest, which is usually small given the large file sizes generated by time-resolved 3D imaging, can often drift out of the field of view. Real-time tracking allows feedback to be applied to the stage to correct for that drift.

Ever-present polydispersity is typically neglected, except in the simple case of binary systems, wherein two-color imaging enables the two species to be differentiated (Royall, Louis, and Tanaka, 2007). More recently algorithms that identify the size of each particle have been developed (Kurita, Ruffner, and

Weeks, 2012; Leocmach and Tanaka, 2013). Ideas to extract more information than possible using conventional techniques have also been implemented, such as comparing simulated trial coordinates and experimental data (Statt *et al.*, 2016), as well as maximal precision methods (Bierbaum *et al.*, 2017). One might imagine that machine-learning techniques could be applied to the vexing problem of obtaining particle coordinates from confocal microscopy images, as proposed by Bailey, Grillo, and Isa (2022) for a dilute suspension of out-of-equilibrium (active) colloids. However, this is a challenging problem in the case of concentrated colloidal dispersions in three dimensions, not least because of the paucity of "ground truth" (other than synthetic data) against which a neural network can be trained (Kawafi, 2023).

When comparing experimental particle-resolved data for hard spheres with numerical simulations, the effects of polydispersity and particle tracking errors should never be omitted. High-quality data nevertheless imply an error of 0.05σ in particle position and a few percent missing or additional ghost particles (Royall, Louis, and Tanaka, 2007; Ivlev *et al.*, 2012). This problem may be mitigated to some extent by mimicking such features in computer simulation data (Royall, Louis, and Tanaka, 2007; Pinchaipat *et al.*, 2017), and through other techniques, as extensively reviewed (Hunter and Weeks, 2012; Ivlev *et al.*, 2012; Lu and Weitz, 2013).

Optical tweezers. The development of lasers had yet another important consequence for colloid experiments. A tightly focused laser beam can serve as optical tweezers by trapping colloidal particles and manipulating them (Ashkin, 1970). These setups have great potential to enable *in situ* observation of phenomena that depend upon exquisite control of constituent particles (Grier, 1997; Grier, 2003). Like microscopy, 3D implementation of optical tweezers carries challenges, related mainly to the requirement of refractive index matching colloids and solvent for imaging while simultaneously mismatching refractive indexes for tweezing. The first fully 3D system for colloids was introduced by Vossen *et al.* (2004) and single-lens 3D tweezer methods have since been developed (Curran *et al.*, 2014). By scanning the optical tweezers along a line, it is possible to determine the effective interaction potential between colloids (Crocker *et al.*, 1999); see Sec. IX.B. Note, however, that the maximum number of particles that can be tweezed is limited to $\sim 10^2$ and that tweezing leads to a relatively weak confinement, of the order of a few $k_\mathrm{B}T$ at most (Williams *et al.*, 2013).

C. Size does matter: Colloid dynamics in different experiments

Light-scattering and microscopy techniques have typically been used for rather different-sized colloidal particles. The former can operate with particles in the 100 s of nanometer size range, while the latter typically uses particles larger than a micron. While the behavior of systems over this size range remains largely unaltered, this distinction has significant consequences for the ability to access phenomena of interest.

As Eq. (1) shows, the Brownian time scales as the volume of the colloidal particle $\tau_B \sim \sigma^3$. In other words, a factor of 10 drop in particle size means that the Brownian time falls by a factor of 1000. As a result, a phenomenon observed on the

timescale of a day in a light-scattering setup with 200 nm diameter colloids might take a year to observe with confocal microscopy with 2 μm diameter particles. In practice, that would make it unobservable. This distinction is particularly important for rare events such as crystal nucleation, for which the "discrepancy regime" is inaccessible to confocal microscopy (see Sec. XIII), and for phenomena with long timescales, such as glass formation (see Sec. XII).

V. HARD-SPHERE SYSTEMS *IN SILICO*

From a numerical simulation perspective, hard spheres might seem to be as simple as it gets. Their interaction is pairwise and short-range and is also trivial to calculate. These features should result in efficient simulations, as is indeed the case for Monte Carlo (MC) (Frenkel and Smit, 2002) and event-driven molecular dynamics (EDMD) schemes (Rapaport, 2004). Both methods perfectly sample the structure and phase behavior of a pure hard-sphere model, and EDMD simulations faithfully reproduce the dynamics of perfect hard spheres in a vacuum. In practice, however, experiments using colloidal spheres inevitably also include a solvent, which has profound dynamical effects, especially in out-of-equilibrium systems; see Secs. VII.D and XI. Hydrodynamic effects can be included at different levels of detail, with Brownian dynamics (BD) simulations, which reproduce the diffusive short-time motion of colloidal particles, being the most straightforward implementation. Simulating hard-sphere colloidal systems away from thermal equilibrium, however, requires more complex methods that explicitly model a coarse-grained version of the background solvent, typically at a significant computational cost. It is nevertheless important to note that, for dense fluids close to equilibrium, the difference between different simulation methods in terms of the dynamics is small (Berthier and Kob, 2007; Montero de Hijes *et al.*, 2017). Detailed comparison of EDMD results even with experimental data found no meaningful differences (Royall, Williams, and Tanaka, 2018).

This section provides an overview of the simulation techniques most commonly used for hard-sphere models and provides references for the methodologies that are mentioned in the remainder of this review. Note that all of these methods should in principle correctly recover the *static* equilibrium properties of hard-sphere systems, including the equation of state and phase behavior, but implement different microscopic dynamics. Additionally, because not all of these simulation methods are easily applicable to perfectly hard spheres, we discuss commonly used models of nearly hard spheres.

A. Monte Carlo methods

Since MC simulations were first used to extract the radial distribution functions and pressure of hard-sphere fluids (Rosenbluth and Rosenbluth, 1954), the scheme has remained instrumental for evaluating much of the static physical behavior of the system. A key strength of the approach is its adaptability. Different thermodynamic ensembles, boundary conditions, or biased sampling can be considered (Frenkel and Smit, 2002). Although standard implementations

of these methods are often straightforward, DL_MONTE (Brukhno *et al.*, 2021), a general purpose code with advanced sampling methods, and the HOOMD-blue package (Anderson, Glaser, and Glotzer, 2020), which includes [CPU- or graphics-processing-unit- (GPU-) based] parallelization for fast simulation of large systems (Anderson *et al.*, 2013), should nevertheless be noted.

The simplest local Metropolis algorithm for hard spheres consists of single-particle attempted displacements, which are accepted only if no overlap is created. Interestingly, in the limit of small step sizes, this algorithm approximates BD (Cichocki and Hinsen, 1990; Sanz and Marenduzzo, 2010). In many scenarios, hard-sphere MC simulations can be made more efficient by incorporating collective displacements, such as cluster moves (Dress and Krauth, 1995; Dijkstra and van Roij, 1997; Buhot and Krauth, 1998; Liu and Luijten, 2004; Almarza, 2009; Ashton *et al.*, 2011), or by employing nonlocal sampling schemes. One particularly effective example is to exchange the diameter of particles in dense mixtures of hard spheres of different sizes (Kranendonk and Frenkel, 1991; Berthier *et al.*, 2016; Ninarello, Berthier, and Coslovich, 2017). In dense mixtures of not-too-dissimilar hard spheres, this *swap* MC approach leads to a major efficiency gain in configurational sampling. In glass-forming hard-sphere mixtures, in particular, the swap MC algorithm can probe the equilibrium fluid structure at packing fractions far beyond the point at which conventional sampling would be essentially arrested; see Sec. XII.D (Berthier *et al.*, 2016; Ninarello, Berthier, and Coslovich, 2017).

Another effective strategy for speeding up configurational sampling of hard spheres is the rejection-free event-chain MC moves introduced by Bernard, Krauth, and Wilson (2009). In event-chain MC simulations, particle displacements involve a chain of neighboring particles. A particle is displaced until it collides with a neighbor, which then becomes the next particle to be displaced. These rejection-free moves can accelerate configurational sampling by more than an order of magnitude compared to single-particle MC simulations in dense systems of hard spheres in two or three dimensions (Bernard, Krauth, and Wilson, 2009; Klement and Engel, 2019; Li *et al.*, 2022). A variant of this approach called Newtonian event-chain MC simulations, which incorporate aspects of Newtonian dynamics into the event-chain moves, were shown to lead to a speedup of yet another factor of about 5 for dense hard-sphere systems (Klement and Engel, 2019).

B. Event-driven simulations

Historically, MC simulations were soon followed by EDMD simulations, which evolve the positions of elastic hard spheres in vacuum (Alder and Wainwright, 1957). In other words, each particle interacts purely via instantaneous elastic collisions and moves at constant velocity between such collisions (Rapaport, 2004). This yields physically realistic dynamics for hard spheres in the absence of a solvent. The efficiency of these simulations strongly hinges on the efficiency of the algorithms used to predict and schedule future collisions (Lubachevsky, 1991; Marín, Risso, and Cordero, 1993; Donev, Torquato, and Stillinger, 2005a; Paul, 2007) and can rival event-chain MC simulations (Klement and Engel,

2019; Smallenburg, 2022) for equilibrating dense systems. As a result, they are vastly more efficient than MC methods based on single-particle moves. From a technical standpoint, EDMD simulations are more challenging to implement and adapt, but publicly available codes have greatly helped spread the approach (Donev, Torquato, and Stillinger, 2005a; Bannerman, Sargant, and Lue, 2011; Smallenburg, 2022). EDMD simulations have also been adapted in order to reproduce Brownian motion (Scala, Voigtmann, and De Michele, 2007), to include swap moves (Bommineni *et al.*, 2019), and to incorporate isotropic compression (Donev, Torquato, and Stillinger, 2005a).

C. Brownian dynamics simulations

Suspensions of colloidal hard spheres embedded in a solvent effectively undergo Brownian motion. The stream of collisions with the much smaller solvent molecules results in the spheres experiencing random forces. The ensuing equation of motion is

$$\frac{d\mathbf{r}(t)}{dt} = \frac{D_S}{k_{\mathrm{B}}T}\mathbf{f}(t) + \sqrt{2D_S}\mathbf{R}(t), \qquad (14)$$

where $\mathbf{r}(t)$ is the colloid position at time t, D_S is the short-time self-diffusion coefficient, and $\mathbf{R}(t)$ is a Gaussian random process with zero mean and unit variance. The total force $\mathbf{f}(t)$ on the particle includes its interactions with neighbors as well as any external forces present in the system.

Simulating Brownian dynamics entails numerically integrating Eq. (14). In practice, this integration is often achieved using a fixed small time step. For hard spheres, however, this approach does not work, because any fixed time step inevitably leads to overlaps. An event-driven approach is possible (Scala, Voigtmann, and De Michele, 2007; Charbonneau, Hu, and Morse, 2024), but typical implementations are not particularly efficient: frequent stochastic updates require one to repredict collisions for all particles after each velocity change; hence, BD simulations are most commonly performed on model systems that interact via a continuous approximation of the hard-sphere potential. (Variants are presented in Sec. V.F.) The implementation approach for BD simulations closely follows standard molecular dynamics (MD) schemes. Each time step consists of calculating the forces on all particles, followed by updating the particle positions. As a result, MD codes can be readily adapted to perform BD simulations, and MD packages such as LAMMPS (Thompson *et al.*, 2022), HOOMD-blue (Anderson, Glaser, and Glotzer, 2020), and ESPRESSO (Weik *et al.*, 2019) provide efficient implementations of BD, including options for parallelization or GPU computation.

D. Simulations including hydrodynamics

All simulation methods described thus far neglect hydrodynamic coupling, which is necessarily present for colloids moving in a solvent. While hydrodynamic interactions do not modify static equilibrium properties, they can play a significant role in the dynamics of colloidal hard spheres (see Sec. VII.D), especially when out-of-equilibrium phenomena

are considered (an issue to which we return in Sec. XI). A number of different numerical methods have therefore been developed to account for hydrodynamic effects in hard-sphere simulations.

Stokesian dynamics (Brady and Bossis, 1988) assumes an incompressible fluid and a low Reynolds number, both of which are typically valid for colloidal hard spheres. Hydrodynamic interactions between colloids are then taken into account via a many-particle mobility matrix that models the solvent flow as a superposition of Stokeslets centered on each colloid. Owing to the slow algebraic decay of this effect, the matrix effectively couples the motion of all particles in the system, making the method computationally expensive, particularly when Brownian forces are included. Significantly better performance can be obtained using the so-called accelerated Stokesian dynamics (ASD) (Sierou and Brady, 2001; Banchio and Brady, 2003). Publicly available implementations can be found in the simulation package ESPRESSO (Weik *et al.*, 2019), as a plug-in (Fiore and Swan, 2019) for HOOMD-blue (Anderson, Glaser, and Glotzer, 2020), and in specialized codes (Yan *et al.*, 2020).

Lattice Boltzmann (LB) methods (Ladd and Verberg, 2001; Cates *et al.*, 2004; Dünweg and Ladd, 2009) divide the solvent into lattice sites, each carrying a set of local solvent densities associated with a discrete set of permitted solvent velocities. These methods reproduce the dynamics of a Newtonian liquid with a given shear viscosity and recover the relevant hydrodynamic variables as moments of the one-particle velocity distribution functions (Succi, 2001). The effect of thermal fluctuations can also be included directly in the discrete Boltzmann equation (Adhikari *et al.*, 2005; Gross *et al.*, 2011). The fluid dynamics then emerges from the evolution of the one-particle distribution function. During each simulation time step, these densities are updated by considering both the streaming of the solvent to neighboring lattice sites and a collision step, which relaxes the distribution of velocities at each lattice site toward the equilibrium distribution. The lattice-based solvent is then coupled to the colloidal particles by imposing boundary conditions at their surface, thus allowing momentum exchange between the solvent and the particles. While explicit treatment of the solvent inherently increases the computational cost, LB methods scale well with particle size and can be readily parallelized for large systems. Simulation codes are also publicly available (Desplat, Pagonabarraga, and Bladon, 2001; Weik *et al.*, 2019; Bonaccorso *et al.*, 2020).

Multiparticle collision dynamics (MPCD) simulations (Malevanets and Kapral, 1999; Kapral, 2008; Gompper *et al.*, 2009; Howard, Nikoubashman, and Palmer, 2019) are similar to LB methods in that they explicitly incorporate the solvent as a simplified fluid evolved via a streaming and a collision update. In MPCD approaches, however, the solvent is modeled using discrete effective particles that move in continuous space. At each time step, all particles first move forward according to their instantaneous velocities (streaming) and then exchange momentum with other nearby solvent particles during a collision step. In the most commonly used collision algorithm, the system is divided into cells, and the velocities of all particles within a cell are mixed via a collective rotation that conserves their total momentum. Owing to this rotation,

MPCD methods using this update are also known as stochastic rotational dynamics (Malevanets and Kapral, 1999; Ihle and Kroll, 2001). Coupling to the colloids can be done either by including the colloidal particles as collision partners in the collision step or via direct interactions between solvent particles and colloids during the streaming step. Note that MPCD methods model compressible solvents. In terms of implementation, MPCD methods are closely connected to standard MD, and public (parallelized) implementations are available in, for example, LAMMPS (Thompson *et al.*, 2022) and HOOMD-blue (Howard, Panagiotopoulos, and Nikoubashman, 2018; Anderson, Glaser, and Glotzer, 2020).

Dissipative particle dynamics (DPD) (Hoogerbrugge and Koelman, 1992; Espanol and Warren, 1995, 2017; Groot and Warren, 1997) is similar to MPCD in spirit but introduces soft repulsive interactions that include both a dissipative and a stochastic term to replace the collision step. These interactions are idealized in such a way that the dynamics of the solvent particles can be resolved with time steps much larger than those used for the steeper colloid interactions, thus significantly lowering the computational cost relative to full-solvent simulations. Coupling to the colloids is achieved by associating each colloid particle with one or more solvent particles that overlap with it, and interact with the remaining solvent. As with the MPCD approach, DPD can be seen as a variation on classical MD, and efficient implementations can be found in several simulation packages, including LAMMPS (Thompson *et al.*, 2022), ESPRESSO (Weik *et al.*, 2019), and HOOMD-blue (Anderson, Glaser, and Glotzer, 2020).

Fluid particle dynamics (FPD) (Tanaka and Araki, 2000) is based on a direct numerical simulation of the Navier-Stokes equations that resolves the problem of coupling the fluid and the colloidal particles by approximating each colloidal particle as highly viscous particle with a smooth viscosity profile at its interface with the fluid. The largest advantage of the method is that it avoids the difficulties associated with moving solid-fluid boundary conditions and that it allows the fluid to couple to additional fields. The fluid itself is also incompressible. Thermal fluctuations can additionally be considered by integrating the fluctuating hydrodynamics equations (Furukawa, Tateno, and Tanaka, 2018). A method akin to FPD is the smooth profile method (SPM) (Nakayama and Yamamoto, 2005), which avoids introducing a large viscosity in the particle domain by separating the calculation of the hydrodynamic forces from that of the boundary conditions. The approach has been applied to a large variety of passive and active soft-matter systems (Yamamoto, Molina, and Nakayama, 2021).

E. Advanced sampling and free-energy methods

For the purpose of studying more detailed aspects of hard-sphere behavior, such as phase boundaries, defects, interfacial properties, and nucleation, a wide variety of advanced simulation techniques have been combined with the previously outlined general approaches. Arguably the most immediate way of obtaining phase boundaries is to simulate the direct coexistence between the two phases of interest, e.g., a hard-sphere fluid and a hard-sphere crystal. In practice, however, this approach suffers from large finite-size

effects, in addition to being sensitive to statistical error as well as to details in the setup of the initial configuration (Espinosa *et al.*, 2013). As a result, studies of equilibrium phase behavior in hard spheres often make use of free-energy calculations. Although free energies typically cannot be directly measured in simulations, thermodynamic integration can be used to determine free-energy differences with respect to some known reference state (Frenkel and Smit, 2002). The series of simulations that define the integration path between the system of interest and a reference system can be chosen in a variety of ways. Common choices are the ideal gas for the fluid phase (Frenkel and Smit, 2002) and an Einstein crystal for an ordered phase (Frenkel and Ladd, 1984; Vega and Noya, 2007), but a variety of other reference states have been employed for hard-sphere systems, including cell models (Hoover and Ree, 1968; Nayhouse, Amlani, and Orkoulas, 2011) and pinning schemes (Schilling and Schmid, 2009; Moir, Lue, and Bannerman, 2021). Note that the hard-sphere system itself has also often been used as a reference system for more complex ones (Patey and Valleau, 1973; Bolhuis and Frenkel, 1997; Dijkstra, Brader, and Evans, 1999; Hynninen and Dijkstra, 2003; Smallenburg and Sciortino, 2013). After obtaining the free energy of all relevant phases for a range of state points, equilibrium phase boundaries can be determined by identifying which phase (or coexistence of phases) has the lowest free energy at any given state point. As an alternative approach, accurate phase coexistence conditions can be extracted by mapping out the free-energy landscape connecting the fluid and crystal phases (Martin-Mayor, Seoane, and Yllanes, 2011; Fernández *et al.*, 2012). Note that all of these methods require initial knowledge of the potential phases of interest, which may require an extensive search for possible crystal structures (Kummerfeld, Hudson, and Harrowell, 2008; Filion and Dijkstra, 2009; Filion *et al.*, 2009; Hudson and Harrowell, 2011; O'Toole and Hudson, 2011; Hopkins, Stillinger, and Torquato, 2012), especially in multi-component mixtures.

Free-energy integration methods also provide routes to calculate the effect of interfaces and defects on the free energy of hard-sphere systems. In particular, the equilibrium concentration of point defects in hard-sphere crystals has been determined by setting up a thermodynamic integration path between systems with and without a defect (Pronk and Frenkel, 2001; van der Meer, Dijkstra, and Filion, 2017). Similar approaches can also be used to determine the fluid-solid interfacial free energy of hard spheres (Sec. VIII) by constructing an integration path between a direct fluid-solid coexistence and a state of two separate bulk phases (Davidchack and Laird, 2000; Davidchack, 2010; Schmitz and Virnau, 2015) or between a pure fluid and a fluid in coexistence with a slab of crystal (Espinosa, Vega, and Sanz, 2014; Sanchez-Burgos *et al.*, 2021). Alternatively, interfacial free energies can be determined from interfacial fluctuations (Davidchack, Morris, and Laird, 2006) or via thermodynamic integration (Bültmann and Schilling, 2020). The free-energy difference between face-centered-cubic (fcc) and hexagonal-close-packed (hcp) crystals and the hcp-fcc interfacial free energy can be computed using the lattice-switch method (Bruce, Wilding, and Ackland, 1997; Pronk and Frenkel, 1999; Wilding and Bruce, 2000).

When studying rare events such as *nucleation*, it is common to use sampling schemes that purposefully bias the simulation toward sampling rare configurations. In particular, umbrella sampling (Torrie and Valleau, 1977; Auer and Frenkel, 2001a; Filion *et al.*, 2010; Kästner, 2011) has been used extensively to determine the barrier to nucleating hard-sphere crystals by calculating the free-energy cost of creating crystalline nuclei of different sizes. This approach, however, assumes that the cluster is in local equilibrium at each cluster size, and therefore ignores the possibility of any nonequilibrium dynamics. Hence, to explore nucleation trajectories that take into account the dynamics of the system, more specialized methods such as forward-flux sampling (Allen, Warren, and ten Wolde, 2005; Allen, Frenkel, and ten Wolde, 2006a, 2006b; Allen, Valeriani, and ten Wolde, 2009; Hussain and Haji-Akbari, 2020), transition path sampling (Bolhuis *et al.*, 2002), and transition interface sampling (Moroni, van Erp, and Bolhuis, 2004) are required. Biasing methods have also found uses in other areas of hard-sphere simulations, such as with potentials that influence crystallization to study hard-sphere glasses (Valeriani *et al.*, 2011; Taffs and Royall, 2016).

F. Simulation models

The general strategy to approximate the hard-sphere interaction is to consider a harshly repulsive continuous interaction potential. Perhaps the simplest of such forms is the inverse power-law potential of exponent n, as given in Eq. (3). In the limit $n \to \infty$, this potential converges to the true hard-sphere potential with diameter σ. As with hard spheres, the thermodynamic behavior of the inverse power-law model with a given exponent n is effectively controlled by a single parameter since a change in the interaction strength ϵ and the particle size σ both have the same trivial effect of scaling the total energy of the system. Experimental measurements of the interactions between sterically stabilized colloids have further been shown to agree well with power-law potentials (Bryant *et al.*, 2002); see Sec. III.A. However, the inverse power law does not naturally capture the short-range nature of the soft interaction that results from steric stabilization.

Another commonly used continuous approximation is the Weeks-Chandler-Andersen (WCA) potential. Originally introduced to consider the separate roles of attraction and repulsion on the structure of simple liquids (Weeks, Chandler, and Andersen, 1971), the WCA potential corresponds to a purely repulsive variant of the Lennard-Jones potential

$$u(r) = \begin{cases} 4\epsilon \left[\left(\frac{\sigma}{r} \right)^{12} - \left(\frac{\sigma}{r} \right)^6 + \frac{1}{4} \right], & r \leq 2^{1/6}\sigma, \\ 0, & r > 2^{1/6}\sigma, \end{cases} \quad (15)$$

with energy parameter ϵ. This interaction form smoothly approaches zero at the cutoff distance $r_c = 2^{1/6}\sigma$. At sufficiently low temperatures (a common choice is $\epsilon/k_B T = 40$), the WCA potential has been shown to map well to hard spheres in terms of the equation of state and nucleation rates (Filion, Ni *et al.*, 2011; Richard and Speck, 2018a; Dasgupta, Coli, and Dijkstra, 2020). Variations of Eq. (15), with different (typically higher) exponents have been designed to match the hard-sphere behavior even more closely. A notable example of

this is the so-called pseudo-hard-sphere potential (Jover *et al.*, 2012), which results in a freezing transition that is close to that of true hard spheres (Espinosa *et al.*, 2013). This class of potentials has a long history as a substitute for hard spheres and has the advantage of being purely short-range and continuous, thus allowing for an easy BD implementation. However, the thermodynamic behavior of this class of models depends on both the chosen temperature and density.

Note that regardless of the exact functional form chosen, a trade-off must generally be made between simulation efficiency and the accuracy of the approximation of the true hard-sphere potential. Generally, although a sharper interaction potential provides a better approximation of hard spheres, it also results in a more rapid variation of the interaction forces as two particles approach. Since MD and BD simulations numerically integrate the force experienced by each particle over time, these faster variations then necessitate a smaller integration time step to maintain accurate results, thus slowing simulations down.

VI. HARD-SPHERE SYSTEMS IN THEORY

As noted in Secs. I and II, hard spheres came into existence as a minimal model system for exploring condensed matter and have been extensively reviewed (Tarazona, 1984; Roth, 2010; Hansen and McDonald, 2013; Santos, Yuste, and Lopez de Haro, 2020). Here we cover only a couple of key theories that are mentioned in later sections, and that we believe had a significant impact on the success of the hard-sphere system.

A. Integral equation theory

Integral equation theory lies at the heart of descriptions of the liquid state (Barker and Henderson, 1976; Hansen and McDonald, 2013). In the context of hard-sphere colloids as model atoms and molecules, it provides an elegant and simple theoretical framework for obtaining predictions that may be directly probed in experiments. For our purposes, integral equation theory boils down to finding approximate solutions (or closures) for the Ornstein-Zernike (OZ) relation

$$h(r) = c(r) + \rho \int h(|\mathbf{r} - \mathbf{r}'|)c(r')d\mathbf{r}', \qquad (16)$$

which relates the total correlation function $h(r) = g(r) - 1$ [with $g(r)$ the radial distribution function] to the direct correlation function $c(r)$.

In the framework of classical density-functional theory (see Sec. VI.C), the direct correlation function is related to the second functional derivative of the excess part of the free-energy functional with respect to the one-particle density of the system (Hansen and McDonald, 2013). A homogeneous and isotropic system at density ρ and temperature T interacting with a pairwise additive potential $u(r)$ is therefore uniquely defined by its $h(r)$ and thus by its $g(r)$, which is measurable in experiments; see Secs. III and IV. Measuring $g(r)$ [or its Fourier transform $S(k)$] is therefore an important means of characterizing the structure and thermodynamics of an experimental system.

The OZ relation can also be solved using a second (closure) relation. A relatively simple relation, first proposed by Percus and Yevick (PY) (Percus and Yevick, 1958), is given by

$$c(r) = \left(\exp[-\beta u(r)] - 1 \right)[h(r) - c(r) + 1]. \qquad (17)$$

This relationship is fairly accurate for strongly repulsive and short-range interactions, such as for hard spheres. In 1963, Wertheim and Thiele independently showed that the PY closure to the OZ equation for a fluid of hard spheres with diameter σ and volume fraction $\phi = \pi\sigma^3\rho/6$ yields for the direct correlation function (Thiele, 1963; Wertheim, 1963)

$$c(r) = \begin{cases} \frac{-(1+2\phi)^2+6\phi[1+(1/2)\phi]^2(r/\sigma)-(1/2)\phi[1+2\phi]^2(r/\sigma)^3}{(1-\phi)^4}, & r \leq \sigma, \\ 0, & r > \sigma. \end{cases}$$

The analytical Fourier transform of $c(r)$ can then be used to solve for the structure factor $S(k)$. The pair correlation function $g(r)$ can subsequently be numerically obtained from $S(k)$. The theoretical predictions agree well with computer simulation results for volume fractions $0 \leq \phi \lesssim 0.5$, i.e., over the entire stable fluid regime. Examples of experimental comparisons against the PY approximation to the OZ equation are shown in Fig. 13 in Sec. VII.

Given $g(r)$, three independent routes can then be followed to extract thermodynamic quantities,

$$P = \rho k_B T - \frac{\rho^2}{6} \int d\mathbf{r} \, r u'(r) g(r), \qquad (18)$$

$$\frac{E}{V} = \frac{3}{2}\rho k_B T + \frac{\rho^2}{2} \int d\mathbf{r} \, u(r) g(r), \qquad (19)$$

$$k_B T \left(\frac{\partial \rho}{\partial P}\right)_T = 1 + \rho \int d\mathbf{r} (g(r) - 1), \qquad (20)$$

which are the virial, caloric, and compressibility routes, respectively. An important exact sum rule for hard spheres can be obtained straightforwardly from Eq. (18),

$$\frac{\beta P}{\rho} = 1 + \frac{2\pi\rho\sigma^3 g(\sigma^+)}{3}, \qquad (21)$$

which relates the pressure of the hard-sphere fluid to the contact value of $g(r)$. Using $g(r)$ from the PY approximation to the OZ equation in Eq. (20) yields the compressibility pressure P_c,

$$\frac{\beta P_c}{\rho} = \frac{1 + \phi + \phi^2}{(1 - \phi)^3}, \qquad (22)$$

while the virial pressure P_v from Eq. (18) gives

$$\frac{\beta P_v}{\rho} = \frac{1 + 2\phi + 3\phi^2}{(1 - \phi)^2}. \qquad (23)$$

The compressibility equation of state overestimates the pressure obtained from simulations, whereas the virial equation of state underestimates the simulation results (Hansen and

McDonald, 2013). It turns out that the Carnahan and Starling (CS) linear combination $P_{CS} = (2P_c + P_v)/3$ (Carnahan and Starling, 1969),

$$\frac{\beta P_{CS}}{\rho} = \frac{1 + \phi + \phi^2 - \phi^3}{(1 - \phi)^3}, \tag{24}$$

is essentially indistinguishable from simulations up to $\phi \simeq 0.5$ (Hansen and McDonald, 2013). Note, however, that Carnahan and Starling used not the simulation results but rather the pressure from the virial expansion for the equation of state (2) to motivate their expression (Carnahan and Starling, 1969). When one uses the analytical expressions for the virial coefficients B_2, B_3, and B_4 and the numerical expressions for B_5 and higher, the equation of state (2) for hard spheres becomes

$$\frac{\beta P}{\rho} = 1 + 4\phi + 10\phi^2 + 18.365\phi^3 + 28.225\phi^4 + 39.74\phi^5$$
$$+ 53.5\phi^6 + 70.8\phi^7 + \cdots. \tag{25}$$

Approximating the virial coefficients as $B_{i+1} = (\pi\sigma^3/6)^i(i^2 + 3i)$ then gives Eq. (24) (Carnahan and Starling, 1969).

While integral equation theory is successful in predicting the structure and thermodynamics of equilibrium hard-sphere fluids, the closures are somewhat uncontrolled and not systematically improvable. A clear manifestation of this effect is that predictions for binary mixtures of hard spheres turn out to be extremely sensitive to the details of the approximation scheme. A more robust approach in this sense is density-functional theory, and especially fundamental measure theory, as described by Tarazona, Cuesta, and Martínez-Ratón (2008) and Roth (2010) and in Sec. VI.C.

B. Cell theory

The crystal branch of the equation of state of hard spheres is less amenable to integral equation theory due to the broken translational and rotational symmetry in the system. One early mean-field theory that can be used as an approximate analytical prediction was introduced by Lennard-Jones and Devonshire (1937) to estimate fluid free energies and is now commonly known as cell theory or free-volume theory when it is applied to solids and, especially, crystals (Wood, 1952; Salsburg and Wood, 1962). In this approach, it is assumed that the Helmholtz free energy $F(N, V, T)$ of the crystal phase can be subdivided into contributions from each particle, and that each can be computed by assuming that all other particles are fixed exactly at their lattice site. In that approximation, the free energy f_1 of a single particle in an fcc lattice is given by

$$\beta f_1(\rho) = -\log \frac{V_{\text{free}}(\rho)}{\Lambda^3}, \tag{26}$$

where V_{free} is the free volume available to the particle confined in the cage of its neighbors and Λ is the thermal de Broglie wavelength. This free volume is then typically approximated as a sphere with diameter $a - \sigma$, with a the nearest-neighbor distance, which is given by $a = (\rho_{\text{max}}/\rho)^{1/3}$. Here the

close-packed density of crystal lattices of monodisperse hard spheres is $\rho_{\text{max}}\sigma^3 = \sqrt{2}$. Hence, cell theory gives the approximate total free energy

$$\frac{\beta F}{N} \simeq \beta f_1 \simeq -\log\left(\frac{4\pi\sigma^3}{3\Lambda^3}\left[\left(\frac{\rho_{\text{max}}}{\rho}\right)^{1/3} - 1\right]^3\right). \tag{27}$$

Taking the derivative with respect to the volume gives the pressure

$$\frac{\beta P}{\rho} = [1 - (\rho/\rho_{\text{max}})^{1/3}]^{-1}. \tag{28}$$

Although Eq. (28) significantly underestimates the pressure (on the order of $\sim 1 k_B T/\sigma^3$), cell theory provides a quick and physically intuitive estimate for the crystal free energy and equation of state. As a result, it is commonly used for pedagogical purposes (Barrat and Hansen, 2003; Kamien, 2007), as well as for back-of-the-envelope estimates of phase transitions. Cell theory has been extended in a variety of ways (Rudd *et al.*, 1968; Koch, Radin, and Sadun, 2005; Charbonneau, Morse *et al.*, 2021), including for binary mixtures of hard spheres (Cottin and Monson, 1993, 1995; van der Meer *et al.*, 2020) and glassy systems. Note that when cell theory is applied to disordered systems, such as glasses, it cannot be expected to take into account the configurational entropy of the system; see Sec. XII. Furthermore, in the fluid regime particles are no longer trapped in cells in a meaningful way, and hence the description should be expected to break down there as well.

C. Classical density-functional theory

Classical density-functional theory (DFT) provides an exact theoretical framework for describing the thermodynamic and structural properties of interacting many-body systems, starting with a microscopic description of the interparticle interactions. The approach is based on the observation that the grand potential of a specified inhomogeneous fluid is a functional $\Omega[\rho(\mathbf{r})]$ of the variational one-body density profile $\rho(\mathbf{r})$, with the properties that (i) the equilibrium density profile $\rho_0(\mathbf{r})$ minimizes the functional $\Omega[\rho(\mathbf{r})]$ and (ii) this minimum equals the equilibrium grand potential $\Omega_0[\rho_0(\mathbf{r})]$. From Ω_0, all thermodynamic properties then follow. For instance, one can obtain the homogeneous system pressure

$$P = -\frac{\Omega_0}{V}. \tag{29}$$

Functional derivatives of the Helmholtz free-energy functional additionally provide correlation functions. In particular, the OZ two-body direct correlation function is related to the second functional derivative of the functional from which the two-body structure of the system follows. Because the exact Helmholtz free-energy functional for a given interaction potential is unknown, DFT depends on approximate free-energy density functionals. The freezing transition of hard spheres has been an important focus for the development of various density-functional approximations. The pioneering work of Ramakrishnan and Yussouff (1977, 1979), and later

several others (Haymet and Oxtoby, 1981; Baus, 1989; Lutsko and Baus, 1990), described the crystal as a perturbation of a uniform fluid phase, using a density expansion of the functional around a homogeneous density. Nonperturbative approaches involve the weighted density approximation by Tarazona (1984), which was based on a Gaussian parametrization for the density profile, or modified weighted density approximations (Denton and Ashcroft, 1989, 1990).

The most successful and widely used DFT for hard spheres to date is the fundamental measure theory (FMT), which was introduced by Rosenfeld (1989). In FMT, the Helmholtz free-energy functional is based on weighted densities that are convolutions of the density profiles with weight functions depending on the geometrical properties of the spheres. Various subsequent extensions and modifications have been proposed to improve the description of various inhomogeneous systems of hard spheres. Further details on this approach can be found in the comprehensive and excellent reviews by Tarazona, Cuesta, and Martínez-Ratón (2008) and Roth (2010). Finally, a recently presented neural functional theory leveraged an exact functional mapping from the density profile to the one-body direct correlation function through a deep neural network (Sammüller *et al.*, 2023). The network was trained on simulation data of hard spheres subjected to diverse external environments and exceeds in accuracy all current density-functional approaches.

VII. BULK EQUILIBRIUM HARD SPHERES

Having in hand the wide array of experimental, numerical, and theoretical methods described in the previous sections, we can now consider the equilibrium behavior of hard-sphere systems. This behavior not only serves as a reference point in nearly all subsequent sections of this review but also is an important scientific matter in its own right.

The first hard-sphere systems studied via computer simulation were monodisperse (Alder and Wainwright, 1957; Wood and Jacobson, 1957), but only quasimonodisperse in colloidal experiments. However, because (as we see later in this section) a mean size polydispersity $s \lesssim 5\%$ barely changes the equilibrium phase diagram (Wilding and Sollich, 2010), both experimental and numerical work has focused on essentially equivalent systems. In this context, a natural starting topic is their bulk phase behavior. Other topics considered include the equation of state as well as the fluid structure and dynamics for both 3D and (quasi-)2D hard spheres.

A. Equilibrium phase behavior of monodisperse hard spheres

Since hard spheres do not interact beyond contact, their Helmholtz free energy comprises only an entropic contribution. Temperature plays but a trivial role, and hence the hard-sphere equilibrium phase diagram depends solely on the volume fraction ϕ (density) of the system. At low ϕ the system is naturally in a fluid phase, whereas at high ϕ the system is in a crystal phase. (In three dimensions, the two are separated by a first-order phase transition.) In other words, at sufficiently high ϕ the crystal entropy is higher than that of the fluid; the regular arrangement of spheres on the crystal lattice provides

each particle with more local free volume to move around than it would have in a fluid at the same density.

As mentioned in Sec. II, the first numerical validations of this theoretical prediction were obtained in the 1950s when the melting of an (fcc crystal was studied (Alder and Wainwright, 1957; Wood and Jacobson, 1957). Since then, considerable efforts have been devoted to pinning down the details of this transition, including the characterization of finite-size effects (Polson *et al.*, 2000). Figure 9 provides an overview of numerical results for the coexistence packing fractions, pressures, and chemical potentials. Apart from a few outliers that are often associated with small system sizes, results for these quantities are in good agreement and have established that the freezing and melting volume fractions of monodisperse hard spheres are $\phi_f \simeq 0.492$ and $\phi_m \simeq 0.543$, respectively. Similar predictions have been obtained from various theoretical treatments, notably fundamental measure theory (Roth, 2010). Experimental measurements on hard-sphere colloids, such as those shown in Fig. 2 (Pusey and van Megen, 1986), agree reasonably well with this result provided that a suitable σ_{eff} is chosen to account for any residual softness; see Sec. III.C.

While these studies do not typically take into account the presence of vacancies in the equilibrium crystal phase, its effect on the coexistence pressure is expected to be smaller than the typical errors considered here ($\beta\Delta P_{\text{coex}}\sigma^3 \simeq -0.0026$) (Pronk and Frenkel, 2001). Simulation results have revealed that the equilibrium fcc crystal is indeed nearly flawless. The equilibrium fraction of defective sites at melting has been computed to be approximately 10^{-4} for vacancies and 10^{-8} for interstitials (Bennett and Alder, 1971; Pronk and Frenkel, 2001, 2004). However, comparing these predictions to experiments is inherently difficult beyond the usual concerns about coexistence determination, given (i) the low concentrations involved, (ii) their sensitivity to the crystal packing fraction, and (iii) the possibility that defects become kinetically trapped during crystal formation (Sec. III.C) (Poon, Weeks, and Royall, 2012; Royall, Poon, and Weeks, 2013).

Although various properties of the bulk crystal phase, including its elastic constants (Runge and Chester, 1987; Pronk and Frenkel, 2003; Sushko and van der Schoot, 2005) and defect diffusivity (van der Meer, Dijkstra, and Filion, 2017), have been studied in detail in simulation, they remain to be systematically investigated in experiments.

Phase behavior in experiment. As noted in Sec. II, interest in hard spheres received a tremendous boost from the experiments of Pusey and van Megen (1986) (see Fig. 2), but earlier work by Hachisu and Kobayashi (1974) and Kose and Hachisu (1974) had already demonstrated that hard-spherelike colloids crystallize. Two systems were used. First, a strongly screened charged stabilized aqueous system (Hachisu and Kobayashi, 1974) and, second, a nonaqueous system (for which electrostatic effects were expected to be minimal) that used what would now be called microgel colloids of crosslinked PMMA dispersed in benzene[10] (Kose and Hachisu, 1974). Given the difficulty of determining effective volume

---

[10]Note that benzene is now typically avoided due to its toxicity.

Source	Method	ϕ_f	ϕ_m	$\beta P_{\text{coex}}\sigma^3$	$\beta\mu_{\text{coex}}$	N
Hoover and Ree (1968)	Single-occupancy cell	0.494	0.545	11.70		∞
Speedy (1997)	Unspecified	0.491(1)	0.543(1)	11.55(11)		
Davidchack and Laird (1998)	Direct coexistence	0.491	0.543	11.55(5)		10752
Wilding and Bruce (2000)	Phase switch			11.49(9)		∞
†Frenkel and Smit (2002)	Ladd-Frenkel	0.4917	0.5433	11.567	16.071	∞
Roth *et al.* (2002)	FMT (White Bear I)	0.489	0.536			
Errington (2004)	Phase switch			11.43(2)		∞
†Fortini and Dijkstra (2006)	Ladd-Frenkel	0.4915(5)	0.5428(5)	11.57(10)	16.08(10)	
Vega and Noya (2007)	Einstein molecule	0.492	0.543	11.54(4)	16.04	∞
Noya *et al.* (2008)	Direct coexistence	0.491(1)	0.543(2)	11.54(4)		5184
Odriozola (2009)	Parallel tempering	0.492(4)	0.545(4)	11.43(17)		∞
Zykova-Timan *et al.* (2010)	Direct coexistence	0.492	0.545	11.576(6)		160000
Nayhouse *et al.* (2011)	Single-occupancy cell	0.4912(6)	0.5425(5)	11.502(19)		∞
Oettel *et al.* (2010)	FMT (White Bear II)	0.495	0.545	11.89	16.40	
de Miguel (2008)	Ladd-Frenkel	0.489(1)	0.541(2)	11.43(11)	15.92(11)	864
†Fernández *et al.* (2012)	Free-energy landscape	0.49188(2)	0.54312(5)	11.5727(10)		∞
Ustinov (2017)	Kinetic MC	0.491	0.543	11.534	16.054	3000
†Pieprzyk *et al.* (2019)	Literature values	0.4917(5)	0.5433(5)	11.5712(10)	16.0758(20)	∞
†Moir *et al.* (2021)	Tethered particle	0.49161(3)	0.54305(4)	11.550(4)	16.053(4)	∞
Consensus		0.4917(2)	0.5431(2)	11.56(2)	16.06(2)	∞

FIG. 9. Table summarizing prior reports of hard-sphere fluid-fcc phase coexistence using computer simulations (black) and DFT [green (gray)]. For each result, we list the main method used to determine the free energy or stability of the solid phase (see also Sec. V), the freezing and melting packing fractions, the coexistence pressure and chemical potential, and the system size considered. A system size of ∞ indicates that results were extrapolated to the thermodynamic limit $N \to \infty$, but the system sizes considered and the extrapolation scheme vary between studies. The final consensus averages results from five studies with high reported accuracy (marked with a dagger), namely, Frenkel and Smit (2002), Fortini and Dijkstra (2006), Fernández *et al.* (2012), Pieprzyk *et al.* (2019), and Moir, Lue, and Bannerman (2021).

fractions for such particles (see Sec. III.C) (Poon, Weeks, and Royall, 2012; Royall, Poon, and Weeks, 2013), however, a quantitative comparison was challenging for this system (Kose and Hachisu, 1974). Later work found that the softness of microgel particles [which can be tuned via their degree of cross-linking (Lyon and Fernandez-Nieves, 2012)] can indeed have a profound effect on phase coexistence (Paulin and Ackerson, 1996), as may be inferred from the discussion of Fig. 6. Experimental efforts to determine the osmotic pressure at freezing were pioneered by Takano and Hachisu (1977) and Hachisu and Takano (1982), who, after drying and measuring the total mass of particles from the fluid phase in a sedimented system, found reasonable agreement with simulation results.

The subsequent development of sterically stabilized PMMA (see Secs. II.B and III.B) brought better controlled hard-sphere-like experimental systems to the field. A key hurdle to achieving quantitative accuracy, however, has been to properly determine their effective ϕ (Poon, Weeks, and Royall, 2012; Royall, Poon, and Weeks, 2013); see Sec. III.C. One might think that, even if colloidal particles have some degree of softness (as is always the case), phase boundaries should nevertheless lead to volume fractions that can be mapped onto the predicted values. In fact, as discussed in Sec. III.C and shown in Fig. 6, it is not that simple, as softness affects the relative coexistence gap between fluid and crystal. As noted by Pusey and van Megen (1986), sedimentation further complicates matters.

One clever method to address the effects of sedimentation was proposed by Paulin and Ackerson (1990). As shown in Fig. 10, the fluid-crystal phase boundary (in vials such as those shown in Fig. 2) tends to move upward as the fluid phase slowly crystallizes. While the system starts as a metastable fluid, with an effective volume fraction that falls within the coexistence regime (see Fig. 3), the final sedimentation-diffusion equilibrium state is a crystal with only a thin fluid phase above. (The thickness of the fluid phase is of the order of the gravitational length defined in Sec. XI, which in this case is much less than the container size.) In Fig. 10, the top of the sediment is characterized by the supernatant A colloidal fluid B interface. Sedimentation proceeds over the course of the experiment (some two months) but after approximately 27 days the colloidal fluid B is no longer visible to the naked eye. The fluid "disappearance" reflects the approach to sedimentation-diffusion equilibrium. The colloidal fluid-crystal C phase separation, however, took only about one day. [An additional, distinct layer in the form of a polycrystalline sediment D also formed, akin to that observed in Fig. 2(c), but plays no role in the subsequent analysis.]

A phase diagram determination from these observations requires a key assumption: that the boundary in the sedimenting system extrapolated back to $t = 0$ reflects the phase-separated system prior to any sedimentation. In other words, $t = 0$ should correspond to a phase-separated system in the
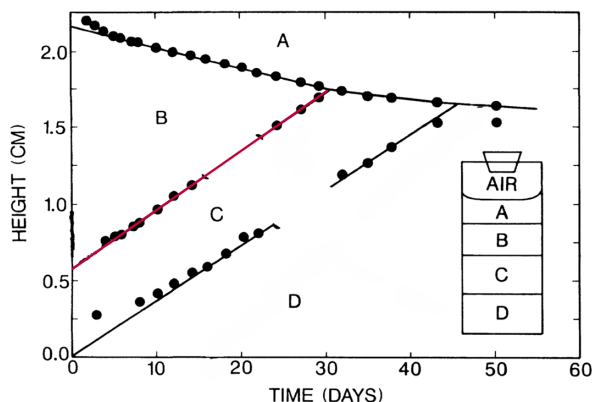
FIG. 10. Determining the equilibrium coexistence volume fraction from the time evolution of a sedimenting suspension. The height of a system in the fluid-crystal coexistence region undergoing sedimentation is recorded as a function of time. After a short waiting period of two days, sharp interfaces form between the clear supernatant A, the fluid phase B, the crystal phase C, and a dense polycrystalline sediment D. Extrapolating the fluid-crystal B-C interface [red (gray) line] back to the time $t = 0$ provides an estimate of the phase boundary prior to sedimentation, i.e., in the absence of gravity. From Paulin and Ackerson, 1990.

absence of gravity. Using different samples of varying initial ϕ, application of the lever rule then gives the equilibrium fluid-crystal coexistence region. This method therefore requires a separation of timescales between that of sedimentation (one month) and that of fluid-crystal phase separation (one day). The resulting phase behavior was later found to be in reasonable agreement with the experimental equation of state (Phan *et al.*, 1996; Rutgers *et al.*, 1996). (See Sec. VII.C for a discussion of reasonable errors in the context of colloidal experiments.)

Polymorphism. At sufficiently high ϕ, one expects the stable crystal to be one of the close-packed structures (known as Barlow packings) considered in the Kepler conjecture (Hales *et al.*, 2017), which consist of stacked layers of spheres arranged at the vertices of a hexagonal (or triangular) lattice. The nonuniqueness of the stacking follows from the fact that each additional layer has two different positions in which it can be placed with respect to the previous one. Computer simulations combined with free-energy calculations have demonstrated that the fcc structure (with an *ABCABC* stacking order) is slightly entropically favored over the hcp structure (with an *ABAB* stacking order) (Frenkel and Ladd, 1984; Bolhuis *et al.*, 1997; Mau and Huse, 1999; Polson *et al.*, 2000; Noya and Almarza, 2015). These calculations indicate a marginally larger freedom of motion for hard spheres in the fcc crystal in comparison to the hcp crystal. An expansion of this entropy in terms of the free volume available to clusters of mobile spheres within a rigid crystal indicates that the collective motion of at least five spheres needs to be considered before fcc is favored (Koch, Radin, and Sadun, 2005). Given that the free-energy difference is only about $10^{-3} k_B T$ per particle, however, spontaneously formed hard-sphere crystals often contain defects in

the fcc stacking sequence, resulting in a random-hexagonal-close-packing (rhcp) structure. This polytype[11] is unlikely to anneal out to the equilibrium fcc crystal phase over any realistic timescale in simulation (Pronk and Frenkel, 1999). However, annealing of rhcp into fcc crystal structures has been observed in x-ray crystallographic experiments of suspensions of small particles (600 nm) (Kegel and Dhont, 2000; Martelozzo *et al.*, 2002). Small external biases can also play a significant role. For instance, crystallization resulting from sedimentation under gravity more strongly favors the formation of fcc (Hoogenboom *et al.*, 2002; Marechal, Hermes, and Dijkstra, 2011), whereas experiments in microgravity result in rhcp crystals (Zhu *et al.*, 1997; Cheng, Zhu *et al.*, 2001). We return to this issue in Sec. XIII.H when we consider the role of polymorph selection in the formation of hard-sphere crystals.

B. Impact of polydispersity on the equilibrium phase diagram

As mentioned in Sec. III, preparing a sample of colloidal spheres necessarily leads to a size distribution $p(\sigma)$ of diameters instead of the idealized identical-sphere model. The standard deviation of $p(\sigma)$ relative to the mean diameter defines the polydispersity s, which typically quantifies this effect.

The phase behavior of systems with small polydispersity ($s \leq 5\%$) is essentially indistinguishable (a $\lesssim 2\%$ difference in coexistence ϕ) from that of monodisperse hard spheres. Going to larger polydispersities, however, strongly suppresses crystallization. A "terminal polydispersity" ($s_t \approx 5\%–12\%$, depending on the higher moments of the distribution) beyond which the crystal cannot be stabilized was therefore initially suggested (Barrat and Hansen, 1986; Pusey, 1987; Ackerson and Schätzel, 1995; Bolhuis and Kofke, 1996; Phan *et al.*, 1998; Bartlett and Warren, 1999).

Follow-up simulations, however, revealed that polydisperse suspensions circumvent this barrier through *fractionation*; see Fig. 11. The solid phase then splits into coexisting solid phases with smaller polydispersity (each limited to $s_* \approx 6\%$) (Kofke and Bolhuis, 1999). In other words, instead of a single crystal with widely different particle sizes (implying large local strains), the system favors the formation of separate crystalline domains of small and large particles. This proposal has since been put on solid theoretical ground through approximate free-energy calculations (Fasolo and Sollich, 2003, 2004) and has been experimentally validated (Martin, Bryant, and van Megen, 2003).

Further support for fractionation can be obtained from computer simulations, albeit with particular methodological care. In standard fixed-volume simulations, accessing equilibrated fractionated solids is obfuscated by the extremely slow nucleation dynamics (see Sec. XIII) and the slow dynamics of domain boundaries. Sollich and Wilding (2010) sidestepped these difficulties by employing constant pressure Monte Carlo simulations that prescribe a size-dependent chemical potential $\Delta\mu(\sigma)$ [instead of fixing the parent distribution $p(\sigma)$].

---

[11] Polytypes are crystal polymorphs whose symmetry differs only along one direction.
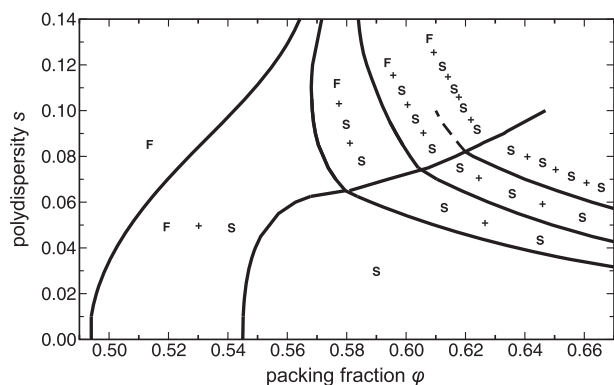
FIG. 11. Phase diagram of polydisperse hard spheres. Data are from Sollich and Wilding's free-energy calculations for a top hat distribution (Fasolo and Sollich, 2004). Beyond 6%, the single solid phase fractionates into coexisting solids of different size distributions with smaller polydispersity. The larger the polydispersity and packing fraction, the larger the number of coexisting phases needed to satisfy the polydispersity constraint on individual crystal phases (Sollich and Wilding, 2010). From Fasolo and Sollich, 2004.

The simulation results qualitatively agree with the theoretical proposal (Wilding and Sollich, 2010; Sollich and Wilding, 2011); see Fig. 11.

Recent swap-assisted EDMD simulations at fixed volume (see Sec. V.A) report ordering of polydisperse hard spheres into complex crystals with a large unit cell, such as Laves and Frank-Kasper phases, instead of fractionating into fcc crystals (Lindquist, Jadrich, and Truskett, 2018; Bommineni *et al.*, 2019). These large unit cells, which incorporate small and large particles, are reminiscent of what is observed in binary mixtures; see Sec. IX. Similarly, polydisperse mixtures with a non-Gaussian size distribution have also been observed to partially crystallize into an AlB_2 structure (Coslovich, Ozawa, and Berthier, 2018). The spontaneous formation of these phases suggests that their formation might be thermodynamically preferable over fractionation (see Fig. 11), but this proposal has yet to be investigated using free-energy calculations. Although this phenomenon has not yet been observed in colloidal hard spheres either, polydisperse charged silica nanospheres do form comparably complex crystal phases (Cabane *et al.*, 2016). The question of the true equilibrium phase diagram of strongly polydisperse hard-sphere mixtures therefore remains open.

C. Equation of state

Equations of state (EOSs) are some of the most fundamental descriptions of equilibrium systems. On the theoretical and numerical side, high-accuracy EOSs are now available for both liquid and crystal phases of hard spheres (Pieprzyk *et al.*, 2019). This work caps decades of systematic improvements; see Alder, Hoover, and Young (1968), Speedy (1997), Speedy (1998b), Almarza (2009), and Santos, Yuste, and Lopez de Haro (2020) and Secs. II and VI. Despite the quantitative success of these efforts, physical insight largely emerges from approximation schemes, which also suffice as reference and calibration for colloid experiments. The expression obtained

by Carnahan and Starling (1969) for the fluid phase [Sec. VI, Eq. (24)] is particularly useful. For the crystal, data fitted to computer simulation results, such as Hall's fit (Hall, 1972) and the Speedy EOS (Speedy, 1998a), play a similar role.

Early experimental attempts at determining the fluid EOS were carried out by Hachisu and Takano (1982) and Vrij *et al.* (1983), and marked methodological improvements were later achieved by Piazza, Bellini, and Degiorgio (1993). Although both approaches obtained the EOS by integrating the equilibrium density profile in a single sedimentation experiment, the latter work used a charge-stabilized system of polytetrafluoroethylene (a polymer colloid similar in some respects to polystyrene but with a somewhat lower refractive index) with a Debye length κ^{-1} much smaller than the particle diameter σ ($\kappa^{-1} = 2$ nm versus $\sigma = 146$ nm), thus yielding a good hard-sphere approximation; see Sec. III.D. These later measurements compared well with the Carnahan-Starling expression for the fluid and reasonably well to Hall's fit to simulation data for the crystal (Hall, 1972). As shown in Fig. 12, subsequent work by Rutgers *et al.* (1996) using x-ray densiometry also found reasonable agreement with theory for the fluid branch as well as for the solid branch for ϕ approaching close packing.

What is reasonable agreement in this context? As discussed in Sec. III.E, although colloidal systems are excellent model systems for demonstrating a range of phenomena of condensed matter, they are not highly accurate standard measures, at least compared to atomic and molecular systems. While the accuracy limit has not been systematically characterized, it seems reasonable that an error in volume fraction of about $\delta\phi \sim 0.01$ should result from measurements that base their phase boundaries on the method of Paulin and Ackerson (1990) discussed in Sec. VII.A.

At low ϕ, however, the results of Piazza, Bellini, and Degiorgio (1993) exhibited a systematic drift far in excess of the expected error. The measured volume fraction dropped
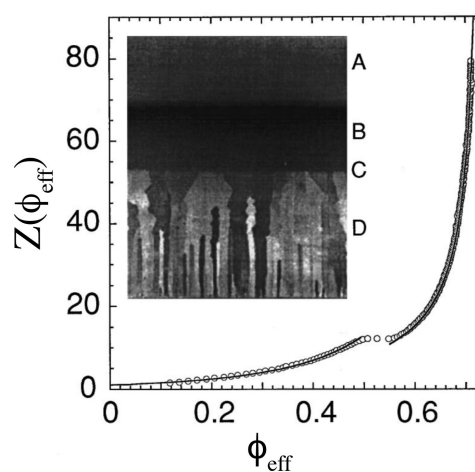

FIG. 12. Experimental determination of the EOS, i.e., $Z(\phi_{eff}) = \beta P(\phi_{eff})/\rho_{eff}$ vs ϕ_{eff}, for $\sigma = 0.720$ μm PMMA particles from the observed sedimentation-diffusion equilibrium: (A) supernatant, $\phi_{eff} \approx 0$; (B) fluid phase, $0 < \phi_{eff} \leq 0.492$; (C) sharp interface; and (D) crystalline phase, $0.543 \leq \phi_{eff} \leq 0.74$. The lines denote the fluid and solid EOSs for true hard spheres. Inset: photograph of 1 cm of the sample. Adapted from Rutgers *et al.*, 1996.
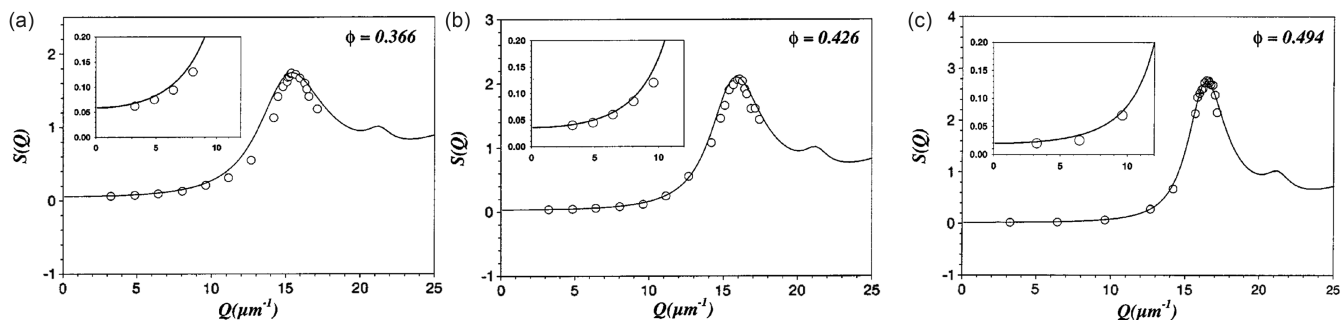
FIG. 13. Structure factor of hard-sphere fluids determined using static light scattering. Experimental data are shown as points and compared with Percus-Yevick predictions (the solid line) at the specified volume fractions. From Moussaïd and Pusey, 1999.

much slower than anticipated as a function of height. In other words, the sedimentation profile was extended. A putative physical mechanism for this extension was later proposed by van Roij (2003). In these systems, colloids and small ions decouple under a gravitational field, with the latter only negligibly affected on the experimental length scale. The resulting macroscopic electric field then partially counters gravity, thus extending the sedimentation profile. Subsequent experiments confirmed that interpretation (Rasa and Phillipse, 2004; Royall, van Roij, and van Blaaderen, 2005).

Particle-resolved studies have enabled new developments in EOS measurements. For example, Dullens, Aarts, and Kegel (2006a) performed numerical Widom particle insertion on experimental particle configurations to determine the chemical potential of colloidal hard spheres under the assumption of a hard-sphere pair potential. The resulting thermodynamic properties, including the EOSs, are good but become statistically inaccessible at higher volume fraction ($\phi \gtrsim 0.43$). The relation between free-volume measurements and free energy has been explored separately in the supercooled regime ($\phi \geq 0.492$) with reasonable quantitative agreement (Zargar *et al.*, 2013; Dang *et al.*, 2022) despite the crudeness of the assumptions underlying cell theory in this regime (Sec. VI.B). Furthermore, as elegant as this approach can seem, the effects of polydispersity and tracking errors can hamper analyses based on particle coordinates. An analysis based on cavity averages, compared with simulation data, found errors of up to 100% in the pressure and up to $10k_B$T in the chemical potential (Schindler and Maggs, 2015).

D. Structure and dynamics of the hard-sphere fluid

Structure. As discussed in Sec. VI, the radial distribution function $g(r)$ and structure factor $S(k)$ of the hard-sphere fluid can be obtained from the Percus-Yevick closure to the Ornstein-Zernike equation. The resulting theoretical predictions have been extensively tested against simulation data (Ree, Keeler, and McCarthy, 1966; Frenkel *et al.*, 1986; Hansen and McDonald, 2013). Experimental studies of colloidal fluids using SLS (see Sec. IV.A) also provide a natural probe for the pair structure. Early SLS experiments (Vrij *et al.*, 1983; de Kruif, Rouw *et al.*, 1985) found that $S(k)$ for hard-sphere-like colloidal suspensions was consistent with the Percus-Yevick expression in the small wave vector limit $k \to 0$. Because $S(k \to 0)$ is directly linked to the isothermal

compressibility of the fluid under consideration, as described by Eq. (11), this correspondence also experimentally validated the hard-sphere EOSs. Subsequent small-angle neutron scattering (de Kruif *et al.*, 1988) and light-scattering experiments (Moussaïd and Pusey, 1999) extended this correspondence over a range of k that included the first peak of $S(k)$; see Fig. 13.

Access to the real-space structure of bulk colloidal fluids, made possible with the advent of confocal microscopy, led to the first experimental measurements of $g(r)$ of hard spheres (van Blaaderen and Wiltzius, 1995). The example in Fig. 14 compares experimental and EDMD simulation results. Note, however, that the measurements, especially the first peak of $g(r)$, are sensitive both to polydispersity and to tracking errors (Royall, Louis, and Tanaka, 2007; Ivlev *et al.*, 2012; Mohanty *et al.*, 2014). Both effects can be explicitly taken into account in simulations in order to improve the match with *in silico* predictions of the experimental $g(r)$. The resulting pair correlation functions match to a high degree of accuracy. Recently a range of solvents was employed to obtain a behavior indistinguishable from hard spheres when real-space $g(r)$ comparisons were carried out. That is, the effects of softness (see Sec. III.C) were found to be negligible (Kale *et al.*, 2023).
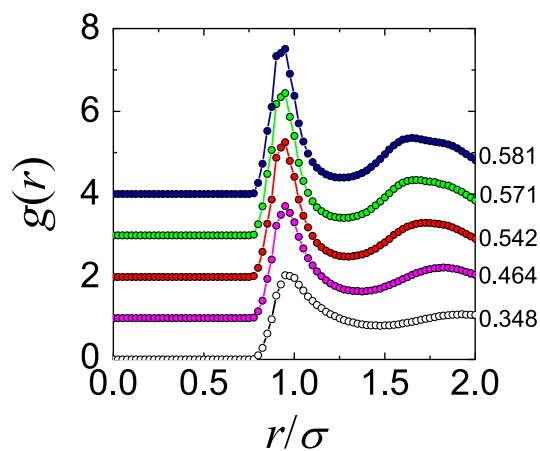

FIG. 14. Radial distribution function of hard-sphere fluids in real space at various effective volume fractions. The points are experimental data, while the lines are simulations of hard-sphere fluids with the experimental polydispersity. Adapted from Royall, Williams, and Tanaka, 2018.
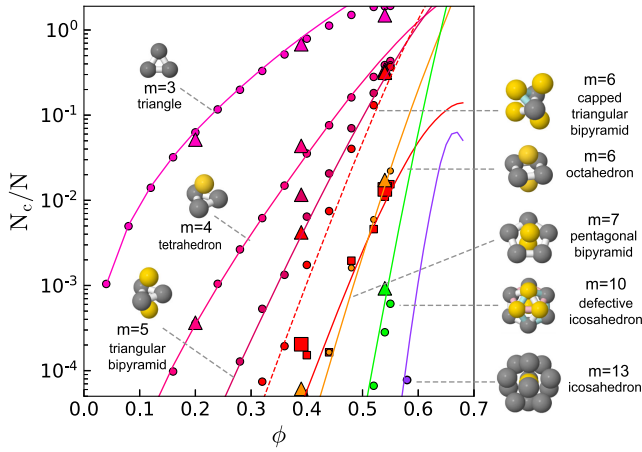
FIG. 15. Higher-order structure in the bulk hard-sphere fluid. Shown are populations of higher-order structures N_c/N containing $m = 3$ to 13 particles, where N_c is the total number of clusters of a certain topology. The lines are from morphometric theory (Robinson *et al.*, 2019; Robinson, Roth, and Royall, 2020). Small data points are from monodisperse Monte Carlo simulations, except for the purple line for $m = 13$ (with $s = 8\%$ polydispersity). Large data points are from a confocal microscopy experiment using particles with $\sigma = 2.0$ μm. Simulations and experiments are analyzed with the topological cluster classification using a simple "bond length" (or pair distance) of 1.2σ (Malins *et al.*, 2013).

Many-body correlation functions and structural features are also easier to extract from real-space than from reciprocal-space information (Royall and Williams, 2015). In particular, it has been possible to compare experiments (Taffs *et al.*, 2013), simulations, and theoretical predictions (Robinson *et al.*, 2019; Robinson, Roth, and Royall, 2020) for the occurrence of clusters that are known to minimize packing constraints (Manoharan, Elsesser, and Pine, 2003; Robinson *et al.*, 2019). As demonstrated in Fig. 15, theoretical predictions of the population of such clusters closely agree with other approaches.

Dynamics. At short times (prior to colliding with a significant number of solvent molecules), colloidal motion is ballistic (Franosch *et al.*, 2011; Hammond and Corwin, 2017). At slightly longer times, however, hard-sphere colloids behave diffusively (Tough *et al.*, 1986) due to their Brownian motion. Owing to the frequent collisions of colloids with solvent molecules, inertia can typically be neglected, thus making their motion overdamped, as in Eq. (14).

Before particles have had the opportunity to interact with their neighbors, their diffusivity can be described by a short-time (real-space) diffusion coefficient D_S. In the dilute limit $\phi \to 0$, neglecting hydrodynamic interactions between colloids, the short-time diffusion coefficient coincides with the free diffusion coefficient ($D_S = D_0$), which for a single colloidal sphere in a solvent with viscosity η is accurately described by the Stokes-Einstein relation

$$D_0 = \frac{k_B T}{3\pi\eta\sigma}. \tag{30}$$

At higher volume fractions, the short-time diffusion coefficient is reduced by hydrodynamic interactions. This slowdown has been demonstrated in a variety of experimental hard-sphere realizations (Ottewill and Williams, 1987; van Megen *et al.*, 1987; Qiu *et al.*, 1990; van Megen and Underwood, 1990; Zhu *et al.*, 1992; Segrè, Behrend, and Pusey, 1995) and reproduced in simulations that specifically account for such interactions (Ladd, 1990; Segrè, Behrend, and Pusey, 1995; Banchio and Nägele, 2008). Various theoretical and empirical descriptions of the relation between D_0 and D_S have also been proposed (Beenakker and Mazur, 1983, 1984; Pusey and Tough, 1983; Lekerkerker and Dhont, 1984; Cohen, Verberg, and De Schepper, 1998; Cichocki, Ekiel-Jeżewska, and Wajnryb, 1999). A common semiempirical expression introduced by Lionberger and Russel (1994),

$$\frac{D_S}{D_0} \simeq (1 - 1.56\phi)(1 - 0.27\phi), \tag{31}$$

extends an earlier result by Batchelor (1976) to quadratic order in ϕ. Figure 16(a) compares experimental results of D_S/D_0 with Eq. (31) as well as with several other theoretical and simulation approaches. Similar experimental results were obtained by Pusey and van Megen (1983), Fraden and Maret (1990), Qiu *et al.* (1990), and Yodh, Kaplan, and Pine (1990). Different simulation methods [force multipole simulations by Ladd (1990) and accelerated Stokesian dynamics by Banchio and Nägele (2008)] accurately describe the experimental data, while the theoretical predictions based on the work of Beenakker and Mazur (1983) agree well up to reasonably high ϕ. Good agreement with the same theory up to $\phi \simeq 0.4$ was also obtained through the experimental work of Orsi *et al.* (2012). The wave vector dependence of D_S has also been investigated and the theoretical predictions verified (van Megen *et al.*, 1985; Segrè, Meeker *et al.*, 1995). In addition, high-speed optical techniques have allowed for the direct observation of colloidal hard-sphere motion during the transition from (short) ballistic timescales to the Brownian regime (Weitz *et al.*, 1989; Zhu *et al.*, 1992; Kao, Yodh, and Pine, 1993).

At still longer times, interactions with neighboring particles hinder colloid mobility. This crowding leads to a subdiffusive regime (as shown by the slope of the mean squared displacement at intermediate times) before motion becomes diffusive once more. This long-time diffusive behavior is now described by a different diffusion coefficient $D_L < D_S$ (Tough *et al.*, 1986). As discussed in Sec. XII, D_L is strongly suppressed at high ϕ in the regime of glassy dynamics. Here we focus on the dynamics in the equilibrium fluid phase alone.

The long-time diffusion coefficient and other transport properties of pure hard spheres (i.e., in the absence of hydrodynamics) have been extensively explored by means of theory and simulations. For instance, early simulations considered the agreement between low-density fluid results with predictions from Enskog's kinetic theory of gases (Alder and Wainwright, 1967; Alder, Gass, and Wainwright, 1970; Easteal, Woolf, and Jolly, 1983; Speedy, 1987; Chapman and Cowling, 1990). As discussed in Sec. V.E, when appropriately rescaled these results are essentially independent of the choice of microscopic dynamics (i.e., Monte Carlo, Brownian, or Newtonian
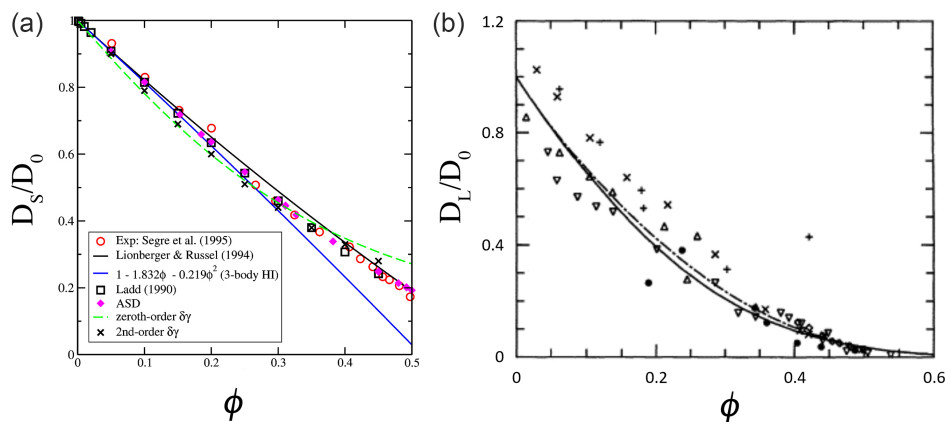
FIG. 16. Self-diffusion coefficient of colloidal hard spheres. (a) Short-time diffusion coefficient obtained from various sources: experiments (Segrè, Behrend, and Pusey, 1995), Eq. (31) by Lionberger and Russel (1994), a theoretical prediction based on up to three-body hydrodynamic interactions (Cichocki, Ekiel-Jeżewska, and Wajnryb, 1999), force multipole simulations by Ladd (1990), accelerated Stokesian dynamics (ASD) simulations (Banchio and Nägele, 2008), and theoretical predictions based on the theory of Beenakker and Mazur (Beenakker and Mazur, 1983; Banchio and Nägele, 2008). From Banchio and Nägele, 2008. (b) Long-time diffusion coefficient from various sources: experiments with hard-sphere-like suspensions by van Megen *et al.* (1987) ($\triangledown$), Segrè, Meeker *et al.* (1995) ($\diamond$), van Blaaderen, Peetermans *et al.* (1992) ($+, \triangle$), Imhof and Dhont (1995b) ($\times$), and Kops-Werkhoven and Fijnaut (1982) ($\bullet$), as well as the theories of Cohen, Verberg, and De Schepper (1998) (the solid line) and Medina-Noyola (1988) (the dash-dotted line). Adapted from Cohen, Verberg, and De Schepper, 1998.

dynamics). For simulations of pure hard spheres, that equivalence has been generally observed (Scala, Voigtmann, and De Michele, 2007; Sanz and Marenduzzo, 2010).

In experimental colloidal hard-sphere fluids, the long-time dynamics is influenced by collisions with neighbors as well as by hydrodynamics. While hydrodynamic interactions typically lead to an overall density-dependent scaling of the dynamical timescales only for systems close to equilibrium, they can significantly influence nonequilibrium behavior; see Secs. XI and XIII.D. Experimental measurements of the diffusion coefficient in a variety of systems (Kops-Werkhoven and Fijnaut, 1982; van Megen *et al.*, 1987; van Blaaderen, Peetermans *et al.*, 1992; Imhof and Dhont, 1995b; Segrè, Meeker *et al.*, 1995) have shown broadly consistent results for D_L/D_0 as a function of ϕ; see Fig. 16(b). Theoretical approaches based on the generalized Langevin equation (Medina-Noyola, 1988), on the expected scaling of diffusion near random close packing (Brady, 1994), or on a mean-field description (Cohen, Verberg, and De Schepper, 1998) provide a reasonably good description of this behavior. Note that, although the experimental data in Fig. 16(b) represent a variety of systems with different polydispersities and electrostatic charge, these effects are largely hidden by the experimental noise. Since both charge and polydispersity shift the effective hard-sphere volume fraction, it is natural to expect a corresponding shift in the dynamics. This effect can be more clearly observed when viscosity measurements are considered (Papir and Krieger, 1970; de Kruif, van Iersel *et al.*, 1985; van der Werff and de Kruif, 1989; Jones, Leary, and Boger, 1991; Imhof *et al.*, 1994; Segrè, Meeker *et al.*, 1995) and is closely matched by the theoretical treatment of Cohen, Verberg, and De Schepper (1998). Charged colloids also exhibit the same scaling, and it has been suggested that the collapse may be more coincidental than fundamental.

The reciprocal-space dynamics of hard spheres has also been extensively studied. Notably experiments by Segrè and Pusey (1996, 1997) on sterically stabilized PMMA particles found an unexpected collapse of the dynamical behavior for large wave vectors: both the wave-vector-dependent diffusion coefficient $D(k,t)$ and the intermediate scattering function $F(k,t)$ collapsed onto a single curve for $k\sigma \gtrsim 5$. Later work on charge-stabilized polystyrene spheres could not reproduce that collapse (Lurio *et al.*, 2000), but that may be due to the presence of residual charges, even if such charges hardly affected the static structure factor. This interpretation is supported by the fact that both mode-coupling theory calculations on pure hard spheres (Fuchs and Mayr, 1999) and additional experiments on sterically stabilized PMMA spheres (Orsi *et al.*, 2012) reproduce the approximate collapse of $F(k,t)$ reported by Segré and Pusey.

While not strictly pertaining to colloidal hard spheres, because the work was carried out using MD simulations of hard spheres in a vacuum, we note that some attention has been given to the tail of the velocity autocorrelation function. Around the freezing volume fraction, this observable turns from positive to negative back to positive (Williams *et al.*, 2006; Martinez *et al.*, 2014) as a result of collisional backscattering in high-density fluids. Unlike some, however, we conclude based on the nature of the phase transition and its equivalence in systems with other microscopic dynamics that the emergence of this dynamical phenomenon is merely coincidental with the thermodynamic freezing point and not evidence of a deeper physical relationship. To summarize, we have a clear and robust theoretical understanding and experimental validation of the diffusion of colloidal hard-sphere fluids at low and intermediate densities.
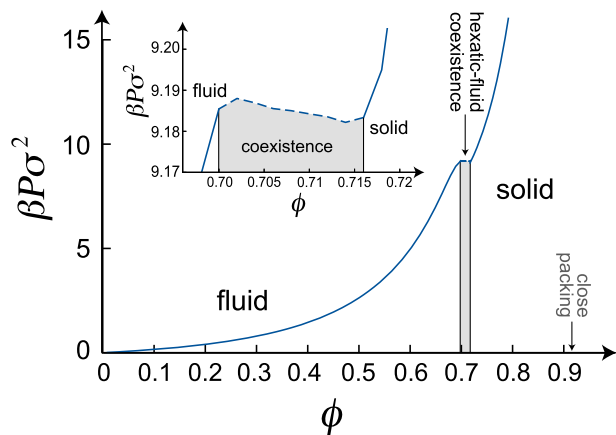
FIG. 17. Hard-sphere phase behavior and EOS in two dimensions as a function of area fraction ϕ. Close packing is found at $\phi_{cp} = 0.909\ldots$. The first-order fluid-hexatic transition is marked by a narrow coexistence region of $\phi \approx 0.700--0.7165$. The hexatic-solid transition is second order at $\phi \approx 0.720$. The EOS for the fluid and solid phases is plotted using the fits given by Liu (2021). Inset: fluid-hexatic phase coexistence.

E. Bulk hard spheres in two dimensions

Equilibrium phase behavior of hard disks. When monodisperse hard spheres are confined to a strictly two-dimensional setup, they behave as hard disks, a model system that has itself long been the focus of theoretical and computational study. However, the phase behavior of hard disks is profoundly different from that of hard spheres.

As shown by Peierls (1955), thermal fluctuations destroy positional order in two-dimensional solids, thus resulting in an algebraic decay of the positional correlation function. Orientational order, however, can persist even in the presence of thermal fluctuations (Mermin and Wagner, 1966). The behavior of these two order parameters is linked to that of two different classes of topological defects. Positional order is destroyed by free dislocations, which can be viewed as additional rows of disks stuck in the crystal and which appear in a dislocation-unbinding transition that shares many similarities with the vortex-unbinding transition predicted by Kosterlitz and Thouless for the two-dimensional *XY* model (Kosterlitz and Thouless, 1973). Halperin and Nelson noted that the unbinding of dislocation pairs, while destroying positional order, can produce a new *hexatic* phase with quasi-long-range orientational order. This quasi-long-range orientational order is in turn destroyed by the unbinding of free dislocations into a pair of disclinations, which

are topological defects where disks have either five or seven neighbors. The resulting melting scenario is named the Kosterlitz-Thouless-Halperin-Nelson-Young (KTHNY) theory (Kosterlitz and Thouless, 1973; Halperin and Nelson, 1978; Young, 1979).

How closely hard disks follow this scenario was debated for decades. Simulations finally settled the question about a dozen years ago (Bernard and Krauth, 2011; Engel *et al.*, 2013). The key difficulty is that finite-size effects cut off the algebraic decay of correlations. Large system sizes are therefore required to assess their relevance. This requirement is compounded by the sluggish decay of structural correlations in the regime of interest. This dual hurdle was first overcome thanks to event-chain MC simulations (Sec. V.A). The results revealed that the solid-hexatic transition is continuous, but that the hexatic-fluid transition is weakly first order with a narrow coexistence region $0.700 < \phi < 0.716$ wherein domains of long-range orientational correlations coexist with short-range orientational correlations; see Figs. 17 and 18. To relate these predictions to experimental systems, the effect of out-of-plane fluctuations was investigated using event-driven molecular dynamics simulations (Qi, Gantapara, and Dijkstra, 2014). These simulations showed that the two-stage melting scenario of hard disks persists even for monolayers of hard spheres with out-of-plane buckling as high as half of a particle diameter. These simulations have further shown that the solid-hexatic transition is of the Kosterlitz-Thouless type and occurs via dissociation of bound dislocation pairs, whereas the hexatic-liquid transition is driven by a spontaneous proliferation of grain boundaries.

Early experimental work aiming at elucidating the nature of the melting transition of colloidal monolayers have qualitatively confirmed a number of KTHNY predictions, but the order of the two transitions could not be unambiguously resolved (Murray and van Winkle, 1987). A study of PMMA spheres suggested a first-order phase transition between the fluid and hexatic phases as well as a first-order phase transition between the hexatic and solid phases (Marcus and Rice, 1997). However, Marcus and Rice argued that this observation could be linked to nonhard attractive or repulsive interactions between particles, which is consistent with an earlier simulation study (Bladon and Frenkel, 1995). A study using microgel spheres with temperature-dependent diameters (Han, Ha *et al.*, 2008) observed a clear two-step melting, even though the temperature resolution was insufficient to identify the order of the transitions.

A definitive experimental elucidation of the nature of the hard-disk phase diagram was later provided by experiments on

Source	ϕ_f	ϕ_h	ϕ_{hs}	$\beta P_{coex}^{fh}\sigma^2$	N
Bernard and Krauth (2011)	0.700	0.716	0.720	9.185	1024^2
Engel *et al.* (2013)	0.700	0.716	0.720	9.185	1024^2
Qi *et al.* (2014)	0.699	0.717	0.725	9.183	1024^2

FIG. 18. Table summarizing prior reports on the phase behavior of hard disks in two dimensions using computer simulations. For each result, we list the area fractions of the coexisting fluid ϕ_f and hexatic ϕ_h phases, the area fraction at the hexatic-solid transition ϕ_{hs}, the coexistence pressure at the fluid-hexatic phase transition $\beta P_{coex}^{fh}\sigma^2$, and the system size considered. Note that the area fraction is defined as $\phi = \pi\sigma^2 N/4A$, with A the system area. Note also that the accuracy is to the last reported digit.
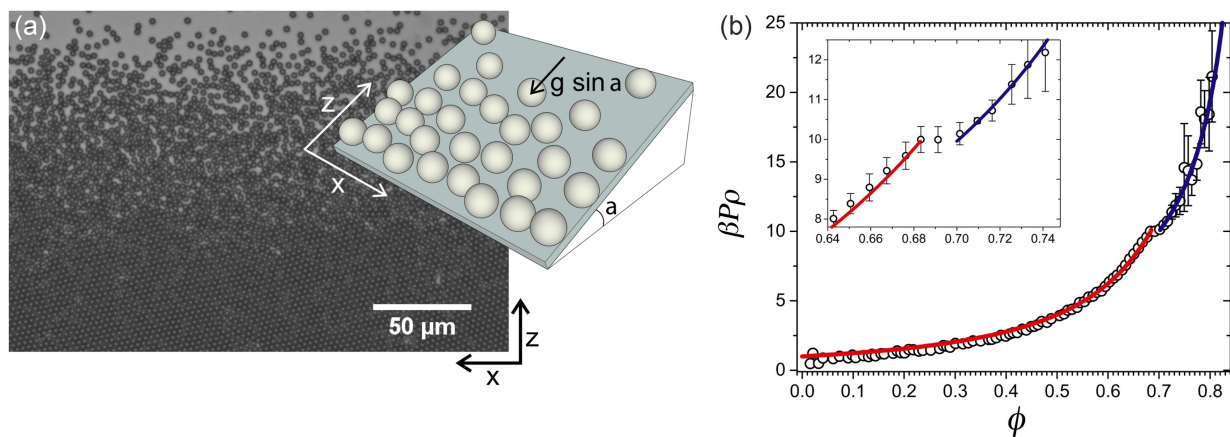
FIG. 19. Experimental determination of the hard-sphere phase behavior in two dimensions. (a) Experimental image of quasi-2D hard spheres in sedimentation-diffusion equilibrium under a slight tilt. (b) The EOS $P/\rho k_{\mathrm{B}}T$. Inset: expanded view of the EOS around the discontinuity. The solid red (gray) line is a prediction of scaled particle theory for the fluid regime [Eq. (32)]. The solid blue (dark gray) line is a semiempirical fit $P/\rho k_{\mathrm{B}}T = a/(\phi_{\mathrm{cp}} - \phi)$. From Thorneywork, Abbott *et al.*, 2017.

a tilted monolayer of colloidal hard spheres in sedimentation-diffusion equilibrium (Thorneywork, Abbott *et al.*, 2017); see Fig. 19. By measuring the density profile at different tilts of the plane, the full EOS was extracted via the barometric law, unveiling a discontinuity at $\phi = 0.68$. By calculating the height-resolved bond-orientational-order (BOO) correlation function in time and a modified Lindemann parameter, this discontinuity was identified as a first-order fluid-hexatic phase transition, and a study of the thermal fluctuations of the interface identified the width of the fluid-hexatic coexistence region as $\Delta\phi \simeq 0.02$. In addition, no finite discontinuities were found between the hexatic-solid transition. In short, reasonably good agreement with the simulation results was observed (with essentially the same level of accuracy as that noted in Sec. VII.C). Later direct comparisons of correlations in translational and BOO in the various phases demonstrated excellent agreement between this experimental model system and simulations (Thorneywork, Abbott *et al.*, 2018).

Whether or not the hexatic phase is present depends strongly on the details of the system. For instance, the fluid-hexatic phase transition becomes metastable with respect to a first-order fluid-solid transition for binary mixtures of large (L) and small (S) disks with a diameter ratio $q = \sigma_L/\sigma_S = 1.4$ for molar fractions of small disks as small as 1% (Russo and Wilding, 2017; Russo, Romano, and Tanaka, 2018). The two-stage melting scenario of a continuous solid-hexatic and a first-order fluid-hexatic transition also becomes metastable with respect to a first-order fluid-solid transition for hard disks with less than 1% of the particles pinned to a triangular lattice (Qi and Dijkstra, 2015). These findings are corroborated with a renormalization group analysis based on the KTHNY theory, which showed that the renormalized Young's modulus of the crystal increases in the presence of pinned particles (Qi and Dijkstra, 2015). The melting transition was shown to be qualitatively changed to the KTHNY scenario for polydisperse disks (Ruiz, Sampedro, Lei, and Ni, 2019), for which a significantly enlarged stability range for the hexatic phase and reentrant melting have been observed.

Equation of state. The EOS of hard disks has been numerically explored since the introduction of the Metropolis algorithm in 1953 (Metropolis *et al.*, 1953) and has been studied extensively ever since (Li *et al.*, 2022). Unlike 3D hard spheres, however, the Percus-Yevick closure to the Ornstein-Zernike equation cannot be solved analytically in two dimensions, thus necessitating the use of numerical integration. As a result, a large number of different approximations for the EOS have been proposed ((Helfand, Frisch, and Lebowitz, 1961; Henderson, 1975; Tejero and Cuesta, 1993; Santos, Lopez de Haro, and Yuste, 1995; Mulero, Cachadina, and Solana, 2009; Boublík, 2011). Scaled particle theory offers a particularly simple one (Helfand, Frisch, and Lebowitz, 1961),

$$\frac{\beta P}{\rho} = \frac{1}{(1-\phi)^2}, \tag{32}$$

which agrees reasonably well with experimental results; see Fig. 19(b). When more accurate results are required, a common approach is to use a polynomial fit to the simulation data of Kolafa and Rottner (2006).

The experimental EOS was measured by Brunner *et al.* (2003) in the fluid regime and by Thorneywork, Abbott *et al.* (2017) for the entire ϕ regime; see Fig. 19. Comparison using test-particle insertion agrees exceptionally well with simulations (Stones, Dullens, and Aarts, 2018). Good agreement between theory and simulations has also been reported for $g(r)$ at various ϕ (Marcus and Rice, 1997; Santana-Solano and Arauz-Lara, 2001; Brunner *et al.*, 2003; Thorneywork *et al.*, 2014).

Dynamics of the hard-disk fluid. The dynamics of 2D confined hard-sphere colloids has been explored experimentally, with early work investigating the decay of the short-time diffusion to its long-time limit (Marcus, Lin, and Rice, 1996). This study was followed by explorations of hydrodynamic effects on the short-time dynamics and related these to the 3D system (Carbajal-Tinoco, Cruz de León,

and Arauz-Lara, 1997; Santana-Solano and Arauz-Lara, 2001; Bonilla-Capilla *et al.*, 2004).

Another way to form a 2D colloidal system is for particles to adhere to an interface between two liquids. The dynamics in such a system provides a good estimate of the drag coefficient of the particles (Peng *et al.*, 2009). Other work has emphasized the importance of hydrodynamic interactions at short times (Thorneywork *et al.*, 2015). Surprisingly, while higher ϕ lead to a lower short-time diffusion coefficient D_S, as expected, the behavior of the long-time diffusion coefficient D_L agrees well with simulation results of a pure hard-disk system. Hence, although hydrodynamics slows down the individual motion of particles at short times, its effect is largely compensated at longer timescales. Recently the degree of confinement to a plane has also been investigated using simulations incorporating hydrodynamic interactions. The long-time diffusion was then found to be enhanced in weaker confinement (Tian, Kob, and Barrat, 2022).

VIII. INTERFACES IN HARD SPHERES

Hard-sphere systems spontaneously form interfaces as a result of fluid-crystal phase separation as well as grain boundaries in the crystal phase. Interfacial effects can also arise by bringing hard spheres into contact with a boundary. This section delves into the various phenomena, starting with the conceptually important case of a single hard wall.

A. Fluid in contact with a wall

Planar wall. A bulk fluid of hard spheres next to a single hard wall is considered to be the simplest inhomogeneous system. Intuitively the presence of a flat wall induces some local structuring of the fluid, which in turn promotes the formation of the crystal phase. Early simulations by Courtemanche and van Swol (1992) and Courtemanche, Pasmore, and van Swol (1993) indeed demonstrated that crystalline layers could spontaneously form near a planar hard wall, even at pressures below bulk freezing. However, note that in simulations, because of periodic boundary conditions, a single wall is essentially a confined system with two walls at a plate separation determined by the system size. Therefore, complete wetting of a hard-sphere crystal at a single wall, also termed prefreezing, is challenging to distinguish from capillary freezing (Groot, Faber, and van der Eerden, 1987; Kegel, 2001; Dijkstra, 2004). Careful simulation studies have now demonstrated that (i) a (111) hard-sphere crystal completely wets a hard wall-fluid interface at about 98.3% of the bulk freezing density via interfacial free-energy calculations (Laird and Davidchack, 2007), and that (ii) a crystalline film at a single wall, independent of the plate separation, grows logarithmically and is clearly distinguishable from capillary freezing (Dijkstra, 2004).

The interface between a hard-sphere fluid and a hard wall also gives rise to an interfacial free energy γ that depends on the fluid volume fraction ϕ. Although a virial-like expansion for this quantity is possible, too few coefficients are known for it to be of much practical use (Charbonneau *et al.*, 2010). Davidchack, Laird, and Roth (2016) numerically studied a hard-sphere fluid close to a planar wall and computed the
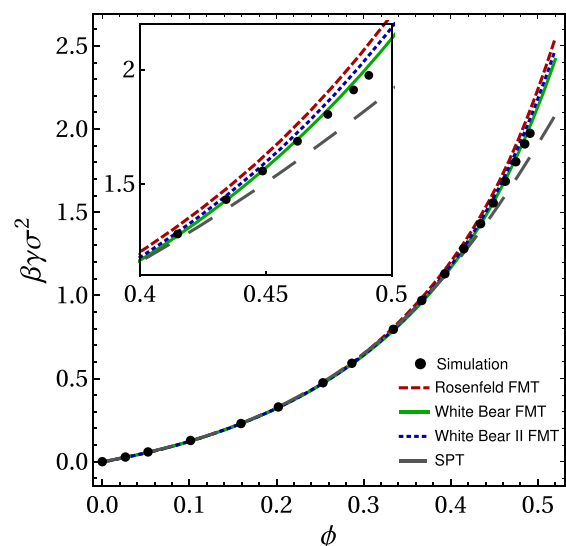

FIG. 20. Interfacial free energy of a hard-sphere fluid in contact with a flat hard wall as a function of ϕ. The lines are theoretical predictions based on fundamental measure theory (FMT) and scaled particle theory (SPT). The points are simulation data. Simulation and FMT data from Davidchack, Laird, and Roth (2016); the SPT expression is based on the work of Heni and Löwen (1999).

density profiles, γ, and the excess adsorption by means of computer simulations and DFT; see Sec. VI.C. They detected systematic deviations between numerical and DFT results for $\phi > 0.3$; see Fig. 20. Similar deviations were previously reported in a study of confined hard-sphere fluids (Deb *et al.*, 2011) that suggested that nontrivial correlations between fluid particles beyond nearest-neighbor shell might develop at higher ϕ. These correlations could not, however, be accurately captured by DFT.

In experiments (Hoogenboom, Vergeer, and van Blaaderen, 2003), the presence of a bottom wall was found to initially induce layering in a sedimenting colloidal fluid; as sediment thickness increased, crystallization occurred within these fluid layers. Crystallization in the first layer appeared to proceed via a first-order transition, consistent with predictions from BD simulation and theory (Biben, Ohnesorge, and Löwen, 1994). Using grand-canonical Monte Carlo simulations including a gravitational field, it was later shown that the fluid crystallized via a first-order freezing transition at which several fluid layers close to the bottom of the sample froze at the same chemical potential (Marechal and Dijkstra, 2007). The number of such layers simultaneously freezing decreases for higher gravitational field strengths.

The presence of a wall can also affect colloid dynamics. Evanescent DLS experiments have studied sterically stabilized PMMA particles for various volume fractions over a range of scattering wave vectors. In the dilute regime, Michailidou *et al.* (2009) observed that the near wall short-time diffusion was slowed down due to particle-wall hydrodynamic interactions. However, for a concentrated suspension, the wall effect progressively diminished at all vectors k and many-body hydrodynamic interactions became less

relevant (Michailidou *et al.*, 2009; Liu, Błaawzdziewicz *et al.*, 2015).

Patterned wall. The wetting behavior of the hard-sphere crystal has also been studied for patterned walls (Heni and Löwen, 2000). In the case of a (111) structured surface, complete wetting of the hard-sphere crystal already sets in at a pressure 29% below the bulk freezing pressure. Even crystal structures that are unstable in bulk can be promoted by the wall surface pattern. As an example, hcp (rather than fcc or rhcp) has been epitaxially grown on a structured template (Hoogenboom *et al.*, 2003). By contrast, surface wetting by the crystal below freezing can be completely suppressed by wall patterns that are incommensurate with the equilibrium crystal structure (Espinosa *et al.*, 2019).

B. Fluid-solid interface

At coexistence, the fluid phase is separated from the ordered solid by a thermally fluctuating fluid-solid interface. Understanding the properties of this interface on a microscopic scale is fundamental to assess crystal nucleation; see Sec. XIII. For a planar fluid-crystal interface at coexistence, one can define the interfacial (or surface) free energy γ as the reversible work needed to form a unit area of a flat interface. The quantity γ generally depends on the orientation of the interface normal ($\hat{n}$) relative to the crystalline axes. When considering the fluctuations of the same interface, the quantity of interest is instead the interfacial stiffness $\tilde{\gamma}$. We discuss efforts to quantify both γ and $\tilde{\gamma}$ here.

Interfacial free energy. In a pioneering numerical simulation, Davidchack and Laird (1998) characterized the face-centered-cubic (100) and (111) fluid-solid interfaces, thus demonstrating that the transition from crystal to fluid occurred over a few crystal planes made of domains of coexisting crystal and fluid phases. They later extended the method developed by Broughton and Gilmer (1986), based on a thermodynamic integration along a reversible path defined by cleaving, to determine γ for hard-sphere fluids, whose value depended on the crystalline lattice structure (Davidchack and Laird, 2000). Their results were then sufficiently precise to assess the anisotropy of the fluid-solid interfacial free energy. This work was followed by more simulation-based efforts to determine γ using a wide variety of approaches, including the analysis of interfacial fluctuations using capillary wave theory (Mu, Houk, and Song, 2005; Davidchack, Morris, and Laird, 2006; Härtel *et al.*, 2012), nonequilibrium work methods (Davidchack, 2010), tethered Monte Carlo simulations (Fernández *et al.*, 2012), classical nucleation theory (Cacciuto, Auer, and Frenkel, 2003), mold integration (Espinosa, Vega, and Sanz, 2014), and thermodynamic integration (Benjamin and Horbach, 2015; Bültmann and Schilling, 2020); see also Sec. V. Härtel *et al.* (2012) additionally used FMT (see Sec. VI), but this approach resulted in significantly higher values than in simulations. An overview of results for γ provided in Fig. 21 lists results for both individual interfaces and an orientationally averaged $\bar{\gamma}$, which is a key quantity in crystal nucleation; see Sec. XIII. Significant variations exist between different methods, especially when compared to the relatively small error bars reported. Schmitz, Virnau, and Binder (2014) and Schmitz

and Virnau (2015) suggested that systematic errors (related to finite-size effects) could be a possible explanation for this disagreement. Benjamin and Horbach (2015) proposed a theoretical tool to obtain reliable estimates for γ in the thermodynamic limit.

To establish whether the fcc or hcp crystal is favored due to a difference in interfacial free energy, Sanchez-Burgos *et al.* (2021) computed γ by means of the mold integration method considering both ordered phases. They concluded that the $(11\bar{2}0)$ plane of the hcp crystal has a slightly higher γ than any of the faces of the fcc polytype. They also found a higher orientationally averaged $\bar{\gamma}$ for the hcp phase when considering spherical nuclei using a seeding approach; see Fig. 22.

Only more recently have interfacial properties been investigated in experiments (Gasser, 2001; Dullens, Aarts, and Kegel, 2006b; Hernández-Guzmán and Weeks, 2009); see Fig. 23. Experimentally γ can be obtained from indirect measurements of crystal nucleation rates using classical nucleation theory; see Sec. XIII. Using this method on PMMA colloids, Gasser (2001) obtained a surprisingly low $\bar{\gamma}$ (see Fig. 21), possibly due to the colloids being softened by electrostatic interactions (see Sec. III.C).

Interfacial stiffness. For rough fluid-crystal interfaces such as in hard spheres,[12] capillary wave theory (CWT) can be applied to define the interfacial stiffness $\tilde{\gamma}$ that controls the resulting waves. The tensorial expression for $\tilde{\gamma}$ is then

$$\tilde{\gamma}_{\alpha\beta}(\hat{n}) = \gamma(\hat{n}) + \frac{\partial^2 \gamma(\hat{n})}{\partial \hat{n}_\alpha \partial \hat{n}_\beta}, \qquad (33)$$

with $\hat{n}_\alpha$ and $\hat{n}_\beta$ two directions orthogonal to $\hat{n}$ (Fisher and Weeks, 1983). While the first contribution [$\gamma(\hat{n})$] describes the free-energy cost of increasing the interfacial area, the second contribution accounts for the free energy required to locally change the crystal orientation.

If the anisotropy of the interfacial free energy is known, $\tilde{\gamma}$ can be calculated directly from Eq. (33), in the manner of Härtel *et al.* (2012). Alternatively, it can be obtained from interfacial fluctuations measured in simulations using CWT (Mu, Houk, and Song, 2005; Davidchack, Morris, and Laird, 2006; Zykova-Timan *et al.*, 2009; Zykova-Timan, Horbach, and Binder, 2010; Härtel *et al.*, 2012). Values from various different approaches are given in Fig. 21. Overall, $\tilde{\gamma}$ shows significantly more anisotropy than γ, but there are also significant discrepancies between different measurements.

Hernández-Guzmán and Weeks (2009) used confocal microscopy to study the interfacial fluctuations of a solid-fluid interface and determined the interfacial stiffness using CWT predictions for the dynamical behavior of an interface between two fluids; see Fig. 23. They obtained a value about twice as high as that obtained from computer simulations; see Fig. 21. Whether this discrepancy stems from the approximation of the crystal-fluid interface as a fluid-fluid interface or from the presence of slight charges on the particles remains to be verified.

---

[12]The roughening transition temperature of thermal systems is system dependent (Schmid and Binder, 1992; Zykova-Timan, Horbach, and Binder, 2010), but hard spheres are always rough.

Interfacial free energy (γ)	Interfacial stiffness ($\tilde{\gamma}$)
$\gamma(111)[k_\mathrm{B}T/\sigma^2]$	$\tilde{\gamma}(111)[k_\mathrm{B}T/\sigma^2]$
0.58 ± 0.01 (Davidchack and Laird, 2000) [CL]	0.80 [$\bar{1}10$] (Mu *et al.*, 2005) [CW]
0.61 ± 0.02 (Mu *et al.*, 2005) [CW]	0.78 ± 0.04 [$\bar{1}10$] (Davidchack, 2010) [NEW]
0.546 ± 0.016 (Davidchack *et al.*, 2006) [CW]	1.025 ± 0.079 (Härtel *et al.*, 2012) [FMT]
0.5416 ± 0.0031 (Davidchack, 2010) [NEW]	0.810 ± 0.005 (Härtel *et al.*, 2012) [CW]
0.636 ± 0.001 (Härtel *et al.*, 2012) [FMT]	0.41 (van Loenen *et al.*, 2019) [CW]$_\mathrm{exp}$
0.600±0.011 (Härtel *et al.*, 2012) [CW]	
0.556± 0.003 (Benjamin and Horbach, 2015) [TI]	
0.544± 0.008 (Schmitz and Virnau, 2015) [SW]	
0.554±0.006 (Sanchez-Burgos *et al.*, 2021) [MI]	
$\gamma(100)[k_\mathrm{B}T/\sigma^2]$	$\tilde{\gamma}(100)[k_\mathrm{B}T/\sigma^2]$
0.62 ± 0.01 (Davidchack and Laird, 2000) [CL]	0.55 [001] (Mu *et al.*, 2005) [CW]
0.64 ± 0.02 (Mu *et al.*, 2005) [CW]	0.44 ± 0.03 [001] (Davidchack *et al.*, 2006) [CW]
0.574± 0.017 (Davidchack *et al.*, 2006) [CW]	0.40 ± 0.02 [001] (Davidchack, 2010) [NEW]
0.582 ± 0.002 (Davidchack, 2010) [NEW]	0.49 ± 0.02 [001] (Zykova-Timan *et al.*, 2010) [CW]
0.636 ± 0.011 (Fernández *et al.*, 2012) [TET]	0.53± 14 [001] (Härtel *et al.*, 2012) [FMT]
0.687 ± 0.001 (Härtel *et al.*, 2012) [FMT]	0.419± 0.005 [001] (Härtel *et al.*, 2012) [CW]
0.639 ± 0.0011 (Härtel *et al.*, 2012) [CW]	
0.586 ± 0.008 (Espinosa *et al.*, 2014) [MI]	
0.596± 0.006 (Benjamin and Horbach, 2015) [TI]	1.2 (Hernandez-Guzman and Weeks, 2009) [CW]$_\mathrm{exp}$
0.581± 0.003 (Schmitz and Virnau, 2015) [SW]	1.3 ± 0.3 (Ramsteiner *et al.*, 2010) [CW]$_\mathrm{exp}$
0.589 ± 0.001 (Bültmann and Schilling, 2020) [TI]	0.47 (van Loenen *et al.*, 2019) [CW]$_\mathrm{exp}$
0.586 ± 0.006 (Sanchez-Burgos *et al.*, 2021) [MI]	
$\gamma(110)[k_\mathrm{B}T/\sigma^2]$	$\tilde{\gamma}(110)[k_\mathrm{B}T/\sigma^2]$
0.64 ± 0.01 (Davidchack and Laird, 2000) [CL]	0.71 [001] (Mu *et al.*, 2005) [CW]
0.62 ± 0.02 (Mu *et al.*, 2005) [CW]	0.49 [$\bar{1}10$] (Mu *et al.*, 2005) [CW]
0.557± 0.017 (Davidchack *et al.*, 2006) [CW]	0.42 ± 0.03 [$\bar{1}10$] (Davidchack *et al.*, 2006) [CW]
0.559 ± 0.002 (Davidchack, 2010) [NEW]	0.70 ± 0.03 [001] (Davidchack *et al.*, 2006) [CW]
0.616 ± 0.011 (Härtel *et al.*, 2012) [FMT]	0.34 ± 0.05 [$\bar{1}10$] (Davidchack, 2010) [NEW]
0.600±0.011 (Härtel *et al.*, 2012) [CW]	0.74 ± 0.02 [001] (Davidchack, 2010) [NEW]
0.577 ± 0.004 (Benjamin and Horbach, 2015) [TI]	0.283 ± 0.035 [$\bar{1}00$] (Härtel *et al.*, 2012)[FMT]
0.559 ± 0.001 (Schmitz and Virnau, 2015) [SW]	0.401 ± 0.005 [$\bar{1}00$] (Härtel *et al.*, 2012) [CW]
0.572 ± 0.007 (Sanchez-Burgos *et al.*, 2021) [MI]	0.86 ± 0.14 [$01\bar{1}$] (Härtel *et al.*, 2012)[FMT]
	0.769 ± 0.005 [$01\bar{1}$] (Härtel *et al.*, 2012) [CW]
	1.0 ± 0.2 (Ramsteiner *et al.*, 2010) [CW]$_\mathrm{exp}$
	0.53 (van Loenen *et al.*, 2019) [CW]$_\mathrm{exp}$
$\bar{\gamma}$ [$k_\mathrm{B}T/\sigma^2$]	
0.617 ± 0.006 (Davidchack and Laird, 2000) [CL]	
0.27 (Gasser, 2001) [CNT]$_\mathrm{exp}$	
0.616 ± 0.003 (Cacciuto *et al.*, 2003) [CNT]	
0.62 ± 0.02 (Mu *et al.*, 2005) [CW]	
0.56 ± 0.01 (Davidchack, 2010) [NEW]	
0.66 ± 0.01 (Härtel *et al.*, 2012)[FMT]	
0.5916 (Sanchez-Burgos *et al.*, 2021) [CNT]	

FIG. 21.   Interfacial free energy γ and stiffness $\tilde{\gamma}$, where (hjk) are the Miller indices of the interfacial crystal plane. For the stiffness we might also indicate the symmetry of the short (in-plane) direction. $\bar{\gamma}$ is averaged over (100), (110), and (111) (of an fcc crystal). Various approaches have been employed for the determination: cleaving (CL), capillary wave (CW), nonequilibrium work (NEW), mold integration (MI), tethered Monte Carlo simulations (TET), CNT analysis of the nucleation rate (CNT), thermodynamic integration (TI), ensemble switch (SW), fundamental measure DFT (FMT) (theory), and experiments []$_\mathrm{exp}$.

Similar values of the interfacial stiffness were obtained by Ramsteiner, Weitz, and Spaepen (2010). After sedimenting hard-sphere silica colloids onto (100) and (110) oriented templates, they located the interface by confocal microscopy and again used CWT to determine $\tilde{\gamma}$. For all three main crystal orientations, they noted that the Fourier amplitudes are independent of the in-plane direction of the associated wave vectors in the long-wavelength limit. This result directly
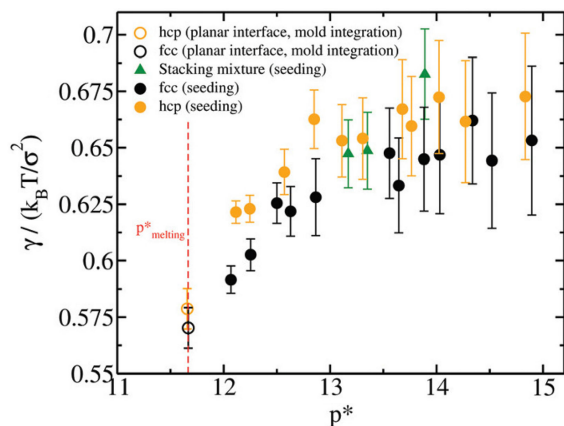
FIG. 22. Interfacial free energy γ for different polytypes at coexistence. For planar interfaces (at the bulk melting pressure), an average $\bar{\gamma}$ was obtained by averaging over different crystal orientations for both polymorphs. The values at higher pressures correspond to $\bar{\gamma}$ estimated for spherical nuclei (from the seeding technique) using CNT. From Sanchez-Burgos *et al.*, 2021.
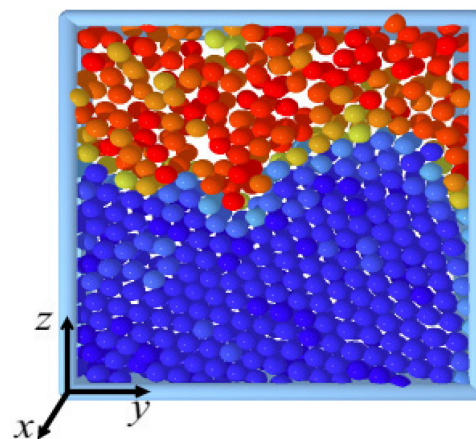

FIG. 23. Rendering of particle coordinates determined from confocal microscopy showing the fluid-crystal interface. Shown is a slice that is two crystalline layers thick. Particles are colored according to the number of ordered neighbors they have. From Hernández-Guzmán and Weeks, 2009.
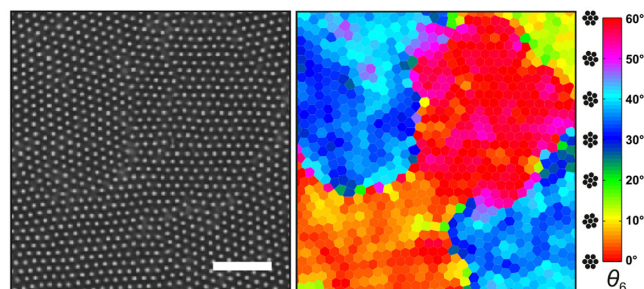

FIG. 24. Grain boundaries in a polycrystalline 2D solid of colloidal hard spheres. Left panel: the particles. The scale bar is 20 μm. Right panel: the Voronoi cells of the particles, colored by the local orientation of the BOO parameter, as encoded in the color bar, which allows for easy distinction between the different domains. Adapted from Lavergne, Aarts, and Dullens, 2017.

contradicts simulation results for the (110) interface, from which a difference consistent with the stiffness tensor of a cubic crystal is expected. Ramsteiner, Weitz, and Spaepen (2010) suggested that the relatively thin fluid layer and the small gravitational length could explain this discrepancy.

van Loenen *et al.* (2019) studied the interfaces between hard-sphere colloidal fluids and fcc crystals sedimented onto differently oriented templates. The values of $\tilde{\gamma}$ that they obtained from CWT were not only much closer to the simulation results than earlier estimates by Hernández-Guzmán and Weeks (2009), but their order was also more consistent with simulation predictions; see Fig. 21.

As these different results show, experimental measurements of the stiffness of nominally the same system have yielded markedly different results. A recent study by MacDowell (2023) suggested that the surface stiffness of colloidal hard spheres, as measured by interface fluctuations, might include a gravity-dependent contribution that could account for this discrepancy. The external field dependence of the interfacial stiffness could then be explained by an improved interface Hamiltonian that provides corrections to the capillarity theory equation, thus reconciling the experimental and theoretical results.

C. Grain boundaries

Grain boundaries form spontaneously in crystalline materials at finite temperature or, in the case of hard spheres, for volume fractions below close packing, i.e., $\phi < \phi_{cp}$. In a polycrystalline material, crystalline grains with differing orientations are separated by an interface made of amorphous grain boundaries. Most of the work on grain boundaries has been performed in two dimensions (Zhang *et al.*, 2009; Gray *et al.*, 2015; Lavergne, Aarts, and Dullens, 2015). Grain boundaries and other defects reduce long-range order of a single crystal (Zhang *et al.*, 2009), thereby deforming the underlying hexagonal order (in two dimensions) due to a

preference for fivefold and sevenfold coordinated particles to be adjacent to impurities (Gray *et al.*, 2015).

Considering a polycrystalline monolayer of colloidal hard spheres (see Fig. 24), Lavergne, Aarts, and Dullens (2017) followed the grain growth process and detected an anomalous slow growth of the BOO correlation length. They invoked the curvature-driven coarsening of the large-angle grain boundaries at a rate dependent on the grain boundary length to explain the effect. When dealing with a polycrystalline monolayer of hard spheres with embedded impurities, Lavergne *et al.* (2016) demonstrated that the size of the impurities determined whether they behaved as interstitial or substitutional impurities in the bulk crystal. Once formed, grain boundaries can also shrink. Spontaneous shrinkage of circular grain boundaries was studied in 2D colloidal crystals by Lavergne *et al.* (2019), who demonstrated that the shrinkage can be driven by three mechanisms: curvature-driven migration, coupled grain boundary migration, and grain boundary sliding.

The grain boundary dynamics is driven by their local curvature and has been thoroughly studied by means of point

sampled surface analysis techniques (Lavergne, Aarts, and Dullens, 2015). While the structure on length scales larger than the grain boundary distances strongly depends on defect concentration, local structural distortions close to a grain boundary occur only over short distances compared to the grain boundary size and are independent of the defect concentration (Gray *et al.*, 2015). The kinetics of grain boundaries is closely related to the topological constraints imposed on their dislocation structure. As an example, Lavergne *et al.* (2018) showed that a local rotational deformation of a 2D colloidal crystal with an optical vortex might originate a grain boundary loop, thus underlining the relevance of defects in the kinetics of grain boundaries.

Thin-film crystals of microgel (N-isopropylacrylamide) with a thickness of 15–20 layers have been studied with video microscopy at a single-particle resolution to observe the thermal roughening of grain boundaries (Liao *et al.*, 2018). Unlike the roughening of free surfaces, the thermal fluctuations of grain boundaries were shown to exhibit both static and dynamic critical-like behavior.

In three dimensions, studies of hard-sphere grain boundaries are much more sparse. Recently Orr *et al.* (2021) introduced a new methodology to detect and characterize grain boundaries in experimental data on colloidal grain boundaries, thus revealing detailed misorientation distributions and grain boundary structures, but much remains to be done.

IX. BINARY HARD-SPHERE MIXTURES

The phase behavior of binary mixtures of L and S hard spheres with diameters σ_L and σ_S, respectively, is rich. Even at close packing, complex binary crystals emerge as the size ratio $q = \sigma_S/\sigma_L$ changes (Hudson and Harrowell, 2011; Hopkins, Stillinger, and Torquato, 2012; Dijkstra, 2014). In this section, we review some of the salient thermodynamic features of

these systems, including the diversity of binary crystal structures that they can form, the structural crossover in binary fluids, fluid-fluid demixing and the quest for its critical point, and the behavior of sedimented monolayers of binary hard-sphere mixtures.

A. Crystal regime

In binary mixtures of hard spheres of two similar sizes, the most stable state at infinite pressure is phase separated into two separate fcc crystals: one of large spheres and one of small spheres. Density-functional theory, computer simulations, and scaled particle theory have revealed further enrichment of the crystal regime at finite pressure, away from close packing. In the limit $q = \sigma_S/\sigma_L \to 1$, the system reduces to a one-component hard-sphere system for which the phase behavior is discussed in Sec. VII.A. As the two components become more dissimilar in size, i.e., $q \lesssim 1$, the freezing transition changes from spindlelike via an azeotrope to the emergence of a eutectic (Barrat, Baus, and Hansen, 1986, 1987; Denton and Ashcroft, 1990; Zeng and Oxtoby, 1990; Kofke, 1991; Kranendonk and Frenkel, 1991; Cottin and Monson, 1997), as shown in Fig. 25.

In the case of spindlelike phase behavior, the coexistence between a fluid and a substitutionally disordered fcc crystal phase is narrow in the sense that only a small composition difference between the two phases develops. When spheres become more dissimilar in size, the fluid-solid region broadens and an azeotropic point appears at around $q = 0.94$ (Kranendonk and Frenkel, 1991). At higher packing fractions a coexistence region between two substitutionally disordered fcc solids appears when the spheres become sufficiently dissimilar, which shifts to lower densities as the size ratio is further increased. When this miscibility gap in the solid phase interferes with the fluid-crystal coexistence, the phase
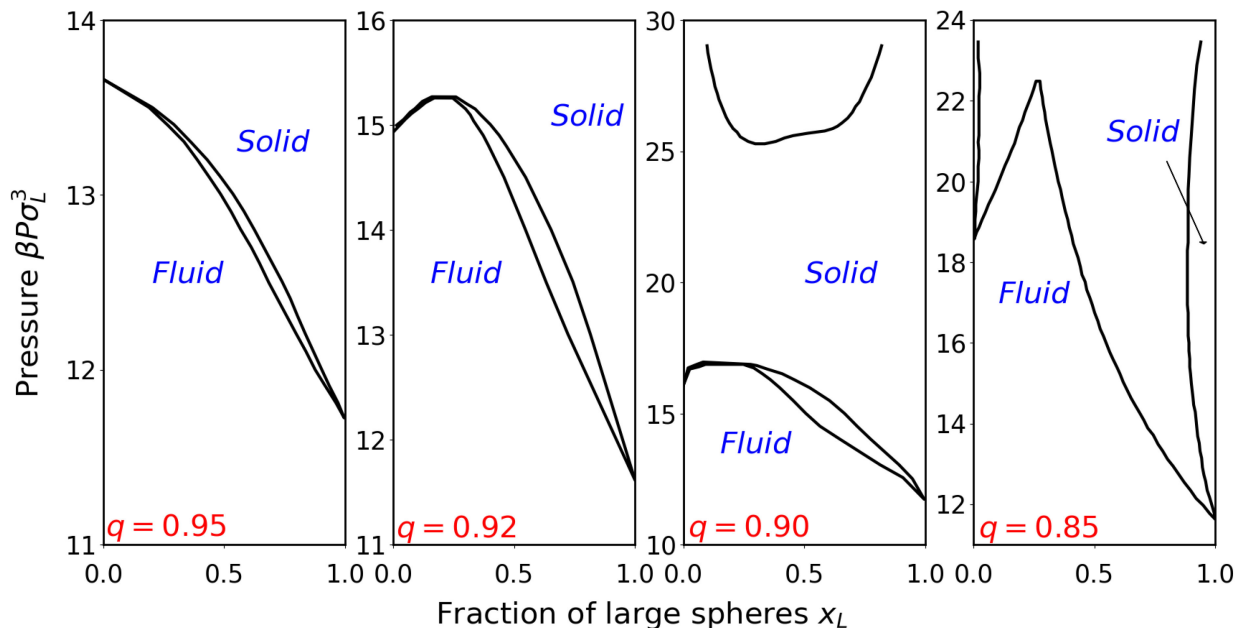

FIG. 25. Phase diagrams of binary hard-sphere mixtures displaying a spindlelike phase behavior at size ratio $q = 0.95$, an azeotropic phase diagram at $q = 0.92$, an azeotropic phase behavior with a solid-solid demixing transition at $q = 0.90$, and an eutectic phase diagram at $q = 0.85$ as obtained from simulations. Data from Kranendonk and Frenkel (1991).

diagram becomes eutectic at $q \simeq 0.875$ (Kranendonk and Frenkel, 1991). Note that only substitutionally disordered fcc phases appear for the size ratio range $q \in (0.85, 1)$, in contrast to what happens at smaller q.

The phase behavior of more asymmetric mixtures was studied in experiments using light scattering (Bartlett, Ottewill, and Pusey, 1990, 1992; Pusey *et al.*, 1994). For size ratios $q = 0.58$ and 0.62, complex binary LS_2 and LS_{13} superlattice structures were found for sterically stabilized PMMA spheres (Bartlett, Ottewill, and Pusey, 1990; Bartlett, Ottewill, and Pusey, 1992). The stability of these superlattice structures, which are analogous to their atomic counterparts AlB_2 and $NaZn_{13}$ (see Fig. 26), was subsequently confirmed by computer simulations for $0.42 < q < 0.625$ (Eldridge, Madden, and Frenkel, 1993a, 1993b, 1993c; Eldridge *et al.*, 1995; Dijkstra, 2014) and by density-functional approaches (Xu and Baus, 1992).

For size ratios $0.2 < q < 0.42$, a superlattice structure isostructural to the rocksalt NaCl was predicted by computer simulations (Trizac, Madden, and Eldridge, 1997) and verified experimentally (Hunt, Jardine, and Bartlett, 2000; Vermolen *et al.*, 2009); see Fig. 26. Surprisingly the experimental observations of NaCl always showed a crystal phase with many vacancies in the sublattice of the small spheres in such a way that the $L:S$ stoichiometry of the crystal is not $1:1$ but rather $1:x$, with $x \leq 1$ (Hunt, Jardine, and Bartlett, 2000; Vermolen *et al.*, 2009). Free-energy calculations from Monte Carlo simulations subsequently showed that an interstitial solid solution constructed by filling the octahedral holes of an fcc crystal of large spheres with small spheres is indeed the stable phase (Filion, Hermes *et al.*, 2011). Upon increasing pressure, the fraction of octahedral holes filled with a small sphere can be completely tuned from 0 (corresponding to a fcc phase of pure large spheres) to 1 (corresponding to a NaCl phase). For less asymmetric size ratios, nonequilibrium interstitial solid solutions are found, which are long-lived on the experimental timescale (Rios de Anda *et al.*, 2017).

For larger size ratios, another set of LS_2 phases, known as Laves phases, were found in computer simulations (Hynninen *et al.*, 2007; Hynninen, Filion, and Dijkstra, 2009; Bommineni, Klement, and Engel, 2020). Three Laves phase structures exist: hexagonal $MgZn_2$, cubic $MgCu_2$, and hexagonal $MgNi_2$. Each is characterized by the stacking of large-sphere dimers in the crystal structure, as shown in Fig. 26. The $MgCu_2$ phase is particularly interesting because it consists of a diamond lattice of large (Mg) spheres and a pyrochlore lattice of small (Cu) spheres. By selectively removing one of the species, one can readily obtain either the diamond or pyrochlore phase. Because both the diamond and pyrochlore phases have a photonic band gap (Hynninen *et al.*, 2007), which makes them potential targets for various applications in optics, Laves phases are strongly sought after. However, these phases are notoriously difficult to self-assemble. At the high packing fractions at which they become thermodynamically stable, the fluid phase is dynamically sluggish (Dasgupta, Coli, and Dijkstra, 2020) and may show instabilities under sedimentation (Milinković, Padding, and Dijkstra, 2011). Additionally, the Laves phases are predicted to contain a significant concentration of substitutional defects (van der Meer *et al.*, 2020), which can disrupt crystal growth and hence hinder self-assembly (Dasgupta and Dijkstra, 2018).

Laves phases have nevertheless been observed experimentally for binary nanoparticle suspensions, which diffuse much faster than micron-scale colloids (see Sec. III.A) (Shevchenko *et al.*, 2006; Evers *et al.*, 2010; Cabane *et al.*, 2016), as well as sub-micron-sized spheres that interact with soft repulsive potentials (Nakagaki *et al.*, 1983; Hasaka, Nakashima, and Oki, 1984; Ma, Fukutomi, and Morone, 1994; Gauthier *et al.*, 2004). The observation of Laves phases in softer spheres is consistent with recent simulation work showing that interparticle softness pushes the glass transition in the binary fluid phase to higher densities and hence enhances crystallization of Laves phases in nearly hard spheres (Dasgupta, Coli, and Dijkstra, 2020). However, Schaertl *et al.* (2018) recently demonstrated self-assembly of Laves phases in a slightly off-stoichiometric mixture of nearly hard microgel particles using static light scattering.

Simulation and theoretical studies using a variety of methodologies have explored other dense possible crystal structures of binary hard-sphere mixtures (Kummerfeld, Hudson, and Harrowell, 2008; Filion and Dijkstra, 2009; Filion *et al.*, 2009; Hudson and Harrowell, 2011; O'Toole and Hudson, 2011; Hopkins, Stillinger, and Torquato, 2012). These surveys have revealed a rich variety of dense packings at different size ratios and compositions that are expected to be stable in the limit of infinite pressures (Hopkins, Stillinger, and Torquato, 2012). However, many of them have yet to be observed in simulations or experiments at finite pressure.

B. Binary fluids: Structural crossover, demixing, and dynamics

Structure: Crossover and demixing. DFT and computer simulations have identified a structural crossover line in the phase diagram of binary hard-sphere fluids. This line marks a rather abrupt change in the wavelength that dominates the asymptotic decay of the radial distribution function (Grodon *et al.*, 2004, 2005). Experimental evidence for this effect was also found in sedimented quasi-2D hard-sphere glasses (Baumgartl *et al.*, 2007) and subsequently in 3D hard-sphere
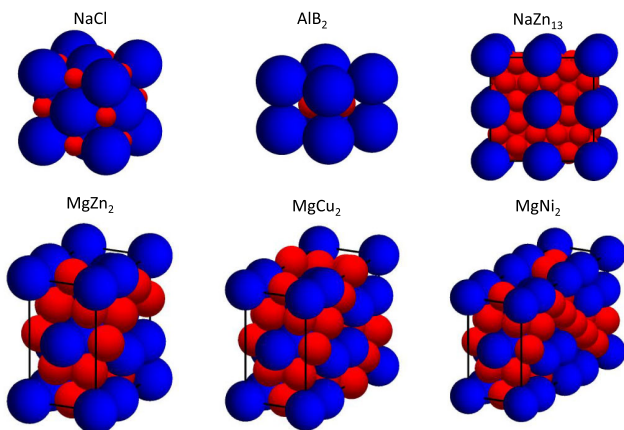

FIG. 26. Binary crystal phases of binary hard spheres. Schematic representations of binary crystal structures known to be stable or nearly stable in binary hard-sphere mixtures are displayed.
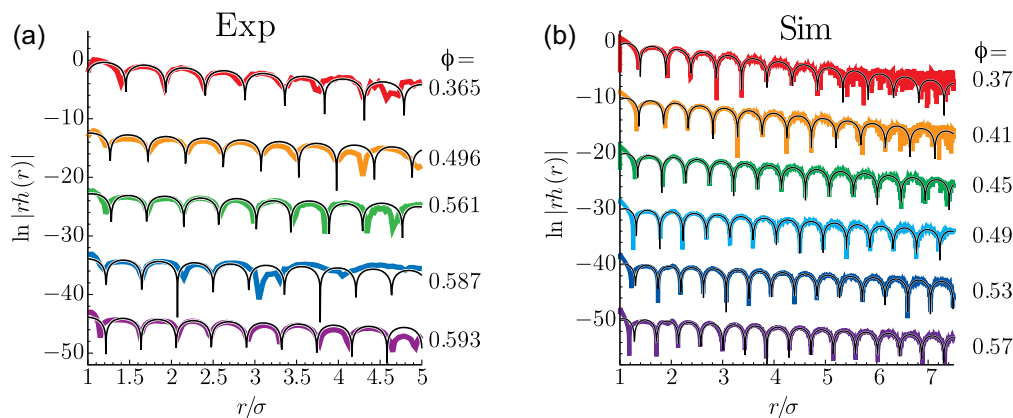
FIG. 27.   Structural crossover in binary hard-sphere fluids. Plots of $\ln |rh_{ij}(r)|$ obtained via (a) a real-space experiment and (b) simulation for L-L, L-S, and S-S total correlation functions. The packing fraction ϕ_S (marked) is increasing from top (blue) to bottom (red) for each case. Curves are shifted vertically for clarity. The black lines are fits from which parameters controlling the crossover are obtained (Grodon *et al.*, 2005). Simulations are for a binary hard-sphere mixture with a size ratio $q = 0.648$. From Statt *et al.*, 2016.

fluids where quantitative agreement with theory and simulation was found (Statt *et al.*, 2016); see Fig. 27.

For smaller size ratios, it has long been debated whether or not a stable fluid-fluid demixing transition exists. Such a spinodal instability in the fluid mixture can be ascribed to the depletion mechanism, which is known to drive phase separation in colloid-polymer suspensions (Asakura and Oosawa, 1954; Long, Osmond, and Vincent, 1973; Vrij, 1977; Lekkerkerker *et al.*, 1992). The depletion effect, which was first described by Asakura and Oosawa in 1954 (Asakura and Oosawa, 1954; Oosawa, 2021), induces an attractive interaction between large colloids due to an unbalanced osmotic pressure of the polymer or small spheres. Alternatively, this effect can be explained by the increase in free volume available to the small spheres upon clustering of the large spheres. The resulting entropy gain for the small spheres would then drive phase separation of the colloids.

The effective depletion interaction between the larger spheres due to the smaller ones has been calculated theoretically (Attard, 1989; Attard and Patey, 1990; Mao, Cates, and Lekkerkerker, 1995; Dickman, Attard, and Simonian, 1997; Götzelmann, Evans, and Dietrich, 1998; Götzelmann *et al.*, 1999; Roth, Evans, and Dietrich, 2000) and extracted from computer simulation (Biben, Bladon, and Frenkel, 1996; Dickman, Attard, and Simonian, 1997; Götzelmann *et al.*, 1999; Ashton *et al.*, 2011). The results exhibit a short-range attraction close to the surface of large hard spheres, followed by several oscillations around zero at larger distances.

Experimental investigations of the depletion interaction include tracking the Brownian trajectory of a large sphere near a wall in a suspension of small spheres with video microscopy (Kaplan, Faucheux, and Libchaber, 1994) and using optical tweezers to study the interaction between two large colloids (Crocker *et al.*, 1999). The latter work showed a discrepancy with subsequent theory (Roth, Evans, and Dietrich, 2000). Later work that determined radial distribution functions from which the interaction may be inferred showed better agreement with simulation and theory (Roth, Evans, and Dietrich, 2000; Royall, Louis, and Tanaka, 2007); see Fig. 28.

Other experimental investigations probing fluid-fluid demixing have suggested that it might be strongly coupled to freezing. For instance, Sanyal *et al.* (1992), using mixtures of polystyrene spheres with $q = 0.2$, observed segregation in regions rich in large spheres and rich in small spheres in the sediment at the bottom of their samples. However, when they suspended the mixture in a density-matched solvent, neither sedimentation nor demixing was seen. van Duijneveldt, Heinen, and Lekkerkerker (1993) observed a phase instability in a fairly narrow concentration range of small and large sterically stabilized silica particles with $q = 0.1667$, but sedimentation obscured whether the transition corresponded
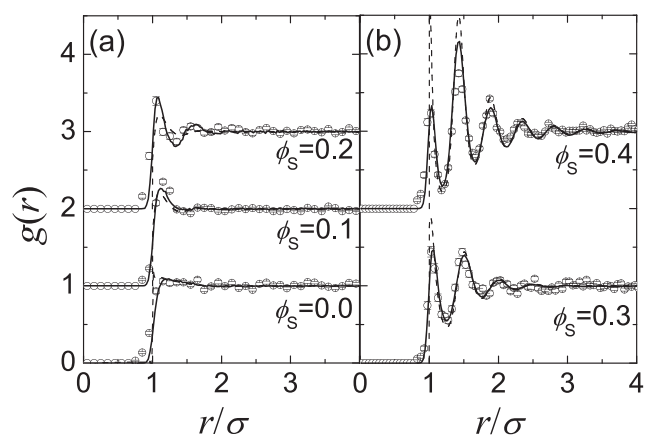

FIG. 28.   Radial distribution function of large colloids in binary hard spheres at various concentrations of the smaller species for (a) low $\phi_S \leq 0.25$ and (b) high $\phi_S > 0.25$. Monte Carlo simulation data at small colloid volume fraction ϕ_S are denoted by solid lines and compared to the experimental data (circles). The dashed lines correspond to $g(r) \approx \exp[-\beta u(r)]$, where $u(r)$ is the effective interaction between the large colloids consisting of the depletion interaction induced by the smaller and a residual electrostatic contribution. In addition to experimental resolution and polydispersity, MC simulations account for residual colloid charge. From Royall, Louis, and Tanaka, 2007.

to fluid-fluid demixing or freezing. Experiments by Kaplan *et al.* (1994) on mixtures of polystyrene particles with $0.069 < q < 0.294$ revealed the existence of a single homogeneous disordered phase, a coexistence between two disordered phases, and a coexistence between one or two disordered phases and a surface crystal on the sample wall. However, bulk crystallization was not observed. A possible reason why no surface crystallization was found in the experiments of van Duijneveldt, Heinen, and Lekkerkerker (1993) is that silica spheres settle quickly relative to polystyrene particles. In the experiments of Dinsmore, Yodh, and Pine (1995) on mixtures of polystyrene particles with $0.083 < q < 0.149$, a phase separation into a disordered fluid phase consisting primarily of small spheres and a crystalline solid of large spheres permeated by a disordered fluid of small spheres was observed at sufficiently high volume fractions. They additionally showed that the crystallites on the surface of the sample cell had the same structure as the bulk crystals, which they attributed to wetting of the bulk phase. Finally, Imhof and Dhont (1995a, 1995b) observed a fluid-solid type of phase separation but no fluid-fluid demixing in experiments on a binary mixture of silica spheres with $q = 0.1075$.

Conflicting results have been reported from various theoretical approaches. Integral equation theory approaches predict that the homogeneous fluid phase of a binary mixture of large and small hard spheres will be stable with respect to demixing (Lebowitz and Rowlinson, 1964; Mansoori *et al.*, 1971), that a spinodal instability will occur in the fluid phase (Biben and Hansen, 1990, 1991a, 1991b; Rosenfeld, 1994), or that the fluid-fluid demixing transition will be metastable with respect to a broad fluid-solid transition when using a simple freezing criterion (Caccamo and Pellicane, 1997). Free-volume theoretical approaches have further predicted that the fluid-fluid phase separation is metastable with respect to freezing (Poon and Warren, 1994; Dinsmore *et al.*, 1997). Furthermore, it has been shown that large spheres could crystallize at the wall well below those corresponding to bulk phase separation due to the presence of small spheres, which is in agreement with experimental observations. A broad fluid-solid coexistence was also found in DFT (Xu and Barentin, 1995), while theoretical approaches based on virial coefficients predicted a fluid-fluid phase separation in the limit of highly asymmetric sizes (Saija and Giaquinta, 1996; Coussaert and Baus, 1997, 1998b), a demixing transition metastable with respect to either a broad or a narrow fluid-solid phase transition (Coussaert and Baus, 1998a), a simple narrow fluid-solid phase transition in the limit $q \to 0$ (Vega, 1998), or a complete absence of a fluid-fluid demixing transition (López de Haro, Tejero, and Santos, 2013). What this broad range of predictions makes clear is that the phase behavior is too sensitive to the details of the specific approximations used in integral equation theories and virial expansion approaches to reach a clear conclusion.

Dijkstra, van Roij, and Evans (1998, 1999b) followed a different approach by mapping the binary hard-sphere mixture onto an effective one-component system by formally integrating out the degrees of freedom of the small spheres in the partition function. Using the two-body depletion potential contribution to the effective Hamiltonian in simulations, this effort revealed that the fluid-solid phase coexistence region

significantly broadens as q becomes small. In addition, it found a stable isostructural solid-solid demixing transition for $q < 0.05$ and fluid-fluid demixing that remains metastable with respect to the fluid-solid transition for $q < 0.10$. These predictions were later validated by simulations of the true binary hard-sphere mixture (Dijkstra, van Roij, and Evans, 1999a, 1999b). However, only recently has the critical point for the fluid-fluid demixing transition been reported (Kobayashi *et al.*, 2021). Kobayashi *et al.* (2021) managed that feat using a two-level simulation approach based on a coarse-grained description with effective two- and three-body interactions and the full fine-grained binary mixture, and then matching the probability distribution for the number of large particles to the 3D Ising universality class scaling form. Even then, a nontrivial dependence on q was also found. In summary, it is now well settled that a fluid-fluid demixing transition exists in a binary mixture of hard spheres for sufficiently large size asymmetries, but this transition is metastable with respect to a broad fluid-solid transition.

Dynamics in binary hard spheres. Dynamics in binary fluids, as probed with multiple light scattering, has shown reasonable agreement with hydrodynamic theory (Kaplan, Yodh, and Pine, 1992). Later Imhof and Dhont (1995b) measured the diffusion in strongly asymmetric mixtures by photobleaching part of the sample and examining the recovery of the fluorescence as the system rearranged. They found good agreement with a previous theory by Batchelor (1983) for the diffusion of the small spheres in the dilute regime but observed significant deviations for the large spheres, which they attributed to the large size disparity in their system. Significant experimental and simulation work has also focused on the dense fluid regime (Williams and van Megen, 2001; Foffi *et al.*, 2003; Götze and Voigtmann, 2003; Marín-Aguilar *et al.*, 2020), thus revealing a sensitive dependence of the diffusivity behavior of both species on the size ratio and composition of the chosen mixtures. This is of particular importance when studying glassy systems (see Sec. XII), in which, depending on q, one might find a single glass (where only the large particles are dynamically arrested) or a double glass (where both species are arrested) (Voigtmann, 2011; Laurati *et al.*, 2018; Lazaro-Lazaro *et al.*, 2019).

C. Sedimented monolayers of binary hard spheres

Analogous to the monodisperse case, binary mixtures of hard spheres can be confined to a quasi-2D setup by allowing them to sediment into a monolayer on a substrate. In this case, the system can be mapped onto a binary hard-disk model, which typically has to be nonadditive in order to account for the centers of the small spheres being positioned below those of the large spheres (Thorneywork *et al.*, 2014). Thorneywork *et al.* performed a detailed characterization of the radial distribution function (Thorneywork *et al.*, 2014), structure factor (Thorneywork, Schnyder *et al.*, 2018), and self-diffusion coefficient (Thorneywork, Aarts *et al.*, 2017) of these systems and found their experimental results to be in good agreement with simulations and theory of model mixtures. An interesting consequence of the depletion interaction in sedimented binary hard spheres is that the large

particles are in fact repelled from the edge of a raised surface (Dinsmore, Yodh, and Pine, 1996).

As in the bulk 3D case, the introduction of a second size of particles vastly increases the phase diagram complexity. In 2D hard disks, fluid-fluid demixing is generally expected only for positively nonadditive hard disks (Sillrén and Hansen, 2010), which would be difficult to achieve in colloidal experiments with hard spheres. In the crystal regime, however, binary hard disks can stabilize extremely diverse behavior. Considering only structures in the limit of infinite pressure, Likos and Henley (1993) identified a wide range of distinct periodic crystals as well as the possibility of a quasicrystal with 12-fold symmetry. For extreme size ratios, the densest possible crystal phases are expected to consist of a hexagonal packing of large disks with an increasing number of small particles inserted into the triangular voids (Uche, Stillinger, and Torquato, 2004). For the specific case of hard spheres sedimented onto a substrate, simulations predict the spontaneous self-assembly of both 12-fold and eightfold quasicrystals (Fayen *et al.*, 2023). Note that while monolayers of hard-sphere mixtures closely approximate true 2D systems, simulations incorporating hydrodynamics on binary mixtures confined between two plates suggest that even small amounts of vertical freedom can significantly speed up dynamics of quasi-2D binary mixtures (Tian, Kob, and Barrat, 2022).

X. CONFINEMENT

As detailed in Sec. VII, the entropy-driven equilibrium phase diagram of bulk hard-sphere systems is fairly well understood. The insertion of one or more confining walls in the fluid, however, decreases the number of possible configurations and generally alters the system structure and phase behavior (Bechinger, 2002; Araújo *et al.*, 2023). In this section, we specifically consider the interfacial behavior of hard-sphere fluids between two hard walls, under quasi-1D and quasi-2D conditions as well as within cylindrical, spherical, and flexible immurement. Note that the case of a single planar wall, which results in an interface albeit not in proper confinement, is presented in Sec. VIII.A.

A. Toward 2D confinement

The effect of confinement between two planar hard walls was first investigated by Pieranski, Strzelecki, and Pansu (1983) using colloidal polystyrene spheres. They observed a sequence of layered solid structures with triangular ($\triangle$) and square ($\square$) symmetry $1\triangle \rightarrow 2\square \rightarrow 2\triangle \rightarrow 3\square \rightarrow 3\triangle \cdots \rightarrow n\square$ upon increasing the plate separation, where n denotes the number of layers. Using MC simulations and cell theory (Sec. VI.B), Schmidt and Löwen (1996, 1997) later mapped out the phase diagram for plate separations ranging from one to two particle diameters and found additional buckled and rhombic phases. The sequence of high-density structures was determined more accurately in subsequent experiments (Neser *et al.*, 1997; Fontecha *et al.*, 2005), further identifying prism phases with both square and triangular symmetry.

Using extensive free-energy calculations in MC simulations, the full phase diagram for plate separations from one to five hard-sphere diameters was mapped out as a function of
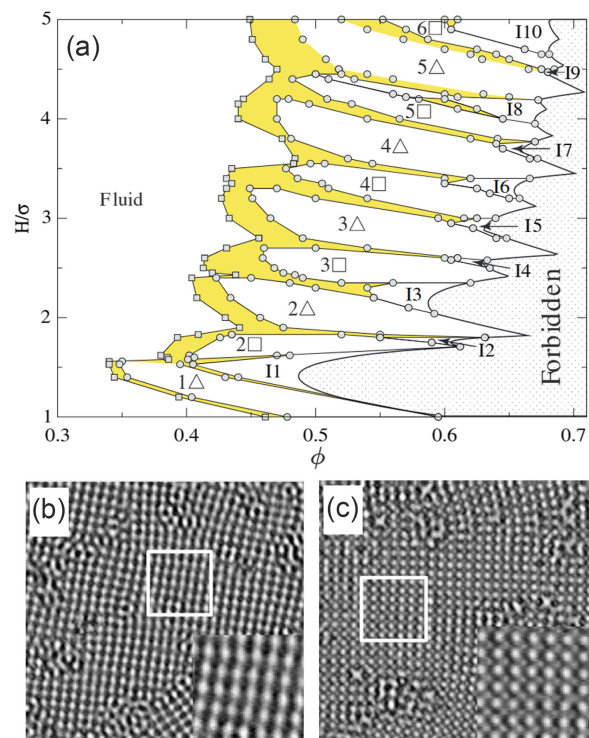

FIG. 29. (a) Equilibrium phase diagram of hard spheres confined between two parallel hard walls with plate separation H vs volume fraction representation. The white, yellow, and dotted regions indicate the stable one-phase region, the two-phase coexistence region, and the forbidden region, respectively. (a) From Fortini and Dijkstra (2006). (b),(c) Optical microscopy images of charged spheres in an aqueous system confined in a wedge geometry. Shown are both (b) a $2\triangle$ phase and (c) a $2\square$ phase. (b),(c) From Fontecha *et al.*, 2005.

volume fraction (Fortini and Dijkstra, 2006); see Fig. 29. These results identify a first-order fluid-solid transition, corresponding to either capillary freezing or capillary melting depending on the plate separation, with the coexisting solid phases consisting of crystalline layers with either triangular or square symmetry. At high densities, prism, buckled, and rhombic phases are found to be thermodynamically stable, in agreement with experiments (Neser *et al.*, 1997; Fontecha *et al.*, 2005; Oğuz *et al.*, 2012). An interesting twist under strong confinement is to consider nonequilibrium behavior where geometric frustration in a buckled triangular lattice leads to behavior reminiscent of spin ice and frustrated magnetic materials. This was realized in experiments with diameter-tunable microgels (Han, Shokef *et al.*, 2008; Shokef and Lubensky, 2009).

Curk *et al.* (2012) used simulations to investigate hard spheres in soft quasi-2D confinement with a parabolic potential along one dimension. As in hard confinement, a sequence of confined hexagonal and square-symmetric packings was found, but none of the intervening ordered phases were observed; the system was found to undergo phase separation instead.

B. Cylindrical confinement

Hard spheres perfectly confined to a 1D line form a *Tonks gas*. This model, which has a rich theoretical history

(Lieb and Mattis, 1966), captures reasonably well the behavior of various condensed-matter systems, such as linear chains of mercury in $Hg_{3-\delta}AsF_6$ (Spal *et al.*, 1980; Chaikin and Lubensky, 1995)[13] and chains of cobalt atoms confined by platinum steps (Gambardella *et al.*, 2002). [Its quantum mechanical relative, the Tonks-Girardeau model, has also been experimentally realized (Bloch, Dalibard, and Zwerger, 2008).]

The Tonks gas can be solved by a transfer matrix (TM) scheme. A rich set of structural and thermodynamic observables can thus be obtained at minimal computational cost. With appropriate discretization schemes, the TM scheme can also be extended to quasi-1D systems (Barker, 1962). Both hard disks between hard lines (Kofke and Post, 1993; Gurin and Varga, 2013; Godfrey and Moore, 2014; Robinson, Godfrey, and Moore, 2016; Hicks *et al.*, 2018; Hu, Fu, and Charbonneau, 2018; Zhang, Godfrey, and Moore, 2020) and hard spheres within a hard cylinder (Kamenetskiy, Mon, and Percus, 2004; Hu, Fu, and Charbonneau, 2018) [as well as more exotic hard shapes (Kantor and Kardar, 2009; Gurin and Varga, 2015; Gurin, Varga, and Odriozola, 2016; Gurin, Odriozola, and Varga, 2017; Gurin *et al.*, 2017)] have thus been considered using this approach.

The TM size, however, jumps markedly as the number of interacting particles increases, which limits the maximal cylinder width that can be computationally resolved. At present it is nevertheless possible to study systems with up to next-nearest-neighbor interactions. Spheres in a cylinder with a diameter of 2σ (and for disks a line spacing of up to $5\sigma/2$) can thus also be solved this way (Hu, Fu, and Charbonneau, 2018). Although limited, this range of cylinder sizes is sufficient for zigzag and helical orders to emerge at high density.

The analysis of these systems provides key insights into quasi-1D ordering. For instance, although 1D systems with finite-range pairwise interactions have long been known to be unable to exhibit a phase transition (Van Hove, 1950) [see also Theorem 5.6.7 of Ruelle (1999)], various numerical simulations of cylindrically confined hard spheres have identified somewhat abrupt structural changes as density increases (Gordillo, Martínez-Haya, and Romero-Enrique, 2006; Koga and Tanaka, 2006; Durán-Olivencia and Gordillo, 2009; Varga, Ballo, and Gurin, 2011). Similarly, it has been proposed that confined disks could exhibit a Kosterlitz-Thouless-type phase transition (Hu and Charbonneau, 2020; Huerta *et al.*, 2020). The TM scheme resolves these apparent paradoxes. First, it confirms that in thermodynamic equilibrium no phase transition is observed (as would be noted in the evolution of the largest TM eigenvalue with density). Second, it reveals the physical origin of the marked structural changes that nevertheless emerge. Because the correlation length that describes the spatial decay of structural order is given by the ratio of the two largest (magnitudewise) TM eigenvalues $\xi \sim \ln(\lambda_1/\lambda_2)$, crossing of subdominant TM

eigenvalues can indeed give rise to marked structural crossovers without any thermodynamic singularity (Hu, Fu, and Charbonneau, 2018).

To observe richer order types, larger cylinder diameters need to be considered. The diameter dependence indeed does not result in continuous structural changes, as is most obvious at close packing. [The effect is also notable at finite pressure (Mon and Percus, 2000).] The associated morphological richness was first studied by Pickett, Gross, and Okuyama (2000), who found that chiral order spontaneously develops for certain diameter ratios. Mughal, Chan, and Weaire (2011) and Mughal *et al.* (2012) later noted that for cylinders of diameter up to $2 \geq D/\sigma = 1 + 1/\sin(\pi/5) \approx 2.70$ close packing is described using a phyllotactic construction because all spheres then coat the cylinder wall. Beyond this diameter regime, not all spheres touch the cylinder wall, which eventually results in a separation between core and shell particles (Fu *et al.*, 2016). As shown in Fig. 30, exotic arrangements, complex helices, and limit periodic structures follow. More or less systematic numerical exploration of these structures ends around $D/\sigma = 4$, but it is conceivable that larger diameters might accommodate even more unusual structures.

Considerable interest has also been paid to the transport dynamics of these systems. In particular, for the hard-sphere case Mon and Percus (2002, 2003) identified a crossover from single-file to Fickian diffusion for sufficiently wide cylinders, i.e., $D \geq 2\sigma$. A transition state theory description of the hopping mechanism that enables sphere passing was later proposed (Wanasundara, Spiteri, and Bowles, 2012), and the impact of microscopic dynamics (Flomenbom, 2010; Sané, Padding, and Louis, 2010) as well as size dispersity (Wanasundara, Spiteri, and Bowles, 2012) on these has been considered.

From the experimental standpoint, hard spheres in quasi-1D confinement have notably been used to rationalize the packing behavior of C_{60} in nanotubes (Mickelson *et al.*, 2003; Khlobystov *et al.*, 2004; Khlobystov, Britz, and Briggs, 2005; Troche *et al.*, 2005), of confined nanoparticles (Tymczenko *et al.*, 2008; Sanwaria *et al.*, 2014), and of vacuolated cells in an embryonic structure (Norman *et al.*, 2018). A few colloid-based realizations have also been achieved (Lohr *et al.*, 2010; Jiang *et al.*, 2013; Liu, de Folter *et al.*, 2015; Fu, Bian *et al.*, 2017), as have granular-scale ones (Bogomolov *et al.*, 1990). In all cases, a good correspondence between theory and experiments is obtained, although the assembly pathway may need to be taken into account to rationalize the observed packings (Mughal *et al.*, 2012; Fu, Bian *et al.*, 2017). Nevertheless, relatively few of the aforementioned numerical and theoretical predictions have been tested directly in colloidal experiments.

C. Quasi-1D confinement

A lower-dimensional generalization of cylindrical confinement considers 2D hard disks between parallel lines a distance D apart. These models have largely been studied for the insight they offer into the physics of disordered systems. Given that the geometry of these systems is a lot simpler than that of spheres in cylindrical confinement, only fairly unremarkable structures form the densest close packing as D

---

[13]Note that the analysis of Spal *et al.* (1980) and Chaikin and Lubensky (1995) did not take advantage of the exact 1D solution. Using this solution to redo the analysis is left as an exercise for the interested reader.

increases. Subtleties in these packings nevertheless lead to the emergence of nontrivial local features (Ashwin and Bowles, 2009; Zhang, Godfrey, and Moore, 2020). Such irregularities have allowed these models to find particular use in clarifying the physics of low-dimensional disordered systems.

Given the robustness of the jamming phenomenology down to 2D systems, such as the algebraic scaling of weak forces and small gaps (see Sec. XII.H), an interesting target has been to consider the structural criticality of quasi-1D systems. For $D < 1 + \sqrt{3}\sigma/2$, jammed states are then isostatic and have a nonzero complexity (Ashwin and Bowles, 2009; Bowles and Ashwin, 2011; Ashwin, Zaeifi Yamchi, and Bowles, 2013; Godfrey and Moore, 2018) but do not exhibit a critical structure. For $1 + \sqrt{3}/2 < D < 2$, however, it is possible to consider states that are structurally critical. Depending on the system details, different critical exponents have been reported (Ikeda, 2020; Zhang, Godfrey, and Moore, 2020). This sensitivity of the structural criticality possibly follows from these systems being below the lower critical dimension for jamming.

These models have also been used to study dense fluids (Godfrey and Moore, 2014; Robinson, Godfrey, and Moore, 2016; Hicks *et al.*, 2018) so as to assess how some of the mean-field theory predictions then fare. Unsurprisingly for such low-dimensional models, a qualitatively different physics is observed. The findings should nevertheless caution against possible confounding physical factors in the study of higher-dimensional fluids, such as the importance of local structure and the possibility of crossovers at fairly large system sizes.

Given the rich physics of such simple models, a seemingly open area of research is their experimental study. Microfluidic channels with colloids (Mark *et al.*, 2010), for instance, might be a promising approach to consider.

D. Spherical confinement

Arguably the most natural way of confining colloidal spheres in three dimensions is inside a larger sphere. As a natural toy model system for small many-body systems, even studies of just a few hard spheres in spherical confinement have attracted significant theoretical attention exploring, for example, the effect of the thermodynamic ensemble on the observed structure (González *et al.*, 1997, 1998) and the thermodynamic

properties of the confined fluid (Urrutia, 2011; Urrutia and Castelletti, 2012; Urrutia and Pastorino, 2014).

As expected, hard-sphere fluids confined to larger spherical cavities are known to show structuring near the cavity walls (Macpherson, Carignan, and Vladimiroff, 1987; Zhou and Stell, 1989; Calleja *et al.*, 1991; Chui, 1991). The dynamics inside the cavity then depends strongly on whether the cavity walls are rough or smooth (Németh and Löwen, 1999), with rough walls more strongly inducing dynamical arrest. In particular, when a glassy fluid of hard spheres is confined in a spherical cavity with rough walls consisting of pinned particles, the dynamics approaches that of a bulk hard-sphere glass for large cavities, thus providing a route to probe dynamical correlations in these systems (Németh and Löwen, 1999; Zhang and Cheng, 2016).

Experimental self-assembly of hard-sphere colloids in spherical confinement can be achieved by confining the colloids inside emulsion droplets (Yi *et al.*, 2002; Manoharan, Elsesser, and Pine, 2003; Manoharan, 2006). When the droplets shrink [due to either evaporation or Ostwald ripening (Schmitt *et al.*, 2016)], the slowly increasing density of the colloids can eventually lead to self-assembly. The resulting structure depends sensitively on the number of colloidal particles within the cluster. Clusters containing only a handful of colloids form small polyhedral clusters whose geometry can often be understood as the densest configuration possible in the circumstances. However, in these small clusters, capillary forces during the final stages of solvent evaporation also play a significant role, and in many cases drive the cluster to minimize the second moment of its mass distribution (Manoharan, Elsesser, and Pine, 2003; Lauga and Brenner, 2004; Yi *et al.*, 2004; Cho, Yi, Kim *et al.*, 2005). For hard spheres, this set of minimal clusters was studied by Sloane *et al.* (1995).

For larger clusters of monodisperse spheres in spherical confinement, the natural tendency of hard spheres to crystallize into an fcc crystal competes with the curvature of the surface. Although sufficiently large clusters ($N \gtrsim 10^5$) form a simple fcc structure, intermediate cluster sizes ($100 \lesssim N \lesssim 10^5$) spontaneously form clusters with icosahedral symmetry (de Nijs *et al.*, 2015). The core of these icosahedral clusters consists of tetrahedral-shaped domains of distorted fcc crystal, with one hexagonal plane from each domain forming the faces of an icosahedron, often called Mackay clusters (Mackay, 1962).
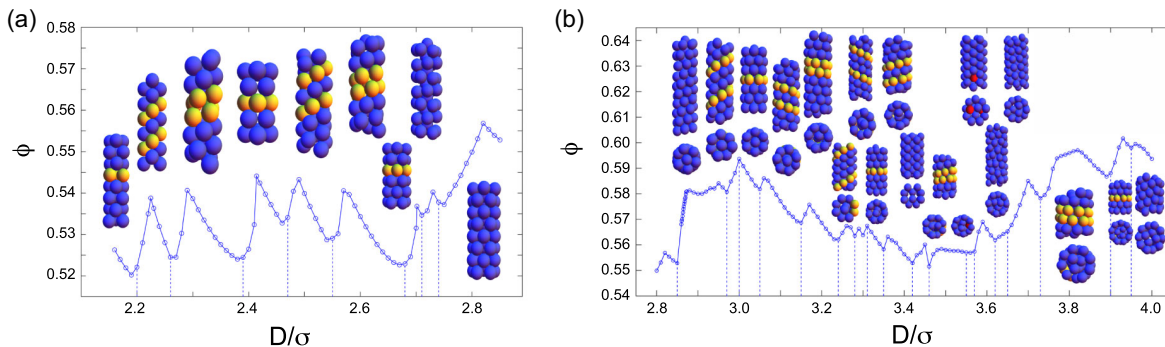

FIG. 30. Close-packing fraction of hard spheres confined in cylinders of diameter D along with some of the structures. These packings (a) are phyllotacticlike for $D/\sigma \lesssim 2.8$ and (b) exhibit a core-shell structure beyond that point. From Fu *et al.*, 2016, and Fu, Steinhardt *et al.*, 2017.

Nanoparticles

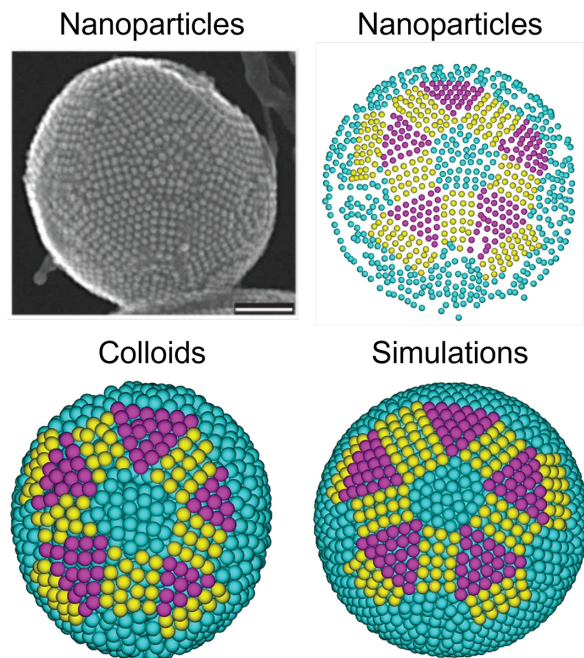## Nanoparticles

Colloids

Simulations

FIG. 31. Icosahedral clusters of spheres self-assembled in spherical confinement. Top row: an electron microscopy image of a cluster of nanoparticles and a reconstruction of its surface layer. Bottom left image: cluster obtained in experiments with micron-sized colloids. Bottom right image: cluster obtained in simulations of hard spheres. Adapted from de Nijs *et al.*, 2015.

For sufficiently large clusters, these domains can be capped by additional surface layers, resulting in a family of anti-Mackay sphere packings with varying surface reconstructions (de Nijs *et al.*, 2015; Wang, Mbah *et al.*, 2018); see Fig. 31. Free-energy calculations based on computer simulations have shown that these clusters are indeed thermodynamically stable configurations for pure hard spheres in spherical confinement (de Nijs *et al.*, 2015), with clusters containing certain "magic numbers" of spheres corresponding to defect-free clusters being particularly stable (Wang, Mbah *et al.*, 2018; Wang *et al.*, 2019).

This already complex behavior can be further tuned by considering, for example, binary mixtures of spheres in spherical confinement. For small clusters, complex anisotropic colloidal supraparticles can result (Cho, Yi, Lim *et al.*, 2005). For larger clusters, Wang, van der Wee *et al.* (2021) demonstrated the formation of clusters consisting of the thermodynamically stable $MgZn_2$ Laves phase when there is an excess of small spheres. However, these clusters turn into an icosahedral cluster consisting of tetrahedral domains of the less stable $MgCu_2$ Laves phase when the fluid composition is isostoichiometric with the Laves phase (Wang *et al.*, 2021).

As the self-assembly behavior of colloidal spheres under spherical confinement is robust on both the nanometer and micrometer scales (de Nijs *et al.*, 2015) and for a variety of materials (Yi *et al.*, 2004), it provides a versatile route for tuning material structure across various length scales. Supraparticles created via this technique have been proposed as building blocks for additional self-assembly steps, such as for creating materials with structural order on two different length scales (Bai *et al.*, 2007). In addition, the icosahedral nature of intermediate-sized clusters of colloidal

spheres may lead to interesting optical effects, including iridescent structural color patterns that can be used to track the self-assembly dynamics inside the clusters in real time (Wang *et al.*, 2020).

E. Flexible confinement

Thus far in this section we have seen that a large variety of packing geometries can be obtained by confining spheres in a container of fixed shape. A different question concerns the most efficient packing of spheres in a natural bin, which is the smallest convex hull (volumewise) that can enclose a certain number of spheres. Counterintuitively, the result is not always a compact cluster of spheres. For a packing of spheres with up to $n = 55$, along with $n = 57, 58, 63, 64$, the linear conformation in which the spheres lie on a straight line, also called a sausage, is denser than a clusterlike or platelike configuration (Gandini and Wills, 1992). The optimal packing for $n = 56$ is not fcc-like, and the exact configuration remains unknown. [By contrast, in four dimensions, this sudden transition from a sausage packing to a cluster shape is conjectured to happen at $n = 375\,769$ spheres and is therefore referred to as the sausage catastrophe (Henk and Wills, 2021).] Hard spheres in a flexible container can be used to model colloids in a fluctuating vesicle, which was studied theoretically and in simulations by Maibaum, Schmidt, and Löwen (2001). Recently such a system of non-close-packed colloids in a flaccid lipid vesicle has been experimentally realized (Marín-Aguilar *et al.*, 2023). Through a combined experimental and simulation study, Marín-Aguilar *et al.* obtained a state diagram that includes linear, planar, and cluster conformations of spheres, as well as bistable states, which alternate between cluster-plate and plate-linear conformations due to membrane fluctuations. In addition, Marín-Aguilar *et al.* (2023) identified truncated polyhedral packings of $56 \leq N \leq 70$ spheres (excluding $N = 57$ and 63) that pack more efficiently than linear arrangements.

In experiments, flexible confinement may be induced by optical tweezers. To our knowledge, in the context of hard spheres, using lasers to induce structuring may be traced to the work of colloid pioneers Chowdhury, Ackerson, and Clark (1985), who did so to induce freezing in quasi-2D systems. A more recent approach has been to confine a system inside a ring of particles held in optical traps. Such traps have well-defined potentials, which means that the osmotic pressure and therefore the EOS could be measured. At low density, the results were found to agree with the bulk EOS. At higher density, by contrast, the fluid takes on a layered structure, thus reflecting the confinement. At still higher density, a bistable state between the layered fluid and a hexagonal structure was observed, reminiscent of the bulk hexatic phase (Williams *et al.*, 2013).

XI. OUT-OF-EQUILIBRIUM PHENOMENA

In this section, we discuss how hard spheres have shed light on material phenomena away from thermal equilibrium. When studying out-of-equilibrium suspensions, it is useful to distinguish linear response around thermal equilibrium, which can be treated perturbatively within the framework of

TABLE I. Péclet numbers $\text{Pe}_x = \tau_B/\tau_x$ relate the diffusive time τ_B, as defined in Eq. (1), to the timescale τ_x of a directed transport process using the particle radius $\sigma/2$ as reference length. $\mu = D_0/k_B T$ is the particle mobility. Sedimentation (the second column) is due to the gravitational force $m_b g$, with the acceleration of gravity g and buoyant mass $m_b = (\pi\sigma^3/6)\delta\rho$, where $\delta\rho$ is the density difference between particle and solvent. In this case the Péclet number can also be written as $\text{Pe}_g = \sigma/2\xi_g$, with gravitational length ξ_g. In the case of shear flow, the timescale of directed transport is $\dot{\gamma}^{-1}$. For normal fluids, the Brownian time τ_B is appropriate, but for glassy systems the Weissenberg number $\dot{\gamma}\tau_\alpha$ is often used instead; see Sec. XII.J.

Drive	General force F	Gravitation g	Drift speed v	Shear flow $\dot{\gamma}$	Glassy flow $\dot{\gamma}$
τ_x	$\frac{\sigma}{2\mu F}$	$\frac{\sigma}{2\mu m_b g}$	$\frac{\sigma}{2v}$	$\dot{\gamma}^{-1}$	$\dot{\gamma}^{-1}$
Pe_x	$\frac{F\sigma}{2k_B T}$	$\frac{\pi\sigma^4\delta\rho g}{12k_B T}$	$\frac{2\sigma v}{D}$	$\dot{\gamma}\tau_B$	$\dot{\gamma}\tau_\alpha$

statistical mechanics, from phenomena that occur due to strong driving beyond the linear regime. Nonequilibrium effects often appear as fluxes of macroscopic observables and transport phenomena. Because particle motion remains governed by thermal fluctuations, the relative magnitude of this transport compared to diffusion, as captured by the various dimensionless Péclet numbers (Table I), for example, for gravitation, shear flow (Russel, Saville, and Schowalter, 1989), or other fields such as optical tweezers (Williams *et al.*, 2016), is a crucial measure of how strongly a system is driven.

Thus far we have largely considered the solvent as a structureless quiescent medium. Out of equilibrium, however, this simplification is often no longer appropriate. The solvent dynamics has to be taken into account. We therefore shift our focus away from hard spheres as a model system and instead consider the colloidal material as a complex fluid. In that context, the full dynamics of a particle-laden Newtonian solvent is described by the Navier-Stokes equation together with a suitable (typically no-slip) boundary condition on the particle surfaces. By eliminating the solvent, forces between suspended particles effectively couple through the mobility tensor, which can in principle be derived from the Oseen tensor (Dhont, 1996). In bulk systems, hydrodynamic coupling is long-range due to momentum conservation of the solvent. Taking these hydrodynamic interactions into account in simulations is feasible but computationally costly; see Sec. V.D for available methods. A recurring theme is the importance of colloidal forces over hydrodynamic coupling. If the latter can be neglected, one can resort to computationally cheaper BD simulations (Sec. V.C).

A. Nonequilibrium sedimentation in hard-sphere colloids

We first consider what is arguably the simplest nonequilibrium situation, namely, the gravitational settling of a suspension. As discussed in Sec. VII.C, waiting for the suspension to relax yields a density profile from which the equation of state may be inferred. While such equilibrium profiles are straightforward to calculate, the approach to

equilibrium from an out-of-equilibrium starting point is a challenging problem to address.

As previously alluded to, a useful way to distinguish different regimes is through the gravitational (or sedimentation) Péclet number

$$\text{Pe}_g = \frac{\tau_B}{\tau_g} = \frac{\sigma/2}{\xi_g} = \frac{\pi\sigma^4\delta\rho g}{12 k_B T}, \tag{34}$$

which is defined as the ratio of the Brownian diffusive time τ_B [Eq. (1)] to the time τ_g for a sphere to sediment its own radius, where $\delta\rho$ is the mass density difference between colloidal particles and the solvent. Alternatively, it can be expressed through the gravitational length $\xi_g = k_B T/m_m g$, with $m_m g$ the buoyant mass. Note that without loss of generality, sedimentation is assumed to occur in the z direction and has no dependence on the x, y coordinates. Equation (34) describes the sedimentation of a single colloid and thus holds in the dilute limit.

For more concentrated systems, when the density varies on length scales sufficient for local packing effects to be neglected, and for which gravitational settling is slow, i.e., $\text{Pe}_g \ll 1$, the time evolution of the sedimentation profile $\phi(z, t)$ largely follows a *batch settling* process (Russel, Saville, and Schowalter, 1989). Under these conditions, the volume fraction at any height and at any time may be captured by a set of relatively simple coupled equations. [For more strongly driven systems, in the granular regime strong swirls due to hydrodynamic coupling can be observed (Segrè, Herbolzheimer, and Chaikin, 1997; Segrè *et al.*, 2001).]

For smaller systems, in which packing effects can be more noticeable (see Sec. X), classical DFT (see Sec. VI.C) is needed. Using dynamical DFT, it is indeed possible to propagate these density profiles forward in time, as shown in Figs. 32(d) and 32(e). The time-dependent density profiles predicted by dynamical DFT agree extremely well with particle-resolved results from BD simulations. With the inclusion of a simple treatment for the volume fraction-dependent slowdown in dynamics due to hydrodynamic interactions (treated with the Hayakawa-Ichiki method), the time evolution of the density profiles of sedimenting hard spheres in experiments has been accurately described (Royall *et al.*, 2007; Schmidt *et al.*, 2008); see Figs. 32(a)–32(e).

This description of sedimentation presumes translational invariance in the x-y plane, which holds empirically for a starting configuration that is approximately homogeneous (Royall *et al.*, 2007; Schmidt *et al.*, 2008). An inhomogeneous configuration such as that shown in Fig. 33(a) presents a much different (and at first sight surprising) proposition. Density fluctuations with a characteristic length scale [Fig. 33(b)] then develop, leading to a behavior reminiscent of the catastrophic Rayleigh-Taylor instability when two immiscible liquids are prepared with the denser liquid above. What is particularly surprising here is that the hard-sphere fluid, which is a single phase, then behaves like a phase-separated system. These complex time-dependent patterns can further be accurately captured by multiparticle collision dynamics simulations (Wysocki *et al.*, 2009, 2010). Therefore, even
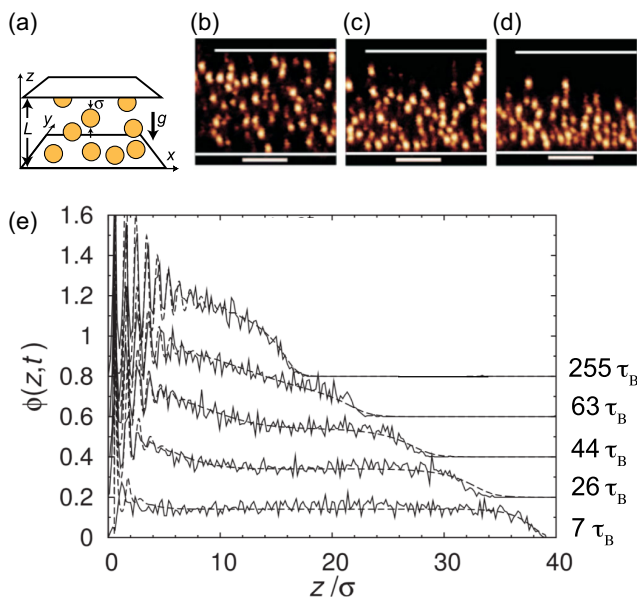
FIG. 32. Nonequilibrium sedimentation of hard spheres on the particle scale. (a) A system of sterically stabilized PMMA particles under the influence of gravity g and vertically confined between two walls separated by a distance L. (b)–(d) Time series of confocal micrographs taken in the (vertical) x-z plane at times (b) $t = 3\tau_B$, (c) $26\tau_B$, and (d) $200\tau_B$. The scale bars denote 20 μm; the horizontal lines indicate the position of the walls. In (b)–(d) the sedimentation Péclet number is $\mathrm{Pe}_g = 0.625$. (e) Time evolution of the sedimentation profile $\phi(z,t)$ for a system with $\mathrm{Pe}_g = 1.11$. The solid lines display experimental data from particle-resolved studies, whereas the dashed lines represent dynamical DFT. No fit parameters are used. From Royall *et al.*, 2007.

phenomena far from equilibrium can be accurately captured by theory and simulation.

Adding a second colloidal species whose gravitational Péclet number can be tuned independently provides a further means of controlling the structural properties of the swirls. Note that these swirls depend mainly on the relative magnitudes of the Péclet numbers of the two species and much less on the composition of the mixture, which would be the case closer to equilibrium (Milinković, Padding, and Dijkstra, 2011); see Sec. IX.

B. Rheology, flow, and shear-induced order

The most common way to probe mechanical properties is to subject a sample to external forces and measure its deformation rate (Larson, 1998; T. Chen *et al.*, 2010; Wagner, 2022). In addition to the packing fraction ϕ, the strain γ (and strain rate $\dot{\gamma}$), not to be confused with the interfacial free energy in Sec. VIII.B, with conjugate stress τ are then needed to characterize a hard-sphere system. The absence of cohesive forces between hard spheres implies that their solids deform easily. The elastic moduli, which encode how a solid linearly deforms in response to an applied force, nevertheless diverge as $\propto k_B T/\sigma^3 (\phi_{cp}/\phi - 1)^2$ upon approaching close packing (Stillinger and Salsburg, 1967; Farago and Kantor, 2000).

Similarly, a hard-sphere fluid starts flowing in response to shear forces, thus entering a dissipative nonequilibrium state. In certain geometries [such as Couette or cone-plate shear cells; see Fig. 34(a)], a uniform strain rate $\dot{\gamma}$ can be achieved, thus defining viscosity $\eta = \tau/\dot{\gamma}$. How strongly a suspension is sheared is described through the dimensionless shear Péclet number $\mathrm{Pe}_{\dot{\gamma}} = \dot{\gamma}\tau_B$, again using the Brownian time τ_B [Eq. (1)] (Table I), characterizing the importance of advection over diffusion. Figure 34(b) shows typical flow curves $\tau(\dot{\gamma}; \phi)$ for dense hard spheres. For the fluid ($\phi = 0.52$) one observes shear thinning with a stress that is smaller than the initial linear increase. The denser ($\phi \geq 0.59$) no-slip samples behave as Herschel-Bulkley fluids following the empirical flow curve $\tau - \tau_0 \propto \dot{\gamma}^n$ with some exponent n. They approach a finite yield stress τ_0 in the limit $\dot{\gamma} \to 0$, thus indicating that the sample behaves as a disordered solid. Rheology therefore provides a mechanical route to probe the glass transition, to which we return in Sec. XII.J.

Traditional rheological studies probe macroscopic volumes through small-amplitude oscillatory shear so as to only weakly perturb the material from thermal equilibrium. In this linear
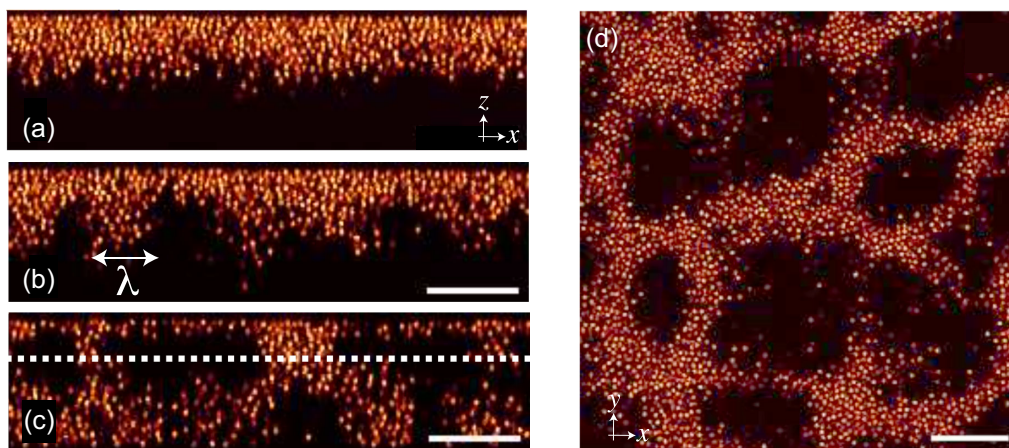

FIG. 33. Rayleigh-Taylor-like instability in hard-sphere colloids. (a)–(c) Time series of images taken with a confocal microscope for $1.43\tau_B$, $5.5\tau_B$, and $11.2\tau_B$. λ denotes the characteristic growing wavelength of the Rayleigh-Taylor instability. (d) Image in x-y plane at the height of the dashed line in (c). From Wysocki *et al.*, 2009.
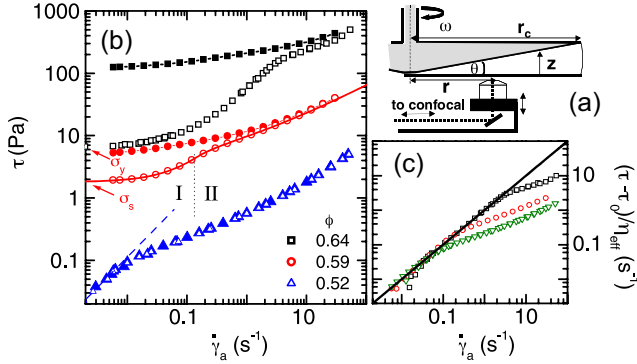
FIG. 34. (a) Sketch of a cone-plate rheometer together with a confocal microscope. (b) Measured shear stress τ as a function of the applied strain rate $\dot{\gamma}_a$ for several packing fractions ϕ below and above the glass transition. The open symbols indicate uncoated smooth plates, while the full symbols show the data for coated plates with no-slip boundary conditions. (c) The excess stress $\tau - \tau_0$ is linear, with the slope η_{eff} defining an effective viscosity. From Ballesta *et al.*, 2008.

response regime with $\text{Pe}_{\dot{\gamma}} \ll 1$, the system reaches a periodic state with stress

$$\tau(t) = \int_{-\infty}^{t} ds \, G(t-s)\dot{\gamma}(s) \qquad (35)$$

leading to the storage modulus $G'(\omega)$ and loss modulus $G''(\omega)$, the real and imaginary parts of the complex shear modulus $G(\omega)$, as a function of the external frequency ω.

For a dilute hard-sphere suspension, Einstein showed that (to linear order in ϕ) $\eta/\eta_{\text{sol}} = 1 + (5/2)\phi$ (Einstein, 1906; Mewis and Wagner, 2011). In other words, the suspension viscosity is larger than for the pure solvent η_{sol} due to volume excluded by the suspended particles. A quadratic-order correction in ϕ arises from the hydrodynamic coupling between spheres, but the value of the coefficient depends on the analytical approach. [Batchelor (1977), for instance, found $6.2\phi^2$.]

At higher strain rates beyond linear response (for $\text{Pe}_{\dot{\gamma}} \approx 1$), shear thinning sets in. Viscosity then decreases upon approaching a plateau η_{∞} (van der Werff and de Kruif, 1989), as has been observed in BD simulations without hydrodynamics (Strating, 1999). The phenomenon can therefore be linked to a change in the local arrangement of particles (Xu, Rice, and Dinner, 2013) through the excess shear stress

$$\Delta\tau = -\frac{1}{2}k_{\text{B}}T\rho^2 \int d^3r \frac{xy}{r} g(\mathbf{r})\delta(r-\sigma). \qquad (36)$$

The pair distribution function $g(\mathbf{r})$ is then no longer isotropic (Lin *et al.*, 2013; Lin, Cheng, and Cohen, 2014) because an external force or flow defines a preferred direction. In particular, its contact value $g^+(\sigma, \theta)$, using polar coordinates within the *x*-*y* plane through the particle center, varies with orientation and derived quantities like pressure become anisotropic with the off-diagonal component determining the shear stress; cf. Eq. (36). In linear response, Brady
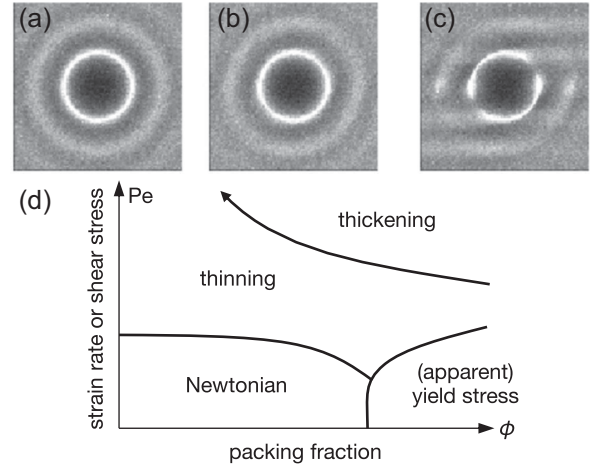

FIG. 35. The microstructure $g(r)$ deforms in shear flow at (a) $\text{Pe}_{\dot{\gamma}} = 0.1$, (b) $\text{Pe}_{\dot{\gamma}} = 1$, and (c) $\text{Pe}_{\dot{\gamma}} = 10$. (a)–(c) From Foss and Brady, 2000a. (d) Sketch of the different flow regimes of hard-sphere suspensions. The lines indicate crossovers, with shear thinning predominately due to colloidal forces and shear thickening having a hydrodynamic origin. Shear thickening has also been observed in dilute suspensions at high strain rates (Bergenholtz, Brady, and Vicic, 2002). At high packing fractions and high strain rates shear-induced ordering is possible.

(1993) determined the Brownian stress as the equilibrium $g(\sigma^+)$ at contact divided by the short-time self-diffusivity.

The deformation at intermediate Péclet numbers is shown in Figs. 35(a)–35(c). The relationship between macroscopic material properties and microscopic structure is at the heart of theoretical approaches. Much effort has been devoted to predict the deformation of the pair distribution in response to external forces and flows (Squires and Brady, 2005), which allows one to calculate flow curves $\tau(\dot{\gamma})$ from first principles. Combining confocal microscopy (of sufficient frame rate) and rheological measurements provides a powerful means to access the local structure in hard-sphere fluids far from equilibrium (Besseling *et al.*, 2009; Lin *et al.*, 2014).

At even higher strain rates (or shear stresses) and moderate to high packing fractions ($\phi > 0.3$), some experiments report an abrupt (sometimes discontinuous) viscosity increase as the stress is increased, i.e., shear thickening (d'Haene, Mewis, and Fuller, 1993; Bender and Wagner, 1996; Meeker, Poon, and Pusey, 1997; Cheng *et al.*, 2002). A comprehensive understanding of this somewhat counterintuitive behavior (it is notably absent in atomistic and molecular liquids) has remained an open challenge (Brown and Jaeger, 2014). For Brownian hard spheres it is now broadly accepted to be a hydrodynamic phenomenon caused by the reversible formation of "hydroclusters" held together through lubrication forces (Wagner and Brady, 2009). Confocal microscopy evidence (Cheng *et al.*, 2011) has also been used to investigate the hydrodynamic and contact force contributions to shear thickening (Lin *et al.*, 2015). Shear thickening extends to dilute suspensions ($\phi < 0.1$), although only at high strain rates (Bergenholtz, Brady, and Vicic, 2002). [See Fig. 35(d) for a summary.] Shear thickening has also been proposed as the mechanism linking rheology of Brownian hard spheres

($\sigma \lesssim 1$ μm) with the physics of non-Brownian granular hard spheres ($\sigma \gtrsim 50$ μm) (Guy, Hermes, and Poon, 2015).

While the shear-thickening behavior is associated with an abrupt increase in the hydrodynamic stresses between the colloidal spheres, which locks them together, giving rise to the large hydroclusters resistant to flow, hydrodynamic interactions between smooth surfaces predict a continuous shear-thickening transition (Ball and Melrose, 1995, 1996; Foss and Brady, 2000b; Melrose and Ball, 2004). The discontinuous appearance of shear thickening instead is found to depend on the small scale surface asperities of the colloidal particles. These asperities can break the lubrication layer and can give rise to a frictional contribution. The relative motion of the particles is then akin to a stick-slip scenario triggered by the breakage of the lubrication layer (Mari *et al.*, 2015; Hermes *et al.*, 2016; Kawasaki and Berthier, 2018; Morris, 2018; Jamali and Brady, 2019). Simulations have explicitly shown a transition from continuous to discontinuous shear thickening by progressively increasing the surface roughness of the particles (Wang, Jamali, and Brady, 2020). The importance of surface characteristics has also been confirmed in a large variety of experimental works (Fernandez *et al.*, 2013; Hsiao *et al.*, 2017; Hsu *et al.*, 2018; Schroyen *et al.*, 2019). In the absence of inertia, two types of discontinuous shear thickening are predicted to occur, depending on whether the frictional particles are below or above their jamming point, where the thickened phase either flows smoothly or is completely jammed (Wyart and Cates, 2014). Curiously, in experiments an additional high-frequency and low-amplitude shear orthogonal to the primary shearing flow has been shown to suppress shear thickening (Lin, Ness *et al.*, 2016).

The high ϕ and high strain rate regime leads to even more surprising observations. Experiments first revealed (Ackerson and Pusey, 1988; Ackerson, 1990), and BD simulations later confirmed (Strating, 1999), that particles then form layers perpendicular to the shear gradient that slide over each other. The system therefore keeps flowing with a viscosity that suddenly drops at $\mathrm{Pe}_{\dot{\gamma}} \approx 10$. Hard spheres under shear can also exhibit nonuniform flow profiles, so-called shear banding. One mechanism is the formation of an arrested band due to small variations of the local packing fraction that trigger the arrest of a much larger region of the flow (Besseling *et al.*, 2010). Other exotic phenomena include the formation of twinned fcc crystals and sliding layers (Haw, Poon, and Pusey, 1998), strings of particles in hard-sphere fluids (Cheng *et al.*, 2012), and novel configurations that optimized packing (Cohen, Mason, and Weitz, 2004). The nonequilibrium phase behavior of a fluid of colloidal hard spheres under oscillatory shear was investigated in real space with experiments on PMMA colloidal suspensions and BD simulations as a function of the frequency of the oscillations and $0 \leq \mathrm{Pe}_{\dot{\gamma}} \leq 15$, displaying a shear-induced oscillating twinned fcc phase, a sliding layer phase, a string phase, and a tilted layer phase (Besseling *et al.*, 2012).

Shearing hard-sphere crystals opens yet another range of phenomena. These include melting (Wu *et al.*, 2009), shear banding (Cohen, Mason, and Weitz, 2004; Cohen *et al.*, 2006; Dhont and Briels, 2008), and, in the case of confined crystals, buckling phenomena (Schall *et al.*, 2004). It is even possible

to infer information about stresses between defects in hard-sphere crystals through a careful analysis of particle trajectories (Lin, Bierbaum *et al.*, 2016).

C. Microrheology

Trapping a colloidal probe with optical tweezers and imaging its stochastic motion provides insights into the mechanical properties of the host material (Wilson *et al.*, 2009; Puertas and Voigtmann, 2014). This microrheological technique is particularly important for biological materials that are difficult to prepare in sufficient amounts for conventional rheological studies (Wilhelm, 2008) and to resolve local mechanical properties in inhomogeneous (soft) materials. Microrheology also enables the noninvasive determination of rheological properties from optical diffusive wave spectroscopy (Sec. IV.A), i.e., from the scattering of many diffusing probes (Mason and Weitz, 1995b). The method then provides moduli at higher frequencies than those accessible via mechanical measurements.

Depending on whether or not the probe is forced, one distinguishes active from passive microrheology. The latter exploits the fluctuation-dissipation theorem, which greatly simplifies the analysis, while analyzing the data from driven probes requires a preexisting model of the host material. In this context, hard spheres have emerged as a particularly useful reference for colloidal suspensions. Squires and Brady (2005) provided a comprehensive analysis of the deformation of the microstructure (Fig. 36) around a hard probe with diameter σ_{probe} forced through a bath of hard spheres with drift Péclet number $\mathrm{Pe}_v = v(\sigma + \sigma_{\mathrm{probe}})/2D_0$. Here v is the probe speed. Analytical expressions for the viscosity are derived in the limits of small and large Pe, thereby yielding an accurate extrapolation to intermediate Péclet numbers. Forcing a probe through a crystal (Vossen, 2004; Dullens and Bechinger, 2011) and a colloidal glass (Habdas *et al.*, 2004; Gazuz *et al.*, 2009; Gruber *et al.*, 2016) has also been studied.

D. Other out-of-equilibrium phenomena

Time-resolved confocal microscopy has been used to study other out-of-equilibrium phenomena. One such example is the dynamics of colloidal particles in externally created energy landscapes, such as optical potentials generated by interfering laser beams. Other significant examples include ordering of polystyrene spheres in quasiperiodic patterned potentials (Mikhael *et al.*, 2008), driving colloidal monolayers through time-dependent fields (Bohlein, Mikhael, and Bechinger,
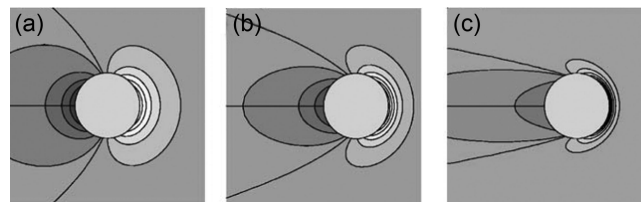

FIG. 36. The microstructure $g(\boldsymbol{r})$ deforms around a driven probe with (a) $\mathrm{Pe}_v = 0.15$, (b) 0.5, and (c) 1.5. From Squires and Brady, 2005.

2012; Brazda *et al.*, 2018), diffusion in random landscapes (Evers *et al.*, 2013), and the transmission of forces through dense colloidal aggregates (Williams *et al.*, 2016).

Following the trajectories of single colloidal particles has also been instrumental in experimentally verifying fluctuation theorems (Wang *et al.*, 2002; Carberry *et al.*, 2004; Blickle *et al.*, 2006) and in verifying a class of exact relations from nonequilibrium statistical physics starting with Jarzynski's seminal work relation (Jarzynski, 1997). [See Seifert (2012) for a comprehensive theoretical review.] In a nutshell, thermodynamic (currentlike) quantities like work and heat can be extended to single stochastic trajectories, which are therefore described by probability distributions constrained by the (near-universal) fluctuation theorems. These relations have also been tested in colloidal suspensions (Gomez-Solano *et al.*, 2015), and recent experimental results, including with colloidal particles, were reviewed by Ciliberto (2017).

More recently "active" colloidal particles have moved into focus. A wealth of interfacial phoretic mechanisms between molecular and colloidal solutes can be exploited to generate self-sustained gradients that move with the colloidal particles and lead to directed motion (revealed as a correlation in displacements absent in passively diffusing particles). One phenomenon where simulations of active hard disks (and spheres) have been, and still are, instrumental is the coexistence of dense and dilute regions following *motility-induced phase separation* (Cates and Tailleur, 2015). Given the absence of cohesive forces, these processes are genuine far-from-equilibrium phase transitions. In light of the many reviews that have been devoted to this rich and fast-moving field (Marchetti *et al.*, 2013; Elgeti, Winkler, and Gompper, 2015; Bechinger *et al.*, 2016; Janssen, 2019), we will not, however, delve into this field further here.

XII. HARD-SPHERE GLASSES AND THEIR FORMATION

At its core, the glass problem consists of understanding how the equilibrium dynamics of a liquid that exhibits no obvious structural change grows to be sufficiently sluggish to freeze particles in place. Although glasses are traditionally associated with cohesive supercooled liquids, dense hard spheres have also long played a key conceptual role. Since the 1976 numerical simulations of Gordon, Gibbs, and Fleming (1976) and Woodcock (1976), hard spheres have in fact been fueling the debate about the nature and location of the glass transition, initially with computer simulations (Frenkel and McTague, 1980; Woodcock, 1981; Woodcock and Angell, 1981; Speedy, 1987), and later with experimental advances such as dynamic light scattering (Sec. IV.A) (Pusey and van Megen, 1987; van Megen and Pusey, 1991; van Megen, Underwood, and Pusey, 1991a, 1991b), real-space analysis (Sec. IV.B) (van Blaaderen and Wiltzius, 1995; Kegel and van Blaaderen, 2000; Weeks *et al.*, 2000; Leocmach and Tanaka, 2012; Hallett, Turci, and Royall, 2018), and rheology (Mason and Weitz, 1995a; Bonn *et al.*, 2017).

In this section, we review the contribution of hard spheres to our understanding of glasses. We first provide some context (Sec. XII.A) before discussing the early work with light scattering (Sec. XII.B), developments made possible by real-space imaging (Sec. XII.C), and more recent work that

approaches much longer timescales than some of the earlier studies (Sec. XII.D). We also consider the effect of confinement (Sec. XII.E) as well as its 2D limit on hard-sphere glass formation (Sec. XII.F). We then move on to the related phenomenon of jamming (Sec. XII.H) and to specific properties of glasses, such as their vibrational behavior (Sec. XII.G), aging (Sec. XII.I), and rheology (Sec. XII.J).

This section, like many others in this review, is limited in scope. Here we exclusively discuss contributions to our understanding of glasses [which has certain universal qualities (Berthier and Biroli, 2011)] that result from hard-sphere studies. We therefore do not include important work that used other systems. For a more complete picture, we refer the interested reader to reviews on the glass transition (Berthier and Biroli, 2011) and on specific aspects such as mean-field theory and high-dimensional work (Charbonneau *et al.*, 2017), dynamical heterogeneity (Berthier *et al.*, 2011), dynamical and structural length scales (Karmakar, Dasgupta, and Sastry, 2014), local structure (Royall and Williams, 2015), jamming (Liu and Nagel, 2010; Torquato and Stillinger, 2010; van Hecke, 2010; Charbonneau *et al.*, 2017; Arceri, Corwin, and O'Hern, 2023), aging (Arceri and Corwin, 2020), and rheology (Bonn *et al.*, 2017).

In this section, we also take a departure from the nomenclature used in the rest of this review. Hard spheres have no liquid phase (Fig. 3, Sec. VII.A). However, because the glass transition in molecular systems is typically driven by cooling a liquid below its melting point such that it is supercooled, the analogous behavior in hard spheres is to compress the system beyond its freezing point P_f [or, following Berthier and Witten (2009) Z_f, for the reduced pressure $Z = \beta P/\rho$] as the control parameter. Therefore, in keeping with much of the hard-sphere glass literature and to emphasize the analogy with molecular systems, we refer to fluid state points thus compressed as supercooled liquids (instead of supercompressed fluids). Similarly, we refer to state points far beyond Z_f as being deeply supercooled. While the reduced pressure Z emphasizes the link with molecular systems (Berthier and Witten, 2009), some of the literature expresses state points in terms of the volume fraction. Here we prefer Z, but when a particular reference uses ϕ we also often use it.

A. Historical theoretical developments and persistent challenges

Understanding the glass transition has been an active area of research for over a century (Berthier and Biroli, 2011), but as it pertains to hard spheres the 1980s saw the independent emergence of two major microscopic theories of the phenomenon: a density-functional description of amorphous solids (Singh, Stoessel, and Wolynes, 1985; Wolynes, 1985; Baus and Colot, 1986; Löwen, 1990), and a kinetic-theory-based (Dorfman, van Beijeren, and Kirkpatrick, 2021) mode-coupling theory (MCT) of glasses (Bengtzelius, Gotze, and Sjolander, 1984; Leutheusser, 1984; Kirkpatrick, 1985; Barrat, Gotze, and Latz, 1989; Fuchs, Hofacker, and Latz, 1992; Goetze, 2009). Using spin glass models as inspiration, the random first-order theory (RFOT) of glasses was then proposed to unify the two descriptions (Kirkpatrick and Wolynes, 1987; Lubchenko and Wolynes, 2007). In short, this framework posits the existence of a dynamical

(or mode-coupling) transition at which ergodicity is lost [at reduced pressure Z_d (or Z_{MCT})–] due to phase space then subdividing into a number of metastable states so large that the transition sees the emergence of a thermodynamic entropy contribution, i.e., a configurational entropy (or complexity).

While this description is now understood to hold in high dimensions (Charbonneau *et al.*, 2017; Parisi, Urbani, and Zamponi, 2020), in two and three dimensions, the situation is more subtle. This largely reflects the fact that this ideal scenario neglects activated processes that can restore ergodicity beyond the MCT transition (thus turning it into a crossover), perhaps even up to the point at which the configurational entropy $S_{\mathrm{conf}} = S - S_{\mathrm{vib}}$ of the supercooled liquid is extrapolated to become equal to that of the crystal (Kauzmann, 1948), where S_{vib} is the vibrational contribution to the entropy (Berthier, Ozawa, and Scalliet, 2019). In the case of molecular liquids, this would happen at a finite (Kauzmann) temperature. The analogous scenario for hard spheres is sketched in Fig. 37, with the configurational entropy of the supercooled liquid becoming equal to that of the crystal at a certain pressure P_K. [Here we use pressure to connect with the crystal in the spirit of the work with molecular systems (Kauzmann, 1948; Cavagna, 2009).] Section XII.D details measurements of the configurational entropy using advanced computer simulation methods that confirm this picture (Berthier *et al.*, 2017).

The drop in configurational entropy is understood to be accompanied by an increase in a structural length scale (Lubchenko and Wolynes, 2007), which would diverge at P_K [unless the transition is avoided (Stillinger, Debenedetti, and Truskett, 2001; Royall *et al.*, 2018)]. Such a length scale
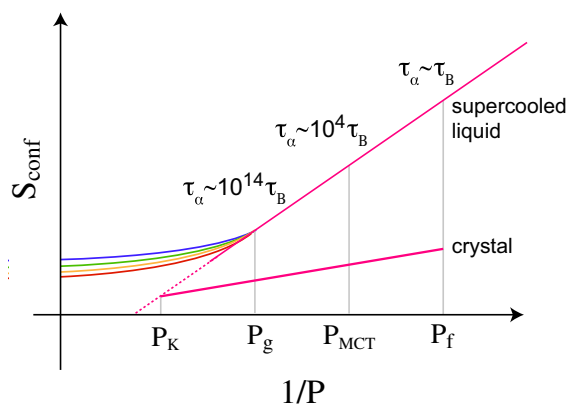

FIG. 37. Road map to the glass transition in hard spheres, with the configurational entropy S_{conf} given as a function of the inverse pressure $1/P$ (osmotic pressure in the case of colloidal systems). Typically S_{conf} of molecular liquids decreases faster than that of crystals as a function of temperature. (The configurational entropy of the crystal is nonzero due to defects.) At some pressure P_K, the supercooled liquid configurational entropy would fall below that of the crystal. P_g is the operational glass transition, which is mapped from that of molecules where the structural relaxation time τ_α typically exceeds that of the liquid by 10^{14} (corresponding to about 100 s). Further compression (fast relative to τ_α) leads to non-equilibrium states (the colored lines). P_{MCT} is the MCT crossover, and P_f is the freezing point. Consideration of the inverse pressure dependence here emphasizes the connection with molecular systems (Kauzmann, 1948; Cavagna, 2009).

may be accessed by point-to-set correlations, which measure the impact of a frozen, disordered boundary (often spherical) on the fluid behavior away from it (often the center of the sphere) (Biroli *et al.*, 2008). Cooperative relaxation at deep supercooling (for $P > P_{\mathrm{MCT}}$ or $Z > Z_{\mathrm{MCT}}$) leads to *dynamical heterogeneity*, with some regions relaxing slower or faster than one another in supercooled liquids (Berthier *et al.*, 2011). The size of these dynamically heterogeneous regions defines a dynamical length scale.

Despite its considerable success and broad epistemic reach, RFOT is far from the only theory of the glass transition to have been formulated and used to interpret results from colloidal hard spheres. A well-studied structural mechanism for dynamical arrest has its roots in the work of Frank (1952), who hypothesized that local fivefold symmetric arrangements of particles would inhibit crystallization. This line of thought was later extended to a dynamical theory built on geometric frustration that imagines domains of particles in fivefold symmetric local environments that grow with supercooling (Tarjus *et al.*, 2005). A related proposal identifies growing structural length scales including regions of local crystalline order (Tanaka, 2005a, 2005b, 2005c, 2022).

Yet another view revolves around facilitated dynamics, which places much emphasis on dynamical correlations and the dynamical facilitation (DF) of particle mobility (Chandler and Garrahan, 2010). While based on simplified kinetically constrained models, it has been applied to particulate systems. DF invokes a dynamical phase transition between a phase in which the system relaxes quickly (the active phase) and a glassy phase with low mobility (the inactive phase). In systems with nontrivial thermodynamics, the inactive phase has a lower configurational entropy than the active phase [somewhat akin to the crystal in the Kauzmann scenario (Fig. 37)] (Royall, Turci, and Speck, 2020). Given this background and context for the glass transition for the purposes of this review, we now consider the research carried out using (or at least inspired by) colloidal hard spheres.

From a practical standpoint, a colloidal hard-sphere glass former must not obviously crystallize. One approach, inspired by atomistic systems such as metallic glasses, is to use binary systems as a means to suppress crystallization. As Sec. IX makes clear, binary systems present a rich phase behavior, but these complex assemblies can be slow to form. Certain binary mixtures have therefore long been used as glass formers, e.g., the model metallic glass former Cu-Zr (Royall and Williams, 2015). A systematic study that used binary hard spheres as a model for these systems has identified suitable compositions and size ratios to suppress crystallization (Zhang *et al.*, 2014).

Interestingly, for highly asymmetric size ratios ($q \lesssim 0.1$), smaller particles deplete larger ones, thus leading to effective attractions, as discussed in Sec. IX.B. The result is a more complex dynamical arrest scenario, reminiscent of colloid-polymer mixtures (Poon, 2002; Royall, Williams, and Tanaka, 2018) in which gelation competes with an attractive glass in addition to the usual hard-sphere glass (Hendricks *et al.*, 2015). Another unexpected behavior includes a critical size asymmetry, at which anomalous collective transport of the small particles appears in a matrix of dynamically arrested large particles (Sentjabrskaja *et al.*, 2016). The rest of this section, nevertheless, considers only relatively small size asymmetries.

B. Reciprocal-space picture: Early studies of the hard-sphere glass transition

When hard-sphere experimental work took off in the 1980s, the relaxation time[14] τ_α window available spanned at most four decades (with respect to a simple colloidal fluid at a volume fraction $\phi \approx 0.5$). Thermodynamic aspects, such as marked changes in configurational entropy, were therefore largely beyond both numerical and experimental reach (Berthier and Biroli, 2011). As a result, early investigations focused mostly on the MCT description of the liquid dynamics, which predicts a dynamical divergence at a volume fraction $\phi_{MCT} \approx 0.58$. For instance, van Megen and Pusey (1991), van Megen, Underwood, and Pusey (1991b), van Megen and Underwood (1993b, 1993c), and van Megen *et al.* (1998) undertook a series of studies of colloidal hard spheres from the MCT perspective, as reviewed by Sciortino and Tartaglia (2005). Other particular highlights from this period include rheological studies of dense colloidal suspensions (Mason and Weitz, 1995a); see Sec. XII.J. Given the relatively short relaxation timescales probed, activated processes could then also be neglected, thus resulting in reasonably good agreement with the MCT predictions. The characteristic power-law growth of the relaxation time and the stretched exponential (or Kohlrauch) form of the correlators, in particular, were found to closely match the MCT prediction (van Megen *et al.*, 1998).

C. Real-space picture: Local structure and dynamical heterogeneity

Local structure in real space. With the use of particle-resolved studies, information about certain features that are otherwise difficult to discern in molecular liquids started to emerge. In their pioneering work, van Blaaderen and Wiltzius (1995) identified the presence of local fivefold symmetric structures in colloidal glasses, as had been predicted by Frank's conjecture (Frank, 1952) and subsequent dynamical descriptions based on geometric frustration (Nelson and Spaepen, 1989; Tarjus *et al.*, 2005). Subsequent efforts to probe specific predictions of that theory, such as growing frustration-limited domains of particles in fivefold symmetric motifs upon supercooling, however, uncovered little evidence of the phenomenon at weak to moderate supercooling ($Z \lesssim Z_{MCT}$) (Charbonneau, Charbonneau, and Tarjus, 2012, 2013; Dunleavy *et al.*, 2015; Royall *et al.*, 2015; Royall, Williams, and Tanaka, 2018). Although some growth of such domains was later found at deeper supercooling (Hallett, Turci, and Royall, 2018, 2020) (see Sec. XII.D), these findings nevertheless suggest that hard-sphere supercooled liquids are strongly geometrically frustrated in the dynamical regime up to the MCT crossover ($Z \lesssim Z_{MCT}$). Dynamical sluggishness can at best be only partially attributed to that effect.

Tracking colloids in supercooled liquids in time: Dynamical heterogeneity. An important contribution to our understanding of the glass transition has come through both
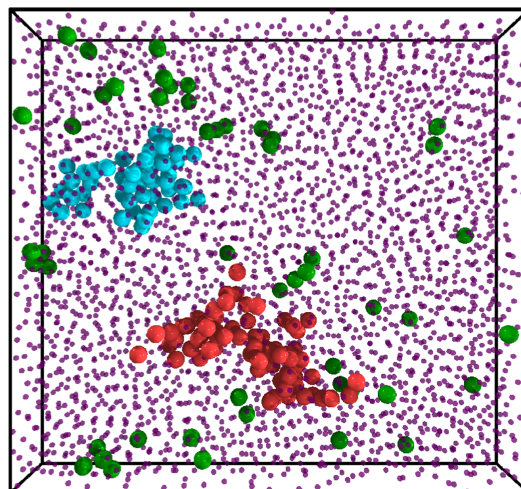

FIG. 38. Dynamical heterogeneity in real space is identified by highlighting the locations of the fastest particles (larger spheres) compared to the other particles (smaller spheres). The latter are drawn smaller for clarity; the particles all have the same physical size, which is the displayed size of the large spheres. Shown is a supercooled sample with $\phi \approx 0.56$ and measurement time $\Delta t^* = 1000$ s. The fastest particles are displaced by about 0.32σ. The red (pale gray) cluster contained 69 particles; the light blue cluster contained 50 particles. From Weeks *et al.*, 2000.

time- and particle-resolved studies. In the context of the glass transition, this feat was first performed in quasi-2D systems by Marcus, Lin, and Rice (1996), Marcus, Schofield, and Rice (1999), and Cui, Lin, and Rice (2001) and was soon after extended to 3D systems by Kegel and van Blaaderen (2000) and Weeks *et al.* (2000). Later work investigated spatially correlated clusters of slow particles (Weeks and Weitz, 2002) that percolate across the system (Conrad *et al.*, 2006). This work brought forward clear evidence of spatially heterogeneous dynamics as the liquid grows increasingly viscous, thus validating earlier computer simulation (Perera and Harrowell, 1996). Colloidal observations provide arguably the most explicit experimental evidence for dynamical heterogeneity in glass-forming systems, a key discovery in the field in recent decades (Ediger, 2000); see Fig. 38.

This feature has since been variously interpreted, including as the fluctuations associated with the avoided dynamical transition predicted by mean-field (RFOT) theory (Berthier and Biroli, 2011) and as constituting an integral part of DF and inhomogeneous MCT (Mishra, Habdas, and Yodh, 2019). More recently real-space studies using hard spheres have also been leveraged to gain insight into DF and to observe the dynamical and structural-dynamical phase transitions in experiments (Pinchaipat *et al.*, 2017; Abou *et al.*, 2018) and simulations (Campo and Speck, 2020). Other tests of that theory include the prediction for the structural relaxation time in two dimensions (Isobe *et al.*, 2016) and three dimensions (Ortlieb *et al.*, 2023) and the identification of the elementary units of relaxation, so-called excitations, which are localized short-term relaxation events seen in 2D colloidal experiments using optical tweezers (Gokhale *et al.*, 2014, 2016; Gokhale, Sood, and Ganapathy, 2016). By contrast, in other studies

---

[14]The relaxation time is typically defined as the time needed for structural correlations to decay to $1/e$ of their initial value.

correlations have been found between short- and long-term relaxation associated with RFOT (Mishra *et al.*, 2019); see Sec. XII.D.

The various interpretations leveraged to make sense of these studies reflect an incomplete first-principles understanding of glass formation. For instance, even though microscopic proposals for the origin of collective fluctuations [traditionally captured by the dynamical susceptibility $\chi_4(t)$] were advanced soon after dynamical heterogeneity was reported (Berthier *et al.*, 2011), only recently has a first-principles explanation (based on displacements being correlated along different dimensions of space) emerged for their single-particle counterpart [traditionally encoded by the non-Gaussian parameter $\alpha_2(t)$ (Biroli *et al.*, 2021; Folena *et al.*, 2022; Charbonneau, Hu, and Morse, 2024)]. Put simply, the dynamical heterogeneity of supercooled liquids remains an active area of research.

Correlation between structure and dynamics in supercooled hard spheres. The aforementioned work that considered fivefold symmetry notwithstanding, a number of studies have demonstrated that a significant amount of information about the dynamics is encoded in the local structure of supercooled hard spheres. Marín-Aguilar *et al.* (2020), for instance, demonstrated a strong link between the number of local tetrahedral clusters in mixtures of hard spheres and their local and global dynamics. Similarly, methods based on information theory (Dunleavy, Wiesner, and Royall, 2012; Jack, Dunleavy, and Royall, 2014; Dunleavy *et al.*, 2015) and machine learning (Boattini *et al.*, 2020; Boattini, Smallenburg, and Filion, 2021; Alkemade *et al.*, 2022) are capable of predicting the local dynamics of glassy hard-sphere systems based on structural data alone, which is analogous to similar observations in other model systems (Bapst *et al.*, 2020).

In some hard-sphere systems, the growth of a static length scale has been related to a dynamical length (Kawasaki, Araki, and Tanaka, 2007; Kawasaki and Tanaka, 2010b; Tanaka *et al.*, 2010; Leocmach and Tanaka, 2012), and to the extent to which the relaxation time increases in response to the control parameter, i.e., the fragility of the supercooled liquid[15] (Tanaka, 2005a, 2005b, 2005c, 2022). In 2D systems, this length scale can be particularly significant (Kawasaki, Araki, and Tanaka, 2007; Tanaka *et al.*, 2010; Russo and Tanaka, 2015); see Sec. XII.F. That length scale often corresponds to "medium-range crystalline order" (Kawasaki, Araki, and Tanaka, 2007; Tanaka *et al.*, 2010) and is therefore distinct from the previously noted fivefold symmetric local order. A more general setup for detecting this length has also been considered (Tong and Tanaka, 2018). Because most of this analysis has been carried out in the regime up to the MCT crossover $P \lesssim P_{\text{MCT}}$ (or $Z \lesssim Z_{\text{MCT}}$) range, where small length scales are typically encountered, it would be most interesting to see what happens at deeper supercooling. It is important to obtain a sharper understanding of why certain systems and

---

[15]In molecular systems, fragility quantifies the rate of increase of the relaxation time upon cooling, with more fragile systems exhibiting a faster rate. For hard-sphere systems, the equivalent is the rate of increase of the relaxation time with either Z or ϕ.
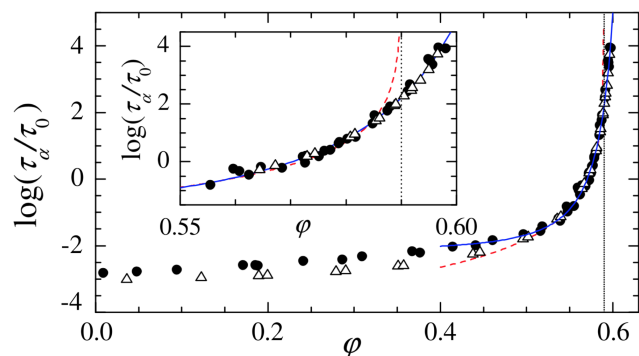

FIG. 39. Relaxation beyond the MCT crossover. Shown is the relaxation timescale for DLS experiments (black circles) and MC simulations (open triangles), respectively, in units of $\tau_0 = 1$ s and $\tau_0 = 7 \times 10^4$ MC steps. The red (pale gray) dashed line is a power-law fit to the MCT critical scaling with a transition (or, rather, a crossover) around $\phi_{\text{MCT}} = 0.590$ (vertical dotted line) and exponent $\gamma = 2.5$. The solid blue line is a fit to DLS data using a modified Vogel-Fulcher-Tammann form with divergence at $\phi_{\text{VFT}} = 0.637$. The inset emphasizes that the MCT singularity is absent. From Brambilla *et al.*, 2009.

analyses provide longer length scales than others (Kawasaki, Araki, and Tanaka, 2007; Kawasaki and Tanaka, 2010b; Tanaka *et al.*, 2010; Dunleavy, Wiesner, and Royall, 2012; Leocmach and Tanaka, 2012; Dunleavy *et al.*, 2015; Hallett, Turci, and Royall, 2018, 2020; Marín-Aguilar *et al.*, 2020), and sometimes even longer than in molecular systems supercooled to T_g (Dauchot, Ladieu, and Royall, 2023) or computer simulations using swap MC (Berthier *et al.*, 2017); see Sec. XII.D. In the case of the more weakly polydisperse samples with the largest length scales, a comparison with the work of Zhang *et al.* (2018) showed that a means to distinguish polycrystals from glasses could be particularly useful; see Sec. XII.F.

D. Deeper supercooling: Beyond the MCT (dynamical) crossover

Since 2010, both experiments (Brambilla *et al.*, 2009; El Masri, Berthier, and Cipelletti, 2010; Hallett, Turci, and Royall, 2018, 2020) and simulations (Brambilla *et al.*, 2009) have been able to equilibrate hard-sphere liquids beyond the MCT crossover, and therefore to probe the activated processes that restore ergodicity in that regime; see Fig. 39.

The use of smaller colloids and the concurrent improvement of imaging capabilities (Sec. IV.B) (Hallett, Turci, and Royall, 2018; Hallett, Turci, and Royall, 2020) have markedly enlarged the range of experimentally accessible relaxation timescales; see Fig. 40 and Sec. IV.C. Among the insights afforded (in addition to the growth of local structures with fivefold symmetry) is the increase of a structural length scale. A length scale may also be extracted from the dynamical heterogeneity (Lačević *et al.*, 2002), which was found to grow concurrently with the structural length scale. Although both exhibited scaling compatible with RFOT-based arguments,

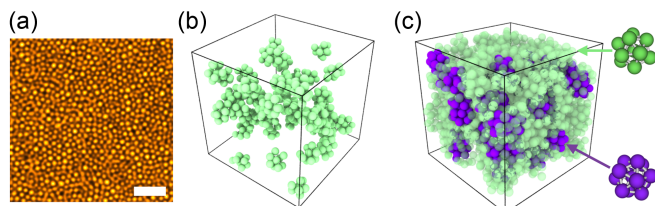$$\xi(Z) = \xi_0 \left(\frac{1}{Z_{\text{VFT}} - Z} \right)^{1/(3-\theta)}, \tag{37}$$

FIG. 40. Resolving small colloids in real space. (a) Stimulated emission depletion nanoscopy image for $\phi = 0.598$. The scale bar corresponds to 3 µm. Rendered coordinates of defective icosahedra (green, top right structure) and full icosahedra (purple, bottom right structure) for (b) $\phi = 0.523$ and (c) 0.598, respectively. From Hallett, Turci, and Royall, 2018.

where ξ_0 is a length at higher pressure and P_{VFT} (or Z_{VFT}) is the compressibility corresponding to the dynamical divergence of the Vogel-Fulcher-Tammann (VFT) fit and $\theta \approx 2.05 \pm 0.1$ (Hallett, Turci, and Royall, 2018), this work is still well short of the 14 orders of magnitude increase in relaxation time corresponding to the operational glass transition. An interesting means of using still smaller particles (which could access longer effective timescales) could be to sacrifice particle-resolved imaging and instead measure fluorescence recovery from photobleaching (van Blaaderen, Peetermans *et al.*, 1992; Simeonova and Kegel, 2004).

An interesting new direction for experiments with small particles benefits from recent developments in synchotron intensity with x rays (Wochner *et al.*, 2009; Lehmkühler *et al.*, 2020; Liu *et al.*, 2022; Striker *et al.*, 2023). This approach has enabled the development of methods such as x-ray photon correlation spectroscopy (XPCS), microbeam x-ray scattering, and x-ray cross-correlation analysis (XCCA). XPCS is the x-ray equivalent of DLS and is therefore sensitive to dynamical information, though at much smaller wavelengths than DLS. Techniques based on the latter two can reveal higher-order structure and have been used to identify local fivefold symmetric order in systems of 100 nm diameter silica particles (Wochner *et al.*, 2009; Lehmkühler *et al.*, 2020; Liu *et al.*, 2022), i.e., smaller than what has been achieved even with superresolution microscopy. Furthermore, XCCA can even be coupled with XPCS to combine higher-order structure and dynamical measurements (Striker *et al.*, 2023). The ability to access, in principle, much smaller particles shows that these methods may enable access to much longer timescales (in terms of τ_B), enabling equilibration at a higher reduced pressure Z than has yet been achieved.

These advances, however, pale in comparison with the scale of the numerical developments based on the swap MC algorithm (Ninarello, Berthier, and Coslovich, 2017). Prior studies of hard spheres had mostly considered minimally size polydisperse mixtures, which benefit from a certain proximity to theoretical frameworks and experiments while suppressing crystallization (Bernu, Hiwatari, and Hansen, 1985; Mountain and Thirumalai, 1987; Eldridge *et al.*, 1995), but Ninarello, Berthier, and Coslovich (2017) showed that astronomical sampling gains can be obtained by enabling diameter exchanges in broadly polydisperse mixtures of hard spheres. Although these ergodicity restoring processes correspond to an extraordinarily unphysical dynamics that at best indirectly
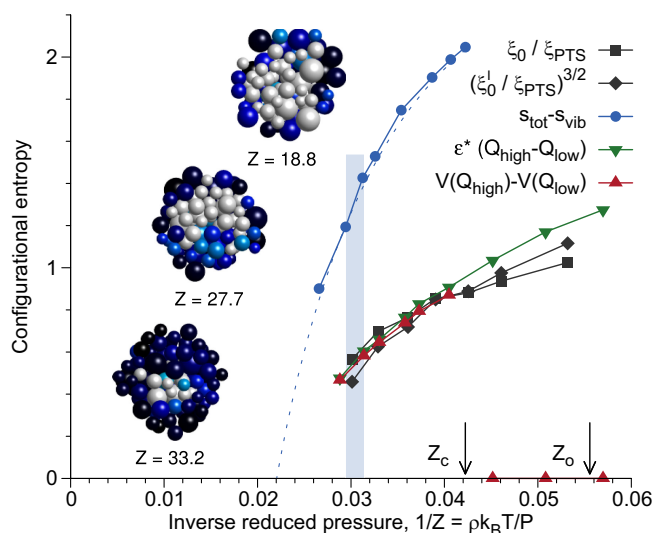

FIG. 41. Different estimators of the configurational entropy consistently extrapolate to their vanishing at a finite reduced pressure; this is congruous with the existence of a Kauzmann-type entropy crisis. Inset: depiction of the growing extent of amorphous order (dark colors) as pressure increases. From Berthier *et al.*, 2017.

informs our understanding of actual liquid dynamics (Ikeda, Zamponi, and Ikeda, 2017; Wyart and Cates, 2017; Berthier, Biroli, Bouchard, and Tarjus, 2019), their reach beyond the MCT scaling regime of the resulting equilibrium configurations has no equal: it can match and even surpass the experimental glass transition of molecular liquids, where the relaxation time is some 10^{14} longer than in the liquid. Note that the relatively high polydispersity required for swap MC to suppress crystallization also seems to reduce the degree of fivefold symmetric structures, thus suggesting a lack of universality for the kind of structural approach employed in geometric frustration (Coslovich, Ozawa, and Berthier, 2018).

As shown in Fig. 41, these configurations have notably enabled crisp complexity measurements in hard-sphere (Berthier *et al.*, 2017) and hard-disk models (Berthier, Charbonneau *et al.*, 2019). These results provide an unprecedented test of the thermodynamic complexity vanishing at a Kauzmann-like entropy crisis at Z_K.

The same configurations have also been used to study certain features of a proposed ergodicity restoring process. Given that equilibrium liquid configurations are metastable (in a mean-field sense) beyond the MCT crossover, it has long been proposed that a nucleationlike process should dominate dynamical relaxation. Thanks to swap MC, the growth of the point-to-set metastability length associated with the growing amorphous order that underlies that mechanism has even been detected (Berthier *et al.*, 2017; Berthier, Biroli, Bouchard, and Tarjus, 2019) significantly beyond what was previously possible (Biroli *et al.*, 2008). The relationship of these observables to actual activated dynamics, however, remains far from controlled. Recent studies have isolated the contribution of an altogether different, hoppinglike, relaxation mechanism (Biroli *et al.*, 2021). The seeming robustness of the coupled (and cooperative or facilitated) relaxation of localized features (Chacko *et al.*, 2021; Kapteijns *et al.*,

2021; Guiselin, Scalliet, and Berthier, 2022; Ortlieb *et al.*, 2023) suggests that a great deal of conceptual tension remains to be resolved.

Other approaches to assess the validity of the RFOT description have also been devised. Evidence for a drop in configurational entropy has been inferred by comparing different regions in deeply supercooled colloid experiments (Hallett, Turci, and Royall, 2018). Alternatively, in deeply supercooled liquids *pinning* a fraction of the particles in place also reduces the configurational entropy, thus bringing the system closer to the Kauzmann transition without further equilibration (Cammarota and Biroli, 2012). In colloidal experiments, a similar setup has been achieved with optical tweezers (Gokhale *et al.*, 2014, 2016; Gokhale, Sood, and Ganapathy, 2016) and by adhering colloids to a substrate (Williams *et al.*, 2018). Spherical confinement (see Sec. X.D) has been used to investigate amorphous order in supercooled liquids through measurements akin to cavity point-to-set correlations (albeit without an equilibrated confining boundary). Experiments confining particles within an emulsion droplet have similarly revealed growing structural length scales (Zhang and Cheng, 2016).

Identifying transitions between metabasins in the free-energy landscape (Rodriguez Fris, Appignanesi, and Weeks, 2011; Rodriguez Fris *et al.*, 2018) through measuring the fractal dimension of so-called cooperatively rearranging regions (CRRs) has also been investigated experimentally. Early results were found to be consistent with more compact CRRs at deep supercooling (Nagamanasa *et al.*, 2015), but equilibrating these conventional colloidal systems past the MCT crossover, where such compaction is expected (Berthier and Biroli, 2011), is difficult. Smaller colloids have since confirmed the compaction of CRRs more convincingly (Ortlieb *et al.*, 2023). The particular scaling properties of CRR surfaces (Biroli and Cammarota, 2017) have also been measured in colloidal systems for $P \lesssim P_{MCT}$ (or $Z \lesssim Z_{MCT}$) and found to be consistent with predictions (Ganapathi *et al.*, 2018).

Obtaining a clear understanding of the actual relaxation dynamics in this regime nevertheless remains fraught with theoretical and experimental challenges. Whichever way this problem moves forward, hard-sphere models and experiments will be involved in advancing our comprehension.

E. The hard-sphere glass transition under confinement

In molecular glass-forming systems, the effect of confinement has long been a challenge to understand because contradictory effects on the relaxation time have been reported (Richert, 2011). Corresponding experimental studies are limited and lie in the weakly supercooled $P \lesssim P_{MCT}$ (or $Z \lesssim Z_{MCT}$) regime. Confinement has nevertheless been shown to robustly induce layering (see Sec. X), which has a profound effect upon dynamical heterogeneity, and markedly increases the overall relaxation time (Nugent *et al.*, 2007; Edmond, Nugent, and Weeks, 2012).

Using walls at which the mobility can be controlled, boundary mobility has been shown to play an important role in the relaxation of confined hard spheres (Hunter, Edmond, and Weeks, 2014). Gradients in dynamics with respect to the boundary appear for more mobile boundaries, whereas for less mobile boundaries gradients are almost entirely suppressed. One quasi-2D system using adaptive confinement (see Sec. X) revealed the emergence of a faster relaxation mechanism at high area fraction, leading to "negative fragility," that is, the relaxation time increasing in a "sub-Arrhenius-like" manner (Williams *et al.*, 2015), which, due to the curvature of the bounary, could be related to void-induced relaxation that has been observed in the bulk (Yip *et al.*, 2020). For a moderately polydisperse, densely packed hard-sphere fluid confined between two smooth hard walls, EDMD simulations showed the emergence of reentrant glass transitions depending on the wall separation, which was in agreement with MCT predictions (Mandal *et al.*, 2014).

F. The glass transition in 2D hard spheres

Two-dimensional glass-forming systems differ significantly from their 3D counterparts. First, the traditional geometrical frustration argument is turned on its head. For hard disks, the local liquid structure is hexagonal, as is the crystal, and therefore no geometrical frustration is expected. As a result, simulations have revealed (Kawasaki, Araki, and Tanaka, 2007; Tanaka *et al.*, 2010) and experiments have confirmed (Tamborini, Royall, and Cicuta, 2015) that structural correlations are more long-range than in the 3D systems mentioned in Sec. XII.A. Second, Mermin-Wagner-like fluctuations result in dynamical correlations that are profoundly different from those in three dimensions (Flenner and Szamel, 2015), as confirmed in an experiment (Vivek *et al.*, 2017).

G. Vibrational properties of hard-sphere glasses

Molecular (rather than colloidal) glasses exhibit unusual vibrational properties. Among these is the boson peak, an excess density of states with respect to the Debye scaling of specific heat found in crystalline materials (Berthier and Biroli, 2011). Colloids exhibit overdamped dynamics and therefore do not have a proper vibrational spectrum. It is nevertheless possible to imagine a *shadow system* with Newtonian interactions that features the same set of configurations (K. Chen *et al.*, 2010). A number of studies have thereby deduced an effective density of states of soft vibrational modes (Ghosh, Chikkadi *et al.*, 2010; Ghosh, Mari *et al.*, 2010; Kaya *et al.*, 2010). This approach has led to experimental evidence for such a boson peak in hard-sphere colloidal systems (K. Chen *et al.*, 2010; Ghosh, Chikkadi *et al.*, 2010; Ghosh, Mari *et al.*, 2010).

The vibrational properties of a hard-sphere glass are also related to the free volume available for each particle. This free volume can be interpreted using a cell-theory-like analysis (Sec. VI.B) on the real-space Voronoi volumes obtained in hard-sphere colloidal glasses. This analysis has demonstrated a decrease in the effective vibrational free energy during aging (Zargar *et al.*, 2013). The local free energy has further been shown to display strong spatial and temporal heterogeneity, and changes in free energy between consecutive snapshots have been correlated algebraically with particle rearrangements. The vibrational properties of the glass have further been shown to correlate with its local free energy, displaying a

large excess of low-frequency modes (Zargar *et al.*, 2014; Dang *et al.*, 2022), despite the limitations of cell theory in the context of disordered materials; see Sec. VI.B.

H. Colloidal hard spheres and the jamming transition

As noted in Sec. II.A, in their pioneering work Bernal *et al.* constructed out-of-equilibrium disordered (or glasslike) solids out of compressed ball bearings. While investigating the structural properties of the liquid state, they also obtained a first controlled model of hard-sphere *jamming* (Bernal and Mason, 1960; Finney, 2013), and of the so-called random close-packing (RCP) volume fraction $\phi_{\mathrm{RCP}} \approx 0.64$ (Scott and Kilgour, 1969). In its purest sense, jamming pertains to crunching hard particles up to infinite pressure such that no thermal motion remains. Rigidity then emerges from particles being immobilized by each other.

A putative relationship between equilibrium and nonequilibrium crunching was first proposed by Angell *et al.* who considered that singularities of the resummed hard-sphere virial expansion might be related to the jamming singularity (Woodcock and Angell, 1981; Song, Stratt, and Mason, 1988). The simplicity of this thermodynamics-based approach was appealing, which probably explains why similar schemes were still considered decades later. Dedicated numerical efforts, however, clearly distinguished the equilibrium liquid branch from the continuum of out-of-equilibrium glass branch(es) (Speedy, 1994; Rintoul and Torquato, 1996; Robles *et al.*, 1998). Particularly telling (and model-free) evidence against the virial-series scheme is the nonuniqueness of the amorphous close-packed density. Depending on the preparation protocol, a wide range of possible densities can indeed be reached (Brambilla *et al.*, 2009; Chaudhuri, Berthier, and Sastry, 2010; Hermes and Dijkstra, 2010a, 2010b; Ozawa *et al.*, 2012; Charbonneau and Morse, 2021).

Edwards and Oakeshott (1989) formulated another influential proposal for dealing with jamming using an equilibrium statistical-mechanics-like description. Despite the approximate nature of this description for any actual jamming protocol (Charbonneau *et al.*, 2017), it turned out to be a versatile and influential framework for granular experiments over the following decades (Baule *et al.*, 2018). Analyses of jamming based on this scheme, however, also suffered from identifying a unique terminal density.

Yet another proposal for unifying glass formation and jamming has been less quantitatively fruitful but more conceptually productive. In the late 1990s, Liu and Nagel (1998) presented a framework for relating glass formation and jamming, commonly known as the jamming phase diagram, that relates volume fraction, temperature, and shear stress. Perhaps one of the most physically stunning features of jamming is that its criticality is largely independent of physical dimension (Donev, Torquato, and Stillinger, 2005b; Skoge *et al.*, 2006; Goodrich, Liu, and Nagel, 2012; Charbonneau, Corwin *et al.*, 2021). Certain critical features remain robustly invariant in going from the exactly solvable limit of $d \to \infty$, obtained through a full replica symmetry breaking calculation, down to amorphous packings of 2D disks (Charbonneau *et al.*, 2015; Charbonneau, Corwin *et al.*, 2021). The corrections that do appear are largely localized,

such as rattlers (floaters) and bucklers (Charbonneau *et al.*, 2017), and can be geometrically identified through simple criteria. Low-energy excitations around jammed configurations, however, remain largely universal (Charbonneau *et al.*, 2016; Kapteijns, Bouchbinder, and Lerner, 2018; Shimada *et al.*, 2020). As many thorough and complementary reviews are available on this topic (Liu and Nagel, 2010; Torquato and Stillinger, 2010; van Hecke, 2010; Charbonneau *et al.*, 2017; Arceri, Corwin, and O'Hern, 2023; Morse and Charbonneau, 2024), here we specifically consider aspects pertinent to hard-sphere colloids.

Since experimental systems of colloids are neither perfectly hard nor at infinite pressure nor perfectly frictionless, one line of enquiry has been to probe how much these differ from purely jammed hard spheres, without thermal motion. Jenkins *et al.* (2011) found that the statistics of load-bearing bridges of colloids in a high volume fraction sediment (i.e., under gravity) were the same as those predicted for granular particles. This work is notable at a technical level, as the coordinates of the particles needed to be determined with exceptionally high precision; see Sec. IV.B. Other examples include the interplay between compression rate (i.e., the rotation rate of the centrifuge in which the sample is placed) and the volume fraction of the final sediment. This was found to vary between random loose packing (RLP) volume fraction $\phi_{\mathrm{RLP}} \approx 0.55$ for rapidly compressed dilute samples and ϕ_{RCP} for samples with an initially high volume fraction that were slowly compressed. This result suggests the presence of some degree of friction, which is particularly important if the timescale of compression is comparable to or less than the Brownian time (Liber *et al.*, 2013).

An interesting connection between systems with thermal motion and the zero-temperature jamming limit has been made with the discovery of a Gardner transition, intermediate between the two, in mean-field treatments (Charbonneau *et al.*, 2014). For equilibrium hard-sphere configurations well beyond the MCT crossover, a quasistatic compression analysis that neglects activated processes predicts the existence of an intermediate Gardner transition at which marginal stability emerges and then persists. By marginal stability it is meant that the system can be perturbed by the smallest external force; that is, its susceptibility diverges (see Fig. 42). Various features of this transition have been reported in hard-sphere simulations, including the growth of structural and dynamical correlations (Charbonneau *et al.*, 2014, 2017). A similar phenomenology was predicted and reported under shear (Jin and Yoshino, 2017, 2021; Jin *et al.*, 2018). In all cases, however, the thermodynamic character of this transition remains an open area of research (Berthier, Ozawa, and Scalliet, 2019; Li *et al.*, 2021). Experimental validation of many of these findings using colloids is also an open challenge. Although inventive detection schemes have been devised (Hammond and Corwin, 2020), identifying signatures of the Gardner transition using particle-resolved studies requires a high precision of coordinate tracking with respect to the particle diameter that can be achieved in vibrated granular systems (Seguin and Dauchot, 2016; Kool, Charbonneau, and Daniels, 2022; Xiao, Liu, and Durian, 2022) but is challenging with colloids; see Sec. IV.B. Given the 2D nature of these granular systems, however,
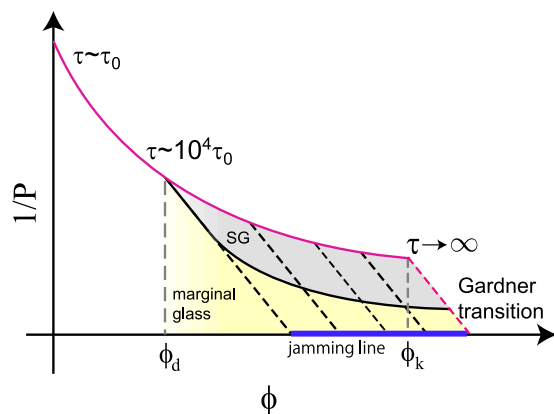
FIG. 42. Road map to the Gardner transition. The inverse pressure $1/P$ is shown as a function of the volume fraction ϕ, with the pink (dark gray) line corresponding to the equilibrium equation of state. At low volume fraction, the system is a fluid, but for $\phi > \phi_{\text{MCT}}$ the system supports many metastable states within a range of pressures, which may be either stable glasses (gray shaded region marked SG) or marginal glasses [yellow (pale gray) shaded region]. These states are distinguished by the anomalous elastic response of the marginal glass; see the main text. The particles are hard, so jammed states correspond to $1/P = 0$ (on the horizontal axis), which are all marginal glasses. The dashed lines describe compressions that are fast relative to τ_α on the equilibrium line.

whatever unusual behavior is reported for these systems is expected to wash out in the thermodynamic limit (Berthier, Biroli, Charbonneau *et al.*, 2019).

I. Aging in hard-sphere glasses

Another important out-of-equilibrium phenomenon in glasses is their aging, which refers to the physical properties of a material displaying a slow time evolution after a sudden quench into the glass regime. In other words, aging is observed when the relaxation time of the system exceeds the experimental observation time, thus breaking time translation invariance. To describe aging, an explicit dependence on the *waiting time* (the time elapsed since the initial quench) t_w is introduced to all structural and dynamical properties.

A large body of theoretical work on aging has focused on mean-field models (Cugliandolo and Kurchan, 1993; Cugliandolo, Kurchan, and Ritort, 1994), which describe a system that is trapped in an energy landscape in which barriers of all possible heights are present and time-correlation functions never completely decay. *Trap models*, which describe phase space as a large collection of metastable states, thus resulting in a broad distribution of trapping times, provide a physically intuitive picture (Bouchaud, 1992; Denny, Reichman, and Bouchaud, 2003). These theoretical approaches make interesting predictions of universal behavior, such as the existence of a long-time stationary regime where time-correlation functions decay as power laws of t/t_w and the possibility of defining an effective temperature T_{eff} (or, for hard spheres, Z_{eff}), to describe the downhill motion of the system in the free-energy landscape (Crisanti and Ritort,

2003). Recent advances, however, have revealed that these broad universality claims are unwarranted. Even simple mean-field models can exhibit aging processes that are much richer (Folena *et al.*, 2022; Folena and Zamponi, 2023). As a result, the theoretical framework for describing aging remains somewhat fragile. Various studies have nevertheless explored this regime using the canonical framework of Cugliandolo and Kurchan (1993).

Although the time window over which colloidal hard-sphere relaxation can be observed is limited, key insight can be obtained by accounting for the nonergodic state of the glass phase. In this context, optical techniques are key (Pusey and van Megen, 1989). A single DLS experiment measures the time-averaged time-correlation function of the intensity of a single speckle. While for an ergodic system this function is equal to the ensemble-averaged one, in the glass state the sample explores only a limited region of phase space, even over long times. It is therefore nonergodic. Early studies have resolved this issue by repeating the measurements over a large number of observations (Pusey and van Megen, 1987), but Pusey and van Megen (1989) developed a procedure, based on approximating the fluctuating component of the density fluctuations with a Gaussian field of zero mean, to extract the intermediate scattering function from a single measurement of the time-averaged correlation function and a measurement of the ensemble-averaged intensity (obtained by quickly scanning the system through the laser beam). To measure slow decays, other methods have been introduced, such as the method of echoes (for which the sample is continuously rotated during the measurement) (Pham *et al.*, 2004), as well as the multispeckle (Bartsch *et al.*, 1997; Cipelletti and Weitz, 1999; El Masri *et al.*, 2005), and time-resolved correlation techniques (Cipelletti *et al.*, 2003; El Masri *et al.*, 2005).

The first observation of aging in a hard-sphere colloidal glass was reported by van Megen *et al.* (1998), who measured the self-intermediate scattering function via DLS by tuning the refractive index of a mixture of optically different (but equally sized) PMMA particles. These experiments showed the waiting-time dependence of the long-time decay of the relaxation functions. These studies were followed by multispeckle and time-resolved correlation studies (El Masri *et al.*, 2005) that confirmed the observation of aging in measurements of the intensity of the correlation function, with relaxation times also showing aging at early times, with a possible plateau at later times. The decay of the intermediate scattering function was shown (Martinez, Bryant, and van Megen, 2008) to change from a simple exponential dependence at short waiting times to an algebraic dependence on time at long waiting times, thus agreeing with the aging time superposition principle that was deduced from mean-field models (Bouchaud, 1992).

In real-space experiments, the dynamics was found to slow upon aging, which is consistent with expectations and with the previously noted reciprocal-space work (Courtland and Weeks, 2003). Studies on binary hard-sphere glass formers have revealed that relaxation can be dominated by the smaller species and that these can facilitate the relaxation of larger particles (Lynch, Cianci, and Weeks, 2008).
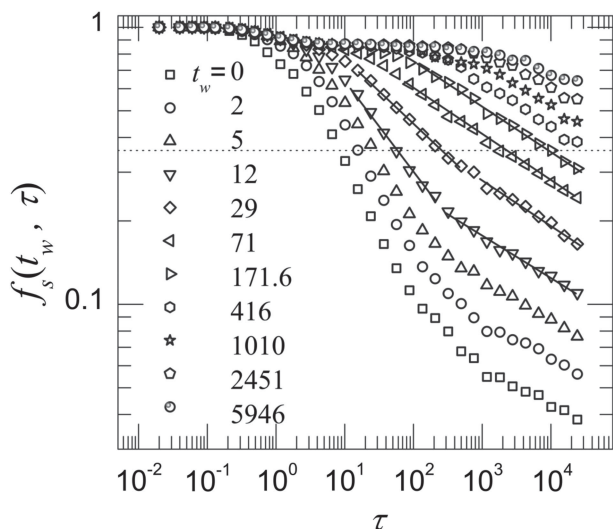
FIG. 43.   Aging behavior in structural relaxation. Upon increasing the waiting time (different symbols correspond to different waiting times), the intermediate scattering function decays more slowly as a function of time (here τ in microscopic units for hard spheres). This corresponds to the system "sinking lower in its energy landscape." From El Masri, Berthier, and Cipelletti, 2010.

Computational studies of aging in hard-sphere systems, which can access up to six decades of relaxation times, have managed to access the decay of time-correlation functions for longer waiting times. In particular, El Masri, Berthier, and Cipelletti (2010) investigated nearly hard spheres with a polydispersity of $s \sim 11.5\%$ at packing fractions in the range $\phi \in [0.553, 0.662]$ and for different waiting times. Aging of the structural quantities was shown to be compatible with either a power law or a slow logarithmic decay. The self-intermediate scattering function, as shown in Fig. 43, displayed at least two distinct decay regimes, depending on the waiting time, with the decay at long waiting times following a power law with time $f_s \sim \tau^{-a}$, with $a \sim 0.15$, suggesting that relaxations occur over a broad time window. The time τ_a after which the asymptotic stationary state is observed increases with packing fraction and, for higher volume fractions, is often outside of what is accessible in experiments. The relaxation time is found to change from a superaging exponential behavior in the waiting time before τ_a to the linear dependence in waiting time after τ_a. The asymptotic regime is also characterized by a subdiffusive behavior of the single-particle dynamics, with the Van Hove functions displaying fat tails at large and small particle displacements. Particles with fast displacements are found to be around 4% to 5% of the system and to have correlated motions limited in space, with the overall displacement of the particles during the aging regime being almost negligible. Despite the subdiffusive dynamics during the aging regime, simulations of weakly polydisperse hard spheres have shown that crystallization can still occur in the bulk (Zaccarelli *et al.*, 2009). Such crystallization without diffusion (Sanz *et al.*, 2011, 2014; Russo and Tanaka, 2012; Yanagishima, Russo, and Tanaka, 2017; Yanagishima *et al.*, 2021) is connected to avalanche-like processes, as discussed in Sec. XIII.I.

J. Hard-sphere glasses far from equilibrium

Steady-state shear. Bulk-rheology experiments (Sec. XI.B) have also been used to study the far-from-equilibrium response of hard-sphere glasses (Ballesta *et al.*, 2008; Koumakis, Schofield, and Petekidis, 2008; Koumakis *et al.*, 2012; Koumakis, Brady, and Petekidis, 2013; Ballesta and Petekidis, 2016). (Phenomena specifically associated with hard-sphere fluids, including shear thinning and thickening, are covered in Sec. XI.B.) At steady state these experiments provide flow curves $\tau(\dot{\gamma})$ similar to Fig. 34(b). Because relating microscopic structure and dynamics often requires theoretical and computational insights, this approach has provided a fertile ground to test theoretical predictions including, *inter alia*, the extension of MCT to treat shear in the "integration through transients" approach (Fuchs and Cates, 2005; Brader, Cates, and Fuchs, 2008, 2012) and the effective model of soft glassy rheology (Sollich *et al.*, 1997; Fielding, 2014). MCT predictions of flow curves have been found to be consistent with rheology experiments on emulsions (Mason and Weitz, 1995a), microgels, save for some hydrodynamic effects that can be taken into account with rescaling (Fuchs and Ballauff, 2005). Steady-state shear is amenable to confocal microscopy provided that the frame rate is fast enough (Besseling *et al.*, 2007, 2009). Particle-resolved data reveal local displacements, and the effect of shear can reveal details of shear bands such as shear-concentration coupling (Besseling *et al.*, 2010; Chikkadi *et al.*, 2014) and Bingham-like slip behavior (Ballesta *et al.*, 2008, 2012).

Strongly confined, quasi-2D systems also offer insight into flow behavior. By animating optical traps confining a circular assembly of particles, the flow field that defines the viscosity has been resolved at the single-particle level. Hard-disk systems have notably been shown not to exhibit any massive increase in viscosity under confinement down to a few diameters (unlike many molecular systems) (Williams *et al.*, 2022). This effect was attributed to the absence of van der Waals interactions. In the same system, particle-resolved data have identified the mechanism of slip between layers (Williams *et al.*, 2016).

Yielding. Upon applying a load to an amorphous solid, yielding occurs at a reasonably characteristic yield stress τ_y (Bonn *et al.*, 2017); see Fig. 44. Prior to yielding, the otherwise elastic response is punctuated by stress release in discrete plastic events known as shear transformation zones (STZs) (Falk and Langer, 1998). Under certain conditions (typically a slow shear rate), as characterized by the Weissenberg number (see Table I), a stress overshoot is found where the steady stress is less than the yield stress $\tau_{\text{steady}} < \tau_y$. With confocal microscopy STZs may be directly visualized. Figure 45 demonstrates how tracking single particles in a dense suspension of hard spheres allows one to build local strain maps and identify STZs (Schall, Weitz, and Spaepen, 2007). Long-range strain correlations may also be investigated (Chikkadi *et al.*, 2011, 2012; Mandal *et al.*, 2013). Further work using confocal microscopy has revealed a microstructural anisotropy in the extension axis, where the maximum of the pair distribution function exhibits a minimum at the stress overshoot (Koumakis *et al.*, 2012, 2016). Related work by some of the same researchers found superdiffusive dynamics
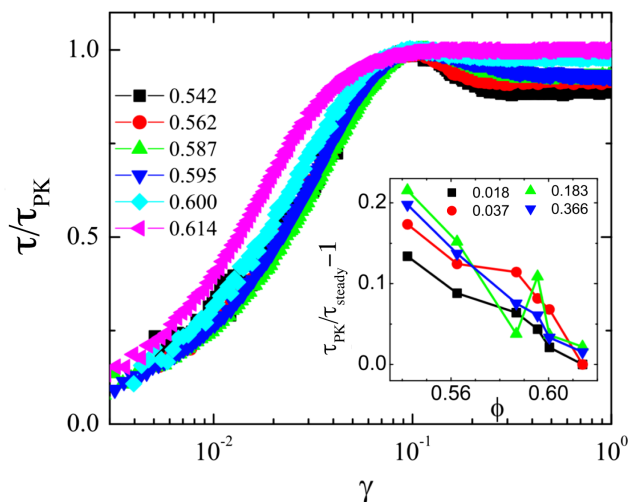
FIG. 44. Stress overshoot in colloidal hard spheres. The stress normalized by the peak stress τ_{PK} at different volume fractions ϕ is as indicated. Inset: the stress peak height scaled by its steady-state value $\tau_{PK}/\tau_{steady} - 1$. The lines correspond to the Weissenberg numbers $Pe_w = \dot{\gamma}\tau_\alpha$ indicated. From Koumakis *et al.*, 2012.
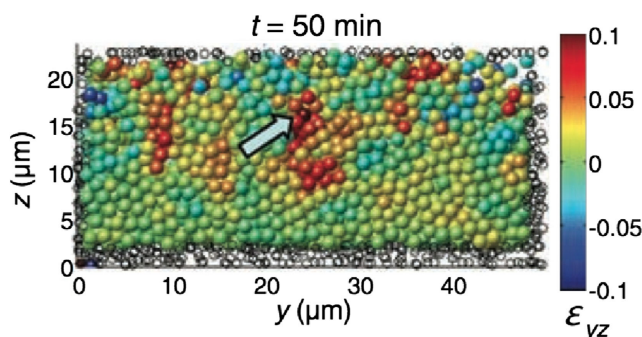

FIG. 45. Response of a 3D colloidal glass to linear shear strain. Cumulative strain γ after 50 min with the particle color denoting the degree of strain. The arrow points to a shear transformation zone, which subsequently relaxed. From Schall, Weitz, and Spaepen, 2007.

approaching yielding that is akin to (albeit underestimated by) that predicted by MCT. The stress overshoot was also weak, likely due to the measurements having been made in the supercooled liquid ($\phi \approx 0.56$) (Zausch *et al.*, 2008; Laurati *et al.*, 2012; Sentjabrskaja *et al.*, 2014). MCT and BD simulations of 2D hard disks qualitatively capture yielding predictions from the theory (Henrich *et al.*, 2009). Binary hard-sphere glasses have also been studied, and for the size ratio $q = 0.2$ some weakening of the system upon inclusion of the smaller species has been reported (Sentjabrskaja *et al.*, 2013), a phenomenon likely related to the fluidization of quiescent systems with depletion attraction (Pham, 2002; Royall, Williams, and Tanaka, 2018).

Creep describes the slow flow that is observed at stresses below the yield stress τ_y. The phenomenon is commonly rationalized using a bulk-rheology-based generalized Maxwell model (Siebenbürger, Ballauff, and Voightmann, 2012), but particle-based descriptions are also rich. For instance, avalanche stress relaxation behavior has been detected in creep

(Jacob, Moghimi, and Petekidis, 2019). Using rheology and light-scattering echo, particle trajectories were further found to be partly reversible under strains that significantly exceed the yield strain (Petekidis, Vlassopoulos, and Pusey, 2003). Confocal microscopy has additionally revealed dynamically heterogeneous regions as a means to link creep and steady-state flow behavior (Sentjabrskaja *et al.*, 2015).

Another means of probing the far-from-equilibrium behavior of a hard-sphere glass is to drag a particle through it using optical tweezers, i.e., microrheology (Sec. XI.C). There it was found that the threshold force for movement of the dragged particle varies strongly with volume fraction, and its velocity fluctuations do not change near the glass transition (Habdas *et al.*, 2004; Gazuz *et al.*, 2009; Gruber *et al.*, 2016). Unlike particle-resolved studies where all imaged particles are tracked through the use of a tweezed probe particle, the latter method can in principle be applied to smaller particles, thus opening the door to deeper supercooling; see Secs. IV.C and XII.D. Finally, flow in channels of colloidal glasses has received relatively little attention, but a surprising oscillatory flow behavior has been reported (Isa, Besseling, and Poon, 2007; Isa *et al.*, 2009).

XIII. NUCLEATION AND GROWTH

Although the thermodynamic phase transition between the fluid and crystal phase of hard spheres is fairly well understood (see Sec. VII), the kinetics of the transformation from one to the other is an active area of research. Many fundamental questions about the process are still largely open, such as the regime of validity of classical nucleation theory (CNT), the discrepancy between numerically computed homogeneous nucleation rates and experimentally measured values, and the glass-forming ability of (quasi)monodisperse hard spheres. This section describes our current understanding of the phase transformation process and further details of some of the associated challenges.

A. A primer on classical nucleation theory

One hundred and fifty years ago Gibbs (1878) suggested that a first-order phase transition should proceed through the formation of a nucleus of the thermodynamically stable phase embedded in the metastable phase. Some of the spatial and temporal crystal-like fluctuations that spontaneously form in the fluid can then give rise to the macroscopic phase transformation. Gibbs proposed that this process may be viewed as two coupled homogeneous systems with a sharp interface, whereby the reversible work required to grow the nucleus determines its probability. The thermodynamic aspects of nucleus cluster formation were later expanded through modeling the dynamics of cluster growth by Volmer and Weber (1926) and Becker and Döring (1935), who formulated CNT (Kelton, 1991; Debenedetti, 1996). In particular, Becker and Döring proposed an infinite set of coupled equations that describe in general terms the coagulation and fragmentation of clusters of different sizes. From this perspective, the basic assumptions of CNT are (i) a single order parameter describes the size evolution of the different clusters and (ii) the nucleation process is Markovian; i.e., the time evolution does

not depend on the state of the system at previous times and clusters can change their size only by gaining or losing a single free component.

For hard-sphere crystallization, in particular, CNT translates as follows. The fluid becomes thermodynamically metastable with respect to the stable solid phase by overcompressing it beyond the fluid-crystal coexistence pressure. Assuming that the nucleus is not strained and occupies a well-defined volume V_s with area A and, when working isothermally in the grand-canonical ensemble with grand potentials $\Omega_\alpha(T, V) = -P_\alpha V$, where $\alpha = f, s$ for the fluid and solid phases, respectively, the presence of a nucleus results in a change of grand potential

$$\Delta\Omega = \Omega_f(V_f) + \Omega_s(V_s) + \bar{\gamma}A - \Omega_f(V) = -\Delta P V_s + \bar{\gamma}A, \quad (38)$$

with $V_s + V_f = V$ and $\Delta P = P_s - P_f$. The penalty for bringing two systems into contact is governed by the interfacial free energy γ discussed in Sec. VIII.B. While γ depends on the interface's crystal orientation and lattice spacing, here we employ a scalar effective $\bar{\gamma}$, which amounts to assuming that the stochastic nucleus dynamics averages over orientation-dependent features. Consequently, we consider spherical droplets with volume $V_s = (4\pi/3)R^3$ and area $A = 4\pi R^2$, thus leaving the radius R as the sole order parameter. The thermodynamic driving force behind nucleation is then the pressure difference $\Delta P = P_s - P_f > 0$ between the pressure P_s inside the nucleus compared to the pressure P_f of the surrounding metastable fluid.

For the nucleus to grow into the equilibrium phase, it has to overcome a nucleation free-energy barrier at the critical radius R^*, as determined through $\partial\Delta\Omega/\partial R|_{R^*} = 0$. We then find the well-known Laplace equation $\Delta P = 2\bar{\gamma}^*/R^*$ provided that $\partial\gamma(R)/\partial R|_{R^*} = 0$, which defines the surface of tension $\bar{\gamma}^* = \bar{\gamma}(R^*)$. Eliminating the critical radius R^* yields the barrier height

$$\Delta\Omega^* = \frac{16\pi(\bar{\gamma}^*)^3}{3(\Delta P)^2} = \frac{1}{2}\Delta P V_s^*. \quad (39)$$

The capillary approximation substitutes for $\bar{\gamma}^*$ the interfacial free energy γ of an infinite planar interface (often taken to be under bulk fluid-crystal coexistence conditions) averaged over all orientations.

In practice, computer simulations are performed at constant volume or constant fluid pressure counting the number of solid particles n in the nucleus. We can relate the aforementioned framework to these simulations through the isothermal Gibbs-Duhem equation

$$\frac{\partial\mu_s}{\partial p} = \frac{1}{\rho_s} = \frac{V_s}{n}, \quad (40)$$

with μ_s the chemical potential of the solid. Assuming the solid density to be independent of pressure (i.e., an incompressible solid), integration of both sides gives

$$\Delta\mu = \mu_s(P_s) - \mu_s(P_f) = \frac{V_s}{n}\Delta P, \quad (41)$$

and hence the nucleation barrier $\Delta G^* = (1/2)\Delta\mu n^*$, with n^* the number of solid particles in the critical nucleus. Using the

fact that the chemical potential $\mu_s(P_s) = \mu_f(P_f)$ is uniform, $\Delta\mu = \mu_f(P_f) - \mu_s(P_f) > 0$ compares the chemical potentials of the fluid and solid at the same pressure P_f. Note that in reality the presence of a curved fluid-crystal interface leads to strain inside the crystal nucleus (Mullins, 1984). As a result, Montero de Hijes *et al.* (2020) showed that the mechanical pressure inside hard-sphere crystal nuclei can in fact be lower than that of the surrounding fluid and argued that ΔP in the Laplace equation should be interpreted as the pressure difference between the two bulk phases at equal chemical potential μ_f, as we did here.

Figure 46(d) depicts free-energy barriers as a function of the nucleus size n, which were obtained from numerical simulations of a hard-sphere fluid at different supersaturated pressures (or, equivalently, metastable fluid volume fractions ϕ) by Auer and Frenkel (2001a). Typical snapshots of the critical nucleus from numerical simulation results are shown in Figs. 46(a)–46(c).

As the nucleation barrier ΔG^* increases, spontaneous fluctuations that might give rise to a cluster of a size n^* grow rarer. These rare events are activated processes for which the
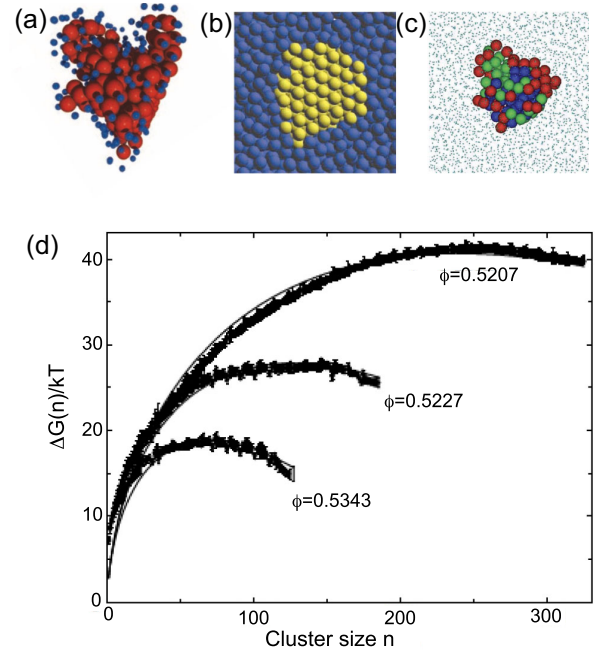

FIG. 46. Nuclei in metastable hard-sphere fluids: detection and free-energy measurement. (a) Nucleus detected in nearly hard spheres by confocal microscopy. The red particles are identified as crystal and blue particles having at least one crystal-like bond according to BOO parameters. The experimental detection of a critical nucleus is particularly challenging (see the text). From Gasser, 2001. (b),(c) Critical nuclei obtained from umbrella sampling simulations. (b) A critical crystal nucleus embedded in a metastable hard-sphere fluid at $\phi = 0.5207$. From Auer and Frenkel, 2004a. (c) Critical cluster in a metastable fluid (smaller particles) at $\phi = 0.5355$. Different colors are used for different criteria to detect crystalline particles. From Filion *et al.*, 2010. (d) Free-energy barriers (symbols) as a function of the largest crystalline cluster size n from umbrella sampling simulations at different ϕ. The solid lines are fits to the CNT functional form. From Auer and Frenkel, 2004a.

average waiting time between events is orders of magnitude longer than the time needed for the event itself to take place. Rare events are therefore intrinsically difficult to investigate. The most valuable observable to study nucleation, accessible both experimentally and numerically, is the nucleation rate J, i.e., the number of independent critical nuclei that give rise to crystal formation formed per unit time and volume. In the rare-event regime (Turnbull and Fisher, 1949), the CNT steady-state nucleation rate can be estimated from the product of two terms: the probability of forming the critical nucleus $\exp(-\beta\Delta G^*)$ and the kinetic prefactor κ, which describes the frequency at which the Gibbs free-energy barrier is crossed. By accounting for the number of critical nuclei whose size fluctuates at the top of the free-energy barrier, we obtain (Kelton, 1991)

$$J = \kappa e^{-\beta\Delta G^*} = \left(\rho_{\text{fluid}}\frac{24 D_L n^{*2/3}}{\lambda^2}Z_{\text{corr}}\right)e^{-\beta\Delta G^*}, \quad (42)$$

where κ expresses the attempt frequency of attaching or detaching a particle from the critical nucleus (or jump frequency) per unit volume and depends on (i) the metastable fluid density ρ_{fluid}, (ii) the long-time diffusivity D_L and jump distance λ, $6D_L/\lambda^2$, and (iii) the number of available attachment sites on a spherical critical nucleus of a size n^*, $4(n^*)^{2/3}$. The Zeldovich correction factor Z_{corr} accounts for the concentration of critical nuclei not truly being an equilibrium concentration during the steady-state nucleation process (Zeldovich, 1942).

As one can deduce from Eq. (42), the larger the driving force $\Delta\mu$ for nucleation to occur, the lower the free-energy barrier height ΔG^*, the smaller the critical nucleus size n^*,

and the higher the nucleation rate J. Figure 47 reports several nucleation rates J as a function of ϕ taken from both experiments and numerical simulations. As shown in Fig. 47, while the experimental and numerical nucleation rates agree at high ϕ (or large $\Delta\mu$), marked discrepancies are observed when $\phi \lesssim 0.525$. The possible origins of this discrepancy have been extensively discussed in the literature and are here reviewed in Sec. XIII.D. Before doing so, however, we first revisit the experimental context for these measurements.

B. Early nucleation experiments

Light-scattering techniques have long been a mainstay of nucleation rate measurements in colloidal suspensions (Schätzel and Ackerson, 1992, 1993; Harland *et al.*, 1995); see Sec. IV.A. The approach, which tracks the time evolution of the static structure factor of the crystallizing suspension $S(k, t)$, detects contributions from both the crystal $S(k)_{\text{xtal}}$ and the fluid $S(k)_{\text{fluid}}$,

$$S(k, t) = X(t)S_{\text{xtal}}(k) + [1 - X(t)]S_{\text{fluid}}(k), \quad (43)$$

where $X(t)$ is the crystalline fraction. Given that the small size of the crystallites results in broadening of the signal, the average linear size can be estimated according to

$$L_{\text{nucl}}(t) = \frac{2\pi K}{w_q(t)}, \quad (44)$$

where $w_q(t)$ is the width of the peak at half maximum and K is the Scherrer constant. [For a cubic crystal, $K = 1.155$
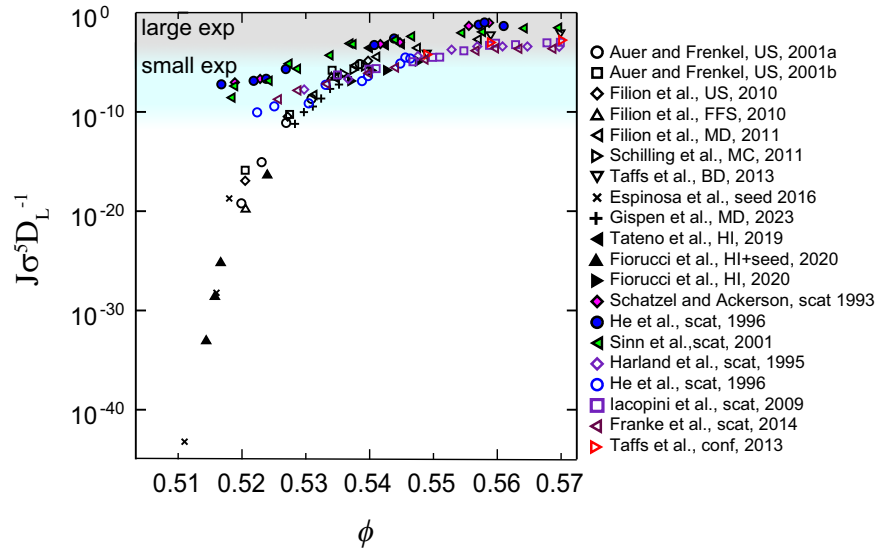

FIG. 47. Reduced nucleation rates $J\sigma^5/D_L$ for hard spheres as a function of the supersaturated fluid volume fraction ϕ comparing experiments (colored symbols) with simulations (black symbols). Simulations are further divided into simulations with (full triangles) and without (open symbols) hydrodynamic interactions. Experiments are approximately divided into nearly density matched (open symbols) and not density matched (full symbols). The method used in each case is umbrella sampling (US), forward-flux sampling (FFS), molecular dynamics (MD), Monte Carlo (MC), seeding (seed), Brownian dynamics (BD), and hydrodynamic interactions (HI) for the simulations, light scattering (scat) and confocal microscopy (conf) for the experiments. The fluid volume fractions are taken as those quoted in the original papers. Gray shading pertains to the dynamical regime accessible to experiments with relatively large colloids; see Sec. IV.C. The regime accessible to experiments using smaller colloids is shaded blue (pale gray).

(Langford and Wilson, 1978).] The number density of average-sized crystals is therefore

$$n(t) = \frac{X(t)}{L_{\mathrm{nucl}}^3(t)}. \tag{45}$$

Harland *et al.* (1995) carried out experiments before density matching of colloids was widely used, using particles with $\sigma = 800$ nm. By determining the number density of colloidal crystals as a function of time $n(t)$, a nucleation rate could then be extracted; see Fig. 47. Later experiments performed in the same lab (Harland and van Megen, 1997) with smaller particles ($\sigma = 400$ nm) showed similar trends. The physical interpretation of the results, however, was not altogether robust. On the one hand, the results successfully agreed with classical nucleation theory in that they could be fitted by Eq. (42) (using the theoretical equations of state of the fluid and crystal to determine $\Delta\mu$) to extract a reasonable value of the fluid-crystal interfacial free energy $\bar\gamma$. On the other hand, compared to the earlier results of Schätzel and Ackerson (1992, 1993), the adimensional nucleation rate $J\sigma^5/D_L$ seemed to depend on particle size, with larger particles nucleating faster than smaller ones (He *et al.*, 1996), which it should not.

These early experiments sought to probe the physics of nucleation using colloidal systems as test beds, given the experimentally tractable timescales and length scales then at hand. While at low supersaturation most of the CNT assumptions appear to be reasonable, beyond the rare-event (or activated) regime the situation is more complex. In particular, the fluctuations in crystallizing systems at $\phi \gtrsim 0.54$ appear to reach a kinetic spinodal limit (Schätzel and Ackerson, 1992, 1993) at which the nucleation barrier for the fluid to crystallize becomes so small that nucleation is no longer rare but takes place on the same timescale as that of the structural relaxation of the fluid; see Sec. XIII.I.

C. Light-scattering versus real-space experiments

Light-scattering measurements remain the state of the art in the weak supersaturation (or rare-event nucleation) regime (Palberg, 2014). The technique is perfectly suited for the relatively small colloids, with $\sigma = 200$–500 nm, then used to keep the long timescale associated with nucleation experimentally tractable; see Secs. IV.C and VII.D. It provides, however, only limited microscopic information about the structure of the nucleus.

Particle-resolved studies allow measurements of the critical nucleus shape and size distribution, along with the detailed structure and dynamics of the surrounding colloidal fluid shown in Fig. 46(a) (Elliot, Haddon, and Poon, 2001; Gasser, 2001, 2009; Ivlev *et al.*, 2012; Taffs *et al.*, 2013; Wood *et al.*, 2018). It can therefore be used to test some of the CNT assumptions, such as whether the solid phase has a density close to its bulk value and whether crystalline defects play a role during the formation of the critical nucleus. However, real-space information comes at a high experimental price. As reflected in Fig. 47, conventional real-space analyses require larger colloids of 2 to 3 μm (Ivlev *et al.*, 2012), which diffuse much slower than those commonly used in light-scattering

experiments; see Sec. IV.C. Even at fairly high supersaturation ($\phi \approx 0.53$), crystallization can take days (Taffs *et al.*, 2013). In addition, the analysis is laborious, so obtaining a statistically meaningful number of nuclei of different sizes and shapes is challenging.

D. The nucleation rate discrepancy

As mentioned in Sec. XIII.B, early nucleation experiments followed the expected physical trend, namely, a low nucleation rate at weak supersaturation that increases with volume fraction and eventually decreases with increasing viscosity (upon approaching the glass transition; see Sec. XII) (Palberg, 1999). Note that this decrease is not visible in Fig. 47, due to the rescaling of the nucleation rate with the diffusion constant D_L, which decreases sharply with increasing volume fraction. However, upon comparing experimental rates (Palberg, 2014) with numerical predictions obtained using rare-event sampling methods developed since the mid-1990s, marked discrepancies have been observed.

The computations of Auer and Frenkel (2001a), in particular, uncovered a pronounced difference in the slope of the nucleation rate curve; see Fig. 47. Since then, different numerical approaches have been used to assess these predictions. From the middle of the fluid-crystal coexistence region and as long as the nucleation barrier is at least a few times larger than the thermal energy, i.e., $0.52 \lesssim \phi \lesssim 0.54$, biasing methods such as seeding (Espinosa *et al.*, 2016), umbrella sampling (Auer and Frenkel, 2001a; Filion *et al.*, 2010; Filion, Ni *et al.*, 2011), and forward-flux sampling (Filion *et al.*, 2010; Richard and Speck, 2018a, 2018b) can be used. For $\phi \gtrsim 0.528$, nucleation is even accessible through direct numerical simulations (Kawasaki and Tanaka, 2010a; Filion, Ni *et al.*, 2011; Gispen and Dijkstra, 2023) and first-passage time methods (Richard and Speck, 2018a). In the density regimes where these methods overlap they provide consistent estimates, thus confirming a 15 order of magnitude increase of the nucleation rate in going from $\phi = 0.52$ to 0.55. By contrast, experiments at best display a variation of 5 orders of magnitude of the nucleation rate over the same volume fraction range; see Fig. 47.

This staggering gap between simulations and experiments of well over 10 orders of magnitude has been called "the second-worst discrepancy in physics" (Russo *et al.*, 2013), with the first being the 120 orders of magnitude discrepancy between the value of the cosmological constant and the quantum energy of the vacuum. Accounting for this mismatch largely remains an open problem, but given the strong consistency between different simulation approaches it is certainly tempting to conclude that some experimental effects are not properly taken into consideration. Potential explanations are plentiful, from experimental details that are not accounted for in simulations to experimental errors in determining the true homogeneous nucleation rate or volume fraction. Claims of a more fundamental lack of understanding of the nucleation process are dubious, as the discrepancy is more pronounced in the low supersaturation regime where the CNT description is most justified. Notably, while the discrepancy in the nucleation rate is significant, that in the volume fraction is rather less. Indeed, a shift of $\delta\phi = 0.01$,

which is akin to the uncertainty on ϕ (see Sec. III.E), would largely alleviate the discrepancy. What it would not explain is why the error in volume fraction is apparently consistently underestimated in experiments.

Here we first review efforts made to address the discrepancy between simulations and experiments before returning to the accuracy of the phase boundaries. For the former, we consider the dependence of the nucleation rate on polydispersity (Auer and Frenkel, 2001b; Pusey *et al.*, 2009), electrostatic interactions (Auer and Frenkel, 2002), hydrodynamics (Radu and Schilling, 2014; Tateno *et al.*, 2019; Fiorucci *et al.*, 2020), sedimentation (Russo *et al.*, 2013; Ketzetzi, Russo, and Bonn, 2018; Wood *et al.*, 2018), and external walls (Espinosa *et al.*, 2019).

Polydispersity. Experimental colloidal systems inevitably exhibit size polydispersity s (see Secs. VII and IX), which can considerably alter the crystallization transition (Fasolo and Sollich, 2003). For moderate polydispersity ($s \lesssim 5\%$ to 6%), even though diffusivity is only negligibly affected (Zaccarelli *et al.*, 2009), the coexistence curves shift to significantly higher ϕ (Sollich and Wilding, 2010). The impact of this shift on nucleation rates was considered in the early paper of Auer and Frenkel (2001b). For $s = 5\%$, the shift of the nucleation curve makes ϕ about 0.015 higher than that for the equivalent nucleation rate in the monodisperse case. However, this shift essentially disappears when the volume fraction is rescaled based on the freezing density of the system (Filion *et al.*, 2010). Note that polydispersity does not alter the slope of the nucleation rate curve. In other words, the rate curves for different s are roughly parallel. Although the shape of the particle size distribution (and not only s) affects both the nucleation and growth kinetics, as shown experimentally by Schöpe, Bryant, and van Megen (2006a, 2007), colloid syntheses that deliver significantly different polydispersity distributions (due to secondary nucleation) give relatively similar experimental nucleation rates (Fig. 47). It therefore seems reasonable to conclude that polydispersity does not contribute significantly to the nucleation rate discrepancy.

Electrostatic charge. The possibility of residual charges on the colloids was also considered early on (Auer and Frenkel, 2002) and modeled through a hard-core Yukawa or Debye-Hückel potential as in Eq. (5). Because systems of interest typically use nonaqueous solvents with low dielectric constants (see Sec. III.C), the degree of electrostatic charging is tiny (especially compared to aqueous systems), and hence linear Poisson-Boltzmann theory should hold (Royall *et al.*, 2006). Some work where no salt was added may exhibit density-dependent interactions due to counterion condensation as a function of volume fraction (Royall *et al.*, 2006). The effective charge drops with increasing ϕ, thus affecting the mapping to an effective hard-sphere volume fraction in a direction that is qualitatively similar to the observed discrepancy. Evidence for some deviation from centrosymmetric interactions between the colloids implicit in linear Poisson-Boltzmann theory in these nonaqueous systems has been detected in crystals (Reinke *et al.*, 2007). Since such effects are highly parameter specific (Royall *et al.*, 2006), it seems rather unlikely that all experiments in this regime, which have used different conditions (solvent dielectric constant, ionic strength, and chemical composition of colloids and solvent),

would exhibit a quantitatively consistent behavior. In any case, these experiments concern confocal microscopy studies using larger colloids in a density-matched solvent. As Fig. 47 shows, it is the experiments that used smaller colloids that are featured in the regime of marked discrepancy (the blue shaded region in Fig. 47). Our analysis in Sec. III.C and the dashed blue line in Fig. 5(a), in particular, suggest that interactions in these systems are close to hard-sphere-like and exhibit little density dependence compared to those of Royall *et al.* (2006).

The dominant contribution is therefore expected to be the softening of the interaction potential due to residual charges. Using the hard-core Yukawa or Debye-Hückel model, the effects of residual charges on the nucleation rate were considered by Auer and Frenkel (2002). They showed that, compared to hard spheres, introducing a small charge increases the nucleation rate via two mechanisms: (i) at constant density because the supersaturation increases (given the shift in fluid-crystal phase boundaries to lower packing fractions) and (ii) at constant supersaturation (i.e., the chemical potential difference $\mu - \mu_{\text{coex}}$) because of a considerable reduction of the fluid-crystal interfacial free energy. However, note that Auer and Frenkel (2002) did not consider the weak, longer-ranged electrostatic interactions pertinent to the studies using smaller PMMA particles in low dielectric constant solvents [Sec. III.C and Fig. 5(a), blue dashed line].

A recent numerical study (de Jager and Filion, 2022) showed that for highly screened electrostatic interactions the phase behavior depends nearly completely on the screening length, with the nucleation barrier increasing with screening length at fixed supersaturation [i.e., measuring the barriers at constant $\phi/\phi_f(\kappa\sigma)$, where $\kappa\sigma$ is the inverse screening length and ϕ_f is the freezing volume fraction]. This trend does not explain the nucleation rate discrepancy between simulations and experiments, as it suggests that the effect of electrostatic charge would be a slowdown in the nucleation rate with respect to hard-sphere simulations rather than a speedup, which might address the discrepancy. Moreover, as the dashed blue line in Fig. 5(a) and the discussion in Sec. III.C indicate, the smaller particles used in the experiments that reached the discrepancy regime had large Debye lengths, i.e., a different interaction than those considered here.

In short, without some new interpretation, electrostatic interactions shift but do not change the density dependence of the nucleation rate. It is therefore hard to see how the observed discrepancy between simulations and experiments could be explained through residual charges alone.

Hydrodynamics. The nucleation rate discrepancy between simulations and experiments hints at possible unexpected nucleation pathways that lead to the efficient formation of large nuclei at small supersaturation in experiments. A careful consideration of long-range hydrodynamic interactions, which can alter the aggregation kinetics of colloidal particles, is therefore in order.

Properly accounting for hydrodynamics in numerical simulations requires specialized techniques that couple the dynamics of hard spheres with either a continuum or a coarse-grained representation of the surrounding fluid solvent; see Sec. V.D. The high numerical cost of these methods considerably shortens the observable timescales compared to

standard BD (or similar) simulations, thus restricting the consideration of nucleation for an even smaller range of fairly high volume fractions. Because this regime is typically where nucleation rates from simulations and experiments agree, these numerical efforts offer only limited physical insight.

Several groups have nevertheless tried to quantify the relevance of hydrodynamics. Radu and Schilling (2014) first considered the effect of hydrodynamics in simulations via the *stochastic rotational dynamics* approach. Surprisingly, an increase of the nucleation rate with increasing solvent viscosity at high volume fractions was then observed. However, these results are caused by the way the hydrodynamic interactions were implemented (Fiorucci *et al.*, 2020). In particular, their implementation ignored the excluded-volume interactions and the mass difference between the solvent and the colloidal particles, both of which impact the resulting hydrodynamic interactions. To examine the effect of hydrodynamics on hard-sphere nucleation, Fiorucci *et al.* (2020) computed nucleation rates at high volume fractions using brute-force MD simulations with hydrodynamics implemented through stochastic rotational dynamics. The results, however, agreed well with studies that neglect hydrodynamic interactions.

Seeding has been considered to evaluate the importance of hydrodynamics on crystal nucleation at low volume fractions. Tateno *et al.* (2019) directly solved the Navier-Stokes equations with the fluid particle dynamics method, while Fiorucci *et al.* (2020) used stochastic rotational dynamics. Both approaches demonstrated that mass transport was considerably slowed down by hydrodynamic lubrication effects and that, if the nucleation rate were rescaled by the long-time diffusion coefficient, it would be practically unaffected by hydrodynamics; see the solid color symbols in Fig. 47. Existing results therefore suggest that hydrodynamics is not likely to be the main origin for the observed discrepancy.

Sedimentation. Another effect that is frequently neglected in simulations is gravity. As introduced in Sec. XI, the strength of gravity is measured by the gravitational Péclet number Pe_g [Eq. (34)]. The nucleation rates reported in Fig. 47 can be grouped according to the sedimentation strength (Russo *et al.*, 2013; Palberg, 2014; Wood *et al.*, 2018): those that pertain to weak ($Pe_g \lesssim 0.01$) and strong sedimentation ($0.1 \lesssim Pe_g \lesssim 1$) differ, with the latter nucleating much faster. Schätzel and Ackerson (1993) and Sinn *et al.* (2001), who studied suspensions of colloidal particles in the regime of relatively strong sedimentation, with $10^{-1} \lesssim Pe_g \lesssim 1$, both obtained comparably high nucleation rates. By contrast, work that considered the case of weaker sedimentation colloidal suspensions with $\xi/\sigma \sim 100$ and $Pe_g \sim 10^{-2}$ (either by employing small particles or using swelling microgels) reported nucleation rates that cluster at lower values and are therefore a few decades closer to the simulation results (Harland and van Megen, 1997; Iacopini, Palberg, and Schöpe, 2009; Franke, Lederer, and Schöpe, 2011).

An assessment of the relative importance of the sedimentation timescale with respect to that of crystallization was carried out with BD simulations (Russo *et al.*, 2013). Relative to experiments, Russo *et al.* considered small system sizes and timescales (compared to experiments) for $Pe_g \lesssim 1$ and found that the nucleation events are the same as in a gravity-free environment for $\phi \gtrsim 0.525$, whereas for $\phi \lesssim 0.525$ sedimentation occurs on shorter timescales than nucleation. Significant deviations therefore have to be expected with respect to the zero gravity case. While gravitational effects can induce density fluctuations that significantly enhance the nucleation rate, the precise mechanism by which this occurs is still unknown. In addition, for experimental system sizes (where the sample height can be $\sim 10^4 \sigma$ or $10^5 \sigma$, compared to $\sim 10^2 \sigma$ in simulation), nucleation typically proceeds faster than sedimentation (Paulin and Ackerson, 1990); see Sec. VII.A. One possibility could be that hydrodynamic interactions affect the structure of hard-sphere systems undergoing sedimentation, as has been shown in the case of strong confinement (Wysocki *et al.*, 2009); see Sec. XI.A. It is therefore tempting to imagine that the higher-order fluid structure might somehow be affected by the hydrodynamic interactions associated with out-of-equilibrium sedimentation, thus influencing the nucleation rate.

Wood *et al.* (2018) used particle-resolved experiments to investigate the population of fivefold symmetric structures that, as originally postulated by Frank (1952), suppress nucleation by increasing the interfacial free energy between the crystal and the fluid (Taffs and Royall, 2016). Wood *et al.* measured the population of fivefold symmetric structures in sedimenting hard-sphere systems with $Pe_g \approx 1$ and found that the population of such structures drops by a factor of 2 with respect to the nonsedimenting density-matched case (Fig. 48). However, simulations that considered hydrodynamic interactions showed insignificant differences in the quantity of clusters exhibiting fivefold symmetry in hard-sphere fluids when exposed to a gravitational field with $Pe_g \leq 2$ (Fiorucci *et al.*, 2020). It is possible that this difference may be explained by the way the boundary conditions are implemented (periodic in the case of the simulations, and hard walls for the experiments). Yet, given that only one direct
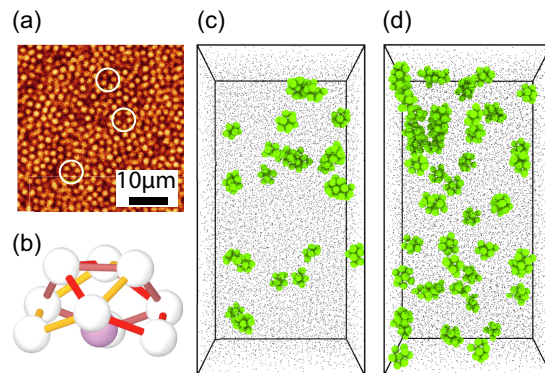

FIG. 48. (a) A single slice through a 3D confocal image stack. Three five-membered rings are circled. (b) Rendering of the defective icosahedron (10B). Five-membered rings are indicated with yellow, red, and dark red bonds. Visualization of the effect of sedimentation upon the structure of the hard-sphere fluid at an average $\phi = 0.45$ for (c) a sedimenting system ($Pe_g \simeq 1.5$), and (d) a density-matched system. Experimental data are rendered after all particle centers have been located with particle tracking. Particles in defective icosahedra are shown in green (to scale), while particles not in defective icosahedra are rendered as gray points. From Wood *et al.*, 2018.

comparison of higher-order structure in sedimenting hard spheres shows a significant discrepancy between simulations and experiments, the effect of sedimentation surely merits further investigation. After all, crystal nuclei themselves originate from higher-order fluid structures.

Wood *et al.* (2018) then carried out computer simulations to mimic the impact of sedimentation. Using umbrella sampling, they negatively biased the population of fivefold symmetric structures so as to match these experimental observations. A drop in fivefold symmetry was then found to reduce the nucleation barrier considerably (by $11k_BT$ at $\phi = 0.52$, corresponding to a nucleation rate increase of approximately 5 orders of magnitude), but still insufficiently to account for the discrepancy; see Fig. 47. Furthermore, Wood *et al.* (2018) used $\mathrm{Pe}_g = 1.5$, which is at the top end of those experiments that sediment strongly. Further investigation is required to determine whether other aspects of the sedimentation process, such as the impact of shear flows and other hydrodynamic effects that couple to gravity, could explain the discrepancy.

Nonhomogeneous nucleation rates. Some have also challenged the assumption that the nucleation rate measured in experiments is that of a homogeneous nucleation process (Gasser, 2001; Espinosa *et al.*, 2019; Wöhler and Schilling, 2022), pointing to the fact that other nucleation and growth channels could be responsible for the discrepancy. For one thing, colloidal fluids are unavoidably in contact with the walls of the sample cell, which can be a source of nucleation sites. Heterogeneous nucleation is presented in a more general context in Sec. XIII.F, but for now we consider its putative contribution to the discrepancy.

To elucidate the effect of different possible surfaces that could lead to heterogeneous nucleation, Espinosa *et al.* (2019) numerically studied the competition between homogeneous and heterogeneous crystallization as a function of wall type, fluid density, and system size. For flat walls and surfaces randomly coated with nonoverlapping spheres of a diameter 3 times larger than those in the fluid [as used in some experiments (Ziese, Maret, and Gasser, 2013)], heterogeneous nucleation overwhelmed homogeneous nucleation for $\phi < 0.535$. By contrast, when the coating was done with nonoverlapping spheres with the same diameter as those of the fluid [as done in other experiments (Taffs *et al.*, 2013)], nucleation was more likely to occur in the bulk given how suppressed heterogeneous nucleation was. However, to our knowledge the older experiments, which used light scattering (Schätzel and Ackerson, 1992, 1993; Harland *et al.*, 1995; He *et al.*, 1996; Harland and van Megen, 1997) to obtain nucleation rates in the discrepancy regime, did not coat surfaces. ["Sintering" of polydisperse particles onto the sample cell walls was typically done in more recent, real-space experiments (Gasser, 2001; Taffs *et al.*, 2013; Ziese, Maret, and Gasser, 2013).] In any case, in the earlier light-scattering experiments, the data were then taken in the center of the sample cell, far from the wall, and it is unlikely that macroscopic iridescent crystals could have migrated from the walls to the center of the cell without those carrying out the experiments noticing. Furthermore, how such a large crystal of hard spheres could sustain the gravitational stresses in these systems, which were not density matched (see Sec. XIII.D), is entirely unclear. Any heterogeneous nucleation effects would

then likely arise from impurities or from colloid clusters that were not completely dispersed in the sample preparation. Although the resulting nucleation rate estimates that account for crystallite formation both in the bulk and at the walls have been argued to coincide with the experimental results, the aforementioned discussion suggests that this coincidence is likely fortuitous.

It was recently proposed that Bragg scattering signals measure polycrystalline growth from different nuclei whose size is described by the Avrami law and therefore cannot access the true homogeneous nucleation rate (Wöhler and Schilling, 2022). Correcting the rate by adding secondary nucleation events occurring at the interface of the already-formed crystals would lead to a considerable increase in the measured number of nuclei. Whether this could really address the large discrepancy indicated in Fig. 47 given the size of the individual colloids, the number of colloids in the nuclei, and the size of the region probed in the experiments remains unclear.

Despite these putative leads, a definitive understanding of the origin of the nucleation rate discrepancy between simulations and experiments remains an outstanding challenge, possibly explained by one or more of the previously described mechanisms or by effects yet to be considered. This leads us back to the question of the accuracy with which phase boundaries have been determined. Our discussions in Secs. III.E and VII.A suggest that an error of $\delta\phi = 0.01$ is reasonable. In light of this observation and the failure to find a clear-cut physical explanation, one may inquire whether there really is a discrepancy at all, given that one could largely make it disappear by shifting the experimental data by adding $\delta\phi = 0.01$ to them.

One argument that has been made is that the slope of the experimental data is different from that of the simulations. With the current (perhaps erroneous) determination of ϕ, then the statement that the slope is different need not hold. Moreover, the lowest nucleation rates measured in experiments of around $J_{\mathrm{exp}}^{\min} \sim 10^{-5}\sigma^5 D_L^{-1}$ are more than 25 orders of magnitude higher than the lowest rates determined in simulations (Fig. 47). Thus, while it may be possible to reconcile the rates from simulations and experiments, what is clear is that massively slower rates have been determined in simulations.

Experimental measurements at lower nucleation rates are desirable and it would seem that using smaller colloids or nanoparticles could be a way forward here; see Sec. IV.C. It may still be possible to achieve some reduction in size using light scattering, but perhaps neutron or x-ray scattering, in particular, the recent developments noted in Sec. XII.C (Wochner *et al.*, 2009; Lehmkühler *et al.*, 2020; Liu *et al.*, 2022), could be approaches of choice in this case. Before leaving this topic, we emphasize one remaining mystery: While the accuracy of the phase boundary measurement could account for the magnitude of the change in volume fraction required to address the discrepancy, why do experiments systematically underestimate the effective volume fraction?

E. Homogeneous nucleation in binary hard-sphere mixtures

In principle, when dealing with a multicomponent suspension such as a binary mixture, CNT cannot be

straightforwardly generalized. [See Ni *et al.* (2011) and references therein, where several attempts are discussed.] When crystal nucleation takes place, fractionation indeed comes into play. The composition of the metastable fluid phase and that of the nucleating crystal phase then differ from the compositions of the coexisting bulk phases, which has repercussions on how to apply the capillary approximation and how to define the interfacial free energy (Oxtoby and Kashchiev, 1994; Laaksonen, McGraw, and Vehkamaki, 1999; Ni *et al.*, 2011).

Ni *et al.* (2011) numerically studied crystal nucleation in varying binary mixtures of hard spheres. They investigated the effect of the order parameter on the cluster composition for nucleation of a substitutional solid solution of identical hard spheres but tagged with different colors and concluded that (i) the composition of noncritical clusters depends on the order parameter choice but can nevertheless be explained by the predictions from CNT, and that (ii) the properties of the critical cluster do not depend on the choice of order parameter. In addition, they studied the nucleation of an interstitial solid solution in a binary hard-sphere mixture with a size ratio $q = 0.3$. For a suitable choice of order parameter, it was found that the composition of noncritical clusters is determined by the chemical equilibrium condition of the small spheres in the crystal nucleus and the fluid phase. One might expect to observe such a chemical equilibrium of the small species in the case of a highly asymmetric binary hard-sphere mixture, where the small spheres can diffuse throughout the entire system, including the nucleated crystal. For less asymmetric binary hard-sphere mixtures, in which the small spheres cannot diffuse freely within the solid cluster, chemical equilibrium of the smaller species is harder to maintain, especially when the nucleated crystal phase has long-range crystalline order for both species, as in the case of a super-lattice structure (Filion, Hermes *et al.*, 2011; Rios de Anda *et al.*, 2017). It would be interesting to investigate what other mechanisms the system resorts to in order to maintain equal chemical potentials of the two species between the fluid and the crystal nucleus.

An enticing application of binary hard-sphere mixtures is their putative role in synthesizing colloidal crystals with diamond and pyrochlore structures, which are characterized by wide photonic band gaps at low refractive index contrasts (Hynninen *et al.*, 2007). Direct assembly is not deemed possible, but given a self-assembled binary mixture of colloidal spheres in a close-packed $MgCu_2$ Laves phase, one could selectively remove one of the sublattices to obtain these low-coordinated crystalline structures. Laves phases are proven to be thermodynamically stable in binary hard-sphere systems with $q \approx 0.8$, and clusters of Laves phases have been reported to form spontaneously in simulations (Bommineni, Klement, and Engel, 2020; Marín-Aguilar *et al.*, 2020). In addition, it was shown using the seeding approach (see Fig. 49) that the barrier heights coincide for all three Laves phases, which is to be expected given that the bulk free-energy differences are small (Dasgupta, Coli, and Dijkstra, 2020). Softened spheres have further been shown to enhance crystallization of Laves phases by suppressing the degree of fivefold symmetry in the binary fluid phase (Dasgupta, Coli, and Dijkstra, 2020). These structures have nevertheless been
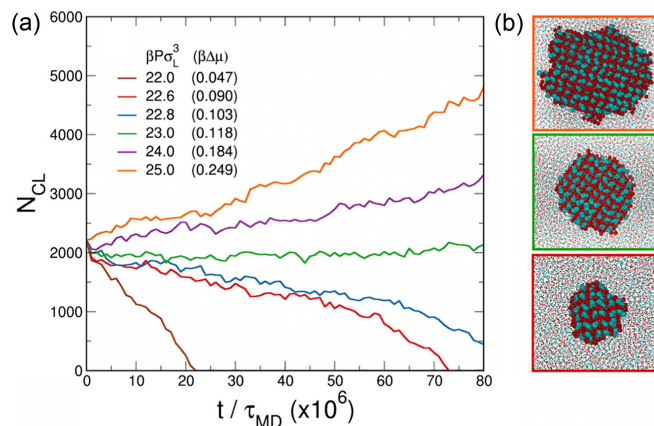

FIG. 49. (a) Largest cluster size N_{CL} with Laves phase symmetry as a function of time t using the seeding approach in MD simulations of a binary mixture of nearly hard spheres in the NPT ensemble at a composition $x_L = N_L/(N_S + N_L) = 1/3$ and a diameter ratio $q = 0.78$ for varying pressures. The initial seed size is 2205 particles of the $MgZn_2$ Laves phase. (b) Snapshots showing the melting of the seed at pressure $\beta P \sigma_L^3 = 22.6$ (bottom box), growth of the seed at $\beta P \sigma_L^3 = 25$ (top box), and a stable seed at the critical pressure $\beta P \sigma_L^3 = 23$ (middle box). The large (small) spheres are colored blue (pale gray) [red (darker grey)]. The fluid particles (particles with a disordered neighborhood) are reduced in size for clarity. From Dasgupta, Coli, and Dijkstra, 2020.

observed to spontaneously crystallize only in hard-sphere experiments with sub-micron-sized colloids (Schaertl *et al.*, 2018). We posit that the slow assembly dynamics may be the culprit, which could be addressed using smaller colloids, or even nanoparticles.

For more asymmetric hard-sphere mixtures, the AB_{13} crystal structure, which is analogous to the $NaZn_{13}$ phase, was predicted to be stable 30 years ago (Eldridge, Madden, and Frenkel, 1993b). The kinetic pathway for homogeneous nucleation of the icosahedral AB_{13} crystal from a binary fluid phase of nearly hard spheres has further been numerically studied by Coli and Dijkstra (2021), who made use of an artificial neural network to identify the AB_{13} phase from the binary fluid phase and the competing fcc crystal phase. Note that AB_{13} crystal nucleation proceeds via a coassembly process with large spheres and icosahedral small-sphere clusters simultaneously attaching to the nucleus. Even though the binary fluid phase is highly structured and exhibits local regions of high BOO parameter,[16] the kinetic pathway follows CNT.

F. Heterogeneous and seeded nucleation

Homogeneous nucleation of a metastable suspension of hard spheres has been extensively studied using numerical methods. Because such nucleation events are rare, and because the critical nucleus could form anywhere in the

---

[16]Three-dimensional BOO parameters detect regions of local crystal-like order. They generalize the 2D BOO introduced in Sec. VII to quantify hexagonal ordering.

system and at any time, experimental detection is particularly challenging. Heterogeneous nucleation, by contrast, happens whenever the phase transition is assisted by inhomogeneities, such as walls [either flat (Cacciuto and Frenkel, 2005; Wette *et al.*, 2009) or structured (Heni and Löwen, 2000; van Teeffelen, Likos, and Lowen, 2008; Xu, Sun, and An, 2010; Hermes *et al.*, 2011)] and impurities (Cacciuto, Auer, and Frenkel, 2004; de Villeneuve, Dullens *et al.*, 2005; de Villeneuve, Verboekend *et al.*, 2005; Sandomirski *et al.*, 2011). Nuclei of the stable phase then form at the surface of these exogenous bodies, thus facilitating their detection. As a result, for hard-sphere colloids the process has been studied extensively by means of both simulations and experiments.

In general, heterogeneous crystallization is controlled by the size, structure, and composition of the seed as well as its inhomogeneities. For simplicity, however, standard seed models consider mostly flat and curved walls. Flat, unstructured walls, in particular, maximize the nucleation and crystal growth rates (Kose and Hachisu, 1976; Espinosa *et al.*, 2019). Because flat walls do not strain the growing crystal, they also minimize the concentration of defects within the structure. Figure 50 shows two snapshots of crystal domains formed after sedimentation on a flat wall, for both (a) experiments with confocal microscopy and (b) BD simulations (Sandomirski *et al.*, 2011). For heterogeneous nucleation on a flat wall, the free-energy cost of forming a critical nucleus can be orders of magnitude smaller than for homogeneous nucleation. Auer and Frenkel (2003) showed that at $\beta P \sigma^3 = 12.1$ ($\phi \simeq 0.497$) the free-energy barrier to nucleation goes from $\Delta G_{\text{hom}}^* = 1334 k_B T$ in the homogeneous case to $\Delta G_{\text{het}}^* = 17 k_B T$ for heterogeneous nucleation of a crystal growing with the (111) plane parallel to the flat wall, thus increasing the nucleation rate by roughly 570 orders of
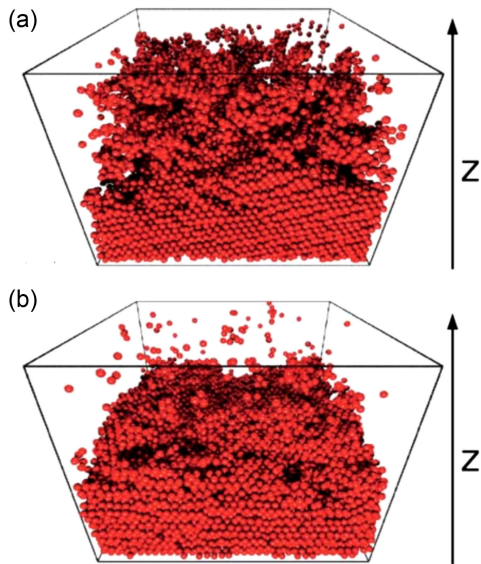
FIG. 50. Heterogeneous crystallization induced by a flat wall. Crystal domains found after sedimentation on a flat substrate are obtained from (a) confocal microscopy and (b) BD simulations. For both snapshots, the overall packing fraction is $\phi = 0.52$, the snapshots are taken after a waiting time of $t = 62\tau_B$, and only the crystalline particles are shown. From Sandomirski *et al.*, 2011.

magnitude over that of homogeneous nucleation under the same thermodynamic conditions. The reduction of the free-energy barrier is predicted from CNT to be

$$\Delta G_{\text{het}}^* = \Delta G_{\text{hom}}^* \frac{(2 + \cos\theta)(1 - \cos\theta)^2}{4}, \qquad (46)$$

where θ is the contact angle between the fluid and solid phases with the wall and is given by $\gamma_{\text{fs}} \cos\theta = \gamma_{\text{wf}} - \gamma_{\text{ws}}$, where γ is the interfacial free energy and the subscripts w, s, and f refer to the wall, solid, and fluid phases, respectively. The condition for which $\gamma_{\text{ws}} + \gamma_{\text{fs}} - \gamma_{\text{wf}} \leq 0$ corresponds to complete wetting of the crystalline surface on the wall. Using the values $\gamma_{\text{wf}} = 1.99 k_B T / \sigma^2$ (Heni and Löwen, 1999) and, for the (111) plane, $\gamma_{\text{ws}} = 1.42 k_B T / \sigma^2$ (Heni and Löwen, 1999) and $\gamma_{\text{fs}} = 0.55 k_B T / \sigma^2$ (Benjamin and Horbach, 2015), we obtain $\gamma_{\text{ws}} + \gamma_{\text{fs}} - \gamma_{\text{wf}} = -0.02 k_B T / \sigma^2$, i.e., complete wetting, as discussed in Sec. VIII. The presence of a barrier $\Delta G_{\text{het}}^* = 17 k_B T$ (Auer and Frenkel, 2003) significantly higher than the thermal energy is thus at odds with CNT predictions. These differences can be adjusted if the contribution from the wall-crystal-melt line tension (with a further correction to include its curvature dependence) (Auer and Frenkel, 2003) is taken into account, and if the value of γ_{wf} is allowed to deviate from its bulk value. Analysis of the simulation trajectories (Auer and Frenkel, 2003) showed that the crystal grows first laterally on the wall rather than extending into the bulk, indicating that heterogeneous nucleation happens close to the wetting threshold.

The effectiveness of a templated wall to induce epitaxial growth has been considered in experiments (Hoogenboom *et al.*, 2003), simulations (Cacciuto and Frenkel, 2005), and theory (Heni and Löwen, 2000). In experiments, the structure and size of the seed cluster can be controlled at will by fixing colloidal particles with laser tweezers or/and by putting a prescribed structure to the undercooled or overcompressed colloidal fluid. In the epitaxial growth of colloidal hard-sphere crystals (Hoogenboom *et al.*, 2003), a structured wall (favoring hcp crystallization) was offered as a template for the colloidal solution. Perfect hcp-crystal growth was achieved for template unit cells that are isotropically stretched compared to the bulk unit cell dimensions. By contrast, isotropically compressed templates give rise to the growth of a perfect fcc. Large mismatches, however, suppress crystallization. The computational study of Cacciuto and Frenkel (2005) showed that disorder in the template can also suppress nucleation if the displacement of the template particles from their lattice sites is comparable to that specified by the Lindemann criterion (10% of the nearest-neighbor distance), while the template retains its full effectiveness for smaller displacements.

Hermes *et al.* (2011) experimentally studied crystal nucleation while initiating the phenomenon by means of a seed structure using optical tweezers. They showed that the nucleation barrier can be lowered by introducing a 2D seed structure into the bulk of a supersaturated fluid, resulting in large crystallites like that shown in Fig. 51. Unlike Cacciuto, Auer, and Frenkel (2004), they did not find hexagonal seeds to be good nucleating agents. However, the square seed worked well, inducing nucleation at low supersaturation, although the
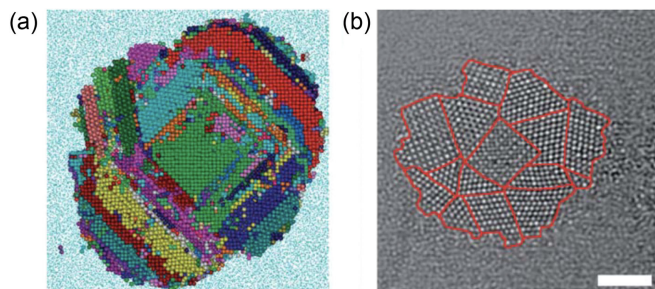
FIG. 51.   Seeding a hard-sphere crystal from a square seed in (a) simulations at $\phi = 0.51$ and (b) experiments with optical tweezers. In (a), the colors correspond to different crystal grains. Crystalline particles are drawn at their normal size, while fluid particles are drawn as dots. In (b), the scale bar is 10 μm. From Hermes *et al.*, 2011.

resulting fcc crystals had significantly more defects than crystals obtained using hexagonal seeds.

Spherical seeds are but a specific case of heterogeneous nucleation promoted by curved walls. And as shown in Fig. 52, just as the crystal growth rate increases with the radius of spherical impurities (de Villeneuve, 2005), strongly curved walls suppress nucleation by straining the growing crystal (Cacciuto, Auer, and Frenkel, 2004; de Villeneuve, 2005). Further, crystals that form on small spherical seeds have a hexagonal structure with the (111) plane bending around the surface of the seed. Seed curvature is accommodated through grain boundaries and defects, and the crystal accumulates elastic energy. These small spherical seeds then accumulate at grain boundaries of nuclei that are nucleated homogeneously in the sample as impurities (Dullens *et al.*, 2008; de Villeneuve *et al.*, 2009). As a function of the seed diameter, one therefore observes a transition from a regime where heterogeneous nucleation is suppressed compared to homogeneous nucleation to one where it dominates. Simulations suggest that the barrier for heterogeneous nucleation is lower than that for homogeneous nucleation for seeds with a radius larger than five particle diameters (Cacciuto, Auer, and Frenkel, 2004). This value is not far from the value found for a flat wall with the randomly absorbed spheres discussed earlier, i.e., 3σ (Espinosa *et al.*, 2019).

Both simulations (Cacciuto, Auer, and Frenkel, 2004) and experiments (Sandomirski *et al.*, 2014; Allahyarov *et al.*, 2015) have reported that an interesting phenomenon occurs once the elastic stress balances the interfacial energy gained through the heterogeneous nucleation on the seed. The crystal nucleus then detaches from the seed before reaching its critical size but continues to grow, eventually reaching the seed, which then acts as an impurity that hinders further growth. This process also prevents the spherical seed from acting as a crystallization catalyst (the catalyst becomes poisoned), as heterogeneous nucleation is inhibited by the detached nucleus nearby. For hard spheres, the phenomenon takes place for seeds of about 30σ (Allahyarov *et al.*, 2015), but this multistep nucleation scenario is expected to occur in all situations in which the seed induces a structural mismatch compared to the equilibrium crystal lattice. Because a perfect match is impossible to achieve, this mechanism is expected to be general and

important for the control of crystal morphology. All of these phenomena are also observed for hard spheres assembling in spherical confinement, i.e., a negative curvature or concave surface, as demonstrated by simulations and discussed in Sec. X (de Nijs *et al.*, 2015). Also in this case, heterogeneous nucleation is favored over homogeneous nucleation, and crystallization begins at the boundary of the spherical confinement, forming a polycrystalline system consisting of 20 tetrahedral fcc domains. When the inward-growing fcc domains cannot accommodate the strain induced by the curvature of the spherical confinement, the crystalline layers at the spherical boundary melt and later recrystallize, forming an anti-Mackay cluster. Cylindrical seeds have also been considered (Auer and Frenkel, 2004b; Cacciuto, Auer, and Frenkel, 2004; Sandomirski *et al.*, 2014). Qualitatively the situation is similar to what is observed with spherical seeds, although with larger nucleation rates (Cacciuto, Auer, and Frenkel, 2004). The presence of only one principal curvature direction (compared to two for spheres) indeed reduces the strain on the growing crystal.

G. Crystal growth

Following nucleation, crystallization proceeds through crystal growth, which is dynamically well separated from the formation of the initial activated process. The growth process is characterized by a crystal-fluid interface with a thickness that ranges from 8 to 16 layers, as confirmed in experiments (Dullens, Aarts, and Kegel, 2006b), simulations (Auer and Frenkel, 2003; Zykova-Timan, Horbach, and Binder, 2010), and theory (Härtel *et al.*, 2012; Oettel *et al.*, 2012). At this stage, the number of crystalline layers grows linearly with time (Ackerson and Schätzel, 1995; Derber *et al.*, 1997; Sandomirski *et al.*, 2011) at a rate that is maximal around $\phi = 0.52$ in simulations and $\phi = 0.53$ in experiments (Sandomirski *et al.*, 2011). The nonmonotonicity is ascribed to the competition between the increasing driving force to crystallize and the decreasing diffusivity D_L of hard spheres as ϕ increases (Sandomirski *et al.*, 2011). Crystal growth is indeed so rapid compared to particle diffusion that a depletion front in the fluid in contact with the crystal has been observed in experiments and simulations (Ackerson and Schätzel, 1995; Derber *et al.*, 1997; Sandomirski *et al.*, 2011). At later times, crystal growth slows down, crystal layers expand slightly, and the depletion zone vanishes.

Light-scattering experiments by Palberg, Schöpe, van Megen, and collaborators studied in detail the process of crystal growth in polydisperse hard spheres (Schöpe, Bryant, and van Megen, 2007; Iacopini, Palberg, and Schöpe, 2009). At volume fractions slightly above melting, it was found that crystal growth is ripening dominated, with the average crystal growth scaling as a power law in time. Upon increasing ϕ, growth gets increasingly hindered, and the initiation of ripeninglike growth is further delayed. Therefore, while samples close to coexistence conditions tend to achieve the highest possible crystal structure quality, samples above melting form crystals with many defects that are later annealed over the entire crystallization process, and with particle rearrangements occurring mostly at grain boundaries.

Experiments of crystal growth in microgravity (Cheng, Chaikin *et al.*, 2001) have observed dendritic growth, which is absent in normal gravity. Here the growth is observed to proceed with a dramatic increase of crystallinity (as measured from the intensity of the scattered light), but without large changes in the average linear dimension of the crystals. The root of this difference, however, remains largely unexplained.

H. Challenges to the fundamental assumptions of CNT

As discussed in Sec. XIII.A, CNT provides a simple yet powerful framework to understand and analyze nucleation data for a large variety of processes. The theory nevertheless depends on several assumptions and approximations, and deviations from these have led to nonclassical versions of the theory.

A fundamental assumption of CNT is its reliance on a single order parameter for describing first-order phase transitions (Prestipino, Laio, and Tosatti, 2014; Jungblut and Dellago, 2016; Russo and Tanaka, 2016a; Lutsko, 2019). This simplification is often appropriate for transitions between phases with the same symmetry, such as the gas-to-liquid phase transition, but the liquid-to-crystal phase transition is different in the sense that both the translational and orientational symmetries of the liquid are then broken. In 2D hard disks at equilibrium, this distinction results in orientational symmetry being broken separately from the translational symmetry, as discussed in Sec. VII. Even though both translational and orientational orders share a same equilibrium phase transition in 3D hard spheres, the two features can evolve differently during the out-of-equilibrium nucleation process (Russo and Tanaka, 2016b; Durán-Olivencia *et al.*, 2018; Lutsko, 2019; Rogal and Leines, 2023). Experiments (Schätzel and Ackerson, 1993; Schöpe, Bryant, and van Megen, 2006a, 2006b, 2007; Iacopini, Palberg, and Schöpe, 2009; Franke, Golde, and Schöpe, 2014; Tan, Xu, and Xu, 2014) and simulations (Schilling *et al.*, 2010, 2011; Russo and Tanaka, 2012, 2016a; Leocmach, Russo, and Tanaka, 2013; Berryman *et al.*, 2016) on precursors, i.e., in the regions where small precritical nuclei are formed, evince that more than one reaction coordinate is involved in hard-sphere nucleation.

Another central assumption of CNT is that the order parameter is taken to be a slow variable with Markovian dynamics (Richard and Speck, 2018a), an assumption that has been challenged (Kuhnhold *et al.*, 2019). These two effects, however, could be argued to be fairly mild deviations from CNT. The rest of Sec. XIII.H describes two more significant effects.

Polymorph selection. During the crystal nucleation process, hard spheres can assemble in one of the infinitely many Barlow packings. As in Sec. VII, we distinguish here three different *polymorphs* (or rather *polytypes*): the fcc, hcp, and rhcp crystals. Because these polymorphs have nearly equal free energies, with only $\sim 10^{-3} k_B T$ per particle favoring fcc (Bolhuis *et al.*, 1997) (see Sec. VII), one might expect that the early stages of nucleation should produce an equal amount of fcc and hcp (often in the form of rhcp), with the fcc becoming the stable crystalline structure only for large crystallites. Some computational studies have reported large deviations from

these predictions; the proportion between fcc and hcp within the nucleus during the later stage of nucleation varies from 2 to 1 up to 3 to 1 (Filion *et al.*, 2010; Russo and Tanaka, 2012). However, experimental work using light-scattering powder crystallography found the initial crystal to be highly random (rhcp) with no preference for one polytype or another, although a preference for fcc was detected at long times; see Sec. VII (Kegel and Dhont, 2000; Martelozzo *et al.*, 2002).

Recent simulation work (Leoni and Russo, 2021) on hard-sphere nucleation has considered the sensitivity of the fcc-to-hcp ratio on the choice of order parameter. While low-dimensional order parameters built on simple BOO parameters found an excess of the fcc phase, high-dimensional order parameters built from a complete set of atomic descriptors for the local environment surrounding each sphere found that the total ratio between fcc and hcp is close to unity for sufficiently large nuclei. The radial composition of the nuclei was also found to be inhomogeneous, with a relative preference for fcc in the core compared to the shell. This preference for fcc was attributed to its small entropic gain in that it allows for stacking disorder to appear along four different directions, compared to a single direction for both hcp and rhcp crystals (namely, the direction perpendicular to the basal plane), although other mechanisms have since been proposed; see Fig. 53. Stacking in multiple directions is accompanied by the formation of a coherent fivefold grain boundary at the intersection of the different stacking directions, as shown in Fig. 54(c). The formation of this fivefold coherent grain boundary was found to be abundant in the early stages of nucleation (O'Malley and Snook, 2003; Leoni and Russo, 2021), as shown in Fig. 54, thus resulting in more compact nuclei with an fcc core that emerges from the more diffuse
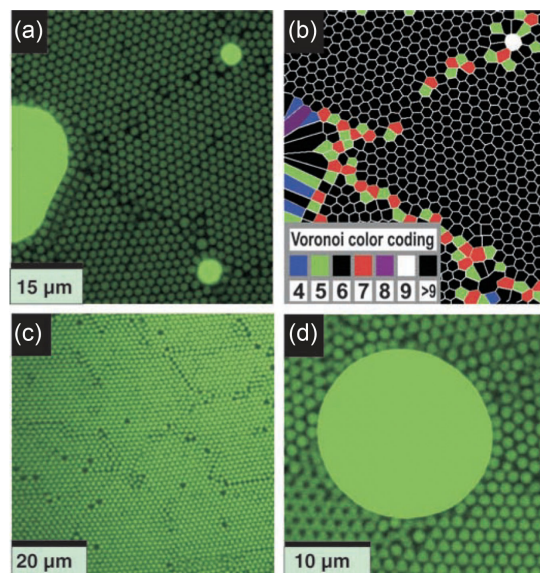

FIG. 52. Experimental work showing crystallization in the presence of curved walls. (a) Grain boundaries connect impurities. (b) Voronoi representation of (a) shows that defects capture the grain boundary. (c) In a sample without impurities, grain boundaries anneal. (d) The mobile layer of single-particle thickness around an impurity with a diameter ratio $\alpha = 0.13$ appears to be fluidlike. From de Villeneuve, 2005.
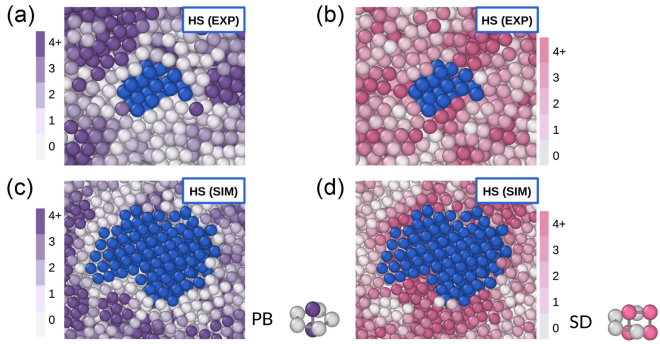
FIG. 53.   The mechanism of polymorph selection in hard-sphere nucleation. (a),(c) Pentagonal bipyramid (PB) and (b),(d) siamese dodecahedron (SD) clusters during crystal nucleation in hard spheres around $\phi = 0.54$. (a),(b) PMMA spheres imaged with confocal microscopy. (c),(d) Simulations of nearly hard spheres. Shown are cut-through images of crystal nuclei. The fcc nucleus is in dark blue (dark gray), while the rest of the particles are colored according to the scale bar (a),(c) on the left or (b),(d) right depending on the number of (a),(c) PB or (b),(d) SD clusters that each particle belongs to. Adapted from Gispen *et al.*, 2023.

precritical nuclei. This mechanism provides a microscopic explanation for the abundance of fcc in the cores. It is also an example of two-step nucleation governed by finite-size effects in that the relative abundance of the different phases changes with the nucleus size. Two-step nucleation mechanisms had previously often been invoked to explain such onionlike structures (Santra, Singh, and Bagchi, 2013; Tan, Xu, and Xu, 2014; Kratzer and Arnold, 2015; Guo *et al.*, 2016; Eslami, Khanjari, and Müller-Plathe, 2017; Adorf *et al.*, 2019).

It was also recently shown that the polymorph selection leading to an abundance of fcc at the core of hard-sphere nuclei is already hidden in the metastable fluid phase, as shown in Fig. 53 (Gispen *et al.*, 2023). Application of the topological cluster classification method of analyzing higher-order fluid structure (Sec. VII.D) (Malins *et al.*, 2013) to both simulation and experimental data revealed that two geometric motifs, or clusters, siamese dodecahedra (SD) and pentagonal bipyramids (PBs), play particularly important roles. PBs are known to suppress nucleation (Taffs and Royall, 2016), while siamese dodecahedra form a crucial link between fcc crystals and the fivefold symmetric fluid in that they feature elements of both in their structure. Siamese dodecahedra are therefore able to fit an fcc nucleus into the hard-sphere fluid. This finding presents a geometric mechanism for polymorph selection of fcc over hcp (Gispen *et al.*, 2023).

Capillarity approximation. Another central tenet of CNT is that crystalline nuclei are governed by the same bulk values as the flat fluid-crystal interface. Although this assumption is violated in the small nucleus regime, CNT can still be considered an effective theory that provides the correct scaling for different thermodynamic quantities, albeit with renormalized constants. For example, an artificially high value of the interfacial free energy needs to be introduced to match computed nucleation rates with CNT predictions. Compared to the flat-interface (equilibrium) value of $\beta\gamma_\infty\sigma^2 \simeq 0.56$ (Espinosa *et al.*, 2016; Bültmann and Schilling, 2020) (see
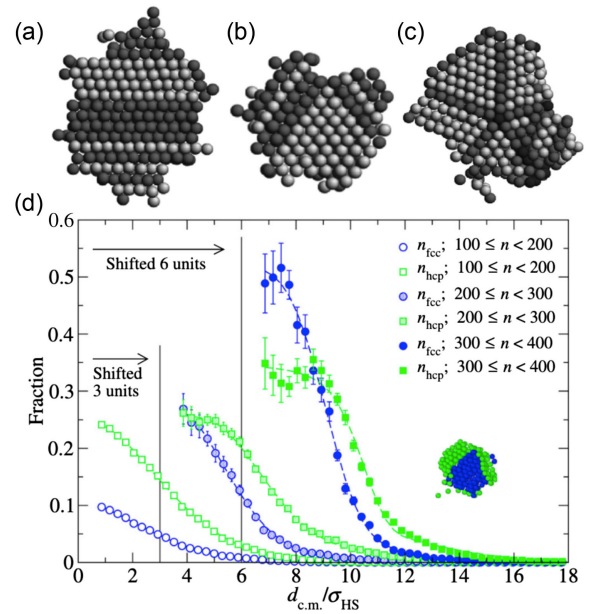

FIG. 54.   Typical grain boundaries formed during hard-sphere nucleation (light spheres are fcc, dark spheres are hcp). (a) Stacking faults. (b) Tetrahedrally shaped fcc domains bounded by stacking faults. (c) Fivefold coherent grain boundary. (a)–(c) From O'Malley and Snook, 2003. (d) The average radial fractional composition of nuclei calculated with respect to the center of mass for different cluster sizes. The section of a typical nucleus with 400 particles is represented. fcc and hcp particles are in blue (dark gray) and green (pale gray), respectively. From Leoni and Russo, 2021.

Sec. V.E), a fit of the nucleation data typically requires values of $\beta\gamma\sigma^2 \simeq 0.76$ (Richard and Speck, 2018a) for the quasie-quilibrium nucleation process. Gispen and Dijkstra (2024) recently demonstrated that simulation data, acquired from seeding, umbrella sampling, and brute-force molecular dynamics simulations, align well with CNT predictions when a density-dependent (or curvature-corrected) interfacial tension was used.

Note that the nucleation theorem (Hill, 1962)

$$\Delta G^*(\mu_f) = \Delta G^*(\mu_0) - \int_{\mu_0}^{\mu_f} d\mu \Delta N^*(\mu) \qquad (47)$$

provides a route for calculating the nucleation work from density profiles of critical nuclei, which can be precisely obtained (for example, through seeding; cf. Sec. V). In Eq. (47) μ_0 denotes a reference state point and ΔN^* is the average number of additional particles in critical nuclei compared to the bulk fluid with chemical potential μ_f. This quantity does not suffer from the ambiguities associated with order parameters used to identify solidlike particles. Figure 55 shows that the prediction from Eq. (47) agrees well with other estimates of the nucleation work. More importantly it shows that the CNT prediction employing the bulk values γ_∞ for the interfacial tension (and pressure difference) severely underestimates the actual nucleation work.
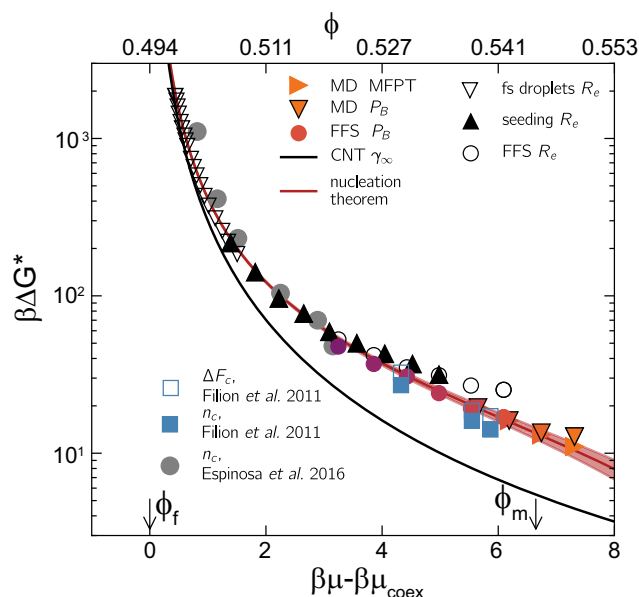
FIG. 55. Nucleation work ΔG^* as a function of the supersaturation obtained from unbiased MD simulations (down and right triangles), forward-flux sampling (circles), and umbrella sampling (squares). The black solid line is the CNT prediction based on the bulk values of the pressure difference and surface tension. The thick solid red line is obtained from the nucleation theorem. The data are plotted as a function of chemical potential with respect to phase coexistence (lower axis), from which the volume fraction is determined using the Carnahan-Starling relation in Eq. (24). The plotted simulation data were obtained in the *NPT* (Filion, Ni *et al.*, 2011; Espinosa *et al.*, 2016) and *NVT* ensembles (Richard and Speck, 2018b). From Richard and Speck, 2018b.

I. Beyond the CNT regime: Crystallization at high volume fractions

Up to $\phi \approx 0.55$, the CNT description qualitatively captures the homogeneous nucleation of a monodisperse suspension of hard spheres; see Sec. XIII.A. Auer and Frenkel (2001a) and Filion *et al.* (2010) calculated the nucleation free-energy barrier height for $\phi \in [0.521, 0.534]$ and found it to drop rapidly upon further increasing ϕ. An approximate extrapolation (Pusey *et al.*, 2009) suggested that the nucleation barrier height becomes of the order of $k_B T$ around $\phi = 0.55$–0.56. In other words, the barrier can then be easily crossed and crystal nucleation is no longer a rare event (in the thermodynamic sense). The lifetime of the metastable liquid is then so short that nucleation can be studied only following rapid density quenches. Depending on the supersaturation of this quench, crystallization proceeds via two distinct mechanisms. For $0.55 \leq \phi \leq 0.58$, the metastable fluid crystallizes via a spinodal-like mechanism. For $\phi \geq 0.58$, the fluid forms an out-of-equilibrium glasslike state and crystallization then proceeds via an avalanche-mediated mechanism.

Spinodal-like crystallization. General phase transformations in the binodal region proceed via a nucleation mechanism, a process initiated by finite-amplitude, localized fluctuations in the metastable fluid. By contrast, phase transformations in the unstable region occur via a spinodal

decomposition mechanism (Gunton, San Miguel, and Sahni, 1983), identified by nonlocal fluctuations with an infinitesimal amplitude. At the mean-field spinodal point (Gunton, San Miguel, and Sahni, 1983), the nucleation barrier vanishes and the stable phase spontaneously grows. The deterministic nonlinear amplification of order parameter fluctuations (Bray, 1994) is then governed by the Cahn-Hilliard equation (Cahn and Hilliard, 1958).

An analogous mechanism has been proposed to explain crystallization for deeply supersaturated ($\phi \gtrsim 0.55$) hard-sphere fluids, where the nucleation barrier becomes negligible (Pusey *et al.*, 2009). Crystallization then proceeds via spatially diffuse collective motion, analogous to spinodal decomposition (Yang, Gould, and Klein, 1988; Trudu, Donadio, and Parrinello, 2006; Cavagna, 2009).

When comparing the crystallization time (the time at which crystallinity reaches 20% of the sample, for example) to the time needed for a particle to diffuse one diameter in the fluid, different behaviors have indeed been detected, depending on the degree of metastability (Pusey *et al.*, 2009). Numerical results (Pusey *et al.*, 2009; Taffs *et al.*, 2013) have been shown to agree with experiments (Harland and van Megen, 1997; Taffs *et al.*, 2013). As shown in Fig. 56, at low metastability the system crystallizes via a nucleation and growth process. Particles freely diffuse before crystal nucleation takes place; a crystalline nucleus has to grow large enough to overcome the nucleation barrier before macroscopic crystallization takes place. By contrast, for $\phi \gtrsim 0.55$, nucleation proceeds without particles moving beyond their own diameter. A local rearrangement of particle positions suffices for crystallization to proceed (Kelton, 1991; Zanotto, 2013). This *spinodal nucleation* regime is characterized by a large driving force for crystallization and a vanishing free-energy barrier (Klein and Leyvraz, 1986; Trudu, Donadio, and Parrinello, 2006; Cavagna, 2009; Pusey *et al.*, 2009), thus resulting in a large density of small crystal nuclei (Pusey and van Megen, 1986; Schätzel and Ackerson, 1993; van Megen and Underwood, 1993a). At even higher supersaturations ($\phi \gtrsim 0.56$), clusters of crystalline particles (Fig. 57) heterogeneously percolate, following many small nuclei coming into contact. Clusters do not grow completely at random; particles become solidlike in the vicinity of solid regions (Sanz *et al.*, 2011; Valeriani *et al.*, 2012).

A similar behavior was reported in the experimental work of Schätzel and Ackerson (1993) and van Megen and Underwood (1993a). In this work, the crystallite size was found to markedly decrease with increasing concentration. Their picture is coherent with the idea of a spinodal nucleation regime, in which increasing supersaturation leads to nucleation on an ever-decreasing spatial scale.

Crystallization in the glassy regime. At higher volume fractions still, hard spheres exhibit glassy dynamics; see Sec. XII. Particle size polydispersity is then key to controlling crystallization. As described in Sec. VII.B, when $s > 5$ to 6%, crystallization is suppressed because the system cannot form a stable crystal with the same composition as the fluid. Crystal formation then requires either size fractionation (Fasolo and Sollich, 2003; Martin, Bryant, and van Megen, 2003) or the assembly of Laves phases (Bommineni *et al.*, 2019), both necessitating transport over larger distances; see
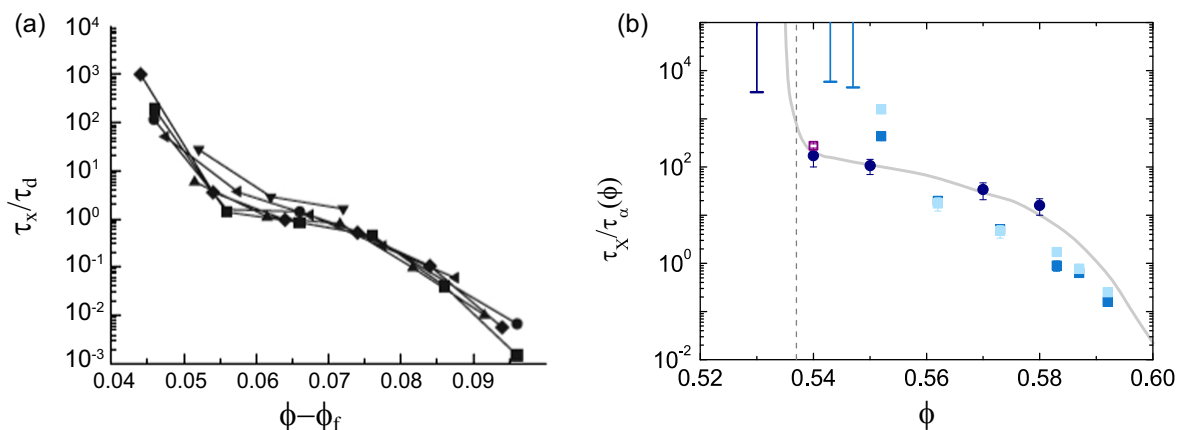
FIG. 56. Spinodal nucleation. (a) Crystallization times τ_X scaled by a time τ_D for a particle to diffuse one diameter as a function of $\phi - \phi_f$. (Recall that a monodisperse system freezes at $\phi_f = 0.492$.) The different points represent polydispersities ranging from $s = 0$ to 6%. The monodisperse system is reported with filled circles. From Pusey *et al.*, 2009. (b) Crystal nucleation times scaled by the relaxation time τ_α. Circles are experimental data obtained via particle-resolved studies, while light and dark squares are simulation data for $s = 4\%$ polydisperse systems with $N = 2048$ and $10\,976$, respectively. The unfilled square is for a monodisperse system with $N = 10\,976$. The dashed lines indicated melting estimated as described in Sec. VII.A. The solid line is a guide for the eye. Error bars extending upward are lower bounds for crystallization times determined from simulations (dark lines) and experiments (light lines) that did not crystallize. From Taffs *et al.*, 2013.
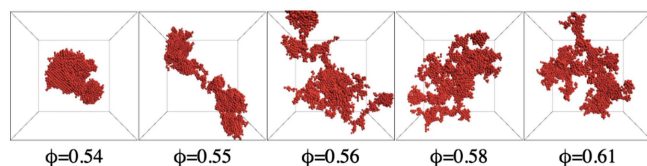

FIG. 57. Snapshots of typical largest crystalline clusters as a function of ϕ at a fixed cluster size ($N_c = 5000$). This size is achieved when (ϕ, X) are, respectively, $(0.54, 0.08)$, $(0.55, 0.15)$, $(0.56, 0.15)$, $(0.58, 0.14)$, and $(0.61, 0.12)$. X is the fraction of crystalline particles. Periodic boundary conditions are taken into account and clusters are centered in the simulation box. From Valeriani *et al.*, 2012.

Sec. VII.A. For $s < 5\%$, however, neither the structural relaxation times of a dense colloidal suspension (Henderson *et al.*, 1996; Sear, 2000; Foffi *et al.*, 2003) nor its dynamics (Zaccarelli *et al.*, 2009) are significantly affected by s.

For $\phi \approx 0.57$–0.58, the crystallization time becomes smaller than the structural relaxation time of the fluid [Figs. 56(a) and 56(b)] (Pusey *et al.*, 2009; Taffs *et al.*, 2013). For $\phi > 0.58$, even though particles move on average less than one particle diameter, crystallization can still proceed (Pusey *et al.*, 2009). Numerical results have shown that a suspension of monodisperse hard spheres (Rintoul and Torquato, 1996; Williams, Snook, and van Megen, 2001) could crystallize even for supersaturations of out-of-equilibrium systems approaching random close packing $\phi_{rcp} \approx 0.64$; see Sec. XII.H. It even proceeds on numerical timescales short compared to the aging time of the amorphous hard-sphere system (Zaccarelli *et al.*, 2009); see Sec. XII.I. In this glassy regime, crystalline clusters percolate as they do in the spinodal regime, even as the relaxation dynamics slows down by several orders of magnitude. In other words, the structure of the growing crystals appears to be unaffected by particle dynamics (Valeriani *et al.*, 2012).

As in computer simulations, the experimental findings of van Megen and Underwood (1993a) in normal gravity demonstrated the presence of a change in the crystallization mechanism at a packing fraction $\phi = 0.58$. They detected homogeneous nucleation of compact nuclei for $\phi < 0.58$ and asymmetric nuclei for $\phi > 0.58$. At a high volume fraction, crystallization happened without particle diffusion. Possibly, nucleation was heterogeneously induced by preformed nuclei, which may not have been fully shear melted prior to the experiment. By contrast, experiments in microgravity showed that slightly polydisperse colloidal suspensions of PMMA hard spheres rapidly crystallize in bulk when $\phi > 0.58$ (Zhu *et al.*, 1997; Chen *et al.*, 2001).

Avalanche-mediated devitrification. Crystallization from a deeply overcompressed suspension occurs without the need of macroscopic diffusion (Sanz *et al.*, 2011) and instead through the gradual formation of crystalline patches (Sanz *et al.*, 2011, 2014). The crystallization mechanism has been related to a series of discrete avalanche-like dynamical events (Kwasniewski, Fluerasu, and Madsen, 2014) characterized by a spatiotemporal burst of particle displacements on a subdiameter scale (Kwasniewski, Fluerasu, and Madsen, 2014; Sanz *et al.*, 2014; Montero de Hijes *et al.*, 2017).

As shown in Fig. 58, during a quiescent interval (Δt_1) most particles rattle locally in their cages and less than 1% undergo significant displacements. At Δt_2 a burst of displacements is recorded, with around 25% of all particles moving more than 3σ. After that, the system returns to quiescence (Δt_3). Such a sequence of events corresponds to an avalanche, and particles that move more than 3σ during the jump are deemed *avalanche particles*. The particle dynamics was thus shown to be intermittent: quiescent periods of motion within the cage of neighbors are punctuated by avalanches in which a correlated subset of particles undergo cage-breaking displacements (Sanz *et al.*, 2014). Note that crystallinity (in black in Fig. 58) and mean squared displacement (in red) jump
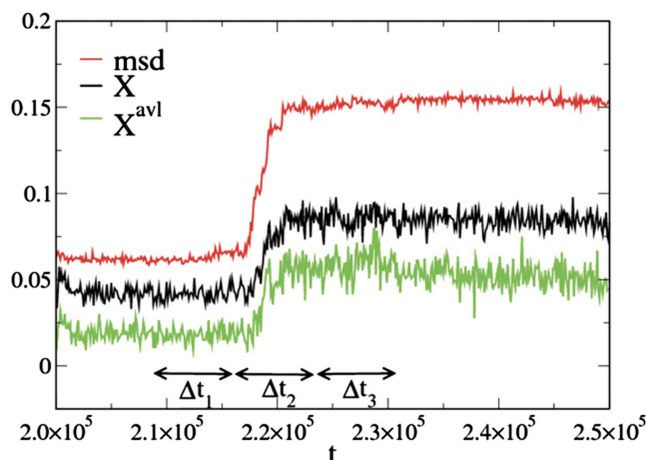
FIG. 58. Development of intermittent, heterogeneous dynamics in concentrated hard-sphere suspensions. Crystallinity X (in black) and mean squared displacement [msd, in red (top line)] vs time around the steplike crystallization event shown at $t = 2.2 \times 10^5$. The green curve (bottom line) X^{avl} is the fraction of avalanche particles that are solidlike. From Sanz *et al.*, 2014.

simultaneously, suggesting that the avalanches responsible for particle displacement are also responsible for crystallization.

The structural propensity to locally crystallize in a medium-range crystalline-order region (Kawasaki and Tanaka, 2010a) is converted into actual crystallinity by the small random disturbances provided by the displacement avalanche. Given that the crystal is locally denser than the glass, the avalanche-mediated crystallization process leads to an increase of the local free volume, thus facilitating a higher mobility of particles next to the newly formed crystalline region. Therefore, crystallization proceeds by a sequence of stochastic events leading to an increased number of crystalline particles, correlated in space by emergent local avalanches (Valeriani *et al.*, 2011).

Yanagishima, Russo, and Tanaka (2017) explored the mechanism behind avalanches, arguing that aging and devitrification are both triggered by a small number of particles that are driven to rearrange in regions of low density and BOO parameter. In particular, avalanches are accompanied by a transient loss of mechanical equilibrium that facilitates a large cascade of motion. The connection between mechanical rigidity and glassy dynamics was explored by Yanagishima *et al.* (2021). By artificially minimizing the heterogeneities in the force network between particles, glasses that are free from aging and crystallization on the simulation timescale were obtained.

Further avalanches (Sanz *et al.*, 2014) have been related to dynamical heterogeneity in that clusters of particles with high and low mobility evolve similarly in space and time. (A description of dynamical heterogeneity in the context of overcompressed hard-sphere fluids is given in Sec. XII.C.) While direct visualization of avalanches has yet to be performed in an experiment, measurements of dynamical heterogeneity (Fig. 38) indicate that this is possible. In these systems, avalanches and dynamical heterogeneity might share a more general tendency to develop in regions of the system akin to *soft spots* regions of high displacement in

low-frequency quasilocalized phonon modes (Brito and Wyart, 2009). A deeper analysis, however, would be needed to better understand this issue.

In a glassy hard-sphere suspension (see Sec. XII.C) Weeks *et al.* (2000), using confocal microscopy, observed small local rearrangements, detecting avalanches, although smaller ones than those found in simulations (Sanz *et al.*, 2014). Whereas Kwasniewski, Fluerasu, and Madsen (2014) reported intermittent dynamics due to avalanches by means of x-ray photon correlation spectroscopy. It is still an open question as to whether these differences are due to different experimental protocols or to some other effect.

J. Nucleation in external fields

Nucleation under gravity. As discussed in Secs. VII.A and XIII.D, colloidal hard-sphere crystallization usually occurs under gravity. (The equilibrium case of a system confined by a wall is considered in Sec. VIII.A.) To begin with, we consider crystal growth for sedimenting particles on flat surfaces. Hilhorst, Wolters, and Petukhov (2010) showed that in sedimentary colloidal crystals obtained from dispersions with high initial volume, persistent fcc crystals are favored by the presence of slanted stacking faults, while regions devoid of those defects tend to grow as an rhcp structure. Simulations by Marechal, Hermes, and Dijkstra (2011) instead attributed the formation of fcc to the free-energy difference between fcc and hcp, and not to the presence of those slanted stacking faults. They also showed that the fraction of fcc increases upon lowering the sedimentation rate or decreasing the initial volume fraction.

Compared to the case of crystal growth on a flat wall, crystal growth from a templated surface has shown that it is possible to obtain surprisingly large defect-free crystals. Jensen *et al.* (2013) controlled the growth of fcc crystal by centrifugation (up to 3000 g) on fcc (100) templates, in contrast to what is observed for (111) and (110) faces (and flat walls), where high centrifugation rates result in defective or amorphous crystals. These results were confirmed in the simulation work of Dasgupta, Edison, and Dijkstra (2017), which also verified the growth of large defect-free crystals from the (100) fcc face.

Out of equilibrium, a limiting Péclet number has been identified for crystallization to occur that depends upon the volume fraction (Ackerson *et al.*, 1999). Gravity has also been found to broaden the interface between crystal and fluid with respect to the equilibrium case. Here the largest value of the gravitational Péclet number used was $\mathrm{Pe}_g = 0.7$ (Dullens, Aarts, and Kegel, 2006b).

Nucleation under confinement. A more complex scenario is that of confinement between two hard walls. In equilibrium a range of structures is obtained (Sec. X). By means of single-particle resolution video microscopy of colloidal films, Peng *et al.* (2015) demonstrated that transitions between square and triangular lattices occurred via a two-step diffusive nucleation pathway involving liquid nuclei (due to the low fluid-crystal interfacial energy). Such a two-step nucleation process has also been observed in the case of a system confined by two parallel walls separated by four diameters (Peng *et al.*, 2015; Qi *et al.*, 2015). Here a solid-solid phase transition was
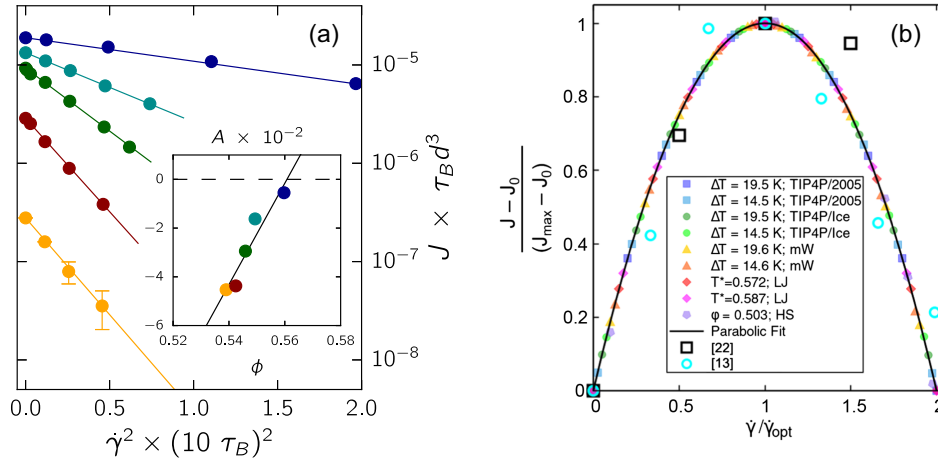
FIG. 59.   Nucleation under shear. (a) Nucleation rate J as a function of squared strain rate $\odot\,\gamma^2$ for several packing fractions decreasing from top $\phi = 0.56$ [blue (dark gray)] to bottom [yellow (pale grey)]. Inset: the slope, which decreases as ϕ increases (faster nucleation). From Richard and Speck, 2015. (b) Shifted and normalized nucleation rates J as a function of strain rate $\dot{\gamma}/\dot{\gamma}_{\rm opt}$ for several model liquids, including hard spheres at $\phi = 0.503$ close to the binodal showing a nonmonotonic behavior. From Goswami, Dalal, and Singh, 2021.

considered in MD and MC simulations. The transition from a solid consisting of five crystalline layers with square symmetry ($\square$) to a solid consisting of four layers with triangular symmetry ($4\triangle$) was shown to occur through a nonclassical nucleation mechanism: a precritical fluid cluster within which a cluster of the stable $4\triangle$ phase then grows with one step (Qi *et al.*, 2015). As discussed in Sec. XIII, crystallization of nanoparticles in spherical confinement proceeds via heterogeneous nucleation (de Nijs *et al.*, 2015), and recently it was shown to exhibit a bifurcation to decahedral or icosahedral structures (Fru Mbah *et al.*, 2023).

Nucleation under shear. Nucleation in the presence of uniform driving, i.e., sedimentation with $Pe_g < 1$, has already been discussed as a possible cause of the nucleation rate discrepancy (Sec. XIII.D). Another important geometry for uniform driving is simple shear flow. One might expect that steadily shearing a hard-sphere suspension would destroy the entropic forces that favor the crystal, and thus prevent the formation of the crystal starting from the supersaturated melt. Experiments nevertheless show that for weak strain rates ($Pe_{\dot{\gamma}} \ll 1$) nucleation persists (Wu *et al.*, 2009). The effect, however, strongly depends on ϕ, with two regimes that are delineated by the nucleation spinodal (Sec. XIII.I), at which the free-energy barrier in quiescent suspensions vanishes. In the activated regime for $\phi < 0.56$, nucleation is suppressed by shear and the nucleation rate drops as we decrease ϕ [Fig. 59(a)]. This reduction can be rationalized by invoking an increase of the effective free-energy barrier[17] $\Delta F(\dot{\gamma}) - \Delta F_0 \propto \dot{\gamma}^2$ (Blaak *et al.*, 2004); cf. Fig. 59(a). This increase is dominated by the additional elastic work to strain the solid nucleus (Mura and Zaccone, 2016), and a more careful numerical investigation of the effective parameters (the elastic modulus and pressure difference) again revealed a strong dependence on droplet size (Richard and Speck, 2019).

It has been posited that the kinetic prefactor is linearly enhanced for packing fractions close to the binodal, leading to nonmonotonic nucleation rates $J(\dot{\gamma}) - J_0 \propto 1 - (\dot{\gamma}/\dot{\gamma}_{\rm opt} - 1)^2$, with the maximum at strain rate $\dot{\gamma}_{\rm opt}$. Figure 59(b) shows the normalized nucleation rate as a function of strain rate for a range of model liquids (Goswami, Dalal, and Singh, 2021). Going to the opposite limit of high packing fractions ($\phi > 0.56$), the quiescent barrier ΔF_0 vanishes and the shear flow again facilitates nucleation by increasing the mobility of single particles, thus helping the arrested dynamics to be overcome at high packing fraction (Koumakis, Schofield, and Petekidis, 2008; Wu *et al.*, 2009; Richard and Speck, 2015).

Binary systems under shear offer the possibility of modeling the effects of polydispersity (which appear to be comparable to quiescent systems) (Maßhoff *et al.*, 2020). These studies also have the potential to explore fractionation in crystallization, which is predicted from numerical simulation and theory; see Sec. VII.B.

K. Melting

While hard-sphere crystallization has received most of the attention, crystal melting is also of physical interest (Löwen, 1994; Dash, 1999). Normally, crystal melting occurs at an existing fluid-crystal interface, without the need for a nucleation event. However, nucleation can play a role in the bulk melting of hard-sphere crystals. Even in the early days of hard-sphere simulations, it was noted that "in the metastable extension of the crystalline phase […] small finite systems can resist melting indefinitely" (Bennett and Alder, 1971). Such crystals are indeed expected to persist up to the Born limit of mechanical stability, at which the elastic moduli of the crystal vanish (Born, 1940; Wang *et al.*, 1997). Between that spinodal-like point and the thermodynamic melting transition, nucleation is expected to be the pathway through which equilibrium is attained. Numerical work has shown the melting to be strongly algorithm dependent (Isobe and Krauth, 2015). Controlled studies of nucleation are much more recent. Wang, Wang *et al.* (2018) revealed that the

---

[17]Although in the driven melt we should think of the reversible work to form a solid droplet instead of an equilibrium free-energy difference.

melting spinodal is found well before the Born instability criterion, but also that homogeneous nucleation efficiently melts an fcc crystal. Homogeneous melting has been investigated using brute-force molecular dynamics, umbrella sampling, and seeding simulations. Gispen and Dijkstra (2024) showed that CNT, augmented with an elastic strain energy correction, accurately predicts the homogeneous melting rate. It was observed that, compared to freezing, melting has a lower driving force due to the proximity of a spinodal instability and a strain energy. In addition, the lower interfacial tension implies opposite signs for the Tolman lengths associated with melting and freezing, a phenomenon that was interpreted with Turnbull's rule. Despite these asymmetries, nucleation rates for freezing and melting are comparable.

Experimentally nonequilibrium melting is challenging to explore. To melt a hard-sphere crystal, one needs to reduce the volume fraction *in situ*, which is itself typically hard. There are therefore few examples. One solution is to use microgel colloids whose effective diameter may be tuned with temperature. These have been shown to melt, providing insight into local mechanisms (Alsayed *et al.*, 2005). As shown in Fig. 60, 3D melting appears to be initiated at grain boundaries.

An inventive development of this approach is to use laser-induced localized heating of a microgel system. Here the system was mildly heated locally using the lens of the microscope. The appeal of this method is that the melting is initiated in the middle of the system far from any wall effects; hence, we can be confident that homogeneous melting will be observed. Melting precursors were observed in the form of local particle-exchange loops surrounded by particles

with large displacements rather than defects. The nucleus size, shape, and time evolution were found to deviate from CNT (Wang *et al.*, 2012). Another option is to produce an equilibrium sedimentation profile and then to invert it (Turci and Royall, 2016). This approach means that melting is observed in a system with somewhat inhomogenous density but may be achievable in most experimental hard-sphere systems without the need for a specialized setup.

An interesting form of reentrant surface melting has been observed in hard spheres in experiments. Here an increase in mobility was found in the layer by the wall when the bulk of the system was crystalline (and exhibited negligible mobility). This increase in mobility was attributed to a 2D-like behavior at the wall (Dullens and Kegel, 2004). Other examples of the role of interfaces include studies of thin films (at the colloidal scale). Depending on the film thickness, thicker films melted from grain boundaries, while thin solid films melt in one step (Peng *et al.*, 2010). In quasi-2D systems, consistent with later equilibrium work (Sec. VII.E), two-step melting from the crystal to the hexatic phase and from the hexatic to the fluid phase has been observed (Han, Ha *et al.*, 2008).

XIV. SUMMARY AND OUTLOOK

We close this review by taking stock of what we have learned from experiments and related work on colloidal hard spheres and consider what the future might hold. As one of the most fundamental model systems in colloidal and statistical physics, hard spheres have played a key role in shaping our understanding of a wide range of phenomena. This progress has been driven partly by the inherent simplicity of the model and partly by the successful intertwining of theoretical and simulation approaches with the experimental realization of hard-sphere colloids. We begin by summarizing the general areas that are well understood, then move on to what we regard as outstanding challenges.

A. What have we learned?

As we discussed in Secs. III and IV, a number of reliable methodologies have been developed to realize hard-sphere-like colloidal particles over a range of size scales. Similarly, simulation methods for hard spheres are by now well established (Sec. V). A key challenge when comparing these is synthesizing particles with interaction potentials as close as possible to the hard-sphere ideal and obtaining reliable quantitative estimates of discrepancies. While up to six significant figures can be achieved in molecular systems, at this point the characterization of state points in colloidal systems in experiments is accurate to at best three (Sec. III.E). Although improvements will continue to emerge, many studies highlighted in this review show that in numerous circumstances good agreement already exists between experiments and simulations. The impact of even slight softness should nevertheless continue to be explored (Taffs *et al.*, 2013; Royall, Williams, and Tanaka, 2018; Dasgupta, Coli, and Dijkstra, 2020; de Jager and Filion, 2022) and to be carefully considered when interpreting experimental results (Sec. III.D).
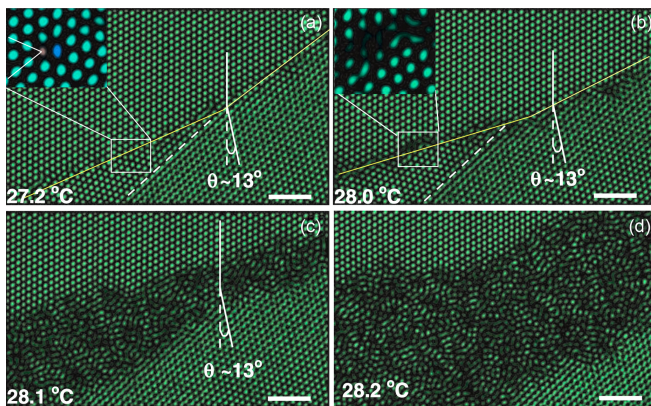

FIG. 60. Premelting of the colloidal crystal at a grain boundary seen through bright-field images at different temperatures (i.e., particle volume fractions) of two crystallites separated by a grain boundary (crystallites tilted at an angle θ with respect to one another). (a) Sample at 27.2 °C. The solid and dashed lines show the grain boundary and a partial dislocation, respectively. The grain boundary cuts the two crystals along two different planes (the yellow line has two slopes). It is composed of an array of dislocations; the two extra planes are indicated by lines in the inset. (b) Sample at 28.0 °C. The grain boundary starts to premelt; nearby particles undergo liquidlike diffusion (inset). The partial dislocation, which is denoted by the dashed line, is not affected. (c),(d) The same sample at 28.1 and 28.2 °C, respectively. The width of the premelt region near the grain boundary increases. Scale bars, 5 μm. From Alsayed *et al.*, 2005.

In terms of methodological advances, the recent development of experimental systems that are truly close to hard spheres for 3D confocal microscopy work, where the larger colloids required need more care in producing hard-sphere-like behavior (Sec. III.C) (Royall, Poon, and Weeks, 2013; Kodger, Guerra, and Sprakel, 2015; Liu *et al.*, 2016; Kale *et al.*, 2023). Other experimental developments include coupling light scattering with rheology (Tamborini and Cipeletti, 2012), as well as deploying spatially resolved light scattering (Golde, Palberg, and Schöpe, 2016), with which one may soon probe dynamical heterogeneity at deeper experimental supercooling than has been achieved thus far. In parallel, the techniques used in particle-resolved studies have been extended to smaller particles that access longer timescales in terms of their Brownian time (Hallett, Turci, and Royall, 2018). This may prove useful in probing dynamics at deeper experimental supercooling. The approach could also be used to investigate crystal nucleation in the regime of supersaturation thus far accessed only by light scattering (with small particles), but with real-space resolution the approach could be used to probe the hard-sphere nucleation discrepancy. Other experimental developments that could be brought to bear to address this discrepancy include seeding with optical tweezers (Hermes *et al.*, 2011; Curran *et al.*, 2014), with which a careful study for a range of well-controlled state points may be expected to yield considerable insight. Experimentally inferring local forces and stresses (Lin, Bierbaum *et al.*, 2016; Dong *et al.*, 2022) may also reveal details into failure mechanisms of amorphous and crystalline solids.

Self-assembly of hard-sphere systems in confinement still often yields surprises, such as the emergence of crystal structures that are not favored in bulk systems (Sec. X.D), and is likely to continue to do so in the future, especially when coupled with size dispersity. Similarly, the careful exploration of various ranges of size ratios in binary hard-sphere mixtures (Sec. IX) has revealed the existence of metastable fluid-fluid demixing as well as the formation of complex crystals. Self-assembly of other crystal phases at size ratios that have not been as carefully explored is expected, given the wealth of structures known to exist at infinite pressure (Hopkins, Stillinger, and Torquato, 2012). More generally the consideration of binary mixtures naturally enriches all of the other phenomena discussed in this review and plays a particularly important role in the study of glass-forming systems.

How external forces and fields modify the structure and dynamics of hard spheres was explored in Sec. XI. The solvent plays an important role in out-of-equilibrium systems in that it then hydrodynamically couples forces. The careful treatment of hydrodynamic interactions (Sec. V.D) has therefore significantly improved our understanding of phenomena such as sedimentation and shear thickening. Theoretical insights have further led to a rather comprehensive picture connecting deformations of the microstructure to the macroscopic material properties probed in rheology experiments.

Hard spheres have played a key role in both computer simulation and the experimental study of glass physics; see Sec. XII. As experimental systems and simulation techniques evolve to probe structure and dynamics at ever deeper supercooling, one hopes that hard-sphere studies will lead to an even stronger framework for understanding glass formation. If it were possible to use still smaller particles in experiment than those used by Hallett, Turci, and Royall (2018), then those could be a means to probe the additional increase of dynamical length scales and the hierarchy in dynamical behavior in experiments (Scalliet, Guiselin, and Berthier, 2022; Ortlieb *et al.*, 2023). Related to this would be the structural relaxation mechanism at deep supercooling. Failure in amorphous soft materials and, in the context of hard spheres, glasses is a most promising area for future work. This brings together multiple challenges of aging nonequilibrium materials. For example, few studies have addressed the Gardner transition (Sec. XII.H) with colloids, and it is tempting to imagine that a combination of shear and force measurement may be a way to do so. A further interesting possibility would be to use hard-sphere experiments to investigate the ductile-brittle transition recently found in computer simulation (Ozawa *et al.*, 2018). Developments in x-ray scattering (see Sec. XII.C) that reveal higher-order structure and dynamical information may be able to play a key role in equilibrating samples much closer to the glass transition, and also in annealing samples that might exhibit brittle behavior (Wochner *et al.*, 2009; Lehmkühler *et al.*, 2020; Liu *et al.*, 2022).

At high volume fraction, it is still not clear whether crystallization in experiments results from residual crystals in the samples arising from their preparation. Indeed, van Megen and Underwood (1993a) suggested that the shear-melting process by which amorphous colloid samples were prepared could leave small shear-aligned nuclei on which a crystal could grow. Concerning simulations, there is the possibility that crystals could be formed during compression of the system to the high concentration regime. These crystals could later act as seeds for further crystallization.

Another important challenge is the observation of avalanche crystallization in experiments. Because avalanches are rare events, one might need a large amount of data to analyze and store in order to find them in confocal microscopy experiments [such as those of Weeks *et al.* (2000)]. Concerning light or x-ray scattering experiments [such as those of Kwasniewski, Fluerasu, and Madsen (2014)], one might vary the size of the scattering volume and use a small number of particles to be able to clearly detect intermittency with long quiescent periods. The reason for suggesting this approach is that in a larger volume containing many particles avalanches might occur simultaneously in different regions of the system, and the dynamics would appear to be much more homogeneous.

B. Open challenges

We now turn to areas in which relatively little work has been done, or in which major developments are sorely needed. At the experimental level, a major bottleneck with particle-resolved studies is the quantity of data produced. Experimental papers with few coordinate sets analyzed are common (Dong *et al.*, 2022). Often the technique seems to promise much, based on the precision of the data, but the quantity obtained is insufficient for the kind of statistically meaningful analysis that would be required to fully exploit the

technique. While great strides have been made in the ability to handle large datasets, the issue often lies in the acquisition of the data, which is limited by the scanning of a single lens across a sample. It therefore is not easy to see how this can be significantly improved, but if some means can be found to increase the rate of data acquisition, then many challenges relating to the quantity of data might be addressed. For example, imagine being able to compare the shapes of nuclei of a certain size between experiment and simulation in the context of the nucleation discrepancy. A further issue is that the system can evolve during the time taken to scan. One direction that has been explored is to "freeze" the solvent by polymerizing it *in situ*. This enables much larger regions to be imaged, and images containing in excess of a million particles have been obtained (with typical values being around 10 000) (van der Wee, 2019).

In monodisperse hard spheres in equilibrium, interfaces remain a major challenge. As discussed in Sec. VIII, numerical and theoretical methods to obtain the interfacial free energy and stiffness vary by up to 30%. Meanwhile, experimental measurements show even greater discrepancies, often differing from simulation and theory by a factor of 2 or more. Given the importance of these quantities in the context of nucleation, there is an interest in arriving at generally agreed values for interfacial free energies and stiffness, and for well-controlled experimental validation. This discrepancy might stem from a high sensitivity of interfacial properties to relatively small deviations from hard-sphere behavior. In other words, if accurate values were established for the hard-sphere interfacial free energy and stiffness, these results could prove to be valuable benchmarks for assessing how close to a hard sphere a given experimental system is. Another interfacial phenomenon, grain boundaries, remains largely unexplored in 3D hard spheres. In simulations this may reflect the need for large system sizes, but in experiments there is much to be done.

Our knowledge of hard-sphere phase behavior becomes more clouded when more than two particle sizes are mixed. Owing to the vastness of the resulting parameter space, the exploration of crystallization in ternary and higher-component systems has been relatively sparse (Stucke and Crespi, 2003; Wang *et al.*, 2016; Koshoji and Ozaki, 2021), and hence a clear overview of the resulting phase behavior is largely missing. For hard-sphere systems with relatively large polydispersity, the equilibrium phase behavior is essentially unknown. Simulations suggest the possible stability of complex crystal structures (Lindquist, Jadrich, and Truskett, 2018; Bommineni *et al.*, 2019), but whether these are indeed thermodynamically stable or realizable in experiments remains an open question. Therefore, the possibility of surprising new physics in mixtures of hard spheres should not be discounted.

The nucleation process in monodisperse hard-sphere systems remains a topic of intense debate. As discussed in Sec. XIII, various reasons have been proposed for the ongoing discrepancy between experimentally measured and theoretically predicted nucleation rates of the hard-sphere crystal phase. However, resolving this issue will remain difficult as long as real-space experiments have trouble probing the timescales required to observe nucleation in the low supersaturation regime where this discrepancy is observed. One possibility would be to probe precritical nuclei. That experiments (Wood *et al.*, 2018) and simulations (Fiorucci *et al.*, 2020) disagree substantially in the measurement of higher-order structures in sedimenting metastable fluids suggests that this might be a fruitful line of enquiry.

Alternatively, using smaller particles could enable particle-resolved studies in the discrepancy regime. Such experiments will have to rely on advances in imaging techniques (Hell, 2007; Hallett, Turci, and Royall, 2018), as well as in possibly machine-learning-based algorithms for obtaining particle coordinates from lower-resolution images (Sec. IV.B). As noted, the potential for the new x-ray scattering methods to access smaller particles may also be important here (Wochner *et al.*, 2009; Lehmkühler *et al.*, 2020; Liu *et al.*, 2022).

Perhaps another approach may yield fruit here, and this would be to determine the volume fraction accurately or measure the nucleation rate at much lower supersaturations. Disappointing as it may be, the possibility that the discrepancy could be resolved by a correct determination of effective volume fraction absolutely cannot be ruled out. However, if there is an issue with experimental determination of the volume fraction, it is systematically underestimated, and why this is remains a profound mystery. That there are two lines in the experimental data (Fig. 47) with significantly differing rates of sedimentation might be seen as a smoking gun. However, investigations of the effects of sedimentation, which can change the higher-order structure of the system and thus reduce the barrier to nucleation, did not fully address the discrepancy (Wood *et al.*, 2018; Fiorucci *et al.*, 2020).

Experimental investigations of polymorph selection pathways remain few and far between [except that of Gispen *et al.* (2023); see Sec. XIII.H]. Confocal microscopy experiments have observed the real-space formation of relatively ordered precursor structures with different symmetries, but understanding their conversion into crystalline nuclei remains a challenge. Furthermore, observation in simulation of a preference for fcc (Leoni and Russo, 2021; Gispen *et al.*, 2023) has not been reproduced in an experiment, which seems to form rhcp (Kegel and Dhont, 2000; Martelozzo *et al.*, 2002). A systematic comparison of polymorph selection at well-matched state points between experiments and simulations would seem to be in order.

Overall the main lesson learned from the rich history and broad applicability of the hard-sphere model is the impressive complexity that emerges from even a simple system. Depending on their density, size dispersity, and environment, hard spheres demonstrate that energetic interactions are not a requirement for the formation of amazingly complex (quasi) crystal structures, probing the complex and heterogeneous dynamics of glassy materials, or gaining insight into far-from-equilibrium phenomena. Investigating these different processes in hard spheres instead provides a framework for understanding the same phenomena for systems driven by more complex interactions, regardless of whether they consist of atoms, molecules, or more complex colloidal building blocks. As a result, hard spheres will inevitably continue to function as a key reference system in statistical physics and colloid science, and as a testing ground for newly developed theoretical and computational techniques. Moreover, as we have highlighted in

this review, hard spheres continue to hold surprises, challenges, and unresolved questions that will inevitably spark new research directions in the years and decades to come.

Data relevant to this work have been archived and can be accessed at the Duke Digital Repository (Royall *et al.*, 2024).

LIST OF SYMBOLS AND ABBREVIATIONS

σ	hard-sphere diameter
σ_{eff}	effective diameter
ϕ	volume (packing) fraction
ϕ_{cp}	close-packing fraction
ρ	number density
P	(osmotic) pressure
Z	compressibility factor $\beta P/\rho$
η	solvent viscosity
τ_{B}	Brownian time
τ_α	α-relaxation time
τ_β	β-relaxation time
β	$1/k_{\text{B}}T$
$u(r)$	pair interaction potential
κ	Debye length
λ_B	Bjerrum length
D_S	short-time diffusion
D_L	long-time diffusion
D_0	free diffusion
J	nucleation rate
ξ_g	gravitational length
v	velocity
q	size ratio
k	wave vector
$S(k)$	structure factor
$g(r)$	radial distribution function
$g(\sigma^+)$	contact value of $g(r)$
γ	Interfacial free energy
τ	shear stress
$\gamma_s, \dot{\gamma}_s$	strain (rate)
s	polydispersity
BD	Brownian dynamics: a common simulation method that approximates the motion of colloids
CHB	cyclohexyl bromide: solvent used for density and refractive index matching of PMMA particles
PHSA	polyhydroxystearic acid: a commonly used stabilizer for the PMMA system
PMMA	polymethyl methacrylate: the most commonly used experimental system for 3D hard spheres

ACKNOWLEDGMENTS

REFERENCES

Abou, B., R. Colin, V. Lecomte, E. Pitard, and F. van Wijland, 2018, J. Chem. Phys. **148**, 164502.

Ackerson, B. J., 1990, J. Rheol. **34**, 553.

Ackerson, B. J., S. E. Paulin, B. Johnson, W. van Megen, and S. M. Underwood, 1999, Phys. Rev. E **59**, 6903.

Ackerson, B. J., and P. N. Pusey, 1988, Phys. Rev. Lett. **61**, 1033.

Ackerson, B. J., and K. Schätzel, 1995, Phys. Rev. E **52**, 6448.

Adhikari, R., K. Stratford, M. Cates, and A. Wagner, 2005, Europhys. Lett. **71**, 473.

Adorf, C. S., T. C. Moore, Y. J. Melle, and S. C. Glotzer, 2019, J. Phys. Chem. B **124**, 69.

Alder, B. J., D. J. Gass, and T. E. Wainwright, 1970, J. Chem. Phys. **53**, 3813.

Alder, B. J., W. G. Hoover, and D. A. Young, 1968, J. Chem. Phys. **49**, 3688.

Alder, B. J., and T. E. Wainwright, 1957, J. Chem. Phys. **27**, 1208.

Alder, B. J., and T. E. Wainwright, 1967, Phys. Rev. Lett. **18**, 988.

Alexander, S., P. M. Chaikin, P. Grant, G. J. Morales, P. Pincus, and D. Hone, 1984, J. Chem. Phys. **80**, 5776.

Alkemade, R. M., E. Boattini, L. Filion, and F. Smallenburg, 2022, J. Chem. Phys. **156**, 204503.

Allahyarov, E., K. Sandomirski, S. U. Egelhaaf, and H. Löwen, 2015, Nat. Commun. **6**, 7110.

Allen, R. J., D. Frenkel, and P. R. ten Wolde, 2006a, J. Chem. Phys. **124**, 194111.

Allen, R. J., D. Frenkel, and P. R. ten Wolde, 2006b, J. Chem. Phys. **124**, 024102.

Allen, R. J., C. Valeriani, and P. R. ten Wolde, 2009, J. Phys. Condens. Matter **21**, 463102.

Allen, R. J., P. B. Warren, and P. R. ten Wolde, 2005, Phys. Rev. Lett. **94**, 018104.

Almarza, N. G., 2009, J. Chem. Phys. **130**, 184106.

Alsayed, A. M., M. F. Islam, J. Zhang, P. J. Collings, and A. Yodh, 2005, Science **309**, 1207.

Andersen, H. C., J. D. Weeks, and D. Chandler, 1971, Phys. Rev. A **4**, 1597.

Anderson, J. A., J. Glaser, and S. C. Glotzer, 2020, Comput. Mater. Sci. **173**, 109363.

Anderson, J. A., E. Jankowski, T. L. Grubb, M. Engel, and S. C. Glotzer, 2013, J. Comput. Phys. **254**, 27.

Antl, L., J. W. Goodwin, R. D. Hill, R. H. Ottewill, S. M. Owens, S. Papworth, and J. A. Waters, 1986, Colloids Surf. **17**, 67.

Araújo, N., *et al.*, 2023, Soft Matter **19**, 1695.

Arceri, F., and E. I. Corwin, 2020, Phys. Rev. Lett. **124**, 238002.

Arceri, F., E. I. Corwin, and C. S. O'Hern, 2023, in *Spin Glass Theory and Far Beyond*, edited by P. Charbonneau, E. Marinari, M. Mézard, F. Ricci-Tersenghi, G. Sicuro, and F. Zamponi (World Scientific, Singapore).

Asakura, S., and F. Oosawa, 1954, J. Chem. Phys. **22**, 1255.

Aschinger, A., and J. Winter, 2012, New J. Phys. **14**, 093035.

Ashkin, A., 1970, Phys. Rev. Lett. **24**, 156.

Ashton, D. J., N. B. Wilding, R. Roth, and R. Evans, 2011, Phys. Rev. E **84**, 061136.

Ashwin, S. S., and R. K. Bowles, 2009, Phys. Rev. Lett. **102**, 235701.

Ashwin, S. S., M. Zaeifi Yamchi, and R. K. Bowles, 2013, Phys. Rev. Lett. **110**, 145701.

Aste, T., and D. Weaire, 2008, *The Pursuit of Perfect Packing*, 2nd ed. (Taylor & Francis, New York).

Attard, P., 1989, J. Chem. Phys. **91**, 3083.

Attard, P., and G. Patey, 1990, J. Chem. Phys. **92**, 4970.

Attia, E., J. C. Dyre, and U. R. Pedersen, 2022, J. Chem. Phys. **157**, 034502.

Auer, S., and D. Frenkel, 2001a, Nature (London) **409**, 1020.

Auer, S., and D. Frenkel, 2001b, Nature (London) **413**, 711.

Auer, S., and D. Frenkel, 2002, J. Phys. Condens. Matter **14**, 7667.

Auer, S., and D. Frenkel, 2003, Phys. Rev. Lett. **91**, 015703.

Auer, S., and D. Frenkel, 2004a, J. Chem. Phys. **120**, 3015.

Auer, S., and D. Frenkel, 2004b, Annu. Rev. Phys. Chem. **55**, 333.

Bai, F., D. Wang, Z. Huo, W. Chen, L. Liu, X. Liang, C. Chen, X. Wang, Q. Peng, and Y. Li, 2007, Angew. Chem. **119**, 6770.

Bailey, M. R., F. Grillo, and L. Isa, 2022, Soft Matter **18**, 7291.

Ball, R., and J. Melrose, 1995, Adv. Colloid Interface Sci. **59**, 19.

Ballesta, P., R. Besseling, L. Isa, G. Petekidis, and W. C. K. Poon, 2008, Phys. Rev. Lett. **101**, 258301.

Ballesta, P., and G. Petekidis, 2016, Phys. Rev. E **93**, 042613.

Ballesta, P., G. Petekidis, L. Isa, W. C. K. Poon, and R. Besseling, 2012, J. Rheol. **56**, 1005.

Banchio, A. J., and J. F. Brady, 2003, J. Chem. Phys. **118**, 10323.

Banchio, A. J., and G. Nägele, 2008, J. Chem. Phys. **128**, 104903.

Bannerman, M. N., R. Sargant, and L. Lue, 2011, J. Comput. Chem. **32**, 3329.

Bapst, V., *et al.*, 2020, Nat. Phys. **16**, 448.

Barker, J. A., 1962, Aust. J. Phys. **15**, 127.

Barker, J. A., and D. Henderson, 1967, J. Chem. Phys. **47**, 4714.

Barker, J. A., and D. Henderson, 1976, Rev. Mod. Phys. **48**, 587.

Barrat, J., M. Baus, and J. P. Hansen, 1986, Phys. Rev. Lett. **56**, 1063.

Barrat, J., M. Baus, and J. P. Hansen, 1987, J. Phys. C **20**, 1413.

Barrat, J., and J. Hansen, 1986, J. Phys. (Paris) **47**, 1547.

Barrat, J. L., W. Gotze, and A. Latz, 1989, J. Phys. Condens. Matter **1**, 7163.

Barrat, J.-L., and J.-P. Hansen, 2003, *Basic Concepts for Simple and Complex Liquids* (Cambridge University Press, Cambridge, England).

Barrett, K., 1973, Br. Polym. J. **5**, 259.

Bartlett, P., R. Ottewill, and P. Pusey, 1990, J. Chem. Phys. **93**, 1299.

Bartlett, P., R. Ottewill, and P. Pusey, 1992, Phys. Rev. Lett. **68**, 3801.

Bartlett, P., and P. Warren, 1999, Phys. Rev. Lett. **82**, 1979.

Bartsch, E., V. Frenz, J. Baschnagel, W. Schärtl, and H. Sillescu, 1997, J. Chem. Phys. **106**, 3743.

Batchelor, G., 1976, J. Fluid Mech. **74**, 1.

Batchelor, G., 1983, J. Fluid Mech. **131**, 155.

Batchelor, G. K., 1967, *An Introduction to Fluid Dynamics* (Cambridge University Press, Cambridge, England).

Batchelor, G. K., 1977, J. Fluid Mech. **83**, 97.

Battimelli, G., G. Ciccotti, and P. Greco, 2020, *Computer Meets Theoretical Physics: The New Frontier of Molecular Simulation* (Springer, New York).

Baule, A., F. Morone, H. J. Herrmann, and H. A. Makse, 2018, Rev. Mod. Phys. **90**, 015006.

Baumgartl, J., R. P. Dullens, M. Dijkstra, R. Roth, and C. Bechinger, 2007, Phys. Rev. Lett. **98**, 198303.

Baus, M., 1989, J. Phys. Condens. Matter **1**, 3131.

Baus, M., and J. L. Colot, 1986, J. Phys. C **19**, L135.

Bechinger, C., 2002, Curr. Opin Colloid Interface Sci. **7**, 204.

Bechinger, C., R. Di Leonardo, H. Löwen, C. Reichhardt, G. Volpe, and G. Volpe, 2016, Rev. Mod. Phys. **88**, 045006.

Becker, R., and W. Döring, 1935, Ann. Phys. (Berlin) **416**, 719.

Beenakker, C., and P. Mazur, 1983, Physica (Amsterdam) **120A**, 388.

Beenakker, C., and P. Mazur, 1984, Physica (Amsterdam) **126A**, 349.

Bender, J., and N. J. Wagner, 1996, J. Rheol. **40**, 899.

Bengtzelius, U., W. Gotze, and A. Sjolander, 1984, J. Phys. C **17**, 5915.

Benjamin, R., and J. Horbach, 2015, Phys. Rev. E **91**, 032410.

Bennett, C. H., and B. J. Alder, 1971, J. Chem. Phys. **54**, 4796.

Bergenholtz, J., J. F. Brady, and M. Vicic, 2002, J. Fluid Mech. **456**, 239.

Bernal, J. D., and J. Mason, 1960, Nature (London) **188**4754, 910.

Bernard, E. P., and W. Krauth, 2011, Phys. Rev. Lett. **107**, 155704.

Bernard, E. P., W. Krauth, and D. B. Wilson, 2009, Phys. Rev. E **80**, 056704.

Bernu, B., Y. Hiwatari, and J.-P. Hansen, 1985, J. Phys. C **18**, L371.

Berryman, J. T., M. Anwar, S. Dorosz, and T. Schilling, 2016, J. Chem. Phys. **145**, 211901.

Berthier, L., and G. Biroli, 2011, Rev. Mod. Phys. **83**, 587.

Berthier, L., G. Biroli, J.-P. Bouchaud, L. Cipelletti, and W. van Saarloos, 2011, *Dynamical Heterogeneities in Glasses, Colloids, and Granular Media*, International Series of Monographs on Physics Vol. 150 (Oxford University Press, Oxford).

Berthier, L., G. Biroli, J.-P. Bouchaud, and G. Tarjus, 2019, J. Chem. Phys. **150**, 094501.

Berthier, L., G. Biroli, P. Charbonneau, E. I. Corwin, S. Franz, and F. Zamponi, 2019, J. Chem. Phys. **151**, 010901.

Berthier, L., P. Charbonneau, D. Coslovich, A. Ninarello, M. Ozawa, and S. Yaida, 2017, Proc. Natl. Acad. Sci. U.S.A. **114**, 11356.

Berthier, L., P. Charbonneau, A. Ninarello, M. Ozawa, and S. Yaida, 2019, Nat. Commun. **10**, 1508.

Berthier, L., D. Coslovich, A. Ninarello, and M. Ozawa, 2016, Phys. Rev. Lett. **116**, 238002.

Berthier, L., and W. Kob, 2007, J. Phys. Condens. Matter **19**, 205130.

Berthier, L., M. Ozawa, and C. Scalliet, 2019, J. Chem. Phys. **150**, 160902.

Berthier, L., and T. A. Witten, 2009, Phys. Rev. E **80**, 021502.

Besseling, R., L. Isa, P. Ballesta, G. Petekidis, M. E. Cates, and W. C. K. Poon, 2010, Phys. Rev. Lett. **105**, 268301.

Besseling, R., L. Isa, E. R. Weeks, and W. C. K. Poon, 2009, Adv. Colloid Interface Sci. **146**, 1.

Besseling, R., E. R. Weeks, A. B. Schofield, and W. C. K. Poon, 2007, Phys. Rev. Lett. **99**, 028301.

Besseling, T., M. Hermes, A. Fortini, M. Dijkstra, A. Imhof, and A. van Blaaderen, 2012, Soft Matter **8**, 6931.

Bi, D., S. Henkes, K. E. Daniels, and B. Chakraborty, 2015, Annu. Rev. Condens. Matter Phys. **6**, 63.

Biben, T., P. Bladon, and D. Frenkel, 1996, J. Phys. Condens. Matter **8**, 10799.

Biben, T., and J.-P. Hansen, 1990, Europhys. Lett. **12**, 347.

Biben, T., and J.-P. Hansen, 1991a, Phys. Rev. Lett. **66**, 2215.

Biben, T., and J.-P. Hansen, 1991b, J. Phys. Condens. Matter **3**, F65.

Biben, T., R. Ohnesorge, and H. Löwen, 1994, Europhys. Lett. **28**, 665.

Bierbaum, M., B. D. Leahy, A. A. Alemi, I. Cohen, and J. P. Sethna, 2017, Phys. Rev. X **7**, 041007.

Biroli, G., J. P. Bouchaud, A. Cavagna, T. S. Grigera, and P. Verrochio, 2008, Nat. Phys. **4**, 771.

Biroli, G., and C. Cammarota, 2017, Phys. Rev. X **7**, 011011.

Biroli, G., P. Charbonneau, E. I. Corwin, Y. Hu, H. Ikeda, G. Szamel, and F. Zamponi, 2021, Phys. Rev. E **103**, L030104.

Blaak, R., S. Auer, D. Frenkel, and H. Löwen, 2004, Phys. Rev. Lett. **93**, 068303.

Bladon, P., and D. Frenkel, 1995, Phys. Rev. Lett. **74**, 2519.

Blickle, V., T. Speck, L. Helden, U. Seifert, and C. Bechinger, 2006, Phys. Rev. Lett. **96**, 070603.

Bloch, I., J. Dalibard, and W. Zwerger, 2008, Rev. Mod. Phys. **80**, 885.

Boattini, E., S. Marín-Aguilar, S. Mitra, G. Foffi, F. Smallenburg, and L. Filion, 2020, Nat. Commun. **11**, 5479.

Boattini, E., F. Smallenburg, and L. Filion, 2021, Phys. Rev. Lett. **127**, 088007.

Bogomolov, V., Y. A. Kumzerov, V. Petranovskii, and A. Fokin, 1990, Sov. Phys. Crystallogr. **35**, 119.

Bohlein, T., J. Mikhael, and C. Bechinger, 2012, Nat. Mater. **11**, 126.

Boles, M. A., M. Engel, and D. V. Talapin, 2016, Chem. Rev. **116**, 11220.

Bolhuis, P., and D. Frenkel, 1997, J. Phys. Condens. Matter **9**, 381.

Bolhuis, P. G., D. Chandler, C. Dellago, and P. L. Geissler, 2002, Annu. Rev. Phys. Chem. **53**, 291.

Bolhuis, P. G., D. Frenkel, S.-C. Mau, and D. A. Huse, 1997, Nature (London) **388**, 235.

Bolhuis, P. G., and D. A. Kofke, 1996, Phys. Rev. E **54**, 634.

Bommineni, P. K., M. Klement, and M. Engel, 2020, Phys. Rev. Lett. **124**, 218003.

Bommineni, P. K., N. R. Varela-Rosales, M. Klement, and M. Engel, 2019, Phys. Rev. Lett. **122**, 128005.

Bonaccorso, F., A. Montessori, A. Tiribocchi, G. Amati, M. Bernaschi, M. Lauricella, and S. Succi, 2020, Comput. Phys. Commun. **256**, 107455.

Bonilla-Capilla, B., A. Ramirez-Saito, M. A. Ojeda-López, and J. Arauz-Lara, 2004, J. Phys. Condens. Matter **24**, 464126, https://iopscience.iop.org/article/10.1088/0953-8984/24/46/464126/meta.

Bonn, D., M. M. Denn, L. Berthier, T. Divoux, and S. Manneville, 2017, Rev. Mod. Phys. **89**, 035005.

Born, M., 1940, Math. Proc. Cambridge Philos. Soc. **36**, 160.

Bosma, G., C. Pathmamanoharan, E. H. A. de Hoog, W. K. Kegel, A. van Blaaderen, and H. N. W. Lekkerkerker, 2002, J. Colloid Interface Sci. **245**, 292.

Boublík, T., 2011, Mol. Phys. **109**, 1575.

Bouchaud, J.-P., 1992, J. Phys. I (France) **2**, 1705.

Bowles, R. K., and S. S. Ashwin, 2011, Phys. Rev. E **83**, 031302.

Brader, J. M., M. E. Cates, and M. Fuchs, 2008, Phys. Rev. Lett. **101**, 138301.

Brader, J. M., M. E. Cates, and M. Fuchs, 2012, Phys. Rev. E **86**, 021403.

Brady, J., 1993, J. Chem. Phys. **99**, 567.

Brady, J. F., 1994, J. Fluid Mech. **272**, 109.

Brady, J. F., and G. Bossis, 1988, Annu. Rev. Fluid Mech. **20**, 111.

Brambilla, G., D. El Masri, M. Pierno, L. Berthier, L. Cipelletti, G. Petekidis, and A. B. Schofield, 2009, Phys. Rev. Lett. **102**, 085703.

Bray, A., 1994, Adv. Phys. **43**, 357.

Brazda, T., A. Silva, N. Manini, A. Vanossi, R. Guerra, E. Tosatti, and C. Bechinger, 2018, Phys. Rev. X **8**, 011050.

Brito, C., and M. Wyart, 2009, J. Chem. Phys. **131**, 024504.

Broughton, J. Q., and G. H. Gilmer, 1986, J. Chem. Phys. **84**, 5759.

Brown, E., and H. M. Jaeger, 2014, Rep. Prog. Phys. **77**, 046602.

Brown, J. C., P. N. Pusey, J. W. Goodwin, and R. H. Ottewill, 1975, J. Phys. A **8**, 664.

Bruce, A., N. Wilding, and G. Ackland, 1997, Phys. Rev. Lett. **79**, 3002.

Brukhno, A. V., J. Grant, T. L. Underwood, K. Stratford, S. C. Parker, J. A. Purton, and N. B. Wilding, 2021, Mol. Simul. **47**, 131.

Brunner, M., C. Bechinger, U. Herz, and H. von Grünberg, 2003, Europhys. Lett. **63**, 791.

Brush, S. G., 1976, *The Kind of Motion We Call Heat*, Vol. 2 (North-Holland, Amsterdam).

Brush, S. G., 2003, *The Kinetic Theory of Gases*, History of Modern Physical Sciences (Imperial College Press, London).

Bryant, G., S. R. Williams, L. Qian, I. K. Snook, E. Perez, and F. Pincet, 2002, Phys. Rev. E **66**, 060501.

Buhot, A., and W. Krauth, 1998, Phys. Rev. Lett. **80**, 3787.

Bültmann, M., and T. Schilling, 2020, Phys. Rev. E **102**, 042123.

Cabane, B., J. Li, F. Artzner, R. Botet, C. Labbez, G. Bareigts, M. Sztucki, and L. Goehring, 2016, Phys. Rev. Lett. **116**, 208001.

Caccamo, C., and G. Pellicane, 1997, Physica (Amsterdam) **235A**, 149.

Cacciuto, A., S. Auer, and D. Frenkel, 2003, J. Chem. Phys. **119**, 7467.

Cacciuto, A., S. Auer, and D. Frenkel, 2004, Nature (London) **428**, 404.

Cacciuto, A., and D. Frenkel, 2005, Phys. Rev. E **72**, 041604.

Cahn, J., and J. Hilliard, 1958, J. Chem. Phys. **28**, 258.

Cairns, R. J. R., R. H. Ottewill, D. W. J. Osmond, and L. Wagstaff, 1976, J. Colloid Interface Sci. **54**, 45.

Calleja, M., A. North, J. Powles, and G. Rickayzen, 1991, Mol. Phys. **73**, 973.

Cammarota, C., and G. Biroli, 2012, Proc. Natl. Acad. Sci. U.S.A. **109**, 8850.

Campo, M., and T. Speck, 2020, J. Chem. Phys. **152**, 014501.

Carbajal-Tinoco, M. D., G. Cruz de León, and J. Arauz-Lara, 1997, Phys. Rev. E **56**, 6962.

Carberry, D. M., J. C. Reid, G. M. Wang, E. M. Sevick, D. J. Searles, and D. J. Evans, 2004, Phys. Rev. Lett. **92**, 140601.

Carnahan, N. F., and K. E. Starling, 1969, J. Chem. Phys. **51**, 635.

Cates, M., K. Stratford, R. Adhikari, P. Stansell, J. Desplat, I. Pagonabarraga, and A. Wagner, 2004, J. Phys. Condens. Matter **16**, S3903.

Cates, M. E., and J. Tailleur, 2015, Annu. Rev. Condens. Matter Phys. **6**, 219.

Cavagna, A., 2009, Phys. Rep. **476**, 51.

Cebula, D. J., R. H. Ottewill, J. Ralston, and P. N. Pusey, 1981, J. Chem. Soc., Faraday Trans. 1 **77**, 2585.

Chacko, R. N., F. P. Landes, G. Biroli, O. Dauchot, A. J. Liu, and D. R. Reichman, 2021, Phys. Rev. Lett. **127**, 048002.

Chaikin, P. M., and T. C. Lubensky, 1995, *Principles of Condensed Matter Physics* (Cambridge University Press, Cambridge, England).

Chandler, D., and J. P. Garrahan, 2010, Annu. Rev. Phys. Chem. **61**, 191.

Chapman, S., and T. G. Cowling, 1990, *The Mathematical Theory of Non-uniform Gases: An Account of the Kinetic Theory of Viscosity, Thermal Conduction and Diffusion in Gases* (Cambridge University Press, Cambridge, England).

Charbonneau, B., P. Charbonneau, and G. Tarjus, 2012, Phys. Rev. Lett. **108**, 035701.

Charbonneau, B., P. Charbonneau, and G. Tarjus, 2013, J. Chem. Phys. **138**, 12A515.

Charbonneau, P., 2025, in *Women in the History of Quantum Physics*, edited by P. Charbonneau, M. Frank, M. van der Heijden, and D. Monaldi (Cambridge University Press, Cambridge, England, to be published).

Charbonneau, P., E. I. Corwin, R. C. Dennis, R. Díaz Hernández Rojas, H. Ikeda, G. Parisi, and F. Ricci-Tersenghi, 2021, Phys. Rev. E **104**, 014102.

Charbonneau, P., E. I. Corwin, G. Parisi, A. Poncet, and F. Zamponi, 2016, Phys. Rev. Lett. **117**, 045503.

Charbonneau, P., E. I. Corwin, G. Parisi, and F. Zamponi, 2015, Phys. Rev. Lett. **114**, 125504.

Charbonneau, P., Y. Hu, and P. K. Morse, 2024, Phys. Rev. E **109**, 054905.

Charbonneau, P., A. Ikeda, J. A. van Meel, and K. Miyazaki, 2010, Phys. Rev. E **81**, 040501(R).

Charbonneau, P., J. Kurchan, G. Parisi, P. Urbani, and F. Zamponi, 2014, Nat. Commun. **5**, 3725.

Charbonneau, P., J. Kurchan, G. Parisi, P. Urbani, and F. Zamponi, 2017, Annu. Rev. Condens. Matter Phys. **8**, 265.

Charbonneau, P., and P. K. Morse, 2021, Phys. Rev. Lett. **126**, 088001.

Charbonneau, P., P. K. Morse, W. Perkins, and F. Zamponi, 2021, Phys. Rev. E **104**, 064612.

Chaudhuri, P., L. Berthier, and S. Sastry, 2010, Phys. Rev. Lett. **104**, 165701.

Chen, K., *et al.*, 2010, Phys. Rev. Lett. **105**, 025501.

Chen, T., Q. Wen, P. Janmey, J. C. Crocker, and A. G. Yodh, 2010, Annu. Rev. Condens. Matter Phys. **1**, 301.

Chen, Z., P. Chaikin, W. Russell, W. Meyer, J. Zhu, R. Rogers, and R. Ottewill, 2001, Mater. Des. **22**, 529.

Cheng, X., J. H. McCoy, J. N. Israelachvili, and I. Cohen, 2011, Science **333**, 1276.

Cheng, X., X. Xu, S. A. Rice, A. R. Dinner, and I. Cohen, 2012, Proc. Natl. Acad. Sci. U.S.A. **109**, 63.

Cheng, Z., P. Chaikin, J. Zhu, W. Russel, and W. Meyer, 2001, Phys. Rev. Lett. **88**, 015501.

Cheng, Z., J. Zhu, P. Chaikin, S.-E. Phan, and W. B. Russel, 2002, Phys. Rev. E **65**, 041405.

Cheng, Z., J. Zhu, W. Russel, W. Meyer, and P. Chaikin, 2001, Appl. Opt. **40**, 4146.

Chikkadi, V., S. Mandal, B. Nienhuis, D. Raabe, F. Varnik, and P. Schall, 2012, Europhys. Lett. **100**, 56001.

Chikkadi, V., D. M. Miedema, M. T. Dang, B. Nienhuis, and P. Schall, 2014, Phys. Rev. Lett. **113**, 208301.

Chikkadi, V., G. Wegdam, D. Bonn, B. Nienhuis, and P. Schall, 2011, Phys. Rev. Lett. **107**, 198303.

Cho, Y.-S., G.-R. Yi, S.-H. Kim, D. J. Pine, and S.-M. Yang, 2005, Chem. Mater. **17**, 5006.

Cho, Y.-S., G.-R. Yi, J.-M. Lim, S.-H. Kim, V. N. Manoharan, D. J. Pine, and S.-M. Yang, 2005, J. Am. Chem. Soc. **127**, 15968.

Chowdhury, A., B. J. Ackerson, and N. Clark, 1985, Phys. Rev. Lett. **55**, 833.

Chui, S., 1991, Phys. Rev. B **43**, 10654.

Cichocki, B., M. Ekiel-Jeżewska, and E. Wajnryb, 1999, J. Chem. Phys. **111**, 3265.

Cichocki, B., and K. Hinsen, 1990, Physica (Amsterdam) **166A**, 473.

Ciliberto, S., 2017, Phys. Rev. X **7**, 021051.

Cipelletti, L., H. Bissig, V. Trappe, P. Ballesta, and S. Mazoyer, 2003, J. Phys. Condens. Matter **15**, S257.

Cipelletti, L., and D. A. Weitz, 1999, Rev. Sci. Instrum. **70**, 3214.

Clark, N. A., J. H. Lunacek, and G. Benedek, 1970, Am. J. Phys. **38**, 575.

Clisby, N., and B. M. McCoy, 2006, J. Stat. Phys. **122**, 15.

Cohen, E., R. Verberg, and I. De Schepper, 1998, Physica (Amsterdam) **251A**, 251.

Cohen, I., B. Davidovitch, A. Schofield, M. P. Brenner, and D. A. Weitz, 2006, Phys. Rev. Lett. **97**, 215502.

Cohen, I., T. G. Mason, and D. A. Weitz, 2004, Phys. Rev. Lett. **93**, 046001.

Coli, G. M., and M. Dijkstra, 2021, ACS Nano **15**, 4335.

Conrad, J. C., P. P. Dhillon, E. R. Weeks, D. R. Reichman, and D. Weitz, 2006, Phys. Rev. Lett. **97**, 265701.

Coslovich, D., M. Ozawa, and L. Berthier, 2018, J. Phys. Condens. Matter **30**, 144004.

Cottin, X., and P. Monson, 1993, J. Chem. Phys. **99**, 8914.

Cottin, X., and P. Monson, 1995, J. Chem. Phys. **102**, 3354.

Cottin, X., and P. Monson, 1997, J. Chem. Phys. **107**, 6855.

Courtemanche, D. J., T. A. Pasmore, and F. van Swol, 1993, Mol. Phys. **80**, 861.

Courtemanche, D. J., and F. van Swol, 1992, Phys. Rev. Lett. **69**, 2078.

Courtland, R. E., and E. R. Weeks, 2003, J. Phys. Condens. Matter **15**, S359.

Coussaert, T., and M. Baus, 1997, Phys. Rev. Lett. **79**, 1881.

Coussaert, T., and M. Baus, 1998a, J. Chem. Phys. **109**, 6012.

Coussaert, T., and M. Baus, 1998b, Phys. Rev. Lett. **80**, 4832.

Crisanti, A., and F. Ritort, 2003, J. Phys. A **36**, R181.

Crocker, J., J. Matteo, A. Dinsmore, and A. Yodh, 1999, Phys. Rev. Lett. **82**, 4352.

Crocker, J. C., and D. G. Grier, 1996, J. Colloid Interface Sci. **179**, 298.

Cugliandolo, L., J. Kurchan, and F. Ritort, 1994, Phys. Rev. B **49**, 6331.

Cugliandolo, L. F., and J. Kurchan, 1993, Phys. Rev. Lett. **71**, 173.

Cui, B., B. Lin, and S. A. Rice, 2001, J. Chem. Phys. **114**, 9142.

Cummins, H. Z., and H. L. Swinney, 1970, *Light Beating Spectroscopy*, Progress in Optics Vol. 8 (Elsevier, New York), Chap. III, pp. 133–200.

Curk, T., A. de Hoogh, F. J. Martinez-Veracoechea, E. Eiser, D. Frenkel, J. Dobnikar, and M. E. Leunissen, 2012, Phys. Rev. E **85**, 021502.

Curran, A., S. Tuohy, D. G. A. L. Aarts, T. Booth, M. J. Wilson, and R. P. A. Dullens, 2014, Optica **1**, 223.

Dang, M. T., L. Gartner, P. Schall, and E. Lerner, 2022, J. Phys. D **55**, 165304.

Dasgupta, T., G. M. Coli, and M. Dijkstra, 2020, ACS Nano **14**, 3957.

Dasgupta, T., and M. Dijkstra, 2018, Soft Matter **14**, 2465.

Dasgupta, T., J. R. Edison, and M. Dijkstra, 2017, J. Chem. Phys. **146**, 074903.

Dash, J. G., 1999, Rev. Mod. Phys. **71**, 1737.

Dauchot, O., F. Ladieu, and C. P. Royall, 2023, C. R. Phys. **24**, 25.

Davidchack, R. L., 2010, J. Chem. Phys. **133**, 234701.

Davidchack, R. L., and B. B. Laird, 1998, J. Chem. Phys. **108**, 9452.

Davidchack, R. L., and B. B. Laird, 2000, Phys. Rev. Lett. **85**, 4751.

Davidchack, R. L., B. B. Laird, and R. Roth, 2016, Condens. Matter Phys. **19**, 23001.

Davidchack, R. L., J. R. Morris, and B. B. Laird, 2006, J. Chem. Phys. **125**, 094710.

Deb, D., A. Winkler, M. Yamani, M. Oettel, P. Virnau, and K. Binder, 2011, J. Chem. Phys. **134**, 214706.

Debenedetti, P., 1996, *Metastable Liquids* (Princeton University, Princeton, NJ).

de Gennes, P. G., 1979, *Scaling Concepts in Polymer Physics* (Cornell University Press, Ithaca).

de Jager, M., and L. Filion, 2022, J. Chem. Phys. **157**, 154905.

de Kruif, C. G., W. J. Briels, R. P. May, and A. Vrij, 1988, Langmuir **4**, 668.

de Kruif, C. G., P. W. Rouw, J. W. Jansen, and A. Vrij, 1985, J. Phys. (Paris), Colloq. **46**, 295.

de Kruif, C. G., E. van Iersel, A. Vrij, and W. Russel, 1985, J. Chem. Phys. **83**, 4717.

de Nijs, B., S. Dussi, F. Smallenburg, J. D. Meeldijk, D. J. Groenendijk, L. Filion, A. Imhof, A. van Blaaderen, and M. Dijkstra, 2015, Nat. Mater. **14**, 56.

Denny, R. A., D. R. Reichman, and J.-P. Bouchaud, 2003, Phys. Rev. Lett. **90**, 025503.

Denton, A., and N. Ashcroft, 1989, Phys. Rev. A **39**, 4701.

Denton, A., and N. Ashcroft, 1990, Phys. Rev. A **42**, 7312.

Derber, S., T. Palberg, K. Schätzel, and J. Vogel, 1997, Physica (Amsterdam) **235A**, 204.

Derjaguin, B. V., and L. Landau, 1941, Acta Physicochim. USSR **14**, 633.

Derksen, J. T. P., F. P. Cuperus, and P. Kloster, 1995, Ind. Crops Prod. **3**, 225.

Desplat, J.-C., I. Pagonabarraga, and P. Bladon, 2001, Comput. Phys. Commun. **134**, 273.

de Villeneuve, V. W., L. Derendorp, D. Verboekend, E. C. Vermolen, W. K. Kegel, H. N. Lekkerkerker, and R. P. Dullens, 2009, Soft Matter **5**, 2448.

de Villeneuve, V. W. A., 2005, Science **309**5738, 1231.

de Villeneuve, V. W. A., R. P. A. Dullens, D. G. A. L. Aarts, E. Groeneveld, J. H. Scherff, W. K. Kegel, and H. N. W. Lekkerkerker, 2005, Science **309**, 1231.

de Villeneuve, V. W. A., D. Verboekend, R. P. A. Dullens, D. G. A. L. Aarts, W. K. Kegel, and H. N. W. Lekkerkerker, 2005, J. Phys. Condens. Matter **17**, S3371.

d'Haene, P., J. Mewis, and G. Fuller, 1993, J. Colloid Interface Sci. **156**, 350.

Dhont, J., and W. J. Briels, 2008, Rheol. Acta **47**, 257.

Dhont, J. K. G., 1996, *An Introduction to Dynamics of Colloids* (Elsevier Science, New York).

Dickman, R., P. Attard, and V. Simonian, 1997, J. Chem. Phys. **107**, 205.

Dijkstra, M., 2004, Phys. Rev. Lett. **93**, 108303.

Dijkstra, M., 2014, in *Advances in Chemical Physics*, Vol. 156, edited by S. A. Rice and A. R. Dinner (John Wiley & Sons, New York), pp. 35–71.

Dijkstra, M., J. M. Brader, and R. Evans, 1999, J. Phys. Condens. Matter **11**, 10079.

Dijkstra, M., and R. van Roij, 1997, Phys. Rev. E **56**, 5594.

Dijkstra, M., R. van Roij, and R. Evans, 1998, Phys. Rev. Lett. **81**, 2268.

Dijkstra, M., R. van Roij, and R. Evans, 1999a, Phys. Rev. Lett. **82**, 117.

Dijkstra, M., R. van Roij, and R. Evans, 1999b, Phys. Rev. E **59**, 5744.

Dinsmore, A., P. Warren, W. Poon, and A. Yodh, 1997, Europhys. Lett. **40**, 337.

Dinsmore, A., A. Yodh, and D. Pine, 1995, Phys. Rev. E **52**, 4045.

Dinsmore, A. D., A. G. Yodh, and D. J. Pine, 1996, Nature (London) **383**, 239.

Donev, A., S. Torquato, and F. H. Stillinger, 2005a, J. Comput. Phys. **202**, 737.

Donev, A., S. Torquato, and F. H. Stillinger, 2005b, Phys. Rev. E **71**, 011105.

Dong, J., F. Turci, R. L. Jack, M. A. Faers, and C. P. Royall, 2022, J. Chem. Phys. **156**, 214907.

Dorfman, J. R., H. van Beijeren, and T. R. Kirkpatrick, 2021, *Contemporary Kinetic Theory of Matter* (Cambridge University Press, Cambridge, England).

Doty, P., and J. T. Edsall, 1951, in *Advances in Protein Chemistry*, Vol. 6, edited by M. L. Anson, J. T. Edsall, and K. Bailey (Elsevier, New York), pp. 35–121.

Doty, P., and R. F. Steiner, 1952, J. Chem. Phys. **20**, 85.

Dress, C., and W. Krauth, 1995, J. Phys. A **28**, L597.

Dullens, R. P., V. W. de Villeneuve, M. C. Mourad, A. Petukhov, and W. K. Kegel, 2008, Eur. Phys. J. Appl. Phys. **44**, 21.

Dullens, R. P. A., 2006, Soft Matter **2**, 805.

Dullens, R. P. A., and C. Bechinger, 2011, Phys. Rev. Lett. **107**, 138301.

Dullens, R. P. A., M. Claesson, D. Derks, A. van Blaaderen, and W. K. Kegel, 2003, Langmuir **19**, 5963.

Dullens, R. P. A., and W. K. Kegel, 2004, Phys. Rev. Lett. **92**, 195702.

Dullens, R. P. A., D. G. A. L. Aarts, and W. Kegel, 2006a, Proc. Natl. Acad. Sci. U.S.A. **103**, 529.

Dullens, R. P. A., D. G. A. L. Aarts, and W. K. Kegel, 2006b, Phys. Rev. Lett. **97**, 228301.

Dunleavy, A. J., K. Wiesner, and C. P. Royall, 2012, Phys. Rev. E **86**, 041505.

Dunleavy, A. J., K. Wiesner, R. Yamamoto, and C. P. Royall, 2015, Nat. Commun. **6**, 6089.

Dünweg, B., and A. J. Ladd, 2009, in *Advanced Computer Simulation Approaches for Soft Matter Sciences III*, edited by C. Holm and K. Kremer (Springer, New York), p. 89.

Durán-Olivencia, F. J., and M. C. Gordillo, 2009, Phys. Rev. E **79**, 061111.

Durán-Olivencia, M. A., P. Yatsyshin, S. Kalliadasis, and J. F. Lutsko, 2018, New J. Phys. **20**, 083019.

Easteal, A., L. Woolf, and D. Jolly, 1983, Physica (Amsterdam) **121A**, 286.

Ediger, M., 2000, Annu. Rev. Phys. Chem. **51**, 99.

Edmond, K. V., C. R. Nugent, and E. R. Weeks, 2012, Phys. Rev. E **85**, 041401.

Edwards, S. F., and R. B. S. Oakeshott, 1989, Physica (Amsterdam) **157A**, 1080.

Einstein, A., 1906, Ann. Phys. (Berlin) **19**, 289.

Eldridge, M., P. Madden, and D. Frenkel, 1993a, Mol. Phys. **80**, 987.

Eldridge, M., P. Madden, and D. Frenkel, 1993b, Nature (London) **365**, 35.

Eldridge, M., P. Madden, and D. Frenkel, 1993c, Mol. Phys. **79**, 105.

Eldridge, M., P. Madden, P. Pusey, and P. Bartlett, 1995, Mol. Phys. **84**, 395.

Elgeti, J., R. G. Winkler, and G. Gompper, 2015, Rep. Prog. Phys. **78**, 056601.

Elliot, M. S., S. B. Haddon, and W. C. K. Poon, 2001, J. Phys. Condens. Matter **13**, L553.

El Masri, D., L. Berthier, and L. Cipelletti, 2010, Phys. Rev. E **82**, 031503.

El Masri, D., M. Pierno, L. Berthier, and L. Cipelletti, 2005, J. Phys. Condens. Matter **17**, S3543.

Engel, M., J. A. Anderson, S. C. Glotzer, M. Isobe, E. P. Bernard, and W. Krauth, 2013, Phys. Rev. E **87**, 042134.

Eslami, H., N. Khanjari, and F. Müller-Plathe, 2017, J. Chem. Theory Comput. **13**, 1307.

Espanol, P., and P. Warren, 1995, Europhys. Lett. **30**, 191.

Espanol, P., and P. B. Warren, 2017, J. Chem. Phys. **146**, 150901.

Espinosa, J. R., E. Sanz, C. Valeriani, and C. Vega, 2013, J. Chem. Phys. **139**, 144502.

Espinosa, J. R., C. Vega, and E. Sanz, 2014, J. Chem. Phys. **141**, 134709.

Espinosa, J. R., C. Vega, C. Valeriani, D. Frenkel, and E. Sanz, 2019, Soft Matter **15**, 9625.

Espinosa, J. R., C. Vega, C. Valeriani, and E. Sanz, 2016, J. Chem. Phys. **144**, 034501.

Evans, R., D. Frenkel, and M. Dijkstra, 2019, Phys. Today **72**, No. 2, 38.

Evers, F., C. Zunke, R. D. L. Hanes, J. Bewerunge, I. Ladadwa, A. Heuer, and S. U. Egelhaaf, 2013, Phys. Rev. E **88**, 022125.

Evers, W. H., B. D. Nijs, L. Filion, S. Castillo, M. Dijkstra, and D. Vanmaekelbergh, 2010, Nano Lett. **10**, 4235.

Falk, M. L., and J. S. Langer, 1998, Phys. Rev. E **57**, 7192.

Faraday, M., 1859, *Experimental Researches in Chemistry and Physics* (Taylor & Francis, London).

Farago, O., and Y. Kantor, 2000, Phys. Rev. E **61**, 2478.

Fasolo, M., and P. Sollich, 2003, Phys. Rev. Lett. **91**, 068301.

Fasolo, M., and P. Sollich, 2004, Phys. Rev. E **70**, 041410.

Fayen, E., M. Impéror-Clerc, L. Filion, G. Foffi, and F. Smallenburg, 2023, Soft Matter **19**, 2654.

Fernandez, N., R. Mani, D. Rinaldi, D. Kadau, M. Mosquet, H. Lombois-Burger, J. Cayer-Barrioz, H. J. Herrmann, N. D. Spencer, and L. Isa, 2013, Phys. Rev. Lett. **111**, 108301.

Fernández, L., V. Martin-Mayor, B. Seoane, and P. Verrocchio, 2012, Phys. Rev. Lett. **108**, 165701.

Fielding, S. M., 2014, Rep. Prog. Phys. **77**, 102601.

Fijnaut, H. M., C. Pathmamanoharan, E. A. Nieuwenhuis, and A. Vrij, 1978, Chem. Phys. Lett. **59**, 351.

Filion, L., and M. Dijkstra, 2009, Phys. Rev. E **79**, 046714.

Filion, L., M. Hermes, R. Ni, and M. Dijkstra, 2010, J. Chem. Phys. **133**, 244115.

Filion, L., M. Hermes, R. Ni, E. Vermolen, A. Kuijk, C. Christova, J. Stiefelhagen, T. Vissers, A. van Blaaderen, and M. Dijkstra, 2011, Phys. Rev. Lett. **107**, 168302.

Filion, L., M. Marechal, B. van Oorschot, D. Pelt, F. Smallenburg, and M. Dijkstra, 2009, Phys. Rev. Lett. **103**, 188302.

Filion, L., R. Ni, D. Frenkel, and M. Dijkstra, 2011, J. Chem. Phys. **134**, 134901.

Finney, J. L., 2013, Philos. Mag. **93**, 3940.

Fiore, A. M., and J. W. Swan, 2019, J. Fluid Mech. **878**, 544.

Fiorucci, G., G. M. Coli, J. T. Padding, and M. Dijkstra, 2020, J. Chem. Phys. **152**, 064903.

Fisher, D., and J. Weeks, 1983, Phys. Rev. Lett. **50**, 1077.

Fisher, I. Z., 1955, Sov. Phys. JETP **1**, 273.

Flenner, E., and G. Szamel, 2015, Nat. Commun. **6**, 7392.

Flomenbom, O., 2010, Phys. Rev. E **82**, 031126.

Foffi, G., W. Götze, F. Sciortino, P. Tartaglia, and T. Voigtman, 2003, Phys. Rev. Lett. **91**, 085701.

Folena, G., G. Biroli, P. Charbonneau, Y. Hu, and F. Zamponi, 2022, Phys. Rev. E **106**, 024605.

Folena, G., and F. Zamponi, 2023, SciPost Phys. **15**, 109.

Fontecha, A. B., H. J. Schöpe, H. König, T. Palberg, R. Messina, and H. Löwen, 2005, J. Phys. Condens. Matter **17**, S2779.

Foord, R., E. Jakeman, C. J. Oliver, E. R. Pike, R. J. Blagrove, E. Wood, and A. R. Peacocke, 1970, Nature (London) **227**, 242.

Forterre, Y., and O. Pouliquen, 2008, Annu. Rev. Fluid Mech. **40**, 1.

Fortini, A., and M. Dijkstra, 2006, J. Phys. Condens. Matter **18**, L371.

Foss, D. R., and J. F. Brady, 2000a, J. Rheol. **44**, 629.

Foss, D. R., and J. F. Brady, 2000b, J. Fluid Mech. **407**, 167.

Fraden, S., and G. Maret, 1990, Phys. Rev. Lett. **65**, 512.

Frank, F. C., 1952, Proc. R. Soc. A **215**, 43.

Franke, M., S. Golde, and H. J. Schöpe, 2014, Soft Matter **10**, 5380.

Franke, M., A. Lederer, and H. J. Schöpe, 2011, Soft Matter **7**, 11267.

Franosch, T., M. Grimm, M. Belushkin, F. M. Mor, G. Foffi, L. Forró, and S. Jeney, 2011, Nature (London) **478**, 85.

Frenkel, D., 2002, Science **296**, 65.

Frenkel, D., and A. J. C. Ladd, 1984, J. Chem. Phys. **81**, 3188.

Frenkel, D., and J. P. McTague, 1980, Annu. Rev. Phys. Chem. **31**, 491.

Frenkel, D., and B. Smit, 2002, *Understanding Molecular Simulation: From Algorithms to Applications*, 2nd ed. (Elsevier, New York).

Frenkel, D., R. Vos, C. de Kruif, and A. Vrij, 1986, J. Chem. Phys. **84**, 4625.

Fru Mbah, J., C. Wang, S. Englisch, P. K. Bommineni, N. R. Varela-Rosales, E. Spiecker, N. Vogel, and M. Engel, 2023, Nat. Commun. **14**, 5299.

Fu, L., C. Bian, C. W. Shields, D. F. Cruz, G. P. Lopez, and P. Charbonneau, 2017, Soft Matter **13**, 3296.

Fu, L., W. Steinhardt, H. Zhao, J. E. S. Socolar, and P. Charbonneau, 2016, Soft Matter **12**, 2505.

Fu, L., W. Steinhardt, H. Zhao, J. E. S. Socolar, and P. Charbonneau, 2017, Duke Digital Repository, 10.7924/G8SF2T3Z.

Fuchs, M., and M. Ballauff, 2005, J. Chem. Phys. **122**, 094707.

Fuchs, M., and M. E. Cates, 2005, J. Phys. Condens. Matter **17**, S1681.

Fuchs, M., I. Hofacker, and A. Latz, 1992, Phys. Rev. A **45**, 898.

Fuchs, M., and M. R. Mayr, 1999, Phys. Rev. E **60**, 5742.

Furukawa, A., M. Tateno, and H. Tanaka, 2018, Soft Matter **14**, 3738.

Gambardella, P., A. Dallmeyer, K. Maiti, M. C. Malagoli, W. Eberhardt, K. Kern, and C. Carbone, 2002, Nature (London) **416**, 301.

Ganapathi, D., K. H. Nagamanasa, A. K. Sood, and R. Ganapathy, 2018, Nat. Commun. **9**, 397.

Gandini, P. M., and J. M. Wills, 1992, Math. Pannon. **3**, 19.

Gao, Y., and M. Kilfoil, 2009, Opt. Express **17**, 4685.

Gasser, U., 2001, Science **292**, 258.

Gasser, U., 2009, J. Phys. Condens. Matter **21**, 203101.

Gauthier, J.-P., E. Fritsch, B. Aguilar-Reyes, A. Barreau, and B. Lasnier, 2004, C. R. Geosci. **336**, 187.

Gazuz, I., A. M. Puertas, T. Voigtmann, and M. Fuchs, 2009, Phys. Rev. Lett. **102**, 248302.

Ghosh, A., V. K. Chikkadi, P. Schall, J. Kurchan, and D. Bonn, 2010, Phys. Rev. Lett. **104**, 248305.

Ghosh, A., R. Mari, V. K. Chikkadi, P. Schall, J. Kurchan, and D. Bonn, 2010, Soft Matter **6**, 3082.

Gibbs, J., 1878, Trans. Conn. Acad. Arts Sci. **3**, 108.

Gispen, W., G. M. Coli, R. van Damme, C. P. Royall, and M. Dijkstra, 2023, ACS Nano **17**, 8807.

Gispen, W., and M. Dijkstra, 2023, J. Chem. Phys. **159**, 086101.

Gispen, W., and M. Dijkstra, 2024, J. Chem. Phys. **160**, 141102.

Godfrey, M. J., and M. A. Moore, 2014, Phys. Rev. E **89**, 032111.

Godfrey, M. J., and M. A. Moore, 2018, Phys. Rev. Lett. **121**, 075503.

Goetze, W., 2009, *Complex Dynamics of Glass-Forming Liquids: A Mode-Coupling Theory* (Oxford University Press, New York).

Gokhale, S., K. H. Nagamanasa, R. Ganapathy, and A. K. Sood, 2014, Nat. Commun. **5**, 4685.

Gokhale, S., K. H. Nagamanasa, A. K. Sood, and R. Ganapathy, 2016, J. Stat. Mech. 074013.

Gokhale, S., A. K. Sood, and R. Ganapathy, 2016, Adv. Phys. **65**, 363.

Golde, S., M. Franke, and H. J. Schöpe, 2013, AIP Conf. Proc. **1518**, 304.

Golde, S., T. Palberg, and H. J. Schöpe, 2016, Nat. Phys. **12**, 712.

Gomez-Solano, J. R., C. July, J. Mehl, and C. Bechinger, 2015, New J. Phys. **17**, 045026.

Gompper, G., T. Ihle, D. M. Kroll, and R. G. Winkler, 2009, in *Advanced Computer Simulation Approaches for Soft Matter*

Sciences III, edited by C. Holm and K. Kremer (Springer, New York), p. 1.

González, A., J. A. White, F. L. Román, and R. Evans, 1998, J. Chem. Phys. **109**, 3637.

González, A., J. A. White, F. L. Román, S. Velasco, and R. Evans, 1997, Phys. Rev. Lett. **79**, 2466.

Goodrich, C. P., A. J. Liu, and S. R. Nagel, 2012, Phys. Rev. Lett. **109**, 095704.

Gordillo, M. C., B. Martínez-Haya, and J. M. Romero-Enrique, 2006, J. Chem. Phys. **125**, 144702.

Gordon, J. M., J. H. Gibbs, and P. D. Fleming, 1976, J. Chem. Phys. **65**, 2771.

Goswami, A., I. S. Dalal, and J. K. Singh, 2021, Phys. Rev. Lett. **126**, 195702.

Götze, W., and T. Voigtmann, 2003, Phys. Rev. E **67**, 021502.

Götzelmann, B., R. Evans, and S. Dietrich, 1998, Phys. Rev. E **57**, 6785.

Götzelmann, B., R. Roth, S. Dietrich, M. Dijkstra, and R. Evans, 1999, Europhys. Lett. **47**, 398.

Gray, A. T., E. Mould, C. P. Royall, and I. Williams, 2015, J. Phys. Condens. Matter **27**, 194108.

Grier, D. G., 1997, Curr. Opin. Colloid Interface Sci. **2**, 264.

Grier, D. G., 2003, Nature (London) **424**, 810.

Grodon, C., M. Dijkstra, R. Evans, and R. Roth, 2004, J. Chem. Phys. **121**, 7869.

Grodon, C., M. Dijkstra, R. Evans, and R. Roth, 2005, Mol. Phys. **103**, 3009.

Groot, R., N. Faber, and J. van der Eerden, 1987, Mol. Phys. **62**, 861.

Groot, R. D., and P. B. Warren, 1997, J. Chem. Phys. **107**, 4423.

Gross, M., M. Cates, F. Varnik, and R. Adhikari, 2011, J. Stat. Mech. P03030.

Gruber, M., G. C. Abade, A. M. Puertas, and M. Fuchs, 2016, Phys. Rev. E **94**, 042602.

Guiselin, B., C. Scalliet, and L. Berthier, 2022, Nat. Phys. **18**, 468.

Gunton, J. D., M. San Miguel, and P. Sahni, 1983, *Phase Transitions and Critical Phenomena* (Academic Press, New York).

Guo, C., J. Wang, J. Li, Z. Wang, and S. Tang, 2016, J. Phys. Chem. Lett. **7**, 5008.

Gurin, P., G. Odriozola, and S. Varga, 2017, Phys. Rev. E **95**, 042610.

Gurin, P., and S. Varga, 2013, J. Chem. Phys. **139**, 244708.

Gurin, P., and S. Varga, 2015, J. Chem. Phys. **142**, 224503.

Gurin, P., S. Varga, M. González-Pinto, Y. Martínez-Ratón, and E. Velasco, 2017, J. Chem. Phys. **146**, 134503.

Gurin, P., S. Varga, and G. Odriozola, 2016, Phys. Rev. E **94**, 050603.

Guy, B. M., M. Hermes, and W. C. K. Poon, 2015, Phys. Rev. Lett. **115**, 088304.

Habdas, P., D. Schaar, A. C. Levitt, and E. R. Weeks, 2004, Europhys. Lett. **67**, 477.

Hachisu, S., and Y. Kobayashi, 1974, J. Colloid Interface Sci. **46**, 470.

Hachisu, S., and K. Takano, 1982, Adv. Colloid Interface Sci. **16**, 233.

Hales, T., *et al.*, 2017, Forum Math. Pi **5**, e2.

Hall, R. K., 1972, J. Chem. Phys. **57**, 2225.

Hallett, J. E., F. Turci, and C. P. Royall, 2018, Nat. Commun. **9**, 3272.

Hallett, J. E., F. Turci, and C. P. Royall, 2020, J. Stat. Mech. 014001.

Halperin, B., and D. R. Nelson, 1978, Phys. Rev. Lett. **41**, 121.

Hammond, A., and E. Corwin, 2017, Phys. Rev. E **96**, 042606.

Hammond, A. P., and E. I. Corwin, 2020, Proc. Natl. Acad. Sci. U.S.A. **117**, 5714.

Han, Y., N. Y. Ha, A. M. Alsayed, and A. G. Yodh, 2008, Phys. Rev. E **77**, 041406.

Han, Y., Y. Shokef, A. M. Alsayed, P. J. Yunker, T. C. Lubensky, and A. Yodh, 2008, Nature (London) **456**, 898.

Hansen, J.-P., and I. McDonald, 2013, *Theory of Simple Liquids*, 4th ed (Academic Press, London).

Harland, J., S. Henderson, S. M. Underwood, and W. van Megen, 1995, Phys. Rev. Lett. **75**, 3572.

Harland, J. L., and W. van Megen, 1997, Phys. Rev. E **55**, 3054.

Härtel, A., M. Oettel, R. E. Rozas, S. U. Egelhaaf, J. Horbach, and H. Löwen, 2012, Phys. Rev. Lett. **108**, 226101.

Hasaka, M., H. Nakashima, and K. Oki, 1984, Trans. Jpn. Inst. Met. **25**, 65.

Haw, M., W. Poon, and P. Pusey, 1998, Phys. Rev. E **57**, 6859.

Haymet, A., and D. W. Oxtoby, 1981, J. Chem. Phys. **74**, 2559.

He, Y., B. J. Ackerson, W. van Megen, S. M. Underwood, and K. Schätzel, 1996, Phys. Rev. E **54**, 5286.

Helfand, E., H. Frisch, and J. Lebowitz, 1961, J. Chem. Phys. **34**, 1037.

Hell, S. W., 2007, Science **316** 5828, 1153.

Henderson, D., 1975, Mol. Phys. **30**, 971.

Henderson, S. I., T. C. Mortensen, S. M. Underwood, and W. van Megen, 1996, Physica (Amsterdam) **233A**, 102.

Hendricks, J., R. Capellmann, A. B. Schofield, S. Egelhaaf, and M. Laurati, 2015, Phys. Rev. E **91**, 032308.

Heni, M., and H. Löwen, 1999, Phys. Rev. E **60**, 7057.

Heni, M., and H. Löwen, 2000, Phys. Rev. Lett. **85**, 3668.

Henk, M., and J. M. Wills, 2021, Beitr. Algebra Geom. **62**, 265.

Henrich, O., F. Weysser, M. E. Cates, and M. Fuchs, 2009, Phil. Trans. R. Soc. A **367**, 5033.

Hermes, M., and M. Dijkstra, 2010a, Europhys. Lett. **89**, 38005.

Hermes, M., and M. Dijkstra, 2010b, J. Phys. Condens. Matter **22**, 104114.

Hermes, M., B. M. Guy, W. C. Poon, G. Poy, M. E. Cates, and M. Wyart, 2016, J. Rheol. **60**, 905.

Hermes, M., E. C. M. Vermolen, M. E. Leunissen, D. L. J. Vossen, P. D. J. van Oostrum, M. Dijkstra, and A. van Blaaderen, 2011, Soft Matter **7**, 4623.

Hernández-Guzmán, J., and E. R. Weeks, 2009, Proc. Natl. Acad. Sci. U.S.A. **106**, 15198.

Hicks, C. L., M. J. Wheatley, M. J. Godfrey, and M. A. Moore, 2018, Phys. Rev. Lett. **120**, 225501.

Hilhorst, J., J. R. Wolters, and A. V. Petukhov, 2010, CrystEngComm **12**, 3820.

Hill, T. L., 1962, J. Chem. Phys. **36**, 3182.

Hiltner, P. A., and I. M. Krieger, 1969, J. Phys. Chem. **73**, 2386.

Hoddeson, L. E., H. Schubert, S. J. Heims, and G. Baym, 1992, in *Out of the Crystal Maze*, edited by L. E. Hoddeson, E. Braun, J. Teichmann, and S. Weart (Oxford University Press, New York), pp. 489–615.

Hoogenboom, J. P., D. Derks, P. Vergeer, and A. van Blaaderen, 2002, J. Chem. Phys. **117**, 11320.

Hoogenboom, J. P., A. K. van Langen-Suurling, J. Romijn, and A. van Blaaderen, 2003, Phys. Rev. Lett. **90**, 138301.

Hoogenboom, J. P., P. Vergeer, and A. van Blaaderen, 2003, J. Chem. Phys. **119**, 3371.

Hoogerbrugge, P., and J. Koelman, 1992, Europhys. Lett. **19**, 155.

Hoover, W. G., and F. H. Ree, 1968, J. Chem. Phys. **49**, 3609.

Hopkins, A. B., F. H. Stillinger, and S. Torquato, 2012, Phys. Rev. E **85**, 021130.

Howard, M. P., A. Nikoubashman, and J. C. Palmer, 2019, Curr. Opin. Chem. Eng. **23**, 34.

Howard, M. P., A. Z. Panagiotopoulos, and A. Nikoubashman, 2018, Comput. Phys. Commun. **230**, 10.

Hsiao, L. C., I. Saha-Dalal, R. G. Larson, and M. J. Solomon, 2017, Soft Matter **13**, 9229.

Hsu, C.-P., S. N. Ramakrishna, M. Zanini, N. D. Spencer, and L. Isa, 2018, Proc. Natl. Acad. Sci. U.S.A. **115**, 5117.

Hu, Y., and P. Charbonneau, 2020, arXiv:2009.11194.

Hu, Y., L. Fu, and P. Charbonneau, 2018, Mol. Phys. **116**, 3345.

Hudson, T. S., and P. Harrowell, 2011, J. Phys. Condens. Matter **23**, 194103.

Huerta, A., T. Bryk, V. M. Pergamenshchik, and A. Trokhymchuk, 2020, Phys. Rev. Res. **2**, 033351.

Hunt, N., R. Jardine, and P. Bartlett, 2000, Phys. Rev. E **62**, 900.

Hunter, G. L., K. V. Edmond, and E. R. Weeks, 2014, Phys. Rev. Lett. **112**, 218302.

Hunter, G. L., and E. R. Weeks, 2012, Rep. Prog. Phys. **75**, 066501.

Hunter, R. J., 2001, *Foundations of Colloid Science* (Oxford University Press, New York).

Hussain, S., and A. Haji-Akbari, 2020, J. Chem. Phys. **152**, 060901.

Hynninen, A.-P., and M. Dijkstra, 2003, Phys. Rev. E **68**, 021407.

Hynninen, A.-P., L. Filion, and M. Dijkstra, 2009, J. Chem. Phys. **131**, 064902.

Hynninen, A.-P., J. H. J. Thijssen, E. C. M. Vermolen, M. Dijkstra, and A. van Blaaderen, 2007, Nat. Mater. **6**, 202.

Iacopini, S., T. Palberg, and H. J. Schöpe, 2009, J. Chem. Phys. **130**, 084502.

Ihle, T., and D. Kroll, 2001, Phys. Rev. E **63**, 020201.

Ihler, R. K., 1979, *The Chemistry of Silica* (John Wiley & Sons, New York).

Ikeda, H., 2020, Phys. Rev. Lett. **125**, 038001.

Ikeda, H., F. Zamponi, and A. Ikeda, 2017, J. Chem. Phys. **147**, 234506.

Imhof, A., and J. Dhont, 1995a, Phys. Rev. Lett. **75**, 1662.

Imhof, A., and J. Dhont, 1995b, Phys. Rev. E **52**, 6344.

Imhof, A., A. van Blaaderen, G. Maret, J. Mellema, and J. Dhont, 1994, J. Chem. Phys. **100**, 2170.

Isa, L., R. Besseling, A. N. Morozov, and W. C. K. Poon, 2009, Phys. Rev. Lett. **102**, 058302.

Isa, L., R. Besseling, and W. C. K. Poon, 2007, Phys. Rev. Lett. **98**, 198305.

Isobe, M., A. S. Keys, D. Chandler, and J. P. Garrahan, 2016, Phys. Rev. Lett. **117**, 145701.

Isobe, M., and W. Krauth, 2015, J. Chem. Phys. **143**, 084509.

Ivlev, A., H. Lowen, G. E. Morfill, and C. P. Royall, 2012, *Complex Plasmas and Colloidal Dispersions: Particle-Resolved Studies of Classical Liquids and Solids* (World Scientific, Singapore).

Jack, R. L., A. J. Dunleavy, and C. P. Royall, 2014, Phys. Rev. Lett. **113**, 095703.

Jacob, A. R., E. Moghimi, and G. Petekidis, 2019, Phys. Fluids **31**, 087103.

Jamali, S., and J. F. Brady, 2019, Phys. Rev. Lett. **123**, 138002.

Janssen, L. M. C., 2019, J. Phys. Condens. Matter **31**, 503002.

Jarzynski, C., 1997, Phys. Rev. Lett. **78**, 2690.

Jenkins, M. C., and S. U. Egelhaaf, 2008, J. Colloid Interface Sci. **136**, 65.

Jenkins, M. C., M. D. Haw, G. C. Barker, W. C. K. Poon, and S. Egelhaaf, 2011, Phys. Rev. Lett. **107**, 038302.

Jensen, K., D. Pennachio, D. Recht, D. Weitz, and F. Spaepen, 2013, Soft Matter **9**, 320.

Jiang, L., J. W. J. de Folter, J. Huang, A. P. Philipse, W. K. Kegel, and A. V. Petukhov, 2013, Angew. Chem., Int. Ed. **52**, 3364.

Jin, Y., P. Urbani, F. Zamponi, and H. Yoshino, 2018, Sci. Adv. **4**, eaat6387.

Jin, Y., and H. Yoshino, 2017, Nat. Commun. **8**, 14935.

Jin, Y., and H. Yoshino, 2021, Proc. Natl. Acad. Sci. U.S.A. **118**, e2021794118.

Jones, D. A. R., B. Leary, and D. V. Boger, 1991, J. Colloid Interface Sci. **147**, 479.

Jover, J., A. Haslam, A. Galindo, G. Jackson, and E. Müller, 2012, J. Chem. Phys. **137**, 144505.

Jungblut, S., and C. Dellago, 2016, Eur. Phys. J. E **39**, 1.

Kac, M., G. E. Uhlenbeck, and P. C. Hemmer, 1963, J. Math. Phys. (N.Y.) **4**, 216.

Kale, S., A. Lederer, M. Oettel, and H. J. Schöpe, 2023, Soft Matter **19**, 2146.

Kamenetskiy, I. E., K. K. Mon, and J. K. Percus, 2004, J. Chem. Phys. **121**, 7355.

Kamien, R. D., 2007, *Entropic Attraction and Ordering*, Vol. 3 (Wiley-VCH Verlag, Weinheim), p. 1.

Kantor, Y., and M. Kardar, 2009, Phys. Rev. E **79**, 041109.

Kao, M., A. Yodh, and D. Pine, 1993, Phys. Rev. Lett. **70**, 242.

Kaplan, P., L. P. Faucheux, and A. J. Libchaber, 1994, Phys. Rev. Lett. **73**, 2793.

Kaplan, P., J. Rouke, A. Yodh, and D. Pine, 1994, Phys. Rev. Lett. **72**, 582.

Kaplan, P. D., A. G. Yodh, and D. J. Pine, 1992, Phys. Rev. Lett. **68**, 393.

Kapral, R., 2008, in *Advances in Chemical Physics*, Vol. 140, edited by S. A. Rice (John Wiley & Sons, New York), pp. 89–146.

Kapteijns, G., E. Bouchbinder, and E. Lerner, 2018, Phys. Rev. Lett. **121**, 055501.

Kapteijns, G., D. Richard, E. Bouchbinder, T. B. Schrøder, J. C. Dyre, and E. Lerner, 2021, J. Chem. Phys. **155**, 074502.

Karmakar, S., C. Dasgupta, and S. Sastry, 2014, Annu. Rev. Condens. Matter Phys. **5**, 255.

Kästner, J., 2011, Comput. Mol. Sci. **1**, 932.

Kauzmann, W., 1948, Chem. Rev. **43**, 219.

Kawafi, A., 2023, Ph.D. thesis (University of Bristol).

Kawaguchi, S., and K. Ito, 2005, in *Polymer Particles*, Advances in Polymer Science Vol. 175, edited by M. Okubo (Springer, New York), pp. 229–328.

Kawasaki, T., T. Araki, and H. Tanaka, 2007, Phys. Rev. Lett. **99**, 215701.

Kawasaki, T., and L. Berthier, 2018, Phys. Rev. E **98**, 012609.

Kawasaki, T., and H. Tanaka, 2010a, Proc. Natl. Acad. Sci. U.S.A. **107**, 14036.

Kawasaki, T., and H. Tanaka, 2010b, J. Phys. Condens. Matter **22**, 232102.

Kaya, D., N. L. Green, C. E. Maloney, and M. F. Islam, 2010, Science **329**, 656.

Kegel, W. K., 2001, J. Chem. Phys. **115**, 6538.

Kegel, W. K., and J. K. G. Dhont, 2000, J. Chem. Phys. **112**, 3431.

Kegel, W. K., and A. van Blaaderen, 2000, Science **287**, 290.

Kelton, K. F., 1991, *Crystal Nucleation in Liquids and Glasses, Solid State Physics* (Academic Press, Boston).

Ketzetzi, S., J. Russo, and D. Bonn, 2018, J. Chem. Phys. **148**, 064901.

Khlobystov, A. N., D. A. Britz, A. Ardavan, and G. A. D. Briggs, 2004, Phys. Rev. Lett. **92**, 245507.

Khlobystov, A. N., D. A. Britz, and G. A. D. Briggs, 2005, Acc. Chem. Res. **38**, 901.

Kirkpatrick, T. R., 1985, Phys. Rev. A **31**, 939.

Kirkpatrick, T. R., and P. G. Wolynes, 1987, Phys. Rev. A **35**, 3072.

Kirkwood, J. G., 1939, J. Chem. Phys. **7**, 919.

Kirkwood, J. G., 1951, *Phase Transformations in Solids* (Wiley, New York), p. 67.

Kirkwood, J. G., and E. Monroe, 1940, J. Chem. Phys. **8**, 845.

Kirkwood, J. G., and E. Monroe, 1941, J. Chem. Phys. **9**, 514.

Klein, W., and F. Leyvraz, 1986, Phys. Rev. Lett. **57**, 2845.

Klement, M., and M. Engel, 2019, J. Chem. Phys. **150**, 174108.

Klix, C. L., K. Murata, H. Tanaka, S. R. Williams, A. Malins, and C. P. Royall, 2013, Sci. Rep. **3**, 2072.

Klug, A., R. E. Franklin, and S. P. F. Humphreys-Owen, 1959, Biochim. Biophys. Acta **32**, 203.

Kobayashi, H., P. B. Rohrbach, R. Scheichl, N. B. Wilding, and R. L. Jack, 2021, Phys. Rev. E **104**, 044603.

Koch, H., C. Radin, and L. Sadun, 2005, Phys. Rev. E **72**, 016708.

Kodger, T. E., R. E. Guerra, and J. Sprakel, 2015, Sci. Rep. **5**, 14635.

Kofke, D. A., 1991, Mol. Simul. **7**, 285.

Kofke, D. A., and P. G. Bolhuis, 1999, Phys. Rev. E **59**, 618.

Kofke, D. A., and A. J. Post, 1993, J. Chem. Phys. **98**, 4853.

Koga, K., and H. Tanaka, 2006, J. Chem. Phys. **124**, 131103.

Kolafa, J., and M. Rottner, 2006, Mol. Phys. **104**, 3435.

Kool, L., P. Charbonneau, and K. E. Daniels, 2022, Phys. Rev. E **106**, 054901.

Kops-Werkhoven, M., and H. Fijnaut, 1982, J. Chem. Phys. **77**, 2242.

Kose, A., and S. Hachisu, 1974, J. Colloid Interface Sci. **46**, 460.

Kose, A., and S. Hachisu, 1976, J. Colloid Interface Sci. **55**, 487.

Kose, A., M. Ozaki, K. Takano, Y. Kobashi, and S. Hachisu, 1973, J. Colloid Interface Sci. **44**, 330.

Koshoji, R., and T. Ozaki, 2021, Phys. Rev. E **104**, 024101.

Kosterlitz, J. M., and D. J. Thouless, 1973, J. Phys. C **6**, 1181.

Koumakis, N., J. F. Brady, and G. Petekidis, 2013, Phys. Rev. Lett. **110**, 178301.

Koumakis, N., M. Laurati, S. U. Egelhaaf, J. F. Brady, and G. Petekidis, 2012, Phys. Rev. Lett. **108**, 098303.

Koumakis, N., M. Laurati, A. R. Jacob, K. J. Mutch, A. Abdellali, A. B. Schofield, S. U. Egelhaaf, J. F. Brady, and G. Petekidis, 2016, J. Rheol. **60**, 603.

Koumakis, N., A. B. Schofield, and G. Petekidis, 2008, Soft Matter **4**, 2008.

Kranendonk, W., and D. Frenkel, 1991, Mol. Phys. **72**, 679.

Kratzer, K., and A. Arnold, 2015, Soft Matter **11**, 2174.

Kuhnhold, A., H. Meyer, G. Amati, P. Pelagejcev, and T. Schilling, 2019, Phys. Rev. E **100**, 052140.

Kummerfeld, J. K., T. S. Hudson, and P. Harrowell, 2008, J. Phys. Chem. B **112**, 10773.

Kurita, R., D. Ruffner, and E. R. Weeks, 2012, Nat. Commun. **3**, 1127.

Kwasniewski, P., A. Fluerasu, and A. Madsen, 2014, Soft Matter **10**, 8698.

Laaksonen, A., R. McGraw, and H. Vehkamaki, 1999, J. Chem. Phys. **111**, 2019.

Lacasse, M.-D., G. S. Grest, and D. Levin, 1996, Phys. Rev. E **54**, 5436.

Lačević, N., F. W. Starr, T. B. Schrøder, V. N. Novikov, and S. C. Glotzer, 2002, Phys. Rev. E **66**, 030101.

Ladd, A. J. C., 1990, J. Chem. Phys. **93**, 3484.

Ladd, A. J. C., and R. Verberg, 2001, J. Stat. Phys. **104**, 1191.

Laird, B., and R. L. Davidchack, 2007, J. Phys. Chem. C **111**, 15952.

Langford, J. I., and A. Wilson, 1978, J. Appl. Crystallogr. **11**, 102.

Larson, R. G., 1998, *The Structure and Rheology of Complex Fluids*, 1st ed. (Oxford University Press, New York).

Lauga, E., and M. P. Brenner, 2004, Phys. Rev. Lett. **93**, 238301.

Laurati, M., T. Sentjabrskaja, J. Ruiz-Franco, S. U. Egelhaaf, and E. Zaccarelli, 2018, Phys. Chem. Chem. Phys. **20**, 18630.

Laurati, M., *et al.*, 2012, J. Phys. Condens. Matter **24**, 464104.

Lavergne, F. A., A. Curran, D. G. A. L. Aarts, and R. P. A. Dullens, 2018, Proc. Natl. Acad. Sci. U.S.A. **115**, 6922.

Lavergne, F. A., A. Curran, D. G. A. L. Aarts, and R. P. A. Dullens, 2019, Eur. Phys. J. B **92**, 142.

Lavergne, F. A., S. Diana, D. G. A. L. Aarts, and R. P. A. Dullens, 2016, Langmuir **32**, 12716.

Lavergne, F. A., D. G. A. L. Aarts, and R. P. A. Dullens, 2015, J. Phys. Condens. Matter **27**, 194117.

Lavergne, F. A., D. G. A. L. Aarts, and R. P. A. Dullens, 2017, Phys. Rev. X **7**, 041064.

Lazaro-Lazaro, E., *et al.*, 2019, Phys. Rev. E **99**, 042603.

Lebowitz, J., and J. Rowlinson, 1964, J. Chem. Phys. **41**, 133.

Lehmkühler, F., *et al.*, 2020, Sci. Adv. **6**, eabc5916.

Lekerkerker, H. N. W., and J. K. G. Dhont, 1984, J. Chem. Phys. **80**, 5790.

Lekkerkerker, H. N., W.-K. Poon, P. N. Pusey, A. Stroobants, and P. Warren, 1992, Europhys. Lett. **20**, 559.

Lennard-Jones, J. E., and A. Devonshire, 1937, Proc. R. Soc. A **163**, 53.

Leocmach, M., J. Russo, and H. Tanaka, 2013, J. Chem. Phys. **138**, 12A536.

Leocmach, M., and H. Tanaka, 2012, Nat. Commun. **3**, 974.

Leocmach, M., and H. Tanaka, 2013, Soft Matter **9**, 1447.

Leoni, F., and J. Russo, 2021, Phys. Rev. X **11**, 031006.

Leunissen, M., 2006, Ph.D. thesis (Utrecht Universiteit).

Leutheusser, E., 1984, Phys. Rev. A **29**, 2765.

Li, B., Y. Nishikawa, P. Höllmer, L. Carillo, A. Maggs, and W. Krauth, 2022, J. Chem. Phys. **157**, 234111.

Li, H., Y. Jin, Y. Jiang, and J. Z. Y. Chen, 2021, Proc. Natl. Acad. Sci. U.S.A. **118**, e2017392118.

Liao, M., X. Xiao, S. T. Chui, and Y. Han, 2018, Phys. Rev. X **8**, 021045.

Liber, S. R., S. Borohovich, A. V. Butenko, A. B. Schofield, and E. Sloutskin, 2013, Proc. Natl. Acad. Sci. U.S.A. **110**, 5769.

Lieb, E. H., and D. C. Mattis, 1966, *Mathematical Physics in One Dimension: Exactly Soluble Models of Interacting Particles*, Perspectives in Physics (Academic Press, New York).

Likos, C., and C. Henley, 1993, Philos. Mag. B **68**, 85.

Lin, N. Y. C., M. Bierbaum, P. Schall, J. P. Sethna, and I. Cohen, 2016, Nat. Mater. **15**, 1172.

Lin, N. Y. C., X. Cheng, and I. Cohen, 2014, Soft Matter **10**, 1969.

Lin, N. Y. C., S. Goyal, X. Cheng, R. Zia, A. Fernando, F. Escobedo, and I. Cohen, 2013, Phys. Rev. E **88**, 062309.

Lin, N. Y. C., B. M. Guy, M. Hermes, C. Ness, J. Sun, W. C. K. Poon, and I. Cohen, 2015, Phys. Rev. Lett. **115**, 228304.

Lin, N. Y. C., J. H. McCoy, X. Cheng, B. Leahy, J. N. Israelachvili, and I. Cohen, 2014, Rev. Sci. Instrum. **85**, 033905.

Lin, N. Y. C., C. Ness, M. E. Cates, J. Sun, and I. Cohen, 2016, Proc. Natl. Acad. Sci. U.S.A. **113**, 10774.

Lindquist, B. A., R. B. Jadrich, and T. M. Truskett, 2018, J. Chem. Phys. **148**, 191101.

Lionberger, R., and W. Russel, 1994, J. Rheol. **38**, 1885.

Liu, A. C. Y., E. J. Bøjesen, R. F. Tabor, S. T. Mudie, A. Zaccone, P. Harrowell, and T. C. Petersen, 2022, Sci. Adv. **8**, eabn0681.

Liu, A. J., and S. R. Nagel, 1998, Nature (London) **396**6706, 21.

Liu, A. J., and S. R. Nagel, 2010, Annu. Rev. Condens. Matter Phys. **1**, 347.

Liu, H., 2021, Mol. Phys. **119**, e1905897.

Liu, J., and E. Luijten, 2004, Phys. Rev. Lett. **92**, 035504.

Liu, P., J. W. de Folter, A. V. Petukhov, and A. P. Philipse, 2015, Soft Matter **11**, 6201.

Liu, Y., J. Bławzdziewicz, B. Cichocki, J. K. G. Dhont, M. Lisicki, E. Wajnry, Y.-N. Young, and P. R. Lang, 2015b, Soft Matter **11**, 7316.

Liu, Y., K. V. Edmond, A. Curran, C. Bryant, B. Peng, D. G. A. L. Aarts, S. Sacanna, and R. P. A. Dullen, 2016, Adv. Mater. **28**, 8001.

Liu, Y., T. Yanagishima, A. Curran, K. V. Edmond, S. Sacanna, and R. P. A. Dullen, 2019, Langmuir **35**, 7962.

Lohr, M. A., A. M. Alsayed, B. G. Chen, Z. Zhang, R. D. Kamien, and A. G. Yodh, 2010, Phys. Rev. E **81**, 040401.

Long, J. A., D. W. J. Osmond, and B. Vincent, 1973, J. Colloid Interface Sci. **42**, 545.

López de Haro, M., C. F. Tejero, and A. Santos, 2013, J. Chem. Phys. **138**, 161104.

Löwen, H., 1990, J. Phys. Condens. Matter **2**, 8477.

Löwen, H., 1994, Phys. Rep. **237**, 249.

Lu, P. J., J. C. Conrad, H. M. Wyss, A. B. Schofield, and D. A. Weitz, 2006, Phys. Rev. Lett. **96**, 028306.

Lu, P. J., and D. A. Weitz, 2013, Annu. Rev. Condens. Matter Phys. **4**, 217.

Lubachevsky, B. D., 1991, J. Comput. Phys. **94**, 255.

Lubchenko, V., and P. G. Wolynes, 2007, Annu. Rev. Phys. Chem. **58**, 235.

Lurio, L., *et al.*, 2000, Phys. Rev. Lett. **84**, 785.

Lutsko, J. F., 2019, Sci. Adv. **5**, eaav7399.

Lutsko, J. F., and M. Baus, 1990, Phys. Rev. Lett. **64**, 761.

Lynch, J. M., G. C. Cianci, and E. R. Weeks, 2008, Phys. Rev. E **78**, 031410.

Lyon, L. A., and A. Fernandez-Nieves, 2012, Annu. Rev. Phys. Chem. **63**, 25.

Ma, G. H., T. Fukutomi, and N. Morone, 1994, J. Colloid Interface Sci. **168**, 393.

MacDowell, L. G., 2023, Phys. Rev. E **108**, L022801.

Mackay, A. L., 1962, Acta Crystallogr. **15**, 916.

Macpherson, A., Y. P. Carignan, and T. Vladimiroff, 1987, J. Chem. Phys. **87**, 1768.

Maibaum, L., M. Schmidt, and H. Löwen, 2001, Phys. Rev. E **63**, 051401.

Malevanets, A., and R. Kapral, 1999, J. Chem. Phys. **110**, 8605.

Malins, A., S. R. Williams, J. Eggers, and C. P. Royall, 2013, J. Chem. Phys. **139**, 234506.

Mandal, S., V. Chikkadi, B. Nienhuis, D. Raabe, P. Schall, and F. Varnik, 2013, Phys. Rev. E **88**, 022129.

Mandal, S., S. Lang, M. Gross, M. Oettel, D. Raabe, T. Franosch, and F. Varnik, 2014, Nat. Commun. **5**, 4435.

Manoharan, V. N., 2006, Solid State Commun. **139**, 557.

Manoharan, V. N., M. T. Elsesser, and D. J. Pine, 2003, Science **301**5632, 483.

Mansoori, G., N. F. Carnahan, K. Starling, and T. Leland, Jr., 1971, J. Chem. Phys. **54**, 1523.

Mao, Y., M. Cates, and H. Lekkerkerker, 1995, Physica (Amsterdam) **222A**, 10.

Marchetti, M. C., J. F. Joanny, S. Ramaswamy, T. B. Liverpool, J. Prost, M. Rao, and R. A. Simha, 2013, Rev. Mod. Phys. **85**, 1143.

Marcus, A. H., B. Lin, and S. A. Rice, 1996, Phys. Rev. E **53**, 1765.

Marcus, A. H., and S. A. Rice, 1997, Phys. Rev. E **55**, 637.

Marcus, A. H., J. Schofield, and S. Rice, 1999, Phys. Rev. E **60**, 5725.

Marechal, M., and M. Dijkstra, 2007, Phys. Rev. E **75**, 061404.

Marechal, M., M. Hermes, and M. Dijkstra, 2011, J. Chem. Phys. **135**, 034510.

Maret, G., and P. E. Wolf, 1987, Z. Phys. B **65**, 409.

Mari, R., R. Seto, J. F. Morris, and M. M. Denn, 2015, Proc. Natl. Acad. Sci. U.S.A. **112**, 15326.

Marín, M., D. Risso, and P. Cordero, 1993, J. Comput. Phys. **109**, 306.

Marín-Aguilar, S., F. Camerin, S. van der Ham, A. Feasson, R. Vutukuri, and M. Dijkstra, 2023, Nat. Commun. **14**, 7896.

Marín-Aguilar, S., H. H. Wensink, G. Foffi, and F. Smallenburg, 2020, Phys. Rev. Lett. **124**, 208005.

Mark, D., S. Haeberle, G. Roth, F. von Stetten, and R. Zengerle, 2010, Chem. Soc. Rev. **39**, 1153.

Martelozzo, V., A. B. Schofield, W. Poon, and P. Pusey, 2002, Phys. Rev. E **66**, 021408.

Martin, S., G. Bryant, and W. van Megen, 2003, Phys. Rev. E **67**, 061405.

Martinez, V. A., G. Bryant, and W. van Megen, 2008, Phys. Rev. Lett. **101**, 135702.

Martinez, V. A., E. Zaccarelli, E. Sanz, C. Valeriani, and W. van Megen, 2014, Nat. Commun. **5**, 5503.

Martin-Mayor, V., B. Seoane, and D. Yllanes, 2011, J. Stat. Phys. **144**, 554.

Mason, T. G., and D. A. Weitz, 1995a, Phys. Rev. Lett. **75**, 2770.

Mason, T. G., and D. A. Weitz, 1995b, Phys. Rev. Lett. **74**, 1250.

Maßhoff, P., I. Elsner, M. A. Escobedo-Sánchez, J. P. Segovia-Guttiérrez, A. Pamvouxoglou, and S. U. Egelhaaf, 2020, J. Phys. Mater. **3**, 035004.

Mau, S.-C., and D. A. Huse, 1999, Phys. Rev. E **59**, 4396.

Medina-Noyola, M., 1988, Phys. Rev. Lett. **60**, 2705.

Meeker, S. P., W. C. K. Poon, and P. N. Pusey, 1997, Phys. Rev. E **55**, 5718.

Melrose, J. R., and R. C. Ball, 2004, J. Rheol. **48**, 937.

Mermin, N. D., and H. Wagner, 1966, Phys. Rev. Lett. **17**, 1133.

Metropolis, N., A. W. Rosenbluth, M. N. Rosenbluth, A. H. Teller, and E. Teller, 1953, J. Chem. Phys. **21**, 1087.

Mewis, J., W. Frith, T. A. Strivens, and W. B. Russel, 1989, AIChE J. **35**, 415.

Mewis, J., and N. Wagner, 2011, *Colloidal Suspension Rheology* (Cambridge University Press, London).

Michailidou, V., G. Petekidis, J. W. Swan, and J. Brady, 2009, Phys. Rev. Lett. **102**, 068302.

Mickelson, W., S. Aloni, W. Q. Han, J. Cumings, and A. Zettl, 2003, Science **300**, 467.

Mikhael, J., J. Roth, L. Helden, and C. Bechinger, 2008, Nature (London) **454**, 501.

Milinković, K., J. T. Padding, and M. Dijkstra, 2011, Soft Matter **7**, 11177.

Mishra, C., P. Habdas, and A. Yodh, 2019, J. Phys. Chem. B **123**, 5181.

Mishra, C., X. Ma, P. Habdas, K. B. Aptowicz, and A. Yodh, 2019, Phys. Rev. E **100**, 020603(R).

Mohanty, P. S., D. Paloli, J. J. Crassous, E. Zaccarelli, and P. Schurtenberger, 2014, J. Chem. Phys. **140**, 094901.

Moir, C., L. Lue, and M. N. Bannerman, 2021, J. Chem. Phys. **155**, 064504.

Mon, K. K., and J. K. Percus, 2000, J. Chem. Phys. **112**, 3457.

Mon, K. K., and J. K. Percus, 2002, J. Chem. Phys. **117**, 2289.

Mon, K. K., and J. K. Percus, 2003, J. Chem. Phys. **119**, 3343.

Montero de Hijes, P., P. Rosales-Pelaez, C. Valeriani, P. Pusey, and E. Sanz, 2017, Phys. Rev. E **96**, 020602(R).

Montero de Hijes, P., K. Shi, E. G. Noya, E. Santiso, K. Gubbins, E. Sanz, and C. Vega, 2020, J. Chem. Phys. **153**, 191102.

Moroni, D., T. S. van Erp, and P. G. Bolhuis, 2004, Physica (Amsterdam) **340A**, 395.

Morrell, W. E., and J. H. Hildebrand, 1936, J. Chem. Phys. **4**, 224.

Morris, J. F., 2018, Phys. Rev. Fluids **3**, 110508.

Morse, D. C., and T. A. Witten, 1993, Europhys. Lett. **22**, 549.

Morse, P. K., and P. Charbonneau, 2024, *Amorphous Packings of Spheres* (Royal Society of Chemistry, Cambridge, England).

Mountain, R. D., and D. Thirumalai, 1987, Phys. Rev. A **36**, 3300.

Moussaïd, A., and P. N. Pusey, 1999, Phys. Rev. E **60**, 5670.

Mu, Y., A. Houk, and X. Song, 2005, J. Phys. Chem. B **109**, 6500.

Mughal, A., H. K. Chan, and D. Weaire, 2011, Phys. Rev. Lett. **106**, 115704.

Mughal, A., H. K. Chan, D. Weaire, and S. Hutzler, 2012, Phys. Rev. E **85**, 051305.

Mulero, A., I. Cachadina, and J. Solana, 2009, Mol. Phys. **107**, 1457.

Mullins, W., 1984, J. Chem. Phys. **81**, 1436.

Mura, F., and A. Zaccone, 2016, Phys. Rev. E **93**, 042803.

Murray, C., and D. van Winkle, 1987, Phys. Rev. Lett. **58**, 1200.

Nagamanasa, S., K. H. Nagamanasa, A. K. Sood, and R. Ganapathy, 2015, Nat. Phys. **11**, 403.

Nairn, J. H., and J. E. Kilpatrick, 1972, Am. J. Phys. **40**, 503.

Nakagaki, M., K. Shinoda, E. Matijević, and B.-i. Tamamushi, 1983, *Frontiers in Colloid Science—In Memoriam: Professor Dr. Bun-ichi Tamamushi*, Progress in Colloid and Polymer Science Vol. 68 (Steinkopff, Dresden).

Nakayama, Y., and R. Yamamoto, 2005, Phys. Rev. E **71**, 036707.

Nayhouse, M., A. M. Amlani, and G. Orkoulas, 2011, J. Phys. Condens. Matter **23**, 325106.

Nelson, D. R., and F. Spaepen, 1989, in *Solid State Physics*, Vol. 42, edited by H. Ehrenreich and D. Turnbull (Academic Press, New York), pp. 1–90.

Németh, Z., and H. Löwen, 1999, Phys. Rev. E **59**, 6824.

Neser, S., C. Bechinger, P. Leiderer, and T. Palberg, 1997, Phys. Rev. Lett. **79**, 2348.

Ni, R., F. Smallenburg, L. Filion, and M. Dijkstra, 2011, Mol. Phys. **109**, 1213.

Ninarello, A., L. Berthier, and D. Coslovich, 2017, Phys. Rev. X **7**, 021039.

Niss, M., 2018, Perspect. Sci. **26**, 185.

Norman, J., E. L. Sorrell, Y. Hu, V. Siripurapu, J. Garcia, J. Bagwell, P. Charbonneau, S. R. Lubkin, and M. Bagnat, 2018, Phil. Trans. R. Soc. B **373**1759.

Noya, E., and N. G. Almarza, 2015, Mol. Phys. **113**, 1061.

Nugent, C. R., K. V. Edmond, H. V. Patel, and E. R. Weeks, 2007, Phys. Rev. Lett. **99**, 025702.

Oettel, M., S. Dorosz, M. Berghoff, B. Nestler, and T. Schilling, 2012, Phys. Rev. E **86**, 021404.

Oğuz, E. C., M. Marechal, F. Ramiro-Manzano, I. Rodriguez, R. Messina, F. J. Meseguer, and H. Löwen, 2012, Phys. Rev. Lett. **109**, 218301.

Ohtsuka, T., C. P. Royall, and H. Tanaka, 2008, Europhys. Lett. **84**, 46002.

Okamoto, S., and S. Hachisu, 1977, J. Colloid Interface Sci. **62**, 172.

O'Malley, B., and I. Snook, 2003, Phys. Rev. Lett. **90**, 085702.

Oosawa, F., 2021, J. Chem. Phys. **155**, 084104.

Orr, N. H. P., T. Yanagishima, E. Maire, and R. P. A. Dullens, 2021, Phys. Rev. Mater. **5**, 123605.

Orsi, D., A. Fluerasu, A. Moussaïd, F. Zontone, L. Cristofolini, and A. Madsen, 2012, Phys. Rev. E **85**, 011402.

Ortlieb, L., T. Ingebrigtsen, J. E. Hallett, F. Turci, and C. P. Royall, 2023, Nat. Commun. **14**, 2621.

O'Toole, P. I., and T. S. Hudson, 2011, J. Phys. Chem. C **115**, 19037.

Ottewill, R., and N. S. J. Williams, 1987, Nature (London) **325**6101, 232.

Overbeek, J. T. G., 1966, Discuss. Faraday Soc. **42**, 7.

Oxtoby, D., and D. Kashchiev, 1994, J. Chem. Phys. **100**, 7665.

Ozawa, M., L. Berthier, G. Biroli, A. Rosso, and G. Tarjus, 2018, Proc. Natl. Acad. Sci. U.S.A. **115**, 6656.

Ozawa, M., T. Kuroiwa, A. Ikeda, and K. Miyazaki, 2012, Phys. Rev. Lett. **109**, 205701.

Palberg, T., 1999, J. Phys. Condens. Matter **11**, R323.

Palberg, T., 2014, J. Phys. Condens. Matter **26**, 333101.

Papir, Y. S., and I. M. Krieger, 1970, J. Colloid Interface Sci. **34**, 126.

Parisi, G., P. Urbani, and F. Zamponi, 2020, *Theory of Simple Glasses: Exact Solutions in Infinite Dimensions* (Cambridge University Press, Cambridge, England), ISBN 9781108126106.

Patey, G., and J. Valleau, 1973, Chem. Phys. Lett. **21**, 297.

Paul, G., 2007, J. Comput. Phys. **221**, 615.

Paulin, S. E., and B. J. Ackerson, 1990, Phys. Rev. Lett. **64**, 2663.

Paulin, S. E., and B. J. Ackerson, 1996, J. Colloid Interface Sci. **178**, 251.

Peierls, R. E., 1955, *Quantum Theory of Solids* (Oxford University Press, New York).

Peng, Y., W. Chen, T. M. Fischer, D. A. Weitz, and P. Tong, 2009, J. Fluid Mech. **618**, 243.

Peng, Y., F. Wang, Z. Wang, A. M. Alsayed, Z. Zhang, A. G. Yodh, and Y. Han, 2015, Nat. Mater. **14**, 101.

Peng, Y., Z. Wang, A. M. Alsayed, A. G. Yodh, and Y. Han, 2010, Phys. Rev. Lett. **104**, 205703.

Percus, J. K., and G. J. Yevick, 1958, Phys. Rev. **110**, 1.

Perera, D., and P. Harrowell, 1996, J. Chem. Phys. **104**, 2369.

Perrin, J., 1913, *Les Atomes* (Felix Alcan, Paris).

Petekidis, G., D. Vlassopoulos, and P. N. Pusey, 2003, Faraday Discuss. **123**, 287.

Petukhov, A. V., D. G. A. L. Aarts, I. P. Dolbnya, E. H. A. De Hoog, K. Kassapidou, G. J. Vroege, W. Bras, and H. N. W. Lekkerkerker, 2002, Phys. Rev. Lett. **88**, 208301.

Pham, K. N., 2002, Science **296**5565, 104.

Pham, K. N., S. U. Egelhaaf, A. Moussaïd, and P. N. Pusey, 2004, Rev. Sci. Instrum. **75**, 2419.

Phan, S.-E., W. B. Russel, Z. Cheng, J. Zhu, P. M. Chaikin, J. H. Dunsmuir, and R. H. Ottewill, 1996, Phys. Rev. E **54**, 6633.

Phan, S.-E., W. B. Russel, J. Zhu, and P. M. Chaikin, 1998, J. Chem. Phys. **108**, 9789.

Piazza, R., T. Bellini, and V. Degiorgio, 1993, Phys. Rev. Lett. **71**, 4267.

Pickett, G. T., M. Gross, and H. Okuyama, 2000, Phys. Rev. Lett. **85**, 3652.

Pieprzyk, S., M. N. Bannerman, A. C. Bra?ka, M. Chudak, and D. M. Heyes, 2019, Phys. Chem. Chem. Phys. **21**, 6886.

Pieranski, P., L. Strzelecki, and B. Pansu, 1983, Phys. Rev. Lett. **50**, 900.

Pinchaipat, R., M. Campo, F. Turci, J. E. Hallett, T. Speck, and C. P. Royall, 2017, Phys. Rev. Lett. **119**, 028004.

Polson, J. M., E. Trizac, S. Pronk, and D. Frenkel, 2000, J. Chem. Phys. **112**, 5339.

Poon, W. C. K., 2002, J. Phys. Condens. Matter **14**, R859.

Poon, W. C. K., P. N. Pusey, and H. N. W. Lekkerkerker, 1996, Phys. World **9**, 27.

Poon, W. C. K., and P. B. Warren, 1994, Europhys. Lett. **28**, 513.

Poon, W. C. K., E. R. Weeks, and C. P. Royall, 2012, Soft Matter **8**, 21.

Prestipino, S., A. Laio, and E. Tosatti, 2014, J. Chem. Phys. **140**, 094501.

Pronk, S., and D. Frenkel, 1999, J. Chem. Phys. **110**, 4589.

Pronk, S., and D. Frenkel, 2001, J. Phys. Chem. B **105**, 6722.

Pronk, S., and D. Frenkel, 2003, Phys. Rev. Lett. **90**, 255501.

Pronk, S., and D. Frenkel, 2004, J. Chem. Phys. **120**, 6764.

Puertas, A. M., and T. Voigtmann, 2014, J. Phys. Condens. Matter **26**, 243101.

Pusey, P., 1987, J. Phys. (Paris) **48**, 709.

Pusey, P., W. C. Poon, S. Ilett, and P. Bartlett, 1994, J. Phys. Condens. Matter **6**, A29.

Pusey, P., and W. van Megen, 1987, Phys. Rev. Lett. **59**, 2083.

Pusey, P., E. Zaccarelli, C. Valeriani, E. Sanz, W. C. Poon, and M. E. Cates, 2009, Phil. Trans. R. Soc. A **367**, 4993.

Pusey, P. N., 2002, *Neutrons, X-Rays and Light* (Elsevier, New York), Chap. 1.

Pusey, P. N., D. W. Schaefer, D. E. Koppel, R. D. Camerini-Otero, and R. M. Franklin, 1972, J. Phys. (Paris), Colloq. **33**, 163.

Pusey, P. N., and R. J. A. Tough, 1983, Faraday Discuss. Chem. Soc. **76**, 123.

Pusey, P. N., and W. van Megen, 1983, J. Phys. (Paris) **44**, 285.

Pusey, P. N., and W. van Megen, 1986, Nature (London) **320**, 340.

Pusey, P. N., and W. van Megen, 1989, Physica (Amsterdam) **157A**, 705.

Pusey, P. N., M. Vaughan, and G. Williams, 1974, J. Chem. Soc., Faraday Trans. 1 **70**, 1696.

Qi, W., and M. Dijkstra, 2015, Soft Matter **11**, 2852.

Qi, W., A. P. Gantapara, and M. Dijkstra, 2014, Soft Matter **10**, 5449.

Qi, W., Y. Peng, Y. Han, R. K. Bowles, and M. Dijkstra, 2015, Phys. Rev. Lett. **115**, 185701.

Qiu, X., X. Wu, J. Xue, D. Pine, D. Weitz, and P. M. Chaikin, 1990, Phys. Rev. Lett. **65**, 516.

Radu, M., and T. Schilling, 2014, Europhys. Lett. **105**, 26001.

Ramakrishnan, T., and M. Yussouff, 1977, Solid State Commun. **21**, 389.

Ramakrishnan, T., and M. Yussouff, 1979, Phys. Rev. B **19**, 2775.

Ramsteiner, I. B., D. A. Weitz, and F. Spaepen, 2010, Phys. Rev. E **82**, 041603.

Rapaport, D. C., 2004, *The Art of Molecular Dynamics Simulation* (Cambridge University Press, Cambridge, England).

Rasa, M., and A. P. Phillipse, 2004, Nature (London) **429**, 857.

Ree, F. H., R. N. Keeler, and S. L. McCarthy, 1966, J. Chem. Phys. **44**, 3407.

Reinke, D., H. Stark, H.-H. von Gruenberg, A. B. Schofield, G. Maret, and U. Gasser, 2007, Phys. Rev. Lett. **98**, 038301.

Reiss, H., H. L. Frisch, and J. L. Lebowitz, 1959, J. Chem. Phys. **31**, 369.

Richard, D., and T. Speck, 2015, Sci. Rep. **5**, 14610 .

Richard, D., and T. Speck, 2018a, J. Chem. Phys. **148**, 124110.

Richard, D., and T. Speck, 2018b, J. Chem. Phys. **148**, 224102.

Richard, D., and T. Speck, 2019, Phys. Rev. E **99**, 062801.

Richert, R., 2011, Annu. Rev. Phys. Chem. **62**, 65.

Rintoul, M. D., and S. Torquato, 1996, J. Chem. Phys. **105**, 9258.

Rios de Anda, I., F. Turci, R. P. Sear, and C. P. Royall, 2017, J. Chem. Phys. **147**, 124504.

Roberts, S. G., T. A. Wood, W. J. Frith, and P. Bartlett, 2007, J. Chem. Phys. **126**, 194503.

Robinson, J. F., M. J. Godfrey, and M. A. Moore, 2016, Phys. Rev. E **93**, 032101.

Robinson, J. F., R. Roth, and C. P. Royall, 2020, Philos. Mag. **100**, 2614.

Robinson, J. F., F. Turci, R. Roth, and C. P. Royall, 2019, Phys. Rev. Lett. **122**, 068004.

Robles, M., M. López de Haro, A. Santos, and S. Bravo Yuste, 1998, J. Chem. Phys. **108**, 1290.

Rodriguez Fris, J. A., G. A. Appignanesi, and E. R. Weeks, 2011, Phys. Rev. Lett. **107**, 065704.

Rodriguez Fris, J. A., E. R. Weeks, F. Sciortino, and G. A. Appignanesi, 2018, Phys. Rev. E **97**, 060601(R).

Rogal, J., and G. D. Leines, 2023, Phil. Trans. R. Soc. A **381**, 20220249.

Rosenbluth, M. N., and A. W. Rosenbluth, 1954, J. Chem. Phys. **22**, 881.

Rosenfeld, Y., 1989, Phys. Rev. Lett. **63**, 980.

Rosenfeld, Y., 1994, Phys. Rev. Lett. **72**, 3831.

Roth, R., 2010, J. Phys. Condens. Matter **22**, 063102.

Roth, R., R. Evans, and S. Dietrich, 2000, Phys. Rev. E **62**, 5360.

Rowlinson, J., 2005, *Cohesion: A Scientific History of Intermolecular Forces* (Cambridge University Press, Cambridge, England), ISBN 9781139435888.

Royall, C. P., P. Charbonneau, M. Dijkstra, J. Russo, F. Smallenburg, T. Speck, and C. Valeriani, 2024, Duke Digital Repository, 10.7924/r4x35163x.

Royall, C. P., J. Dzubiella, M. Schmidt, and A. van Blaaderen, 2007, Phys. Rev. Lett. **98**, 188304.

Royall, C. P., M. A. Faers, S. Fussell, and J. Hallett, 2021, J. Phys. Condens. Matter **33**, 453002.

Royall, C. P., M. E. Leunissen, A.-P. Hyninnen, M. Dijkstra, and A. van Blaaderen, 2006, J. Chem. Phys. **124**, 244706.

Royall, C. P., M. E. Leunissen, and A. van Blaaderen, 2003, J. Phys. Condens. Matter **15**, S3581.

Royall, C. P., A. A. Louis, and H. Tanaka, 2007, J. Chem. Phys. **127**, 044507.

Royall, C. P., A. Malins, A. J. Dunleavy, and R. Pinney, 2015, J. Non-Cryst. Solids **407**, 34.

Royall, C. P., W. C. K. Poon, and E. R. Weeks, 2013, Soft Matter **9**, 17.

Royall, C. P., F. Turci, and T. Speck, 2020, J. Chem. Phys. **153**, 090901.

Royall, C. P., F. Turci, S. Tatsumi, J. Russo, and J. Robinson, 2018, J. Phys. Condens. Matter **30**, 363001.

Royall, C. P., R. van Roij, and A. van Blaaderen, 2005, J. Phys. Condens. Matter **17**, 2315.

Royall, C. P., and S. R. Williams, 2015, Phys. Rep. **560**, 1.

Royall, C. P., S. R. Williams, and H. Tanaka, 2018, J. Chem. Phys. **148**, 044501.

Rudd, W. G., Z. W. Salsburg, A. P. Yu, and F. H. Stillinger, 1968, J. Chem. Phys. **49**, 4857.

Ruelle, D., 1999, *Statistical Mechanics: Rigorous Results* (World Scientific, Singapore).

Ruiz, Sampedro, P., Q.-l. Lei, and R. Ni, 2019, Commun. Phys. **2**, 1.

Runge, K. J., and G. V. Chester, 1987, Phys. Rev. A **36**, 4852.

Russel, W., D. Saville, and W. Schowalter, 1989, *Colloidal Dispersions* (Cambridge University Press, Cambridge, England).

Russo, J., A. C. Maggs, D. Bonn, and H. Tanaka, 2013, Soft Matter **9**, 7369.

Russo, J., F. Romano, and H. Tanaka, 2018, Phys. Rev. X **8**, 021040.

Russo, J., and H. Tanaka, 2012, Sci. Rep. **2**, 505.

Russo, J., and H. Tanaka, 2015, Proc. Natl. Acad. Sci. U.S.A. **112**, 6920.

Russo, J., and H. Tanaka, 2016a, J. Chem. Phys. **145**, 211801.

Russo, J., and H. Tanaka, 2016b, MRS Bull. **41**, 369.

Russo, J., and N. B. Wilding, 2017, Phys. Rev. Lett. **119**, 115702.

Rutgers, M. A., J. H. Dunsmuir, J.-Z. Xue, W. B. Russel, and P. M. Chaikin, 1996, Phys. Rev. B **53**, 5043.

Saija, F., and P. Giaquinta, 1996, J. Phys. Condens. Matter **8**, 8137.

Salsburg, Z. W., and W. W. Wood, 1962, J. Chem. Phys. **37**, 798.

Sammüller, F., S. Hermann, D. de Las Heras, and M. Schmidt, 2023, Proc. Natl. Acad. Sci. U.S.A. **120**, e2312484120.

Sanchez-Burgos, I., E. Sanz, C. Vega, and J. R. Espinosa, 2021, Phys. Chem. Chem. Phys. **23**, 19611.

Sandomirski, K., E. Allahyarov, H. Löwen, and S. U. Egelhaaf, 2011, Soft Matter **7**, 8050.

Sandomirski, K., S. Walta, J. Dubbert, E. Allahyarov, A. B. Schofield, H. Löwen, W. Richtering, and S. Egelhaaf, 2014, Eur. Phys. J. Special Topics **223**, 439.

Sané, J., J. T. Padding, and A. A. Louis, 2010, Faraday Discuss. **144**, 285.

Santana-Solano, J., and J. L. Arauz-Lara, 2001, Phys. Rev. Lett. **87**, 038302.

Santos, A., M. Lopez de Haro, and S. B. Yuste, 1995, J. Chem. Phys. **103**.

Santos, A., S. B. Yuste, and M. Lopez de Haro, 2020, J. Chem. Phys. **153**, 120901.

Santra, M., R. S. Singh, and B. Bagchi, 2013, J. Phys. Chem. B **117**, 13154.

Sanwaria, S., A. Horechyy, D. Wolf, C.-Y. Chu, H.-L. Chen, P. Formanek, M. Stamm, R. Srivastava, and B. Nandan, 2014, Angew. Chem., Int. Ed. **53**, 9090.

Sanyal, S., N. Easwar, S. Ramaswamy, and A. Sood, 1992, Europhys. Lett. **18**, 107.

Sanz, E., and D. Marenduzzo, 2010, J. Chem. Phys. **132**, 194102.

Sanz, E., C. Valeriani, E. Zaccarelli, W. C. K. Poon, M. E. Cates, and P. N. Pusey, 2014, Proc. Natl. Acad. Sci. U.S.A. **111**, 75.

Sanz, E., C. Valeriani, E. Zaccarelli, W. C. K. Poon, P. Pusey, and M. E. Cates, 2011, Phys. Rev. Lett. **106**, 215701.

Scala, A., T. Voigtmann, and C. De Michele, 2007, J. Chem. Phys. **126**, 134109.

Scalliet, C., B. Guiselin, and L. Berthier, 2022, Phys. Rev. X **12**, 041028.

Schaertl, N., D. Botin, T. Palberg, and E. Bartsch, 2018, Soft Matter **14**, 5130.

Schall, P., I. Cohen, D. A. Weitz, and F. Spaepen, 2004, Science **305**, 1944.

Schall, P., D. A. Weitz, and F. Spaepen, 2007, Science **318**5858, 1895.

Schätzel, K., 1991, J. Mod. Opt. **38**, 1849.

Schätzel, K., and B. J. Ackerson, 1992, Phys. Rev. Lett. **68**, 337.

Schätzel, K., and B. J. Ackerson, 1993, Phys. Rev. E **48**, 3766.

Schilling, T., S. Dorosz, H. J. Schöpe, and G. Opletal, 2011, J. Phys. Condens. Matter **23**, 194120.

Schilling, T., and F. Schmid, 2009, J. Chem. Phys. **131**, 231102.

Schilling, T., H. J. Schöpe, M. Oettel, G. Opletal, and I. Snook, 2010, Phys. Rev. Lett. **105**, 025701.

Schindler, M., and A. C. Maggs, 2015, Eur. Phys. J. E **38**, 97.

Schmid, F., and K. Binder, 1992, Phys. Rev. B **46**, 13565.

Schmidt, M., and H. Löwen, 1996, Phys. Rev. Lett. **76**, 4552.

Schmidt, M., and H. Löwen, 1997, Phys. Rev. E **55**, 7228.

Schmidt, M., C. P. Royall, J. Dzubiella, and A. van Blaaderen, 2008, J. Phys. Condens. Matter **20**, 494222.

Schmiedeberg, M., T. K. Haxton, S. R. Nagel, and A. J. Liu, 2011, Europhys. Lett. **96**, 36010.

Schmitt, J., S. Hajiw, A. Lecchi, J. Degrouard, A. Salonen, M. Impéror-Clerc, and B. Pansu, 2016, J. Phys. Chem. B **120**, 5759.

Schmitz, F., and P. Virnau, 2015, J. Chem. Phys. **142**, 144108.

Schmitz, F., P. Virnau, and K. Binder, 2014, Phys. Rev. Lett. **112**, 125701.

Schneider, J., M. Wiemann, A. Rabe, and E. Bartsch, 2017, Soft Matter **13**, 445.

Schöpe, H. J., G. Bryant, and W. van Megen, 2006a, Phys. Rev. E **74**, 060401.

Schöpe, H. J., G. Bryant, and W. van Megen, 2006b, Phys. Rev. Lett. **96**, 175701.

Schöpe, H. J., G. Bryant, and W. van Megen, 2007, J. Chem. Phys. **127**, 084505.

Schroyen, B., C.-P. Hsu, L. Isa, P. van Puyvelde, and J. Vermant, 2019, Phys. Rev. Lett. **122**, 218001.

Sciortino, F., and P. Tartaglia, 2005, Adv. Phys. **54**, 471.

Scott, G. D., and D. M. Kilgour, 1969, J. Phys. D **2**, 863.

Sear, R., 2000, J. Chem. Phys. **113**, 4732.

Segrè, P. N., O. P. Behrend, and P. N. Pusey, 1995, Phys. Rev. E **52**, 5070.

Segrè, P. N., E. Herbolzheimer, and P. Chaikin, 1997, Phys. Rev. Lett. **79**, 2574.

Segrè, P. N., F. Liu, P. Umbanhowar, and D. A. Weitz, 2001, Nature (London) **409**, 594.

Segrè, P. N., S. P. Meeker, P. N. Pusey, and W. C. K. Poon, 1995, Phys. Rev. Lett. **75**, 958.

Segrè, P. N., and P. N. Pusey, 1996, Phys. Rev. Lett. **77**, 771.

Segrè, P. N., and P. N. Pusey, 1997, Physica (Amsterdam) **235A**, 9.

Segrè, P. N., W. van Megen, P. N. Pusey, K. Schätzel, and W. Peters, 1995, J. Mod. Opt. **42**, 1929.

Seguin, A., and O. Dauchot, 2016, Phys. Rev. Lett. **117**, 228001.

Seifert, U., 2012, Rep. Prog. Phys. **75**, 126001.

Sentjabrskaja, T., E. Babaliari, J. Hendricks, M. Laurati, G. Petekidis, and S. U. Egelhaaf, 2013, Soft Matter **9**, 4524.

Sentjabrskaja, T., P. Chaudhuri, M. Hermes, W. C. K. Poon, J. Horbach, S. U. Egelhaaf, and M. Laurati, 2015, Sci. Rep. **5**, 11884.

Sentjabrskaja, T., M. Hermes, W. C. K. Poon, C. D. Estrada, R. Castañda Priego, S. U. Egelhaaf, and M. Laurati, 2014, Soft Matter **10**, 6546.

Sentjabrskaja, T., E. Zaccarelli, C. De Michele, F. Sciortino, P. Tartaglia, T. Voigtmann, S. U. Egelhaaf, and M. Laurati, 2016, Nat. Commun. **7**, 11133.

Shevchenko, E. V., D. V. Talapin, N. A. Kotov, S. O'Brien, and C. B. Murray, 2006, Nature (London) **439**7072, 55.

Shimada, M., H. Mizuno, L. Berthier, and A. Ikeda, 2020, Phys. Rev. E **101**, 052906.

Shokef, Y., and T. C. Lubensky, 2009, Phys. Rev. Lett. **102**, 048303.

Siebenbürger, M., M. Ballauff, and T. Voightmann, 2012, Phys. Rev. Lett. **108**, 255701.

Sierou, A., and J. F. Brady, 2001, J. Fluid Mech. **448**, 115.

Sillrén, P., and J.-P. Hansen, 2010, Mol. Phys. **108**, 97.

Simeonova, N. B., and W. K. Kegel, 2004, Phys. Rev. Lett. **93**, 035701.

Singh, Y., J. P. Stoessel, and P. G. Wolynes, 1985, Phys. Rev. Lett. **54**, 1059.

Sinn, C., A. Heymann, A. Stipp, and T. Palberg, 2001, in *Trends in Colloid and Interface Science XV*, Progress in Colloid and Polymer Science Vol. 118, edited by P. G. Koutsoukos (Springer, New York), p. 266.

Skoge, M., A. Donev, F. H. Stillinger, and S. Torquato, 2006, Phys. Rev. E **74**, 041127.

Sloane, N. J., R. H. Hardin, T. Duff, and J. H. Conway, 1995, Discrete Comput. Geom. **14**, 237.

Smallenburg, F., 2022, Eur. Phys. J. E **45**, 32.

Smallenburg, F., and F. Sciortino, 2013, Nat. Phys. **9**, 554.

Smith, W. O., P. D. Foote, and P. F. Busang, 1929, Phys. Rev. **34**, 1271.

Sollich, P., F. Lequeux, P. Hébraud, and M. E. Cates, 1997, Phys. Rev. Lett. **78**, 2020.

Sollich, P., and N. B. Wilding, 2010, Phys. Rev. Lett. **104**, 118302.

Sollich, P., and N. B. Wilding, 2011, Soft Matter **7**, 4472.

Song, Y., R. M. Stratt, and E. A. Mason, 1988, J. Chem. Phys. **88**, 1126.

Spal, R., C. E. Chen, T. Egami, P. J. Nigrey, and A. J. Heeger, 1980, Phys. Rev. B **21**, 3110.

Speedy, R. J., 1987, Mol. Phys. **62**, 509.

Speedy, R. J., 1994, Mol. Phys. **83**, 591.

Speedy, R. J., 1997, J. Phys. Condens. Matter **9**, 8591.

Speedy, R. J., 1998a, J. Phys. Condens. Matter **10**, 4387.

Speedy, R. J., 1998b, Mol. Phys. **95**, 169.

Squires, T. M., and J. F. Brady, 2005, Phys. Fluids **17**, 073101.

Statt, A., R. Pinchaipat, F. Turci, R. Evans, and C. P. Royall, 2016, J. Chem. Phys. **144**, 144506.

Stillinger, F. H., P. G. Debenedetti, and T. M. Truskett, 2001, J. Phys. Chem. B **105**, 11809.

Stillinger, F. H., and Z. W. Salsburg, 1967, J. Chem. Phys. **46**, 3962.

Stones, A. E., R. P. A. Dullens, and D. G. A. L. Aarts, 2018, J. Chem. Phys. **148**, 241102.

Strating, P., 1999, Phys. Rev. E **59**, 2175.

Striker, H. N., I. Lokteva, M. Dartsch, F. Dallari, C. Goy, F. Westermeier, V. Markmann, S. C. Hövelmann, G. Grübel, and F. Lehmkühler, 2023, J. Phys. Chem. Lett. **14**, 4719.

Stucke, D. P., and V. H. Crespi, 2003, Nano Lett. **3**, 1183.

Succi, S., 2001, *The Lattice Boltzmann Equation: For Fluid Dynamics and Beyond* (Oxford University Press, Oxford).

Sushko, N., and P. van der Schoot, 2005, Phys. Rev. E **72**, 067104.

Tadros, T. F., 2018, *Formulation Science and Technology* (De Gruyter, Berlin).

Taffs, J., and C. P. Royall, 2016, Nat. Commun. **7**, 13225.

Taffs, J., S. R. Williams, H. Tanaka, and C. P. Royall, 2013, Soft Matter **9**, 297.

Takano, K., and S. Hachisu, 1977, J. Chem. Phys. **67**, 2604.

Tamborini, E., and L. Cipeletti, 2012, Rev. Sci. Instrum. **83**, 093106.

Tamborini, E., C. P. Royall, and P. Cicuta, 2015, J. Phys. Condens. Matter **27**, 194124.

Tan, P., N. Xu, and L. Xu, 2014, Nat. Phys. **10**, 73.

Tanaka, H., 2005a, J. Non-Cryst. Solids **351**, 3371.

Tanaka, H., 2005b, J. Non-Cryst. Solids **351**, 3385.

Tanaka, H., 2005c, J. Non-Cryst. Solids **351**, 3396.

Tanaka, H., 2022, J. Non-Cryst. Solids X **13**, 100076.

Tanaka, H., and T. Araki, 2000, Phys. Rev. Lett. **85**, 1338.

Tanaka, H., T. Kawasaki, H. Shintani, and K. Watanabe, 2010, Nat. Mater. **9**, 324.

Tarazona, P., 1984, Mol. Phys. **52**, 81.

Tarazona, P., J. A. Cuesta, and Y. Martínez-Ratón, 2008, in *Theory and Simulation of Hard-Sphere Fluids and Related Systems*, Lecture Notes in Physics Vol. 753, edited by A. Mulero (Springer, New York), pp. 247–341.

Tarjus, G., S. A. Kivelson, Z. Nussinov, and P. Viot, 2005, J. Phys. Condens. Matter **17**, R1143.

Tateno, M., T. Yanagishima, J. Russo, and H. Tanaka, 2019, Phys. Rev. Lett. **123**, 258002.

Tejero, C., and J. Cuesta, 1993, Phys. Rev. E **47**, 490.

Thiele, E., 1963, J. Chem. Phys. **39**, 474.

Thompson, A. P., *et al.*, 2022, Comput. Phys. Commun. **271**, 108171.

Thorneywork, A. L., D. G. Aarts, J. Horbach, and R. P. Dullens, 2017, Phys. Rev. E **95**, 012614.

Thorneywork, A. L., J. L. Abbott, D. G. Aarts, P. Keim, and R. P. Dullens, 2018, J. Phys. Condens. Matter **30**, 104003.

Thorneywork, A. L., J. L. Abbott, D. G. A. L. Aarts, and R. P. A. Dullens, 2017, Phys. Rev. Lett. **118**, 158001.

Thorneywork, A. L., R. Roth, D. G. Aarts, and R. P. Dullens, 2014, J. Chem. Phys. **140**, 161106.

Thorneywork, A. L., R. E. Rozas, R. P. Dullens, and J. Horbach, 2015, Phys. Rev. Lett. **115**, 268301.

Thorneywork, A. L., S. K. Schnyder, D. G. Aarts, J. Horbach, R. Roth, and R. P. Dullens, 2018, Mol. Phys. **116**, 3245.

Tian, J., W. Kob, and J.-L. Barrat, 2022, J. Chem. Phys. **156**, 164903.

Tong, H., and H. Tanaka, 2018, Phys. Rev. X **8**, 011041.

Torquato, S., and F. H. Stillinger, 2010, Rev. Mod. Phys. **82**, 2633.

Torrie, G. M., and J. P. Valleau, 1977, J. Comput. Phys. **23**, 187.

Tough, R., P. Pusey, H. Lekkerkerker, and C. van Den Broeck, 1986, Mol. Phys. **59**, 595.

Trizac, E., M. Madden, and P. Eldridge, 1997, Mol. Phys. **90**, 675.

Troche, K. S., V. R. Coluci, S. F. Braga, D. D. Chinellato, F. Sato, S. B. Legoas, R. Rurali, and D. S. Galvão, 2005, Nano Lett. **5**, 349.

Trudu, F., D. Donadio, and M. Parrinello, 2006, Phys. Rev. Lett. **97**, 105701.

Turci, F., and C. P. Royall, 2016, J. Stat. Mech. 084004.

Turnbull, D., and J. Fisher, 1949, J. Chem. Phys. **17**, 71.

Tymczenko, M., L. F. Marsal, T. Trifonov, I. Rodriguez, F. Ramiro-Manzano, J. Pallares, A. Rodriguez, R. Alcubilla, and F. Meseguer, 2008, Adv. Mater. **20**, 2315.

Uche, O., F. Stillinger, and S. Torquato, 2004, Physica (Amsterdam) **342A**, 428.

Uhlenbeck, G. E., *et al.*, 1963, *Round Table on Statistical Mechanics* (Interscience Publishers, New York).

Urrutia, I., 2011, J. Chem. Phys. **135**, 024511.

Urrutia, I., and G. Castelletti, 2012, J. Chem. Phys. **136**, 224509.

Urrutia, I., and C. Pastorino, 2014, J. Chem. Phys. **141**, 124905.

Valeriani, C., E. Sanz, P. N. Pusey, W. C. K. Poon, M. E. Cates, and E. Zaccarelli, 2012, Soft Matter **8**, 4960.

Valeriani, C., E. Sanz, E. Zaccarelli, W. Poon, M. Cates, and P. Pusey, 2011, J. Phys. Condens. Matter **23**, 194117.

van Blaaderen, A., A. Imhof, W. Hage, and A. Vrij, 1992, Langmuir **8**, 1514.

van Blaaderen, A., J. Peetermans, G. Maret, and J. Dhont, 1992, J. Chem. Phys. **96**, 4591.

van Blaaderen, A., and P. Wiltzius, 1995, Science **270**5239, 1177.

Vanderhoff, J. W., J. F. Vitkuske, E. B. Bradford, and T. Alfrey, 1956, J. Polym. Sci. **20**, 225.

van der Meer, B., M. Dijkstra, and L. Filion, 2017, J. Chem. Phys. **146**, 244905.

van der Meer, B., F. Smallenburg, M. Dijkstra, and L. Filion, 2020, Soft Matter **16**, 4155.

van der Waarden, M., 1950, J. Colloid Sci. **5**, 317.

van der Wee, E., 2019, Ph.D. thesis (Utrecht Universiteit).

van der Wel, C., R. K. Bhan, H. C. Frijters, Z. Gong, A. D. Hollingsworth, S. Sacanna, and D. J. Kraft, 2017, Langmuir **33**, 8174.

van der Werff, J. C., and C. G. de Kruif, 1989, J. Rheol. **33**, 421.

van Duijneveldt, J. S., A. Heinen, and H. Lekkerkerker, 1993, Europhys. Lett. **21**, 369.

van Hecke, M., 2010, J. Phys. Condens. Matter **22**, 033101.

van Helden, A. K., and A. Vrij, 1980, J. Colloid Interface Sci. **78**, 312.

Van Hove, L., 1950, Physica (Amsterdam) **16**, 137.

van Loenen, S. Z., T. E. Kodger, E. A. Padston, S. Nawar, P. Schall, and F. Spaepen, 2019, Phys. Rev. Mater. **3**, 085605.

van Megen, W., T. C. Mortensen, S. R. Williams, and J. Müller, 1998, Phys. Rev. E **58**, 6073.

van Megen, W., R. H. Ottewill, S. M. Owens, and P. N. Pusey, 1985, J. Chem. Phys. **82**, 508.

van Megen, W., and P. N. Pusey, 1991, Phys. Rev. A **43**, 5429.

van Megen, W., and S. Underwood, 1990, Langmuir **6**, 35.

van Megen, W., and S. Underwood, 1993a, Nature (London) **362**, 616.

van Megen, W., and S. M. Underwood, 1993b, Phys. Rev. E **47**, 248.

van Megen, W., and S. M. Underwood, 1993c, Phys. Rev. Lett. **70**, 2766.

van Megen, W., S. M. Underwood, R. H. Ottewill, N. S. J. Williams, and P. N. Pusey, 1987, Faraday Discuss. Chem. Soc. **83**, 47.

van Megen, W., S. M. Underwood, and P. N. Pusey, 1991a, J. Chem. Soc., Faraday Trans. **87**, 395.

van Megen, W., S. M. Underwood, and P. N. Pusey, 1991b, Phys. Rev. Lett. **67**, 1586.

van Roij, R., 2003, J. Phys. Condens. Matter **15**, S3569.

van Teeffelen, S., C. Likos, and Lowen, 2008, Phys. Rev. Lett. **100**, 108302.

Varga, S., G. Ballo, and P. Gurin, 2011, J. Stat. Mech. P11006.

Vega, C., 1998, J. Chem. Phys. **108**, 3074.

Vega, C., and E. G. Noya, 2007, J. Chem. Phys. **127**, 154113.

Vermolen, E., A. Kuijk, L. Filion, M. Hermes, J. Thijssen, M. Dijkstra, and A. van Blaaderen, 2009, Proc. Natl. Acad. Sci. U.S.A. **106**, 16063.

Verwey, E., and J. Overbeek, 1948, *Theory of the Stability of Lyophobic Colloids* (Elsevier, Amsterdam).

Vincent, B., 2012, J. Colloid Interface Sci. **170**, 56.

Vincent, B., 2018, R. Soc. Chem. Hist. Group Newsl. **74**, 10, https://www.rsc.org/globalassets/03-membership-community/connect-with-others/through-interests/interest-groups/historical/newsletters/historical-group-newsletter-summer-2018.pdf.

Vivek, S., C. P. Kelleher, P. Chaikin, and E. R. Weeks, 2017, Proc. Natl. Acad. Sci. U.S.A. **114**, 1850.

Voigtmann, T., 2011, Europhys. Lett. **96**, 36006.

Volmer, M., and A. Weber, 1926, Z. Phys. Chem. (Frankfurt am Main) **119**, 227.

Vossen, D., 2004, Ph.D. thesis (Utrecht University).

Vossen, D. L. J., A. van der Horst, M. Dogterom, and A. van Blaaderen, 2004, Rev. Sci. Instrum. **75**, 2960.

Vrij, A., 1977, in *Colloid and Surface Science*, edited by E. Wolfram (Elsevier, New York), pp. 471–483.

Vrij, A., J. W. Jansen, J. K. G. Dhont, C. Pathmamanoharan, M. M. Kops-Werkhoven, and F. H. M., 1983, Faraday Discuss. **76**, 19.

Vrij, A., E. A. Nieuwenhuis, H. M. Fijnaut, and W. G. M. Agterof, 1978, Faraday Discuss. Chem. Soc. **65**, 101.

Wagner, N. J., 2022, in *Recent Advances in Rheology: Theory, Biorheology, Suspension, and Interfacial Rheology*, edited by D. De Kee and A. Ramachandran (AIP Publishing, Melville, NY), pp. 6-1–6-32.

Wagner, N. J., and J. F. Brady, 2009, Phys. Today **62**, No. 10, 27.

Walbridge, D. J., and J. A. Waters, 1966, Discuss. Faraday Soc. **42**, 294.

Wanasundara, S. N., R. J. Spiteri, and R. K. Bowles, 2012, J. Chem. Phys. **137**, 104501.

Wang, D., E. B. van der Wee, D. Zanaga, T. Altantzis, Y. Wu, T. Dasgupta, M. Dijkstra, C. B. Murray, S. Bals, and A. van Blaaderen, 2021, Nat. Commun. **12**, 1.

Wang, D., *et al.*, 2021, Nat. Phys. **17**, 128.

Wang, F., Z. Wang, Y. Peng, Z. Zheng, and Y. Han, 2018, Soft Matter **14**, 2447.

Wang, G. M., E. M. Sevick, E. Mittag, D. J. Searles, and D. J. Evans, 2002, Phys. Rev. Lett. **89**, 050601.

Wang, J., J. Li, S. Yip, D. Wolf, and S. Phillpot, 1997, Physica (Amsterdam) **240A**, 396.

Wang, J., C. F. Mbah, T. Przybilla, B. Apeleo Zubiri, E. Spiecker, M. Engel, and N. Vogel, 2018, Nat. Commun. **9**, 5259.

Wang, J., C. F. Mbah, T. Przybilla, S. Englisch, E. Spiecker, M. Engel, and N. Vogel, 2019, ACS Nano **13**, 9005.

Wang, J., U. Sultan, E. S. Goerlitzer, C. F. Mbah, M. Engel, and N. Vogel, 2020, Adv. Funct. Mater. **30**, 1907730.

Wang, L., X. An, D. Wang, and Q. Qian, 2016, AIP Adv. **6**, 015115.

Wang, M., S. Jamali, and J. F. Brady, 2020, J. Rheol. **64**, 379.

Wang, Z., F. Wang, Y. Peng, Z. Zheng, and Y. Han, 2012, Science **338**, 87.

Weeks, E. R., J. C. Crocker, A. C. Levitt, A. Schofield, and D. A. Weitz, 2000, Science **287**, 627.

Weeks, E. R., and D. A. Weitz, 2002, Chem. Phys. **284**, 361.

Weeks, J. D., D. Chandler, and H. C. Andersen, 1971, J. Chem. Phys. **54**, 5237.

Weik, F., R. Weeber, K. Szuttor, K. Breitsprecher, J. de Graaf, M. Kuron, J. Landsgesell, H. Menke, D. Sean, and C. Holm, 2019, Eur. Phys. J. Special Topics **227**, 1789.

Weitz, D. A., D. J. Pine, P. N. Pusey, and R. Tough, 1989, Phys. Rev. Lett. **63**, 1747.

Weitz, D. A., J. X. Zhu, D. J. Durian, H. Gang, and D. J. Pine, 1993, Phys. Scr. **T49B**, 610.

Wertheim, M. S., 1963, Phys. Rev. Lett. **10**, 321.

Wette, P., A. Engelbrecht, R. Salh, I. Klassen, D. Menke, D. Herlach, S. Roth, and H. Schöpe, 2009, J. Phys. Condens. Matter **21**, 464115.

Wheatley, R. J., 2013, Phys. Rev. Lett. **110**, 200601.

Wilding, N., and A. Bruce, 2000, Phys. Rev. Lett. **85**, 5138.

Wilding, N. B., and P. Sollich, 2010, J. Chem. Phys. **133**, 224102.

Wilhelm, C., 2008, Phys. Rev. Lett. **101**, 028101.

Williams, I., E. C. Oğuz, P. Bartlett, H. Lowen, and C. P. Royall, 2013, Nat. Commun. **4**, 2555.

Williams, I., E. C. Oğuz, P. Bartlett, H. Lowen, and C. P. Royall, 2015, J. Chem. Phys. **142**, 024505.

Williams, I., E. C. Oğuz, T. Speck, P. Bartlett, H. Löwen, and C. P. Royall, 2016, Nat. Phys. **12**, 98.

Williams, I., F. Turci, J. E. Hallett, P. Crowther, C. Cammarota, G. Biroli, and C. P. Royall, 2018, J. Phys. Condens. Matter **30**, 094003.

Williams, I. P., E. C. Oğuz, H. Löwen, W. C. K. Poon, and C. P. Royall, 2022, J. Chem. Phys. **156**, 184902.

Williams, R., and R. S. Crandall, 1974, Phys. Lett. **48A**, 225.

Williams, S., I. Snook, and W. van Megen, 2001, Phys. Rev. E **64**, 021506.

Williams, S., and W. van Megen, 2001, Phys. Rev. E **64**, 041502.

Williams, S. R., G. Bryant, I. Snook, and W. van Megen, 2006, Phys. Rev. Lett. **96**, 087801.

Wilson, L. G., A. W. Harrison, A. B. Schofield, J. Arlt, and W. C. K. Poon, 2009, J. Phys. Chem. B **113**, 3806.

Wochner, P., C. Gutt, T. Autenrieth, T. Demmer, V. Bugaev, A. Díaz Ortiza, A. Duri, F. Zontone, G. Grübel, and H. Dosch, 2009, Proc. Natl. Acad. Sci. U.S.A. **106**, 11511.

Wöhler, W., and T. Schilling, 2022, Phys. Rev. Lett. **128**, 238001.

Wolynes, P. G., 1985, J. Non-Cryst. Solids **75**, 443.

Wood, N., J. Russo, F. Turci, and C. P. Royall, 2018, J. Chem. Phys. **149**, 204506.

Wood, W. W., 1952, J. Chem. Phys. **20**, 1334.

Wood, W. W., and J. D. Jacobson, 1957, J. Chem. Phys. **27**, 1207.

Woodcock, L. V., 1976, J. Chem. Soc., Faraday Trans. 2 **72**, 1667.

Woodcock, L. V., 1981, Ann. N.Y. Acad. Sci. **371**, 274.

Woodcock, L. V., and C. A. Angell, 1981, Phys. Rev. Lett. **47**, 1129.

Wu, Y. L., D. Derks, A. van Blaaderen, and A. Imhof, 2009, Proc. Natl. Acad. Sci. U.S.A. **106**, 10564.

Wyart, M., and M. E. Cates, 2014, Phys. Rev. Lett. **112**, 098302.

Wyart, M., and M. E. Cates, 2017, Phys. Rev. Lett. **119**, 195501.

Wysocki, A., C. P. Royall, R. Winkler, G. Gompper, H. Tanaka, A. van Blaaderen, and H. Löwen, 2009, Soft Matter **5**, 1340.

Wysocki, A., C. P. Royall, R. G. Winkler, G. Gompper, H. Tanaka, A. van Blaaderen, and H. Löwen, 2010, Faraday Discuss. **144**, 245.

Xiao, H., A. J. Liu, and D. J. Durian, 2022, Phys. Rev. Lett. **128**, 248001.

Xu, H., and C. Barentin, 1995, J. Phys. Condens. Matter **7**, L13.

Xu, H., and M. Baus, 1992, J. Phys. Condens. Matter **4**, L663.

Xu, W., Z. Sun, and L. An, 2010, J. Chem. Phys. **132**, 144506.

Xu, X., S. A. Rice, and A. R. Dinner, 2013, Proc. Natl. Acad. Sci. U.S.A. **110**, 3771.

Yamamoto, R., J. J. Molina, and Y. Nakayama, 2021, Soft Matter **17**, 4226.

Yan, W., E. Corona, D. Malhotra, S. Veerapaneni, and M. Shelley, 2020, J. Comput. Phys. **416**, 109524.

Yanagishima, T., J. Russo, R. P. Dullens, and H. Tanaka, 2021, Phys. Rev. Lett. **127**, 215501.

Yanagishima, T., J. Russo, and H. Tanaka, 2017, Nat. Commun. **8**, 15954.

Yang, J., H. Gould, and W. Klein, 1988, Phys. Rev. Lett. **60**, 2665.

Yethiraj, A., and A. van Blaaderen, 2003, Nature (London) **421**6922, 513.

Yi, G.-R., V. N. Manoharan, S. Klein, K. R. Brzezinska, D. J. Pine, F. F. Lange, and S.-M. Yang, 2002, Adv. Mater. **14**, 1137.

Yi, G.-R., V. N. Manoharan, E. Michel, M. T. Elsesser, S.-M. Yang, and D. J. Pine, 2004, Adv. Mater. **16**, 1204.

Yip, C.-T., M. Isobe, C.-H. Chan, S. Ren, K.-P. Wong, Q. Huo, C.-S. Lee, Y.-H. Tsang, Y. Han, and C.-H. Lam, 2020, Phys. Rev. Lett. **125**, 258001.

Yodh, A., P. Kaplan, and D. Pine, 1990, Phys. Rev. B **42**, 4744.

Young, A., 1979, Phys. Rev. B **19**, 1855.

Yunker, P. J., K. Chen, M. D. Gratale, M. A. Lohr, T. Still, and A. G. Yodh, 2014, Rep. Prog. Phys. **77**, 056601.

Zaccarelli, E., C. Valeriani, E. Sanz, W. C. K. Poon, M. E. Cates, and P. N. Pusey, 2009, Phys. Rev. Lett. **103**, 135704.

Zanotto, E., 2013, *Crystals in Glass: A Hidden Beauty* (Wiley–American Ceramic Society, Hoboken, NJ).

Zargar, R., B. Nienhuis, P. Schall, and D. Bonn, 2013, Phys. Rev. Lett. **110**, 258301.

Zargar, R., J. Russo, P. Schall, H. Tanaka, and D. Bonn, 2014, Europhys. Lett. **108**, 38002.

Zausch, J., J. Horbach, M. Laurati, S. U. Egelhaaf, J. M. Brader, T. Voightmann, and M. Fuchs, 2008, J. Phys. Condens. Matter **20**, 404210.

Zeldovich, J., 1942, Zh. Eksp. Teor. Fiz. **12**, 525.

Zeng, X., and D. W. Oxtoby, 1990, J. Chem. Phys. **93**, 4357.

Zhang, B., and X. Cheng, 2016, Phys. Rev. Lett. **116**, 098302.

Zhang, H., D. J. Srolovitz, J. F. Douglas, and J. A. Warren, 2009, Proc. Natl. Acad. Sci. U.S.A. **106**, 7735.

Zhang, I., R. Pinchaipat, N. B. Wilding, M. A. Faers, P. Bartlett, R. Evans, and C. P. Royall, 2018, J. Chem. Phys. **148**, 184902.

Zhang, K., W. Wendell Smith, M. Wang, Y. Liu, J. Schroers, M. D. Shattuck, and C. S. O'Hern, 2014, Phys. Rev. E **90**, 032311.

Zhang, Y., M. J. Godfrey, and M. A. Moore, 2020, Phys. Rev. E **102**, 042614.

Zhou, Y., and G. Stell, 1989, Mol. Phys. **66**, 767.

Zhu, J., D. J. Durian, J. Müller, D. Weitz, and D. Pine, 1992, Phys. Rev. Lett. **68**, 2559.

Zhu, J., M. Li, R. Rogers, W. Meyer, R. Ottewill, S.-S. S. Crew, W. Russel, and P. Chaikin, 1997, Nature (London) **387**6636, 883.

Ziese, F., G. Maret, and U. Gasser, 2013, J. Phys. Condens. Matter **25**, 375105.

Zykova-Timan, T., J. Horbach, and K. Binder, 2010, J. Chem. Phys. **133**, 014705.

Zykova-Timan, T., R. Rozas, J. Horbach, and K. Binder, 2009, J. Phys. Condens. Matter **21**, 464102.